

Atom-Precise Organometallic Cluster Construction

-Exploring the Molecular Zinc Tool Box

Dan Hung Banh

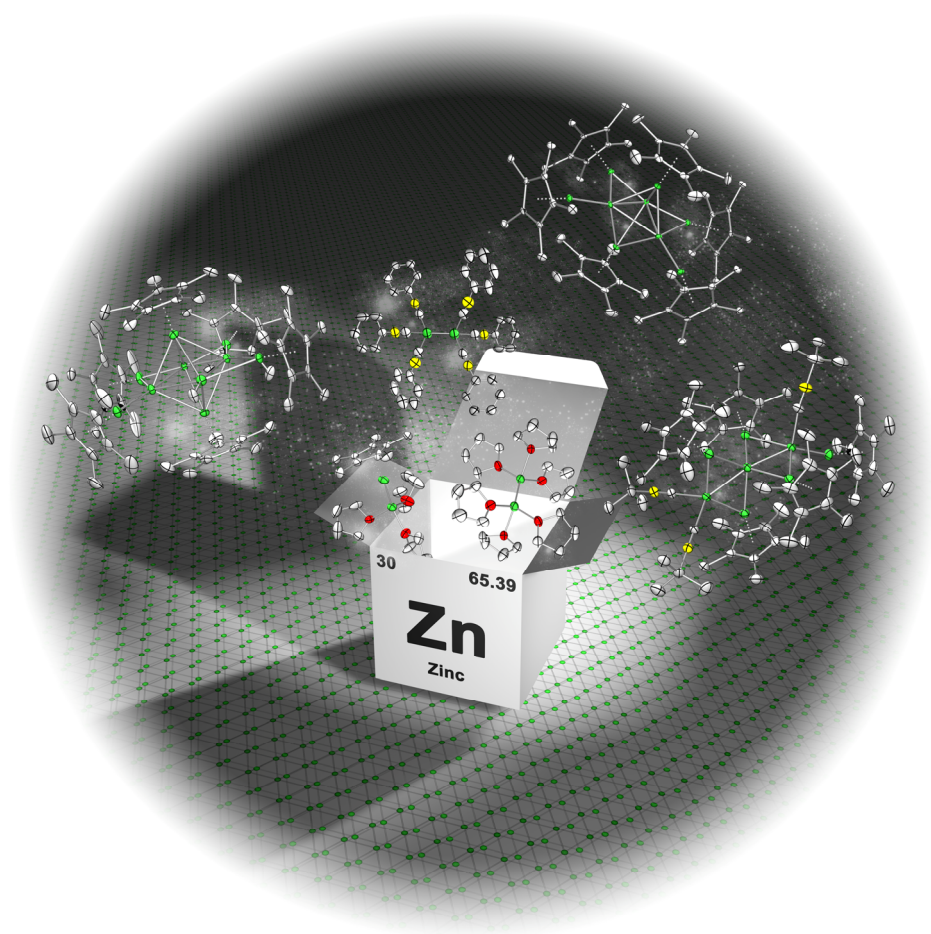
Vollständiger Abdruck der von der Fakultät Chemie der Technischen Universität München zur Erlangung des akademischen Grades eines Doktors der Naturwissenschaften (Dr. rer. nat.) genehmigten Dissertation.

Vorsitzender: Prof. Dr. Thomas Fässler
Prüfende der Dissertation: 1. Prof. Dr. Roland A. Fischer
2. Prof. Dr. Philip P. Power
3. Prof. Dr. Stephan Schulz

Die Dissertation wurde am 19.09.2017 bei der Technischen Universität München eingereicht und durch die Fakultät für Chemie am 07.11.2017 angenommen.

Atom-Precise Organometallic Cluster Construction

-Exploring the Molecular Zinc Tool Box



Dissertation

Dan Hung Banh

Eidesstattliche Erklärung

Ich erkläre an Eides statt, dass ich die bei der promotionsführenden
Einrichtung Fakultät für Chemie

der TUM zur Promotionsprüfung vorgelegte Arbeit mit dem Titel:

Atom-Precise Organometallic Cluster Construction – Exploring the Molecular Zinc Tool Box

in der Fakultät für Chemie, Lehrstuhl für Anorganische und Metallorganische Chemie

Fakultät, Institut, Lehrstuhl, Klinik, Krankenhaus, Abteilung

unter der Anleitung und Betreuung durch: Prof. Dr. Roland A. Fischer ohne sonstige Hilfe erstellt und bei der Abfassung nur die gemäß § 6 Ab. 6 und 7 Satz 2 angebotenen Hilfsmittel benutzt habe.

Ich habe keine Organisation eingeschaltet, die gegen Entgelt Betreuerinnen und Betreuer für die Anfertigung von Dissertationen sucht, oder die mir obliegenden Pflichten hinsichtlich der Prüfungsleistungen für mich ganz oder teilweise erledigt.

Ich habe die Dissertation in dieser oder ähnlicher Form in keinem anderen Prüfungsverfahren als Prüfungsleistung vorgelegt.

Die vollständige Dissertation wurde in _____
veröffentlicht. Die promotionsführende Einrichtung

hat der Veröffentlichung zugestimmt.

Ich habe den angestrebten Doktorgrad noch nicht erworben und bin nicht in einem früheren Promotionsverfahren für den angestrebten Doktorgrad endgültig gescheitert.

Ich habe bereits am _____ bei der Fakultät für _____
_____ der Hochschule _____
unter Vorlage einer Dissertation mit dem Thema _____
_____ die Zulassung zur Promotion beantragt mit dem Ergebnis: _____

Die öffentlich zugängliche Promotionsordnung der TUM ist mir bekannt, insbesondere habe ich die Bedeutung von § 28 (Nichtigkeit der Promotion) und § 29 (Entzug des Doktorgrades) zur Kenntnis genommen. Ich bin mir der Konsequenzen einer falschen Eidesstattlichen Erklärung bewusst.

Mit der Aufnahme meiner personenbezogenen Daten in die Alumni-Datei bei der TUM bin ich

einverstanden, nicht einverstanden.

Garching, 15.09.2017, Unterschrift

Acknowledgement

First of all, I would like to express my special thanks to my supervisor **Prof. Dr. Roland A. Fischer**. I am very grateful that he has taken me into his group and has been hosting me for more than six years now. I appreciate the exceptional degree of scientific freedom, which I enjoyed over the four years of being a PhD student. I am thankful for the excellent support and trust regarding to my work and the great opportunities to present my results at diverse conferences. Your scientific enthusiasm has always been contagious and a motivation. Thank you very much!

I would also like to thank **Prof. Dr. Philip Power** and **Prof. Dr. Stephan Schulz** for accepting to be co-referees of this dissertation.

Furthermore, I want to address my special thanks to **Dr. Christian Gemel** for his constant support, interest, creative ideas and all the hour lasting discussions during work time as well as out of work time that contribute to this thesis.

I would particularly like to thank **Kerstin Freitag** for her extraordinary scientific support, for sharing the interest in zinc chemistry and the excellent team work. This includes the shared suffer and joy of everyday lab life, the frequent excitement for uncharacterized red solutions and novel shiny crystals or the raised blood pressure when solving a crystal structure. Among others the regular bets, which have led to diverse loses and wins on both sites or the special experiments regarding advanced scientific lab skills (bleaching, shredder, alum), made everyday lab work merrier. Besides, I am thankful for all the weekly discussions about our common blue-white sometimes unbearable friends. Thank you for your friendship.

I am thankful to **Sabine Pankau** for the exceptional support in dealing with administrative issues during my time at the Ruhr University Bochum, for always being patient and solving

administrative issues almost instantly. Likewise, I want to thank **Jacinta Essling** for her help with administrative problems.

I also want to thank the AMC office team **Gabriele Querbach** and **Martin Schellerer** as well as **Irmgard Grötsch** for their administrative support at the Technical University Munich.

I am very grateful to **Prof. Dr. Simon Aldridge** for being my formal mentor with regard to my PhD study at the Technical University Munich and giving me the opportunity to visit his lab for three months at the University of Oxford. I really enjoyed the time in Oxford and am very thankful for this great scientific and cultural experience.

Furthermore, I would like to thank the following people and institutions without whom this work would be to a great extent data deficient:

- **Prof. Dr. Jean-Yves Saillard, Dr. Samia Kahlal, Dr. Régis Gautier** and **Julius Hornung** for all the quantum chemical calculations for my compounds.
- **Dr. Rüdiger W. Seidel** and **Dr. Alexander Pöthig** for their support in solving single crystal X-ray structures.
- **Hans Joachim Hauswald** for the countless hours he patiently spent measuring low temperature NMR spectra of my samples.
- **Microanalysis laboratory Kolbe** for all the EA and AAS measurements.
- **Dr. Alexander Pöthig, Philipp Altmann** and **David Mayer** for the support conducting single crystal X-Ray measurements at the Technical University Munich.

I thank **Uschi Herrmann** for keeping some order in the chaos of the labs at the Ruhr University Bochum.

Furthermore, I want to thank **Martin Schellerer** for providing the lab at the Technical University of Munich with chemicals and supply.

I am thankful to all my bachelor and master students: **Christine Schulz, Gregor Lipinski, Katharina Dilchert, Thilo Kratz, Thomas Dunkel** and **Tobias Stalder**.

Moreover, I want to thank all the former and current **members of the Fischer group** for an excellent working atmosphere, the daily lunches together and all the after work activities, *e.g.* barbecue, watching football, the legendary chemical party *etc.* Herein, I especially address my thanks to **Kerstin Freitag, Dr. Mariusz Molon, Inke Hante, Katharina Dilchert, Dr. Sebastian Henke, Dr. Gregor Kieslich, Dr. Christoph Rösler, Dr. Andreas Schneemann** and **Philipp Altmann**.

I especially want to thank **Dr. Mariusz Molon** for sharing his humour and exceptional creativity and ideas. Although it was a quiet short time we spend together in the lab and in the office, it was a great time. Thank you for your support and friendship.

Besides, I would like to thank **Inke Hante** for sharing the same view on many aspects, for constantly being open for discussions, which among others led to our cleverly designed alternative career plans and for her friendship.

Special thanks go to **Katharina Dilchert** for her assistance work in the lab and her friendship.

Furthermore, I thank my **gourmet friends Kerstin Freitag** and **Inke Hante** for discussing and testing latest products and developments on the food and drink market. I have enjoyed our regular get together, especially at Bochum Kulinarisch.

I am thankful to the **Fonds der Chemischen Industrie** for a PhD scholarship, the **Ruhr University Research School Plus** for funding my research stay in Oxford and the **Technical University Munich Graduate School** for financial support.

I thank the **Frauensportgruppe** for participating in the weekly badminton meetings and all the efforts to keep my exhaustion level as low as possible when teaming up with me.

I thank the **LFC Werne** for all the more or less magnificent football games every Monday evening.

Last but not least I would like to thank my parents **Muoi Tao** and **Quang Banh** as well as my siblings **Quyen Arenskötter** and **Minh Banh** for supporting me.

“Do. Or do not. There is no try”

(Yoda – Star Wars: The Empire Strikes Back)

CONTENT

1	Introduction	1
1.1	Metal Clusters.....	1
1.1.1	Naked Metal Clusters	2
1.1.2	Dendrimer Stabilized Metal Clusters	5
1.1.3	Metalloid Clusters	7
1.2	Cluster Models.....	14
1.2.1	Jellium Model.....	14
1.2.2	Wade-Mingos Rule	17
1.3	Zinc rich Compounds: On the Borderline between Coordination and Cluster Chemistry	18
1.4	$[\text{Zn}_2\text{Cp}^*_2]$ – A Milestone in Low-Valent Zinc Chemistry	20
1.4.1	First Reactivity Studies of $[\text{Zn}_2\text{Cp}^*_2]$ towards Protonic Reagents and Lewis bases	23
1.4.2	Derivatives $[\text{Zn}_2\text{L}_n]$ ($\text{L} \neq \text{Cp}^*$) of $[\text{Zn}_2\text{Cp}^*_2]$	26
1.4.3	Stable Cationic $\text{Zn}^{\text{I}}\text{-Zn}^{\text{I}}$ Bonded Species in the Environment of the Weakly Coordinating Anion $[\text{BAr}_4^{\text{F}}]^-$	29
1.5	From Simple Coordination Chemistry to Hume-Rothery Type Clusters	32
2	Motivation	39
3	Summary	41
4	Results and Discussion.....	46
4.1	Effects of Different Ligands on $[\text{Cp}^*\text{Zn}_2(\text{THF})_3][\text{BAr}_4^{\text{F}}]$ and $[\text{Zn}_2(\text{THF})_6][\text{BAr}_4^{\text{F}}]_2$	46
4.1.1	Synthesis of $[\text{Cp}^*\text{Zn}_2(\text{THF})_3][\text{BAr}_4^{\text{F}}]$ (1 $[\text{BAr}_4^{\text{F}}]$)	46
4.1.2	Spectroscopic and Structural Features of $[\text{Cp}^*\text{Zn}_2(\text{THF})_3][\text{BAr}_4^{\text{F}}]$ (1 $[\text{BAr}_4^{\text{F}}]$).	47
4.1.3	Synthesis of $[\text{Zn}_2(\text{THF})_6][\text{BAr}_4^{\text{F}}]_2$ (2 $[\text{BAr}_4^{\text{F}}]_2$)	51
4.1.4	Synthesis of $[\text{Zn}_2(\text{CNPh})_6][\text{BAr}_4^{\text{F}}]_2$ (3 $[\text{BAr}_4^{\text{F}}]_2$)	52

4.1.5	Spectroscopic and structural features of $[\text{Cp}^*\text{Zn}_2(\text{CNPh})_6][\text{BAr}_4^{\text{F}}]_2$ (3 $[\text{BAr}_4^{\text{F}}]_2$).....	53
4.1.6	Summary	54
4.2	Atom Precise Zinc Clusters	55
4.2.1	Synthesis of $\{[\text{Zn}_{10}](\text{Cp}^*)_6\text{Me}\}[\text{BAr}_4^{\text{F}}]$ (4 $[\text{BAr}_4^{\text{F}}]$)	57
4.2.2	Spectroscopic and Structural Features of $\{[\text{Zn}_{10}](\text{Cp}^*)_6\text{Me}\}[\text{BAr}_4^{\text{F}}]$ (4 $[\text{BAr}_4^{\text{F}}]$).....	58
4.2.3	Synthesis of $\{[\text{Zn}_9](\text{Cp}^*)_6\}$ (5).....	61
4.2.4	Spectroscopic and Structural Features of $\{[\text{Zn}_9](\text{Cp}^*)_6\}$ (5)	62
4.2.5	Synthesis of $\{[\text{Zn}_8](\text{Cp}^*)_5(\text{CN}^t\text{Bu})_3\}[\text{BAr}_4^{\text{F}}] \cdot 4 \text{C}_6\text{H}_5\text{F}$ (6 $[\text{BAr}_4^{\text{F}}] \cdot 4 \text{C}_6\text{H}_5\text{F}$) ..	64
4.2.6	Structural Features of $\{[\text{Zn}_8](\text{Cp}^*)_5(\text{CN}^t\text{Bu})_3\}[\text{BAr}_4^{\text{F}}] \cdot 4 \text{C}_6\text{H}_5\text{F}$ (6 $[\text{BAr}_4^{\text{F}}] \cdot 4 \text{C}_6\text{H}_5\text{F}$)	65
4.2.7	Theoretical Investigations on $\{[\text{Zn}_{10}](\text{Cp}^*)_6\text{Me}\}^+$ (4) and $\{[\text{Zn}_9](\text{Cp}^*)_6\}$ (5)...	66
4.2.8	Summary	72
4.3	Nanobrass	73
4.3.1	Synthesis of $[\text{Zn}_2\text{CuCp}^*_3]$ (7) and $[\text{M}_7\text{Cp}^*_5]$ (8)	74
4.3.2	Spectroscopic and Structural Features of $[\text{M}_7\text{Cp}^*_5]$ (8).....	75
4.3.3	Synthesis of $[\text{Zn}_5\text{Cu}_2\text{Cp}^*_5][\text{BAr}_4^{\text{F}}]$ (9 $[\text{BAr}_4^{\text{F}}]$).....	78
4.3.4	Spectroscopic and structural features of $[\text{Zn}_5\text{Cu}_2\text{Cp}^*_5][\text{BAr}_4^{\text{F}}]$ (9 $[\text{BAr}_4^{\text{F}}]$).....	80
4.3.5	Theoretical investigations on $[\text{Zn}_5\text{Cu}_2\text{Cp}^*_5]^+$ (9).....	83
4.3.6	Summary	91
5	Outlook.....	93
6	Experimental Section	95
6.1	General Methods.....	95
6.2	Nuclear Magnetic Resonance Spectroscopy (NMR).....	95
6.3	Infrared Spectroscopy (IR)	97
6.4	Elemental Analysis (EA) and Atom Absorption Spectroscopy (AAS).....	97
6.5	Mass Spectrometry (MS)	97

6.5.1	Liquid Injection Field Desorption Ionization (LIFDI) MS	97
6.5.2	Electrospray Ionization (ESI) MS	98
6.6	Single Crystal X-ray Diffraction (XRD)	98
6.7	Starting Compounds	99
6.8	Synthesis and Characterisation of Compounds	100
6.9	Supplementary NMR spectra of <i>in situ</i> experiments from chapter 4.3	106
6.10	Packing of the salts 1 [BAr ^F] ₂ , 3 [BAr ^F] ₂ · 4 CH ₂ Cl ₂ , 4 [BAr ^F] ₄ · 5 C ₆ H ₅ F,	
	6 [BAr ^F] ₄ · 4 C ₆ H ₅ F and 9 [BAr ^F] ₄ · 5 C ₆ H ₅ F in the respective unit cell	107
6.11	Computational details	110
6.11.1	Computational Details for {[Zn ₁₀](Cp*) ₆ Me} ⁺ (4), {[Zn ₁₀](Cp) ₆ Me} ⁺	
	(4'), {[Zn ₉](Cp) ₅ Me ₂ } ⁺ (4''), {[Zn ₉](Cp*) ₆ } (5) and {[Zn ₉](Cp) ₆ } (5')	110
6.11.2	Computational Details for [Zn ₅ Cu ₂ Cp* ₅] ⁺ (9)	114
6.12	Crystallographic Data	116
7	Literature	119
8	Supplement	127
8.1	Conferences: Poster Presentations	127
8.2	Publications	127
8.2.1	Thesis Related Publications	127
8.2.2	Other Publications	128
8.3	Curriculum Vitae	129

LIST OF FIGURES

Figure 1. Supersonic jet source	2
Figure 2. Gas aggregation source.....	3
Figure 3. Ion sputtering source and laser ablation source	4
Figure 4. Phenylazomethin dendrimer	5
Figure 5. Schematic set-up of a co-codensation apparatus	8
Figure 6. Molecular structures of $[Al_7R_6]^-$ and $[Al_{12}R_8]^-$ ($R = N(SiMe_3)_2$) and the topological relation of the aluminum atom arrangement with the solid state structure of elemental Al	10
Figure 7. Arrangement of aluminium atoms in $[Al_{69}R_{18}]^{3-}$ and $[Al_{77}R_{20}]^{2-}$ ($R = N(SiMe_3)_2$) ..	11
Figure 8. Stepwise fragmentation of $[Ga_{13}(GaR)_6]^-$ ($R = C(SiMe_3)_3$).....	12
Figure 9. Two different projections of the $[Ga_{84}R_{20}]^{4+}$ anion ($R = N(SiMe_3)_2$)	13
Figure 10. Molecular structure of $[Cu_{13}\{S_2CN^iBu\}_6(C\equiv CCO_2Me)_4]^+$	14
Figure 11. Cluster shapes according to the improved ellipsoids jellium model normalized to a constant volume.....	16
Figure 12. Molecular structure of $[Mo(ZnMe)_9(ZnCp^*)_3]$	19
Figure 13. Molecular structures of $[Mo(ZnMe)_9(ZnCp^*)_3]$, $[Ru(ZnMe)_6(ZnCp^*)_4]$, $[Rh(ZnMe)_6(ZnCp^*)_3]$ and $[Pd(ZnMe)_4(ZnCp^*)_4]$	20
Figure 14. Molecular structure of $[Zn_2Cp^*_2]$	22
Figure 15. HOMO-4 corresponding to the Zn-Zn interaction in $[Zn_2Cp^*_2]$	23
Figure 16. Molecular structure of $[Ge_9Zn-ZnGe_9]^{6-}$	28
Figure 17. Molecular structure of $[Cp^*_3Zn_4(Et_2O)_2][BAR_4^F]$	29
Figure 18. Molecular structure of the $[Zn_2(THF)_6]^{2+}$ dication	30
Figure 19. Molecular structures of $[Ga_2(ZnCp^*)_2(GaCp^*)_4]^{2+}$ and $[Zn_2(\mu-GaCp^*)_2GaCp^*_4]^{2+}$	31
Figure 20. Molecular structures of $[Pd(GaCp^*)_2(ZnCp^*)_2(ZnZnCp^*)_2]$ and $[Pd(ZnCp^*)_4(ZnZnCp^*)_4]$	32
Figure 21. Molecular structures of $[Pd(ZnCp^*)_4(ZnMe)_2\{Zn(tmeda)\}]$ and $[Cp^*Ni(ZnCp^*)_3]$	34
Figure 22. Molecular structures of $[Pd(CN^iBu)_2(ZnCp^*)_4]$ and $[Ni(ZnCp^*)(ZnMe)(PMe_3)_3]$..	36
Figure 23. Analogy between H_2 and $[Zn_2Cp^*_2]$	37
Figure 24. Molecular structure of $[(ZnCp^*)_4(Cu(CN^iBu))_4]$ and a cutout of a $[Zn_{16}Cu_{10}]$ cluster from the solid state structure of γ -brass showing the inversed tetrahedral motifs.....	38

Figure 25. Overview of the synthesized compounds 1-4 or of their cations: 1, 2, 3 and 4	43
Figure 26. Overview of the synthesized compounds 5-8 or of their cations: 5, 6, 7 and 8	44
Figure 27. Overview of the synthesized cation 9	45
Figure 28. Molecular structure of the cation $[\text{Cp}^*\text{Zn}_2(\text{THF})_3]^+$ (1)	49
Figure 29. Molecular structures of $[\text{Cp}^*\text{Ru}(\text{ZnCp}^*)_3(\text{ZnMe})_2]$ and $[(\text{Ph}_2\text{P}(\text{NDipp})_2)_2\text{Zn}_2]$	49
Figure 30. Steric influence of two adjacent $[\text{BAR}_4^{\text{F}}]^-$ anions on $[\text{Cp}^*\text{Zn}_2(\text{THF})_3]^+$ in the solid state.....	50
Figure 31. Molecular structure of the dication $[\text{Zn}_2(\text{CNPh})_6]^{2+}$ (3)	54
Figure 32. Molecular structure of $\{[\text{Zn}_{10}](\text{Cp}^*)_6\text{Me}\}^+$ (4).....	60
Figure 33. Molecular structure of $[\text{Zn}_{\text{cen}}@(\text{Zn}_8\text{Bi}_4)_{\text{ico}}@(\text{Bi}_7)]^{5-}$ and $[\text{Ni}(\text{ZnCp}^*)_4(\text{ZnMe})_4]$	60
Figure 34. ^1H NMR of 5 · 2 PhMe in CD_2Cl_2 at temperatures between $(-30) - (-90)^\circ\text{C}$	62
Figure 35. Molecular structure of $\{[\text{Zn}_9](\text{Cp}^*)_6\}$ (5)	63
Figure 36. Relation of the Zn cores of 4 and 5	64
Figure 37. Molecular structure of $\{[\text{Zn}_8](\text{Cp}^*)_5(\text{CN}^t\text{Bu})_3\}^+$ (6).....	66
Figure 38. Occupied t_{2g} skeletal orbitals of $[\text{B}_6\text{H}_6]^{2-}$ and the related t_{2g} -derived orbitals of 4 . 68	
Figure 39. The major Kohn-Sham orbitals of the model cluster $\{[\text{Zn}_9](\text{Cp})_5\text{Me}_2\}^+$ (4'' , C_{2v}) associated with the five SEPs.....	69
Figure 40. The major Kohn-Sham orbitals of the model cluster $\{[\text{Zn}_9](\text{Cp})_6\}$ (5' , C_{2v}) associated with the four SEPs.	70
Figure 41. ELF color density plot of a slice through the $\text{Zn}_2\text{-Zn}_9\text{-Zn}_5$ plane 4'	71
Figure 42. Zinc cores of the ligand-protected clusters $\{[\text{Zn}_{10}](\text{Cp}^*)_6\text{Me}\}^+$ (4), $\{[\text{Zn}_9](\text{Cp}^*)_6\}$ (5) and $\{[\text{Zn}_8](\text{Cp}^*)_5(\text{CN}^t\text{Bu})_3\}^+$ (6)	72
Figure 43. Molecular structure of $[\text{M}_7\text{Cp}^*_5]$ ($\text{M} = \text{Zn}$ or Cu) (8).....	78
Figure 44. Molecular structure of $[\text{Zn}_5\text{Cu}_2\text{Cp}^*_5]^+$ (9)	83
Figure 45. Molecular graph and contour map of the Laplacian $\nabla^2\rho(r)$ of 9	84
Figure 46. ELF color density plot of a slice through the $\text{Cu}_1\text{-Cu}_2\text{-Zn}_3$ plane and the $\text{Zn}_3\text{-Zn}_4\text{-Zn}_5$ plane in the cation 9	85
Figure 47. Deformation densities $\delta\rho$ which are associated with pair-wise orbital interactions in $[\text{Zn}_5\text{Cu}_2\text{Cp}^*_5]^+$ (9)	88
Figure 48. Preliminary molecular structure of $\{[\text{Cu}_3\text{Zn}_5](\text{Cp}^*)_4(\text{CN}^t\text{Bu})_4\}^+$ (10)	94
Figure 49. Introducing solvent to a J. Young NMR tube at low temperatures.	96
Figure 50. ^1H NMR spectra of a 1:1 mixture of $\text{Cu}(\text{OAc})$ and $[\text{Zn}_2\text{Cp}^*_2]$ in C_6D_6 at room temperature over a period of 3 days.	106

Figure 51. ^1H NMR of a 1:2 mixture of $[\text{Zn}_2\text{CuCp}^*_3]$ and $[\text{Cp}^*\text{Zn}_2(\text{Et}_2\text{O})_3][\text{BAr}_4^{\text{F}}]$ at temperatures between $(-50) - 18$ °C in flourobenezene/ C_6D_6 (90:10 Vol%).	106
Figure 52. Packing of $\mathbf{1}[\text{BAr}_4^{\text{F}}]_2$ in the unit cell.	107
Figure 53. Packing of $\mathbf{3}[\text{BAr}_4^{\text{F}}]_2 \cdot 4 \text{CH}_2\text{Cl}_2$ in the unit cell.	108
Figure 54. Packing of $\mathbf{4}[\text{BAr}_4^{\text{F}}] \cdot 5 \text{C}_6\text{H}_5\text{F}$ in the unit cell.	108
Figure 55. Packing of $\mathbf{6}[\text{BAr}_4^{\text{F}}] \cdot 4 \text{C}_6\text{H}_5\text{F}$ in the unit cell.	109
Figure 56. Packing of $\mathbf{9}[\text{BAr}_4^{\text{F}}] \cdot 5 \text{C}_6\text{H}_5\text{F}$ in the unit cell.	109
Figure 57. Optimized structure of $\{[\text{Zn}_{10}](\text{Cp}^*)_6\text{Me}\}^+$ ($\mathbf{4}$) (PBE0/Def2-TZVPP)	110
Figure 58. Optimized structure of $\{[\text{Zn}_{10}](\text{Cp})_6\text{Me}\}^+$ ($\mathbf{4}'$) (PBE0/Def2-TZVPP)	111
Figure 59. Optimized structure of $\{[\text{Zn}_{10}](\text{Cp})_5\text{Me}_2\}^+$ ($\mathbf{4}''$) (PBE0/Def2-TZVPP)	111
Figure 60. Optimized structure of $\{[\text{Zn}_9](\text{Cp}^*)_6\}^+$ ($\mathbf{4}$) (PPBE0/Def2-TZVPP)	112
Figure 61. Optimized structure of $\{[\text{Zn}_9](\text{Cp})_6\}^+$ ($\mathbf{5}'$) (PPBE0/Def2-TZVPP)	113
Figure 62. Optimized structure of $[\text{Zn}_5\text{Cu}_2\text{Cp}^*_5]^+$ ($\mathbf{9}$) (BP86/TZVPP)	114

LIST OF SCHEMES

Scheme 1. Irregular stepwise complexation of DPA-PyTMP with PtCl ₄	6
Scheme 2. Synthesis of AlCl ₃	8
Scheme 3. Improved route for the synthesis of [Zn ₂ Cp* ₂] by Carmona <i>et al.</i>	21
Scheme 4. Formation of [Cp*Zn{(CNXyl)(C ₅ Me ₅)}] from [Zn ₂ Cp* ₂].....	23
Scheme 5. Preparation of the Lewis acid-base adducts [Cp*Zn-Zn(LB) ₂ (η ¹ -Cp*)].....	24
Scheme 6. Synthesis of Zn ^I -Zn ^I bonded species exhibiting O-donor ligands	25
Scheme 7. Synthesis of [Zn ₂ L ₂] species <i>via</i> (1) reductive coupling and (2) protonation of [Zn ₂ Cp* ₂]	26
Scheme 8. Reversible reaction of [Zn ₂ (μ-η ² -Me ₂ Si(NC ₆ H ₃ -2,6- <i>i</i> Pr ₂) ₂)] to [Zn ₂ (Me ₂ Si(NC ₆ H ₃ -2,6- <i>i</i> Pr ₂) ₂) ₂] ²⁻	27
Scheme 9. Synthesis of different [Zn ₂ L ₂] compounds <i>via</i> protonation of [Zn ₂ Cp* ₂] with LH	28
Scheme 10. Two different pathways to synthesise [Cp*Zn ₂ (THF) ₃][BAr ₄ ^F] (1 [BAr ₄ ^F])	47
Scheme 11. Synthesis of [Zn ₂ (THF) ₆][BAr ₄ ^F] ₂ (2 [BAr ₄ ^F] ₂) <i>via</i> precipitation from a THF solution of [Cp*Zn ₂ (THF) ₃][BAr ₄ ^F] (1 [BAr ₄ ^F]).....	51
Scheme 12. Synthesis of [Zn ₂ (CNPh) ₆][BAr ₄ ^F] ₂ (3 [BAr ₄ ^F] ₂).	52
Scheme 13. Reactivity of [Zn ₂ (THF) ₆][BAr ₄ ^F] ₂ (2 [BAr ₄ ^F] ₂).....	55
Scheme 14. Synthesis of the first examples of medium sized ligand protected zinc clusters: {[Zn ₁₀](Cp*) ₆ Me} ⁺ (4), {[Zn ₉](Cp*) ₆ } (5), and {[Zn ₈](Cp*) ₅ (CN ^{<i>t</i>} Bu) ₃ } ⁺ (6).....	57
Scheme 15. Synthesis of {[Zn ₁₀](Cp*) ₆ Me}[BAr ₄ ^F] (4 [BAr ₄ ^F]).....	58
Scheme 16. Synthesis of {[Zn ₉](Cp*) ₆ } (5).....	61
Scheme 17. Synthesis of {[Zn ₈](Cp*) ₅ (CN ^{<i>t</i>} Bu) ₃ }[BAr ₄ ^F] · 4 C ₆ H ₅ F (6 [BAr ₄ ^F] · 4 C ₆ H ₅ F). ...	65
Scheme 18. Synthesis of [Zn ₂ CuCp* ₃] (7) and [M ₇ Cp* ₅] (M = Zn or Cu) (8).....	74
Scheme 19. Systematic determination of the composition and the assignment of Zn/Cu to the correct position in the molecular structure of 8	76
Scheme 20. Synthesis of [Zn ₅ Cu ₂ Cp* ₅][BAr ₄ ^F] (9 [BAr ₄ ^F]).....	79
Scheme 21. Systematic determination of the composition and the assignment of Zn/Cu to the correct position in the molecular structure of 9	81
Scheme 22. Possible fragmentation patterns for the EDA of 9	86
Scheme 23. Related compounds to 9 , which can be evaluated by quantum mechanical methods	90

LIST OF TABLES

Table 1. List of the synthesized compounds.	45
Table 2. EDA-NOCV results for $[\text{Zn}_5\text{Cu}_2\text{Cp}^*_5]^+$ (9) at BP86/TZVPP upon homolytic fragmentation giving the interacting fragments $[(\mu_3\text{-ZnZnCp}^*)(\text{ZnCu}_2\text{Cp}^*_3)]$ and $[\mu_3\text{-ZnZnCp}^*]^+$	88
Table 3. EDA-NOCV results for $[\text{Zn}_5\text{Cu}_2\text{Cp}^*_5]^+$ (9) at BP86/TZVPP upon homolytic fragmentation giving the interacting fragments $[(\mu_3\text{-ZnZnCp}^*)(\text{ZnCu}_2\text{Cp}^*_3)]^{++}$ and $[\mu_3\text{-ZnZnCp}^*]^+$ as well as upon heterolytic fragmentation giving the interacting fragments $[(\mu_3\text{-ZnZnCp}^*)(\mu_3\text{-ZnZnCp}^*)]^{2+}$ and $[\text{ZnCu}_2\text{Cp}^*_3]^-$	89
Table 4. Selected thesis related reactions and preliminary outcome.....	105
Table 5. Comparison of the Zn-Zn distances as determined from the molecular structure of 4 in the solid state and the calculated values obtained from the geometry optimized models 4 , 4' and 4''	112
Table 6. Comparison of the Zn-Zn distances as determined from the molecular structure of 5 in the solid state and the calculated values obtained from the geometry optimized models 5 and 5'	113
Table 7. Comparison of selected interatomic distances and angles as determined from the molecular structure of 9 in the solid state and the calculated values obtained from the geometry optimized model 9	115

LIST OF ABBREVIATIONS

AAS	Atom Absorption Spectroscopy
BAr_4^{F}	$\text{B}\{(\text{C}_6\text{H}_3(\text{CF}_3)_2)\}_4$
Calc.	Calculated
Centr.	Centroid
cod	1,5-Cycloocatadiene
Cp	Cyclopentadienyl
Cp^*	Pentamethylcyclopentadienyl
DDP	$\text{HC}(\text{CMeNC}_6\text{H}_3\text{-2,6-}^i\text{Pr}_2)_2$
DFT	Density Functional Theory
Dipp	2,6-Diisopropylphenyl
dmap	4-(Dimethylamino)pyridine
EA	Elemental Analyses
ELF	Electron Localization Function
ESI	Electrospray Ionisation
Et	Ethyl
^iPr	<i>iso</i> -propyl
IR	Infrared
LIFDI	Liquid Injection Field Desorption Ionisation
Me	Methyl
MO	Molecular Orbital

NBO	Natural Bond Orbital
NHC	N-Heterocyclic Carbene
Ph	Phenyl
SEP	Skeletal Electron Pair
^t Bu	<i>tert</i> -butyl
THF	Tetrahydrofuran
TMEDA	<i>N,N,N',N'</i> -Tetramethylethan-1,2-diamine

1 INTRODUCTION

1.1 Metal Clusters

When looking at the periodic table of elements it is apparent, that the majority of elements are metals. Hence it is hardly surprising, that a lot is known about the properties of bulk metals and their stable compounds such as metal salts, oxides or sulfides. The formation and cleavage of metal-metal bonds are essential processes in nature and their elucidation is important for the technological evolution of mankind. It is therefore all the more surprising, that relatively little is known about intermediate species on the way from molecular metal species to the bulk metal or vice versa. F.A. Cotton referred to these intermediates as metal atom clusters, which he defined as “those containing a finite group of metal atoms which are held together entirely, mainly, or at least to a significant extent, by bonds directly between the metal atoms even though some non-metal atoms may be associated intimately with the cluster.”^[1] Clusters link molecular compounds with the bulk metal phases and are also called a “new phase of matter” as they often exhibit properties, which differ from those of the bulk phase and their discrete constituents.^[2] This is attributed to their discrete energy-level structure and the high surface to volume ratio. In particular, small clusters can change their properties abruptly upon removal or addition of single atoms.^[3] Due to their unique properties it can be expected, that clusters are a source of novel materials, if they can be isolated in high yield with preservation of their structure and integrity. A distinction is made between three different types of metal atom clusters: a) naked metal clusters, which are not further supported by any stabilizing ligands (average oxidation number $n_{av} = 0$), b) metalloid clusters, which exhibit naked metal atoms only bonded to other metal atoms as well as ligand bearing metal atoms. However, the number of metal-metal interactions exceeds the number of metal-ligand interactions. The compounds feature a mixed valence for the metal atoms with an average oxidation number between the bulk metal and the metal salts ($0 \leq n_{av} \leq n_{salt}$) and c) salt like metal atom clusters, which contain numerous non-metal atoms in the cluster core ($n_{av} = n_{salt}$). A simpler and more general way of categorisation is by employing the number of atoms N forming the clusters as a measure. Microclusters exhibit $N \leq 10$, small clusters $10 < N < 100$, large clusters $100 < N < 1000$, nanoclusters $N > 1000$, at which there is a gradual transition to nanoparticles when N becomes larger than 10^6 .^[3]

In general, naked metal clusters of virtually any element with up to tens of thousands of atoms can be produced by molecular beam methods. In the following sections the most common techniques for producing such kinds of molecular beams are discussed.

1.1.1 Naked Metal Clusters

Supersonic Jets: The design of this source consists of a hot oven, in which the metal is vaporized (Figure 1).^[4, 5] The metal vapour obtained is mixed with an inert gas, whereas the pressure of the inert gas is several atmospheres and the pressure of the metal vapour 10-100 mbar. This mixture is allowed to expand into a vacuum through a small nozzle, resulting in a supersonic molecular beam. Due to the adiabatic expansion the beam is cooled drastically, leading to a super saturation of the metal vapour, which finally leads to cluster formation.^[6, 7] The cluster growth is terminated by a decrease of the vapour density with increased distance from the nozzle exit (within a few nozzle diameters). This technique is especially suitable to produce intense continuous beams of low boiling point metals. The cluster sizes range from <10 up to several thousand atoms.

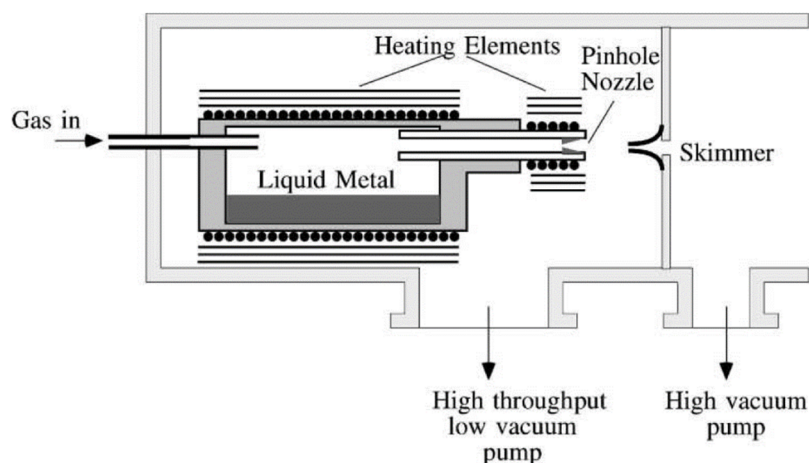


Figure 1. Supersonic jet source.^[8] Reprinted from C. Binns, *Surface Science Reports*, **2001**, *44*, 1-49, Copyright (2001), with permission from Elsevier.

Gas aggregation: These kind of sources are also called “smoke sources”, because the formation principle is known from nature for example for smoke, fog or clouds. The gas aggregation

technique is based on the vaporization of the metal by an oven into a cold flow of inert aggregation gas (Figure 2).^[9] This causes a low diffusion rate of the atoms away from the source, resulting in high super saturation and consequently cluster growth. A special feature is the growth of the clusters by successive single-atom addition due to the low temperature of the inert gas. The low temperature is maintained by additional cooling of the aggregation chamber. The actual cluster size is mainly determined by the time the clusters stay in the aggregation chamber. There is a broad range of cluster sizes achievable, which go as high as over 20000 atoms for alkaline metal clusters, depending on the operational conditions. These sources are especially used to produce metal clusters (Pb, Bi, Sb, Zn, Cu, Ni, Ag, Li, Na, Cs).^[9-13]

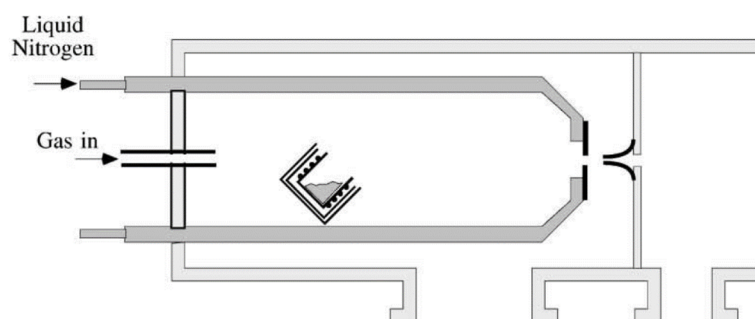


Figure 2. Gas aggregation source.^[8] Reprinted from C. Binns, *Surface Science Reports*, 2001, 44, 1-49, Copyright (2001), with permission from Elsevier.

Surface Erosion: Other techniques are not based on thermal evaporation of the metal but rather on surface erosion. Regarding this, material is removed from a target either by particle impact (sputtering), laser radiation (laser ablation) or by applying high electric fields.^[2] The sputtering sources often utilize ionized noble gas (Ar^+ or Xe^+ with energies between 3 and 30 keV), which are accelerated in the form of an ion beam towards the target material (Figure 3, left).^[14-16] As a consequence of this bombardment ionized and neutral clusters are ablated. The initial temperature of the clusters is very high. Cooling occurs *via* in-flight evaporation, *i.e.* emission of single atoms. This often leads to the formation of thermodynamically stable cluster entities. In addition, the high inert gas pressure decreases the sputtering rate due to collisions of the ion beam particles with the inter gas and subsequent loss of energy which is required to sputter atoms from the target material. Laser ablation can be used to obtain clusters from any metal.^[11, 17, 18] By focussing a pulsed laser (10 – 20 mJ, 10 ns) onto a small surface area $\leq 1\text{mm}^2$ of the target metal, atoms and small clusters are emitted (Figure 3, right). Similar to the sputtering

technique the clusters are very hot, therefore cooling occurs *via* evaporation of constituents. However, a combination with the supersonic jet and/or gas aggregation technique is possible in order to obtain cold clusters.^[19, 20] In this respect, a laser ablation source consisting of a strong Nd:YAG or excimer laser and a rotating target is located between a pulsed gas valve and a nozzle. The gas valve provides cold aggregation gas and the nozzle ensure adiabatic expansion of the inert gas/metal vapour mixture into a vacuum chamber. Pulse-arc-cluster-ion sources (PACISs) are very similar to laser ablation sources except the clusters are formed by a high electrical discharge (10 μ s) rather than a laser pulse. In this way neutral as well as charged clusters (10 %) can be obtained.^[21]

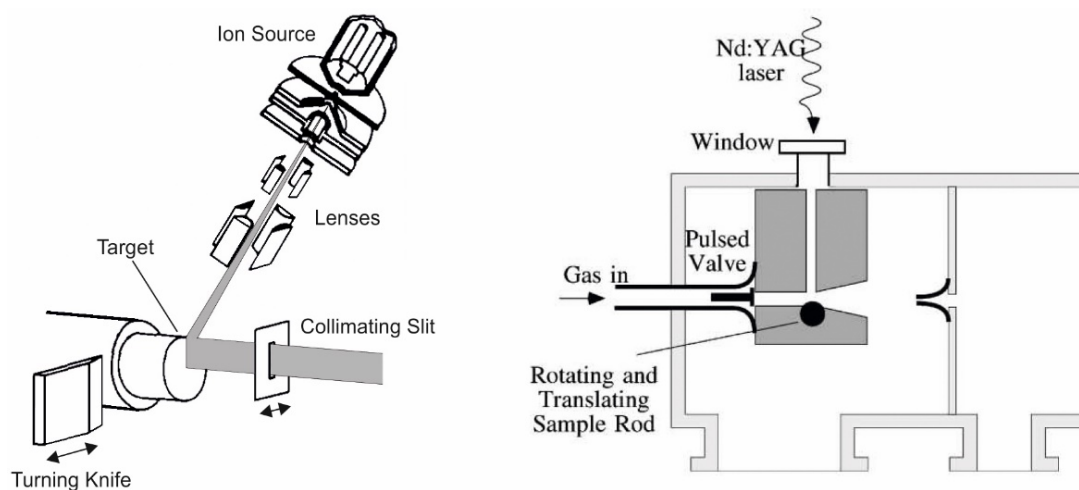


Figure 3. Ion sputtering source (left) and laser ablation source (right).^[8, 22] Reprinted (adapted) from J. Politiek, P. K. Rol, J. Los and P. G. Ikelaar, *Review of Scientific Instruments*, **1968**, *39*, 1147-1150, with the permission of AIP Publishing (left). Reprinted from C. Binns, *Surface Science Reports*, **2001**, *44*, 1-49, Copyright (2001), with permission from Elsevier (right).

The choice of the appropriate technique for the desired experimental result is important. Thermal evaporation is limited to the maximum temperature, which the crucible material can tolerate. In addition, reactions with the crucible material have to be considered. Sputtering allows the use of any target materials and is not limited to metals alone. However, the cluster yield is relative low. Laser vaporisation provides high density metal vapour streams in a very short time (10^{-8} s), but the laser itself is quite expensive and only discontinuous molecular beams can be produced. In comparison a PACIS is less expensive, gives a higher yield of clusters per pulse and allows a higher pulse rate.

1.1.2 Dendrimer Stabilized Metal Clusters

However, all the techniques mentioned above are based on the gas phase preparation of naked clusters. Though size control of these species is possible for charged cluster species *via* mass analysers, the mass production and stabilization of these clusters is very difficult. Especially the stabilization of such clusters without loss of the extraordinary properties which is associated to the cluster surface is challenging. The preparation of naked atom precise subnanometer clusters in bulk-quantity *via* solution phase synthesis was unknown until 2009. Yamamoto *et al.* optimized a method of Crooks *et al.*,^[23] who employed poly(amidoamine) dendrimers as nanoreactors for the size-controlled synthesis of nanoparticles on a single nanometer scale. At this, the basic sites of the dendrimers are saturated with Lewis acidic metal salts by complexation. These metallo-dendrimer complexes are subsequently treated with an appropriate reducing agent, leading to the formation of dendrimer stabilized nanoparticles.^[24]^[25] Yamato *et al.* improved this approach with respect to size control on a subnanometre scale. They designed a novel phenylazomethine based dendrimer (DPA-TMP, Figure 4, left), which allows stepwise layer-by-layer complexation from the inner imine to the outer imine groups due to decreasing coordination constants from the inner to the outer layers.^[26]

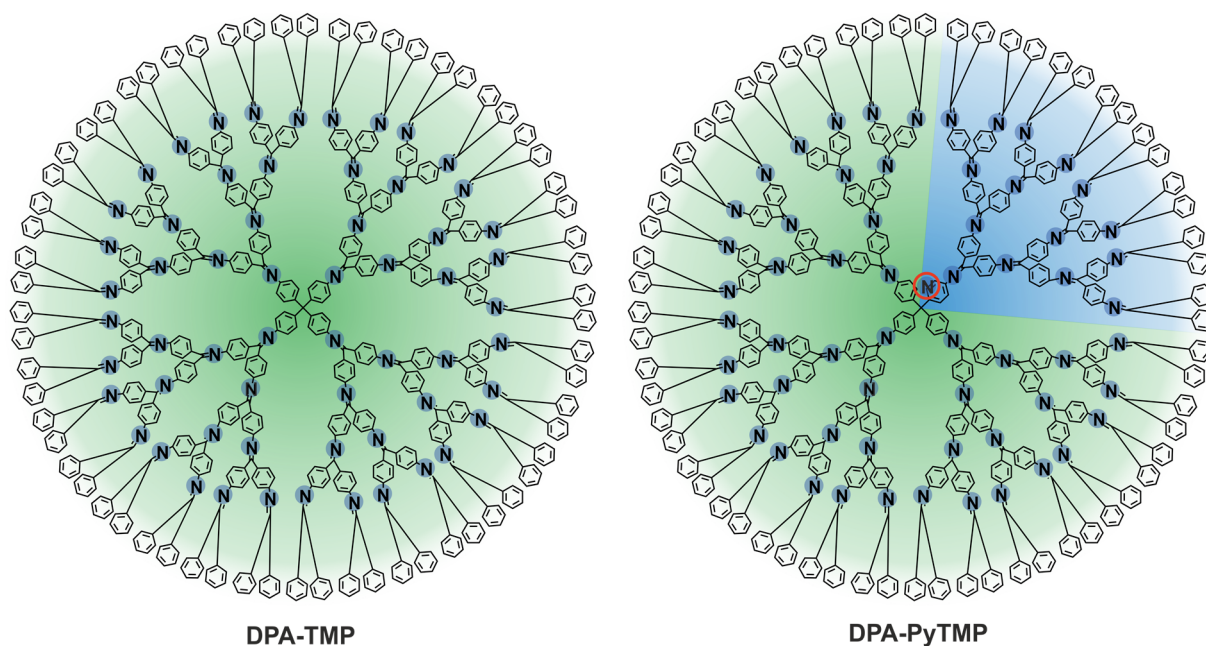
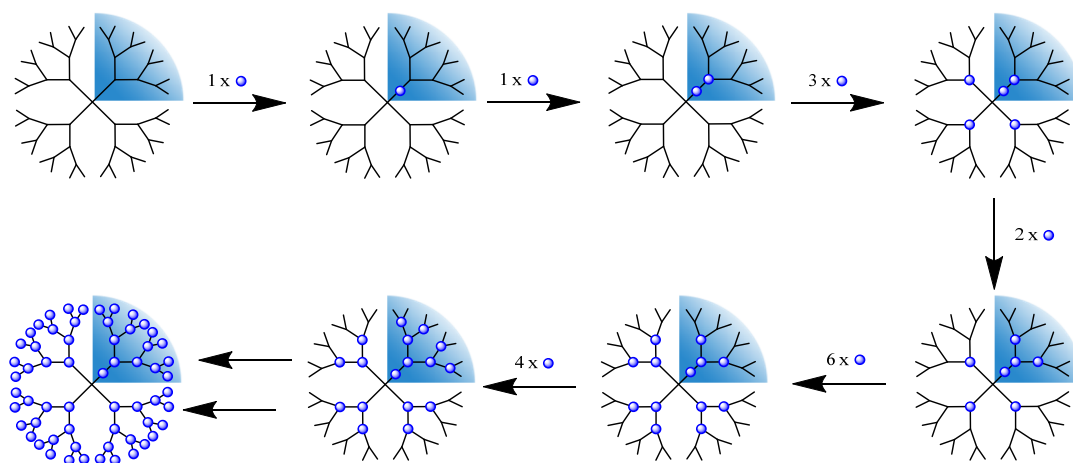


Figure 4. Phenylazomethin dendrimer (DPA) with a tetraphenylmethane (TMP) core (left), phenylazomethin dendrimer (DPA) with a triphenylpyridylmethane (PyTMP) core (right). The basicity gradients are indicated by the intensity of the colours green and blue.

In this way platinum clusters have been prepared using PtCl_4 as a metal salt and NaBH_4 as a reducing agent. In accordance to the dendrimer architecture, when 12, 28 and 60 equivalents of metal salt are added, the deviation of assembled metal units is minimized due to layer saturation. Consequently, almost monodisperse atom precise Pt_{12} , Pt_{28} and Pt_{60} clusters can be obtained after reduction. Recognizing the great potential of this dendrimer system as a key to access atom precise clusters, further manipulation of this dendrimer has been conducted in order to increase the number of isolable $[\text{Pt}_n]$ cluster ($n =$ positive natural number). The tetraphenylmethyl core of the dendrimer was substituted by a pyridyl-triphenylmethyl core (DPA-PyTMP dendrimer, Figure 4, right).^[27, 28] The introduction of the pyridyl group strongly affects the basicity of the consecutive imine groups of the respective branch. The basicity of the imine groups of the pyridyl bearing branch is increased compared to the imine groups of the same layer with phenyl roots. This leads to an irregular stepwise complexation with especially monodisperse metal assemblies when 1, 2, 5, 7, 13, 17, *etc.* equivalents of PtCl_4 are added (Scheme 1). In fact, the dendrimer supported almost monodisperse Pt_{13} , Pt_{17} and Pt_{19} clusters have been isolated.



Scheme 1. Irregular stepwise complexation of DPA-PyTMP with PtCl_4 (blue sphere).

Though stabilized by a dendrimer system, the surfaces of the clusters are still accessible for oxygen as the clusters still show significant catalytic activity for oxygen reduction reaction. Moreover, the dendrimer was successfully substituted by stabilizing CO ligands when Pt_{13} @dendrimer was treated with a constant stream of CO as ESI MS measurements of the reaction solution shows an intact $[\text{Pt}_{13}(\text{CO})_{15}]^{2-}$ entity in the gas phase. The main advantage of

this method is that the atomicity of the clusters can be tuned by altering the stoichiometry between dendrimer and precursor salt independent of the intrinsic stability of the resulting cluster species. Nevertheless, a certain degree of dispersity, even though small, cannot be prevented and the method is dependent on the feasibility of appropriate metal salts to coordinate to the basic sites of the dendrimer. In order to obtain absolutely atom precise metal clusters, which can be isolated as crystalline materials and subsequently analysed by physicochemical means, *e.g.* visualisation of the solid state structure or elucidation of its chemical reactivity, strong ligand stabilisation preventing cluster agglomeration is necessary. Using bottom up synthetic methods, molecular defined stable organometallic clusters can be prepared.

1.1.3 Metalloid Clusters

With regard to metalloid clusters, the majority of the results have been achieved with precious metals, *e.g.* Au, Ag, Pd, Pt.^[29] The straightforward synthesis of these clusters, their stability and inertness towards air and sometimes even water allows easy access to these clusters. Upon reduction of metal salts in the presence of stabilizing ligands, the reduced metal atoms assemble in a broad range of structures and nuclearities protected by ligands such as phosphines, chalcogenides, halides or carbonyls. The $[\text{Au}_{55}(\text{PPh}_3)_{12}\text{Cl}_6]$ cluster prepared by Schmid *et al.* is regarded as a prototype of these clusters.^[30] In contrast, it is much more difficult to obtain metalloid clusters of base metals, expecting high reactivity and sensitivity toward moisture and air. However, Schnöckel *et al.* succeeded in the synthesis of metalloid aluminum and gallium clusters *via* controlled disproportionation of the respective metastable monohalides MX, in the presence of appropriate stabilizing ligands.^[31, 32] The monohalides are prepared in a sophisticated way using the co-condensation technique. In the following the preparation of AlCl is described as a prime example for this method. AlCl can be synthesized in a 40 mmol scale within two hours employing a co-condensation apparatus shown in Figure 5.

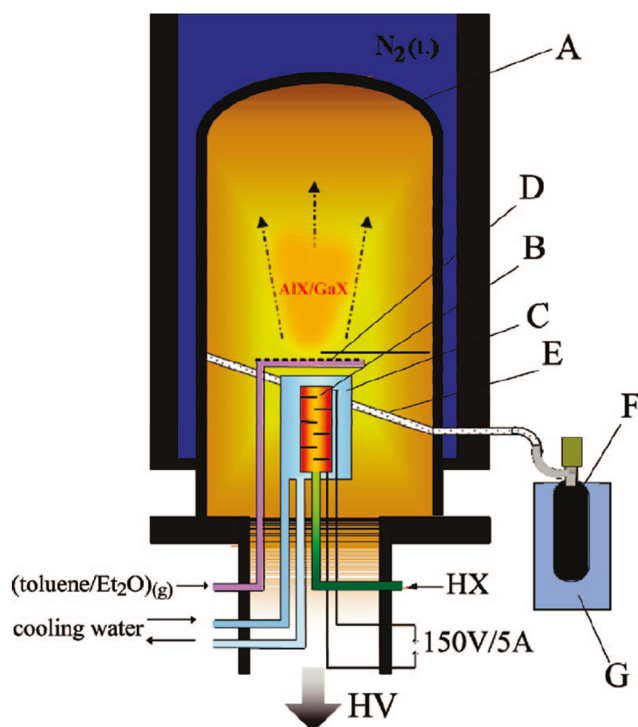
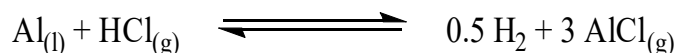


Figure 5. Schematic set-up of a co-condensation apparatus: A = stainless steel vessel (30 L), B: = resistively heated graphite cell containing Ga or Al, C = cooling shield, D: inlet of donor solvent, E: drainage channel, F: Schlenk tube, G: Dewar with dry ice.^[32] Reprinted with permission from H. Schnöckel, *Chemical Reviews*, **2010**, *110*, 4125-4163. Copyright (2010) American Chemical Society.

A reactor containing several graphite cells filled with aluminum is heated resistively to $\sim 1000\text{ }^{\circ}\text{C}$ inside a stainless steel high vacuum chamber. The resultant molten aluminum is treated with a continuous flow of HCl leading to the formation of gaseous AlCl.



Scheme 2. Synthesis of AlCl.

Due to the high vacuum, collisions of the single gaseous AlCl molecules are avoided, and they subsequently condense unaltered at the liquid nitrogen cooled ($-196\text{ }^{\circ}\text{C}$) walls of the reaction chamber. In pure form, AlCl starts to agglomerate and disproportionate at $-100\text{ }^{\circ}\text{C}$. In order to increase the stability a mixture of solvent (toluene) and donor components (e.g. NEt_3 , Et_2O or

THF) is co-condensed at the walls of the reaction chamber. The solvent mixture melts at ~ -100 °C and the resultant AlCl solution is extracted from the reaction chamber *via* a drainage channel into a precooled (-78 °C) Schlenk vessel. These solutions are stable at -78 °C for several months. Depending on the employed halide X and the additional donor and its concentration, the metastable monohalides MXs disproportionate in a temperature range between -40 and 50 °C to give the respective bulk metal and trihalide species. By adding ligand salts LiR during the disproportionation process, the halides X^- are substituted by ligands R^- upon metathesis reactions. In this way, metal clusters which nucleate on the way to the formation of the bulk metal are stabilized using a range of bulky ligands R (R = e. g. $N(SiMe_3)_2$, $C(SiMe_3)_3$, Cp^* , P^tBu_2 , $Si(SiMe_3)_3$).^[31] Because disproportionation already commences at low temperatures, metalloids aluminum and gallium clusters with an increasing number of naked metal atoms can be obtained with increasing reaction temperature. Note, that the metathesis reaction and disproportionation are to occur in a similar temperature range. Otherwise oligomerisation or the formation of the bulk metal is to be expected, when the substitution or the disproportionation reaction is preferred. However, by systematic exploration of this exceptional synthetic approach, a great library of metalloids aluminum and gallium clusters have been prepared.

In particular metalloids clusters, which not only exhibit “naked” metal atoms (metal atoms bonded only to other metal atoms) but also feature structural motifs, characteristic of the bulk phase are isolated. As to the “annealing” process at low temperatures, it is feasible that the single metal atoms slowly arrange in a way as it is expected from the bulk metal (end of disproportionation). Regarding this, $[Al_7R_6]^-$ and $[Al_{12}R_8]^-$ (R = $N(SiMe_3)_2$) were isolated from a AlCl solution at -7 °C and room temperature,^[33, 34] respectively. With regard to the arrangement of the aluminum atoms, $[Al_7R_6]^-$ exhibits two corner connected tetrahedrons and in $[Al_{12}R_8]^-$ the metals atoms are arranged in a step like fashion. These topologies remarkably resemble the packing of the metal atoms in the solid state of elemental aluminum (Figure 6).

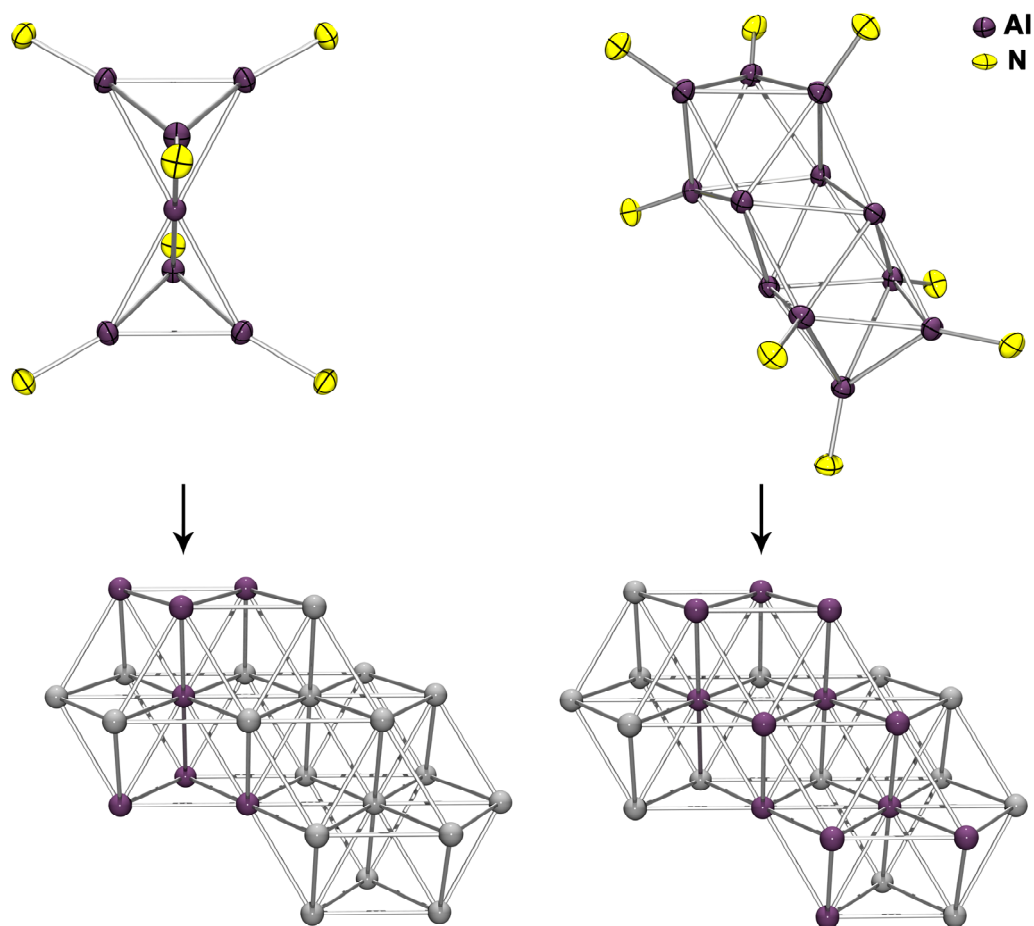


Figure 6. Molecular structures of $[\text{Al}_7\text{R}_6]^-$ (left) and $[\text{Al}_{12}\text{R}_8]^-$ (right) ($\text{R} = \text{N}(\text{SiMe}_3)_2$) and the topological relation of the aluminum atom arrangement with the solid state structure of elemental aluminum (bottom). Carbon, hydrogen and silicon atoms are omitted for clarity.

The size of the obtainable clusters increases when the AlCl solution is further heated to $60\text{ }^\circ\text{C}$ for a short time to give $[\text{Al}_{69}\text{R}_{18}]^{3-}$.^[35] On the other hand $[\text{Al}_{77}\text{R}_{20}]^{2-}$ can be isolated under the same reaction conditions by employing the less reactive AlI instead.^[36] These compounds are the largest aluminum clusters known. The aluminum atoms are arranged in shells (Figure 7), whereas both clusters exhibit centred structures with one aluminum atom in the center surrounded by 12 nearest aluminum neighbors. However, the Al_{13} cores in $[\text{Al}_{69}\text{R}_{18}]^{3-}$ and $[\text{Al}_{77}\text{R}_{20}]^{2-}$ are significantly different with decahedral and icosahedral (distorted in the direction of a cuboctahedron) shape, respectively. Note, that the Al - Al distances from the inner to the outer layer decreases. Therefore, an increased degree of Al - Al bond localization from the core to the periphery of the clusters is indicated. As a result, a rather delocalized situation similar to the bulk metal is predominantly found in the center of the clusters. At this point it is noteworthy that the metal atoms arrange as prescribed by close packing in the solid state of the element.

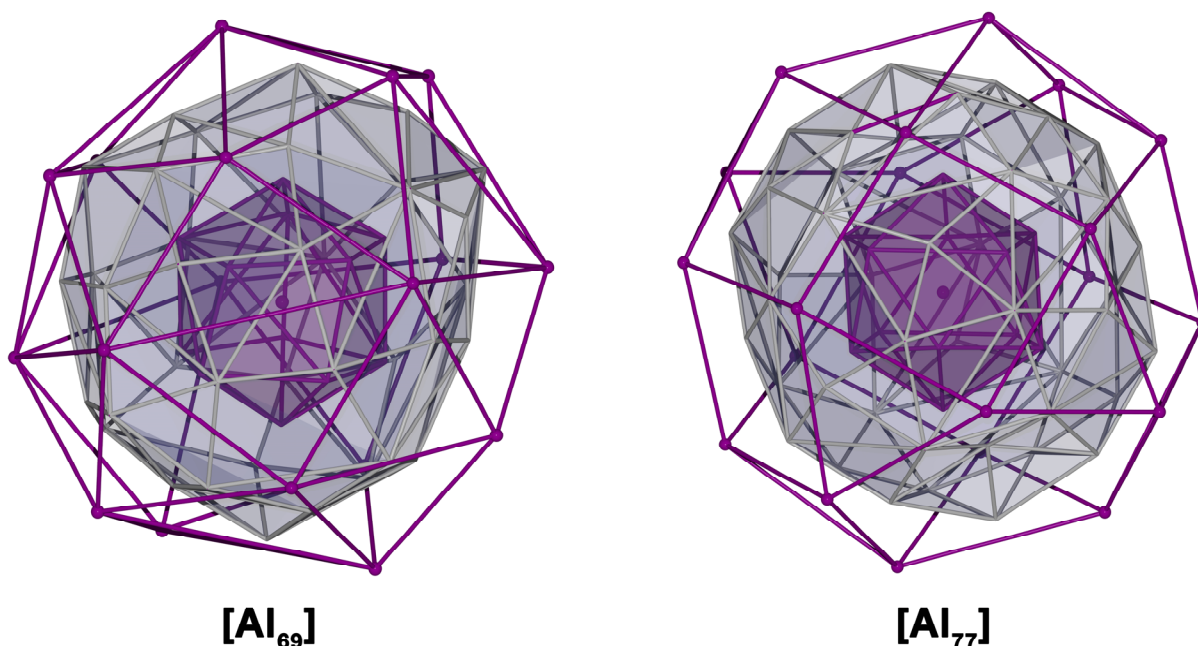


Figure 7. Arrangement of aluminium atoms in $[\text{Al}_{69}\text{R}_{18}]^{3-}$ (left) and $[\text{Al}_{77}\text{R}_{20}]^{2-}$ (right) ($\text{R} = \text{N}(\text{SiMe}_3)_2$). The shells of aluminum atoms are represented in different colours.

However, the AlR shell has a structural effect on this arrangement causing distortions of the cluster core from optimal geometries. Hence the ligand R is also crucial for the arrangement of the metal atoms. In this way, steric, as well as electronic effects can be tuned by ligand choice and as a consequence different topologies of clusters are feasible by altering the R-group. For example, the use of Cp* instead of $\text{N}(\text{SiMe}_3)_2$ as a protective group induces different clusters. By this means, $[\text{Al}_{50}\text{Cp}^*_{12}]$ was prepared from a AlBr solution at $-30\text{ }^\circ\text{C}$.^[37] An icosahedral AlCp* shell covers an icosidodecahedral Al₃₀ unit, which on the other hand encloses a distorted square-based Al₈ anti-prism.

In contrast to aluminum, gallium as a bulk element features seven different modifications demonstrating the flexibility of gallium atoms to achieve different connectivities. This is also in accordance to the great variety of structural motifs found in metalloidal gallium clusters. One remarkable example is $[\text{Ga}_{19}\text{R}_6]^-$ ($\text{R} = \text{C}(\text{SiMe}_3)_3$), which exhibits a centered structure.^[38] The central gallium atom is surrounded by 12 closest gallium neighbors, arranged in a geometry between anticuboctahedron and icosahedron similar to the Al₁₃ core in $[\text{Al}_{77}\text{R}_{20}]^{2-}$.^[36] The six remaining GaR groups are each bonded to three gallium atoms of the Ga₁₃ core each. The remarkable coordination number 12 of the central gallium atom is otherwise only known for high pressure modifications of elemental gallium (Ga(II) and Ga(III)). The cluster was

characterized by ESI mass spectrometry, at which point the compound was transferred intact into the gas phase.^[39] Collision induced dissociation (CID) experiments showed that the cluster fragments by stepwise dissociation of carbenoid GaR groups, eventually giving a naked $[\text{Ga}_{13}]^-$ cluster (Figure 8).^[40] This result was complimented by laser desorption/ionisation experiments on crystals of $[\text{Ga}_{19}\text{R}_6]^-$, which yielded the $[\text{Ga}_{13}]^-$. In this regard, $[\text{Ga}_{19}\text{R}_6]^-$ is not considered a $[\text{Ga}_{19}]^{5+}$ core enclosed by six R^- ligands but as one in which the six GaR units act as a protecting ligand shell for a naked $[\text{Ga}_{13}]^-$. Hence the designation $[\text{Ga}_{13}(\text{GaR})_6]^-$ is a more appropriate notation to describe this cluster. This compound strikingly links the two classes of naked and metalloid clusters.

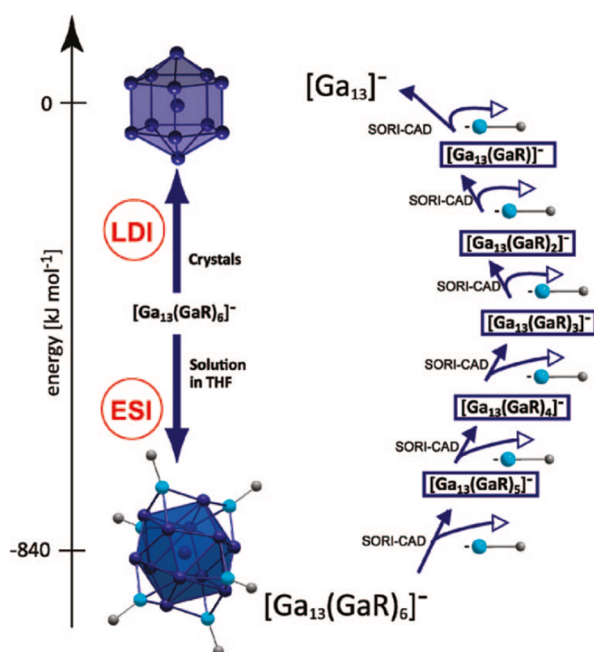


Figure 8. Stepwise fragmentation of $[\text{Ga}_{13}(\text{GaR})_6]^-$ ($\text{R} = \text{C}(\text{SiMe}_3)_3$) in the gas phase *via* CID and ionisation of $[\text{Ga}_{13}(\text{GaR})_6]^-$ *via* laser desorption/ionisation of solid crystals containing $[\text{Ga}_{13}(\text{GaR})_6]^-$. Only the nitrogen atoms of the ligands are depicted for clarity.^[32] Reprinted with permission from H. Schnöckel, *Chemical Reviews*, **2010**, *110*, 4125-4163. Copyright (2010) American Chemical Society.

The largest main group metalloid cluster isolated so far is $[\text{Ga}_{84}\text{R}_{20}]^{4+}$ ($\text{R} = \text{N}(\text{SiMe}_3)_2$) (Figure 9).^[41] The unique core of this species exhibits a Ga_2 unit (Ga-Ga distance = 2.34 Å), which resembles the Ga_2 (Ga-Ga distance = 2.45 Å) dumbbell in α -gallium. This core is surrounded by a shell of 32 metalloid gallium atoms in the form of a football with icosahedral caps. Note, that the icosahedral topology is a typical feature of elemental δ -gallium. The $[\text{Ga}_2\text{Ga}_{32}]$ moiety

is encircled by a belt of additional 30 metalloid gallium atoms. The final layer consists of 20 protecting GaR groups. In total there are 64 naked gallium atoms. There are 42 crystallographically (and in principle chemically) different gallium atoms, making this cluster a species with a high degree of mixed valence character.

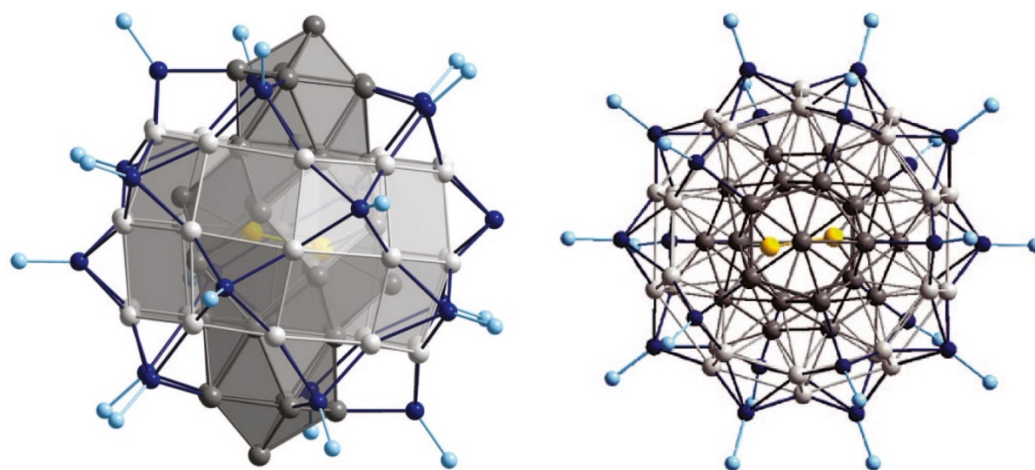


Figure 9. Two different projections of the $[\text{Ga}_{84}\text{R}_{20}]^{4-}$ anion ($\text{R} = \text{N}(\text{SiMe}_3)_2$). Nitrogen atoms are represented in light blue, there are in total 64 naked Ga atoms = 2 (yellow) + 32 (dark grey) + 30 (light grey) and 20 ligand bearing gallium atoms in dark blue. Only the nitrogen atoms of the ligands are depicted for clarity.^[32] Reprinted with permission from H. Schnöckel, *Chemical Reviews*, **2010**, *110*, 4125-4163. Copyright (2010) American Chemical Society.

Despite these great achievements involving aluminum and gallium clusters, still for most of the base (non-precious) metals, metalloid clusters are unknown. However, Hayton *et al.* succeeded in preparing a $[\text{Cu}_{25}]$ nanocluster in the form of $[\text{Cu}_{25}\text{H}_{22}(\text{PPh}_3)_{12}]\text{Cl}$ with partial $\text{Cu}(0)$ character.^[42] Herein, $\text{Cu}(\text{OAc})$ and CuCl were treated with Ph_2SiH_2 in the presence of stabilizing PPh_3 ligands. The copper hydride cluster features a Cu_{13} centered, distorted icosahedral core, which differs from the fcc structure found in elemental copper. However, most recently $[\text{Cu}_{13}\{\text{S}_2\text{CN}^n\text{Bu}_2\}_6(\text{C}\equiv\text{CR})_4]^+$ ($\text{R} = \text{CO}_2\text{Me}$ and $3\text{-FC}_6\text{H}_4$) was prepared by treating $[\text{Cu}_{28}\text{H}_{15}(\text{S}_2\text{CN}^n\text{Bu}_2)_{12}]\text{PF}_6$ with an excess of alkyne.^[43] The alkyne is used to deprotonate the copper hydride species upon which hydrogen is formed. This *in situ* formed hydrogen acts as a reducing agent to give Cu^0 from Cu^{I} . The resulting $[\text{Cu}_{13}\{\text{S}_2\text{CN}^n\text{Bu}_2\}_6(\text{C}\equiv\text{CR})_4]^+$ clusters exhibit an extraordinary centered cuboctahedral architecture, which is in accordance to the fcc structure of bulk copper.

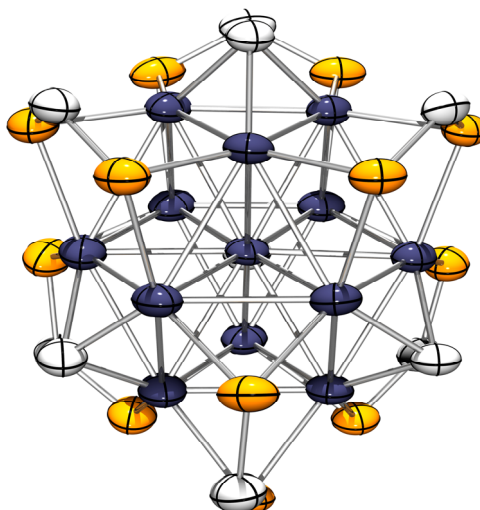


Figure 10. Molecular structure of $[\text{Cu}_{13}\{\text{S}_2\text{CN}^n\text{Bu}_2\}_6(\text{C}\equiv\text{CCO}_2\text{Me})_4]^+$ showing the cuboctahedral $[\text{Cu}_{13}]$ unit. Copper atoms are represented in midnight blue, sulphur in orange and carbon in grey. The N^nBu_2 and CCO_2Me groups are omitted for clarity.

1.2 Cluster Models

In order to elucidate the bonding and the stability of large metal cluster species, tedious quantum chemical calculations have to be performed. However, several models have been developed which correlate the number of cluster valence electrons with the stability of a cluster entities. Note, that all electron counting rules are based on the principle that electrons occupy orbitals in a fashion leading to closed-shell species. This means, that a stable compound exhibits fully occupied low energy MOs, which are separated from vacant high energy MOs by a significant energy gap (HOMO-LUMO gap). As to that, a larger gap corresponds to a more thermodynamically stable compound (Jahn-Teller stability).

1.2.1 Jellium Model

In 1984 Knight *at el.* reported on the production and detection of alkali metal cluster of up to 100 atoms in the gas phase *via* mass spectrometry.^[44] Furthermore, they noticed a specific pattern in the mass spectra, in that, clusters corresponding to certain number of atoms N are formed with an especially high abundance, relative to their immediate neighbours ($N = 8, 20, 40, 58, \dots$). These numbers are called “magic numbers” and they refer to clusters with

pronounced stability. Knight *at el.* correlated these numbers to valence electrons causing spherical shell-closing and therefore a particularly large HOMO-LUMO gap. Regarding this the electronic structure of alkaline metal clusters is based on shells and can be explained with the quantum mechanical spherical jellium model. In this respect a cluster is considered as a uniform positively charged sphere containing an electron gas. The Schrödinger equation can be solved for an electron moving inside this sphere, while affected by a central spherical potential. For this purpose, the radial Woods-Saxon potential has proven to be of use.

$$U(r) = \frac{-U_0}{e^{\frac{r-r_0}{\sigma}} + 1}$$

U_0 = Sum of the Fermi energy and the work function of the bulk metal

r_0 = Effective radius of the cluster sphere

σ = 1.5 bohr = constant scaling distance

The potential describes an almost square well with rounded sides. As this potential is only dependant on the distance r of the electron from the center, the solution of the Schrödinger equation can be separated into a radial $R_{nl}(r)$ and an angular $Y_{ml}(\vartheta, \varphi)$ part.

$$\Psi_{nlm}(r, \vartheta, \varphi) = R_{nl}(r)Y_{ml}(\vartheta, \varphi)$$

Due to the boundary conditions imposed by the potential, the energies obtained by solving the differential equation are quantized. The energies are characterised in an analogous way to atoms with n as the principal, l as the angular momentum and m as the magnetic quantum number. Shell closing arises by complete filling of the sub shells in accordance to their energy level $1s < 1p < 1d < 2s < 1f < 2p < 1g < 2d < 3s < 1h\dots$, whose order is dependent on the applied potential $U(r)$. Hence, electronically closed shells are expected for the following (magic) numbers of electrons 2, 8, 18, 20, 34, 40, 58, 68, 70, 92, *etc.* Therefore, the jellium model nicely predicts the stability of alkali metal clusters that have been detected by mass spectrometry. However, it turns out that the model of the electronic shell structure is not restricted to alkali metal clusters but can be applied in general for many metal cluster systems.^[45] Nevertheless, the model of spherical clusters is an oversimplification and is only applicable to closed shell clusters. For open shell structures a distortion of the spherical shape is expected according to the Jahn Teller theorem.^[46] Thus, the spherical model is no longer appropriate and for instance the lifting of the degeneracy of the angular momentum is to be expected in order to form an

energetically beneficial ground state. In first approximation Clemenger *et al.* introduced an ellipsoid shell model which is actually based on a potential for a three dimensional harmonic oscillator.^[47] In addition, the shape of the model adjusts to the electronic structure while maintaining the cluster volume. The spheroid exhibits two equal and one unequal axes allowing oblate and prolate structures. Of course the next step was to extend this model by allowing distortions also in the third axes. Hence either spherical, spheroidal or ellipsoidal cluster shapes are possible. As a consequence, energetically favoured subshell closing causing the distortion of the spherical shape of a cluster could be modelled. Based on this an alkaline metal cluster exhibiting 4 VEs (valence electrons) would be prolate due to the doubly occupied p_x state ($1s^2 1p_x^2 p_y^0 p_z^0$). A cluster with 6 VEs would be oblate by doubly occupying the p_x and p_y state ($1s^2 1p_x^2 1p_y^2 1p_z^0$). The 7 atom cluster would be the first three-dimensional cluster by additionally singly occupying the p_z state ($1s^2 1p_x^2 1p_y^2 1p_z^1$). 8 VEs lead to a closed shell spherical cluster ($1s^2 p^6$) as a distortion would not lead to an energetically more beneficial electron configuration.

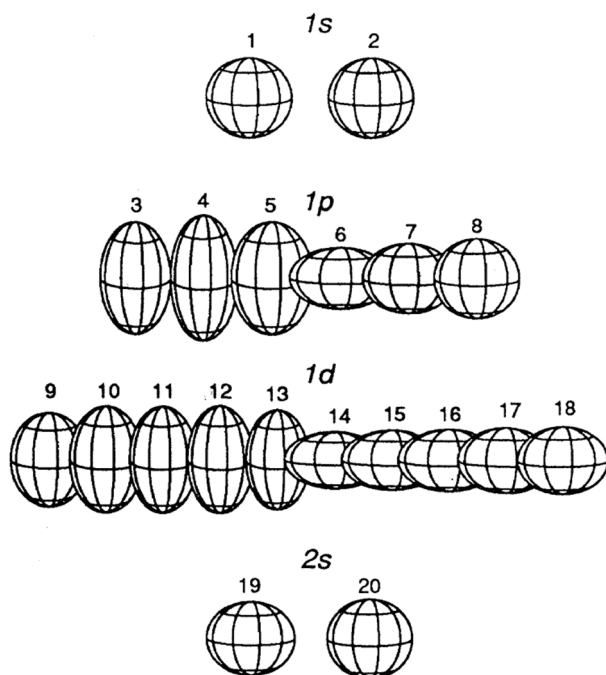


Figure 11. Cluster shapes according to the improved ellipsoids jellium model normalized to a constant volume.^[48] Reprinted with permission from W. A. de Heer, *Reviews of Modern Physics*, **1993**, *65*, 611-676. Copyright (1993) by the American Physical Society.

Accordingly, closed shell clusters should prefer spherical shapes while open shell clusters should prefer prolate or oblate shapes. In this way the Clemenger model does not only account for the main peaks in the mass spectrum of alkaline metal clusters but also to the fine structure.

Further examples for the applicability of the jellium models are the mentioned $[Al_{50}Cp^*_{12}]$ or $[Cu_{13}\{S_2CN^mBu_2\}_6(C\equiv CR)_4]^+$ giving closed shell structures with 138 and 2 VEs respectively. Furthermore, the fragmentation of $[Ga_{13}(GaR)_6]^-$ to give $[Ga_{13}]^-$ in ESI-MS can be explained by the high electronic stability, which is featured by the 40 VEs closed shell structure of $[Ga_{13}]^-$.

1.2.2 Wade-Mingos Rule

Another well established electron counting rule is the Wade-Mingos rule.^[49, 50] It is applicable to main group and transition metal clusters. Wade and Mingos contemporaneously recognized that the shape of a deltahedral cluster can be related to its cluster electron count. This rule is especially associated with boron clusters as role models of the applicability of this concept. However, the first elucidation of the electronic structure of deltahedral clusters were based on Longuet-Higgins' theoretical considerations on boron compounds.^[51] As to that the stoichiometry of boron hydrides were conceptually acquired from elemental boron exhibiting 12 vertex icosahedral and borides exhibiting 6 vertex octahedral clusters by cleaving the bonds between individual deltahedral species and terminating the open boron sides with hydrogen. For example, a 12 vertex icosahedron $[B_{12}H_{12}]$ composed of 12 BH fragments can be derived in this way. In total there are $12 \times 5 = 60$ MOs available. Considering the condition of compounds to be thermodynamically stable when a large HOMO-LUMO gap exists, in this case the respective gap was found to be between the 25th and 26th MOs. However, $B_{12}H_{12}$ only has 48 valence electrons. In order to "close the shell" 2 additional electrons are required predicting a stable icosahedral borane to be charged $[B_{12}H_{12}]^{2-}$. Regarding this $4n + 2 = 50$ cve (cluster valence electrons, n = number of vertices forming the closed cluster) are necessary to fill all low lying MOs. From these low lying orbitals 12 MOs are associated with bonding $2c2e$ B-H interactions leaving $n + 1 = 13$ MOs, which can be assigned to bonding interactions in the skeletal framework of the cluster. With only 5 connected (with regard to B-B interactions) boron atoms available, the 13 skeletal electron pairs do not suffice to enable $2c2e$ bonds, exclusively. This implies the valence electrons are delocalized throughout the whole cluster bonding framework.

These results were generalized by Wade and Mingos for main group clusters as follows:^[52]

“For a deltahedron of order n , there are $n + 1$ SEP (skeletal electron pair) associated with cluster bonding”.

This rule is applicable for closed clusters as well as for open clusters, whereas for the latter case n indicates the number of vertices of the closed cluster from which the open cluster is derived.

Although it is tempting to give these electron counting rules universal validity, there is no model which is applicable for all type of clusters. It is important to recognize the limitations of each model and apply them respectively with great care. There might be metal clusters to be synthesized which require additional models, where well established models fail.

1.3 Zinc rich Compounds: On the Borderline between Coordination and Cluster Chemistry

With regard to metalloids cluster chemistry, one of the blank spots in the periodic table of the elements concerns derivatives of zinc. The first achievements in the direction of zinc cluster chemistry in general were made by Fischer *et al.* in 2008. They reported on an entirely new synthetic pathway to access zinc rich coordination compounds.^[53] The treatment of the homoleptic complex $[\text{Mo}(\text{GaCp}^*)_6]$ with an excess of ZnMe_2 gives the extraordinary species $[\text{Mo}(\text{ZnMe})_9(\text{ZnCp}^*)_3]$ (Figure 12). According to the work of Alfred Werner the highest possible coordination number for complexes of the type $[\text{ML}_n]$ ($M = \text{metal}$) with monodentate ligands L is nine.^[54] The number of zinc ligands in $[\text{Mo}(\text{ZnMe})_9(\text{ZnCp}^*)_3]$ clearly exceeds this limit restricting the quantity of possible donor-acceptor interactions between a central metal M and coordinated ligands. At first glance, the icosahedral arrangement of the zinc atoms around the molybdenum atom might suggest categorization of this compound with the known endohedral clusters $M@E_n$ ($n > 9$), *e.g.* $[\text{Pt}@Pb_{12}]^{2-}$.^[55] However, quantum chemical calculations for the model compound $[\text{Mo}(\text{ZnH})_{12}]$, reveal a different situation, showing a unique electronic structure. In total 18 valence electrons (6 from molybdenum and 12 from the ZnR fragments) are available for all intermetallic bonding interactions. Six Zn-Mo-Zn two-electron-three-center bonds originate from the interaction of six pairs of ZnH fragments with six degenerated sd^5 -hybridized orbitals (C_{5v} symmetry) of the molybdenum. The remaining, six electrons are delocalized over the zinc icosahedron causing weak Zn-Zn interactions, complementing the closed shell structure of $[\text{Mo}(\text{ZnMe})_9(\text{ZnCp}^*)_3]$. By definition, a cluster

requires a bond system which directly connects each atom to its neighbors in the polyhedron.^[1] In contrast a coordination compound exhibits donor-acceptor bonds between the central metal atom and the ligands.^[56] Neither of the two definitions is totally in accordance to the electronic structure of $[\text{Mo}(\text{ZnMe})_9(\text{ZnCp}^*)_3]$, though both phenomena are somehow touched. As a consequence, $[\text{Mo}(\text{ZnMe})_9(\text{ZnCp}^*)_3]$ can be regarded as a prototype for compounds on the borderline between coordination and cluster compounds. This link between molecular and solid state chemistry also manifest, when the overall geometric structure of the $[\text{MoZn}_{12}]$ core is considered in particular. Exactly the same structural motif can be found in the solid state phase of $\text{MoZn}_{20.44}$.^[57] One of the dominant motifs in this zinc rich binary phase is the $[\text{MoZn}_{12}]$ icosahedron. As a result, $[\text{Mo}(\text{ZnMe})_9(\text{ZnCp}^*)_3]$ can be regarded as a molecular cut-out of the respective Hume-Rothery phase.

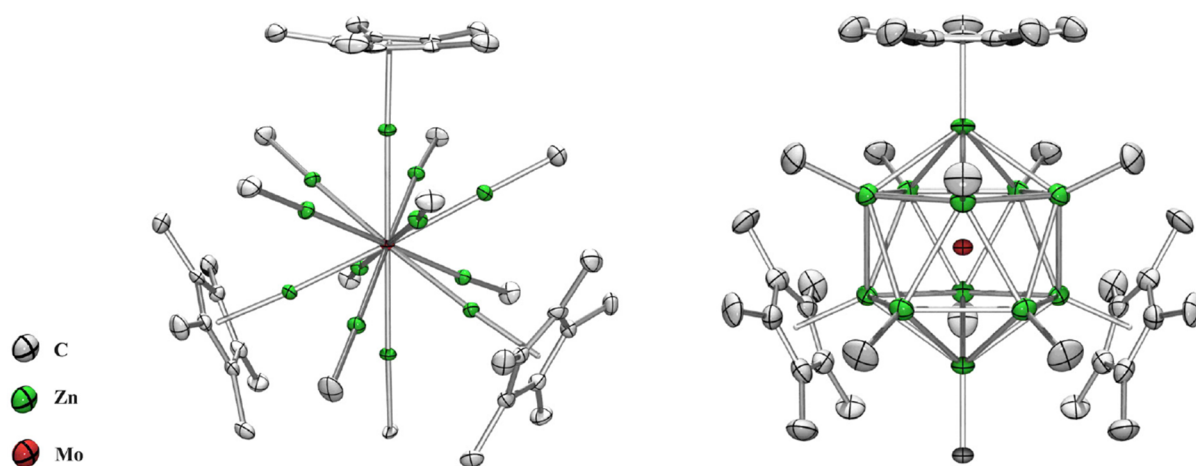


Figure 12. Left: Molecular structure of $[\text{Mo}(\text{ZnMe})_9(\text{ZnCp}^*)_3]$ without hydrogen atoms. Right: Icosahedral coordination environment formed by the zinc atoms around the molybdenum atom.^[58] Reprinted from T. Cadenbach, T. Bollermann, C. Gemel, I. Fernandez, M. v. Hopffgarten, G. Frenking und R. A. Fischer, *Angew. Chem. Int. Ed.*, **2008**, *47*, 9150-9154. Copyright (2008) Wiley-VCH Verlag GmbH & Co. KGaA, Weinheim.

In addition, this concept can be applied to other homoleptic GaCp^* transition metal (TM) complexes giving a series of compounds $[\text{TM}(\text{ZnR})_n]$ (TM = Mo, Ru, Rh, Pd; R = Me, Et, Cp*; $n = 8 - 12$) (Figure 13).^[58] The mechanism includes Ga/Zn exchange, probably involving radical species, in which redox processes take place. Formally Zn^{II} is reduced to Zn^{I} and Ga^{I} is oxidized to Ga^{III} . *In situ* NMR studies show that Me_2GaCp^* is formed as a Ga^{III} byproduct. Each two electron donor GaCp^* ligand is substituted by two one electron donor ZnR ligands. As a

consequence, the electron count does not change. In all cases the 18 valence electron rule is fulfilled.

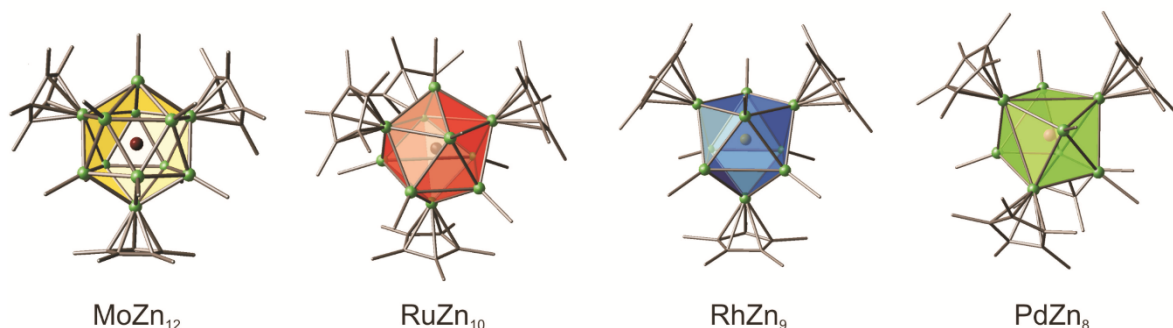


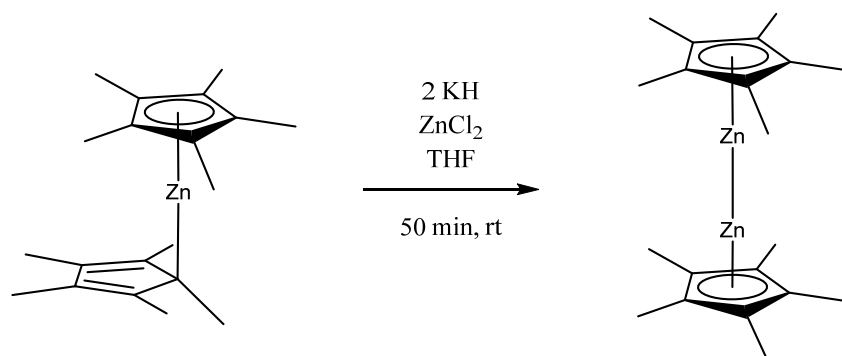
Figure 13. Molecular structures of $[\text{Mo}(\text{ZnMe})_9(\text{ZnCp}^*)_3]$, $[\text{Ru}(\text{ZnMe})_6(\text{ZnCp}^*)_4]$, $[\text{Rh}(\text{ZnMe})_6(\text{ZnCp}^*)_3]$ and $[\text{Pd}(\text{ZnMe})_4(\text{ZnCp}^*)_4]$ without hydrogen atoms and the respective coordination polyhedron around the central M.^[58] Reprinted (adapted) with permission from T. Cadenbach, T. Bollermann, C. Gemel, M. Tombul, I. Fernandez, H. M. van, G. Frenking and R. A. Fischer, *J. Am. Chem. Soc.*, **2009**, *131*, 16063-16077. Copyright (2009) American Chemical Society.

1.4 $[\text{Zn}_2\text{Cp}^*_2]$ – A Milestone in Low-Valent Zinc Chemistry

For many years the preparation of molecular compounds of the type LMML ($M = \text{Hg}, \text{Cd}, \text{Zn}$) have seemed to be an insuperable challenge. The common in nature found, group 12 species exhibit the oxidation state +II. An exception is mercury, which also appears in nature in the oxidation state +I. Though a lot of salt like, ionic species exhibiting the $[\text{Hg}_2]^{2+}$ dication, like Hg_2Cl_2 (Calomel), have been known for decades, the first molecular compound containing a Hg-Hg σ -bond was not synthesized before 1999 by Apeloig *et al.* in the form of the silyl derivative $[\text{Hg}_2(\text{Si}\{\text{SiMe}_2\text{SiMe}_3\}_3)_2]$, which exhibits a pronounced stability even in air.^[59] The first compound featuring a $[\text{Cd}_2]^{2+}$ unit has already been structurally characterized in 1986 in form of the ionic $[\text{Cd}_2][\text{AlCl}_4]_2$,^[60] whereas the first molecular compound featuring a $\text{Cd}^{\text{I}}\text{-Cd}^{\text{I}}$ bond has been obtained in 1993 in form of $[\text{Cd}_2\text{Tp}^{\text{Me}_2}]$ ($\text{Tp}^{\text{Me}_2} = \text{hydrotris}(3,5\text{-dimethylpyrazolyl})\text{borate}$). However, the $[\text{Cd}_2]^{2+}$ unit was only evidenced by $\text{Cd}^{111}\text{-Cd}^{113}$ coupling in the ^{113}Cd NMR spectrum and no molecular structure could be determined to confirm this suggestion.^[61] The first respective structurally characterised $[\text{Cd}_2\text{L}_2]$ species was prepared

in 2006 by Power and coworkers in the form of the terphenyl stabilized compound $[\text{Cd}_2(\text{Ar}^{\text{Dipp}})_2]$ ($\text{Ar}^{\text{Dipp}} = \text{C}_6\text{H}_3\text{-}2,6\text{-(C}_6\text{H}_3\text{-}2,6\text{-}i\text{Pr}_2)_2$).^[62]

In the case of zinc the existence of the $[\text{Zn}_2]^{2+}$ dication was first evidenced by Raman spectroscopy in 1967 in a zinc solution of fused ZnCl_2 .^[63] Additionally, it was found in zeolite matrices and even mononuclear, paramagnetic Zn^+ units were reported to be formed in a microporous crystalline silicoaluminophosphate.^[64-66] In 1995 the dihydride Zn_2H_2 was obtained *via* matrix-isolation techniques at 12 K and subsequently characterized by deuterium substitution and vibrational spectroscopy assisted by quantum chemical calculations.^[67, 68] In 2004 Carmona *et al.* eventually succeeded a breakthrough in the preparation of decamethylzincocene $[\text{Zn}_2\text{Cp}^*_2]$, the first molecular compound exhibiting an intact $\text{Zn}^{\text{I}}\text{-Zn}^{\text{I}}$ bond.^[69] This incident can be regarded as the milestone in low valent chemistry, giving access to a synthetically readily available Zn^{I} source. The treatment of $[\text{ZnEt}_2]$ with $[\text{ZnCp}^*_2]$ leads to the formation of $[\text{ZnEtCp}^*]$ and $[\text{Zn}_2\text{Cp}^*_2]$, whereby the ratio of the two products is strongly dependent on the reaction conditions. The reaction mechanism for the formation of $[\text{Zn}_2\text{Cp}^*_2]$ is still not fully elucidated. However, when the reaction is conducted in Et_2O at $-10\text{ }^\circ\text{C}$, $[\text{Zn}_2\text{Cp}^*_2]$ can be obtained as the main product with only trace amounts of $[\text{ZnEtCp}^*]$. One year later Carmona and coworkers published a more efficient synthesis for $[\text{Zn}_2\text{Cp}^*_2]$ based on the reaction of ZnCl_2 with KCp^* in the presence of KH as a reducing agent.^[70] Further improvement resulted by directly using $[\text{ZnCp}^*_2]$ as a Cp^* source, which is otherwise formed from KCp^* and ZnCl_2 (Scheme 3).^[71] However, the most effective way (100 % yield) for the synthesis of $[\text{Zn}_2\text{Cp}^*_2]$ was reported by Stephan *et al.* in 2013 by direct hydrogenolysis (68 bar H_2) of $[\text{ZnCp}^*_2]$.^[72]



Scheme 3. Improved route for the synthesis of $[\text{Zn}_2\text{Cp}^*_2]$ by Carmona *et al.*

The crystal structure shows an almost linear geometry ($\text{Cp}^*_{\text{centr.}}\text{-Zn-Zn} = 177.4(1)$) with a $\text{Zn}^{\text{I}}\text{-Zn}^{\text{I}}$ core (Zn-Zn distance = 2.305 Å) stabilized by two η^5 coordinated Cp^* rings, which are aligned in a parallel and eclipsed fashion to each other (Figure 14). NMR, IR and quantum mechanical studies exclude the presence of additional bridging hydrides in the structure.

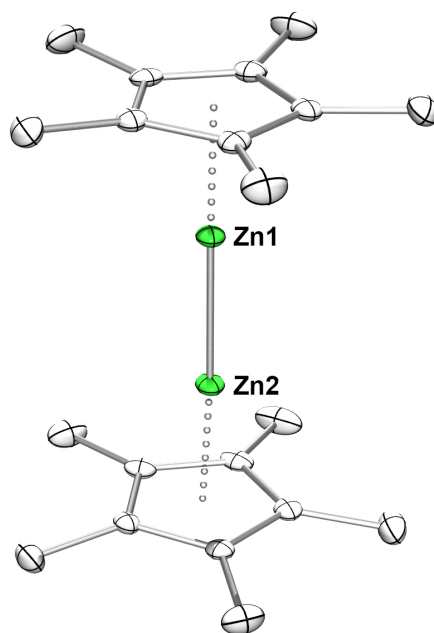


Figure 14. Molecular structure of $[\text{Zn}_2\text{Cp}^*_2]$. Hydrogen atoms are not shown for clarity.

Complementing this experimental data, a lot of theoretical studies have been performed, mostly dealing with the spectroscopic properties of the dizincocene and the bonding situation in this molecule.^[73-86] At this, the Zn-Zn bond arises due to the interaction between the singly occupied HOMOs of two neutral $\{\text{Cp}^*\text{Zn}\}$ fragments. There are four quasi-degenerate occupied orbitals, which are formed via combinations of the e_1 orbitals of the Cp^* unit with little participation of the Zn p orbitals (HOMO to HOMO-3). However, the additional HOMO-4 of $[\text{Zn}_2\text{Cp}^*_2]$ arises predominantly due to interactions between the Zn 4s orbitals (96 %) and is the main contributor of the Zn-Zn bond (Figure 15).^[71] In order to obtain some measure of the stability of $[\text{Zn}_2\text{Cp}^*_2]$, the disproportionation and Zn-Zn bond dissociation energy was calculated. For the disproportionation energy, *i.e.* $[\text{Zn}_2\text{Cp}_2] \rightarrow \text{Zn}(0) + [\text{ZnCp}_2]$ values of 17 and 20 kcal/mol were obtained. For the bond dissociation energy (BDE) of $[\text{Zn}_2\text{Cp}^*_2]$ values ranging between 66-72 kcal/mol were reported. According to energy decomposition analyses the overall energy is mainly attributed to electrostatic interaction rather than orbital interactions.

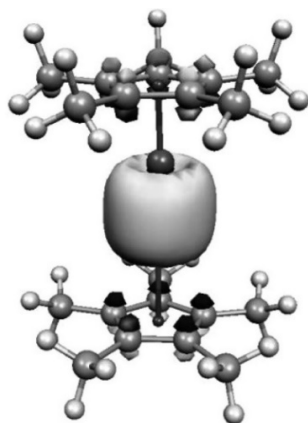
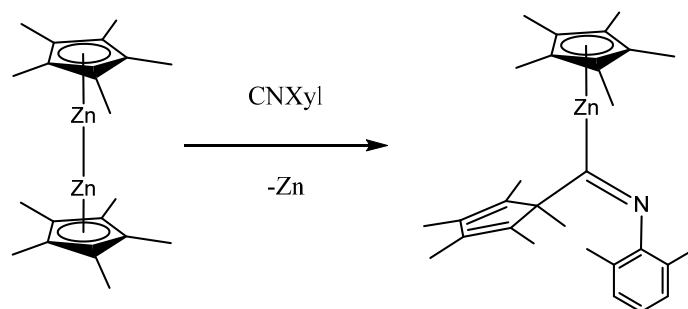


Figure 15. 3D-isosurface of the HOMO-4 corresponding to the Zn-Zn interaction in $[\text{Zn}_2\text{Cp}^*_2]$.^[71] Reprinted with permission from A. Gorrane, I. Resa, A. Rodriguez, E. Carmona, E. Alvarez, E. Gutierrez-Puebla, A. Monge, A. Galindo, D. del Río and R. A. Andersen, *J. Am. Chem. Soc.*, **2007**, *129*, 693-703. Copyright (2009) American Chemical Society.

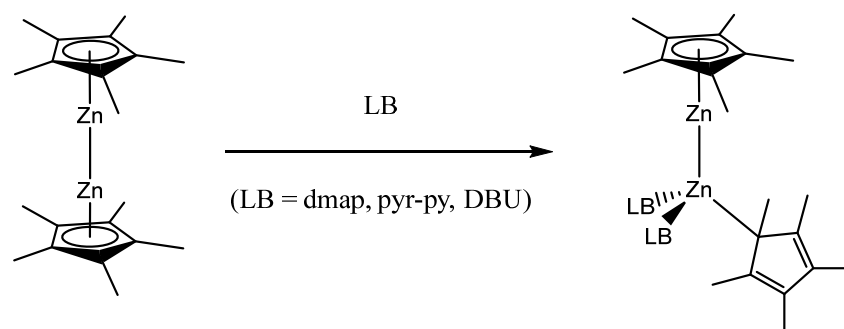
1.4.1 First Reactivity Studies of $[\text{Zn}_2\text{Cp}^*_2]$ towards Protonic Reagents and Lewis bases

From the beginning, a lot of effort has been invested in order to elucidate the reactivity of Carmona's reagent. $[\text{Zn}_2\text{Cp}^*_2]$ turned out to be unreactive towards H_2 , CO and CO_2 gas as well as a series of Lewis bases such as the nitrogen and phosphorus donors NEt_3 , TMEDA, pyridine, bipyridine, PPh_3 and PMe_3 .^[71] In contrast, the $\text{Zn}^{\text{I}}\text{-Zn}^{\text{I}}$ entity is prone to disproportionation when treated with the protonic reagents H_2O , MeOH or $t\text{BuOH}$. Aside from Zn^0 and $\text{Zn}(\text{OR})_2$ ($\text{R} = \text{H}$, Me or $t\text{Bu}$), Cp^*H is formed as a byproduct.^[69] Similarly, the treatment of $[\text{Zn}_2\text{Cp}^*_2]$ with the isocyanide CNXyl ($\text{Xyl} = \text{C}_6\text{H}_3\text{-2,6-Me}_2$) gives the disproportionation products Zn^0 and the iminoacyl complex $[\text{Cp}^*\text{Zn}\{(\text{CNXyl})(\text{C}_5\text{Me}_5)\}]$, which can also be obtained from the reaction of $[\text{ZnCp}^*_2]$ with the isocyanide.



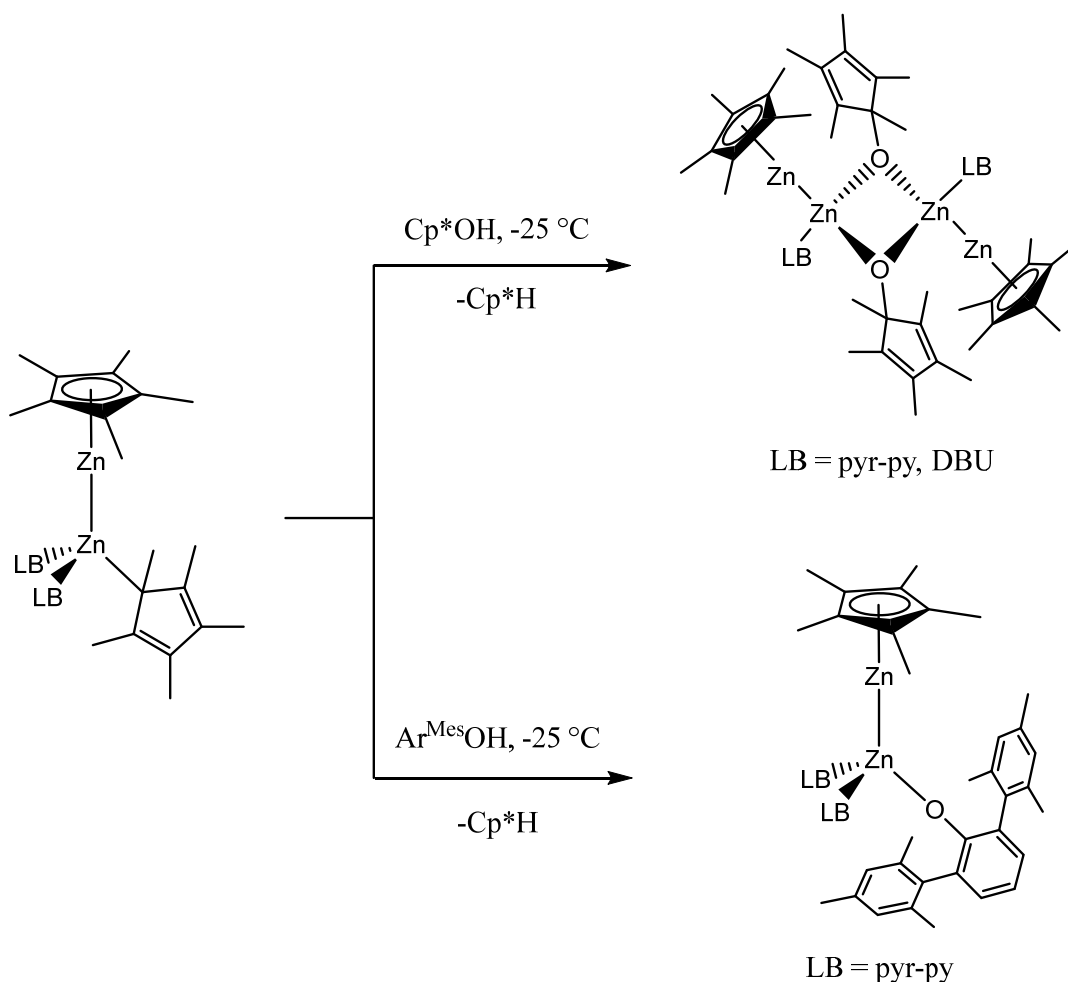
Scheme 4. Formation of $[\text{Cp}^*\text{Zn}\{(\text{CNXyl})(\text{C}_5\text{Me}_5)\}]$ from $[\text{Zn}_2\text{Cp}^*_2]$.

The attempts by Carmona *et al.* to prepare mixed ligand compounds of the type $[\text{Cp}^*\text{Zn-ZnAr}']$ ($\text{Ar}' = \text{C}_6\text{H}_3\text{-2,6-(C}_6\text{H}_3\text{-2,6-}^i\text{Pr}_2)_2$ and $\text{C}_6\text{H}_3\text{-2,6-(C}_6\text{H}_3\text{-2,6-Me}_2)_2$) were unsuccessful.^[87] The treatment of $[\text{Zn}_2\text{Cp}^*_2]$ with $[\text{ZnAr}'_2]$ in C_6D_6 under stirring for 24 h at room temperature, as well as under reflux conditions, does not give the desired heteroleptic complexes. In an alternative approach $[\text{Zn}_2\text{Cp}^*_2]$ is reacted with respective terphenyl lithium salts in Et_2O , but this leads to the disproportionation of the Zn^{I} species into metallic zinc and the half-sandwich complexes $[\text{Cp}^*\text{ZnAr}']$. Analogous complexes $[\text{Cp}^*\text{ZnR}]$ ($\text{R} = \text{Me, Mes}$) can be isolated from the reaction of $[\text{ZnCp}^*_2]$ with ZnR_2 in pentane, respectively.^[71] In contrast to the reactions of Carmona's reagent $[\text{Zn}_2\text{Cp}^*_2]$ with the mentioned rather weak nitrogen and phosphorus Lewis bases, the treatment with the strong Lewis bases LB (LB = 4-dimethylaminopyridine (dmap, $\text{pK}_a(\text{dmap}^+) = 17.95$), 4-pyrrolidinopyridine (pyr-py, $\text{pK}_a(\text{Hpyr-py}^+) = 18.33$) and 1,8-diazabicyclo[5.4.0]undec-7-ene (DBU, $\text{pK}_a(\text{HDBU}^+) = 24.34$, pK_a values in acetonitrile) and the NHCs 1,3-di-*tert*-butylimidazol-2-ylidene (tBu) and 1,3-Bis(2,4,6-trimethylphenyl)-4,5-dihydroimidazol-2-ylidene (SIMes) proceed under preservation of the $\text{Zn}^{\text{I}}\text{-Zn}^{\text{I}}$ moiety and the formation of the Lewis acid-base adducts $[\text{Cp}^*\text{Zn-Zn}(\text{LB})_2(\eta^1\text{-Cp}^*)]$ (Scheme 5) and $[\text{Cp}^*\text{Zn-Zn}(\text{NHC})(\eta^2\text{-Cp}^*)]$.^[87-89] Note, that the geminal coordination fashion of the bases to the $\text{Zn}^{\text{I}}\text{-Zn}^{\text{I}}$ moiety is thermodynamically favoured.^[88] While $[\text{Cp}^*\text{Zn-Zn}(\text{dmap})_2(\eta^1\text{-Cp}^*)]$ and $[\text{Cp}^*\text{Zn-Zn}(\text{NHC})(\eta^2\text{-Cp}^*)]$ are stable under inert gas atmosphere in the solid state at room temperature, the compounds $[\text{Cp}^*\text{Zn-Zn}(\text{pyr-py})_2(\eta^1\text{-Cp}^*)]$ and $[\text{Cp}^*\text{Zn-Zn}(\text{DBU})_2(\eta^1\text{-Cp}^*)]$ though stable in solution of Et_2O , decompose rapidly as solid materials at room temperature. Hence, these species could only be characterized by NMR spectroscopy, nevertheless in an unambiguous way. The ^1H NMR spectra of all compounds show in addition to the resonances of the respective bases only one Cp^* signal at room temperature indicating a fast fluxional behavior of the Cp^* groups.



Scheme 5. Preparation of the Lewis acid-base adducts $[\text{Cp}^*\text{Zn-Zn}(\text{LB})_2(\eta^1\text{-Cp}^*)]$.

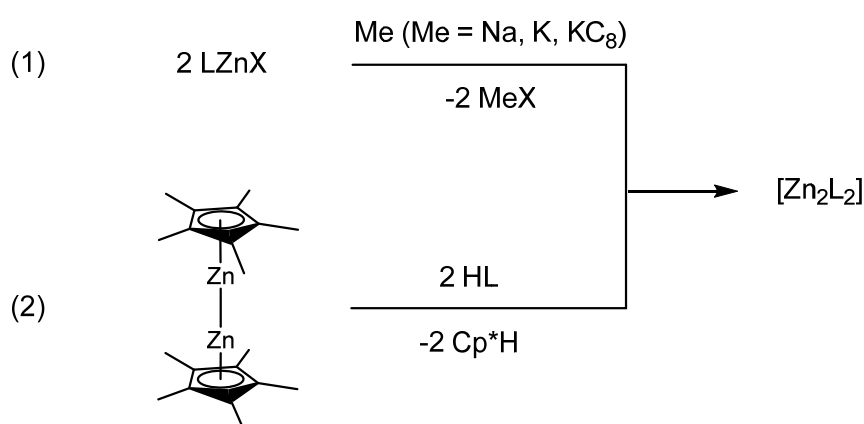
Furthermore, $[\text{Cp}^*\text{Zn-Zn}(\text{pyr-py})_2(\eta^1\text{-Cp}^*)]$ and $[\text{Cp}^*\text{Zn-Zn}(\text{DBU})_2(\eta^1\text{-Cp}^*)]$ were employed as precursors for the first $\text{Zn}^{\text{I}}\text{-Zn}^{\text{I}}$ complexes bearing oxygen donors. In 2010 Carmona *et al.* treated these acid-base adducts with Cp^*OH at $-25\text{ }^\circ\text{C}$ giving $[\text{Zn}_2\text{Cp}^*(\text{pyr-py})(\mu\text{-OCp}^*)]_2$ and $[\text{Zn}_2\text{Cp}^*(\text{DBU})(\mu\text{-OCp}^*)]_2$ with bridging Cp^*O ligands, respectively (Scheme 6).^[87, 90] Both compounds are thermally unstable and they rapidly decompose during dissolution at temperatures above $-40\text{ }^\circ\text{C}$, suggesting, that bulkier RO- groups are necessary to stabilize an oxygen bonded dizinc species. According to this, the reaction of $[\text{Cp}^*\text{Zn-Zn}(\text{pyr-py})_2(\eta^1\text{-Cp}^*)]$ with the sterically more demanding terphenol $\text{Ar}^{\text{Mes}}\text{OH}$ ($\text{HOC}_6\text{H}_3\text{-2,6-(C}_6\text{H}_3\text{-2,4,6-Me}_3)_2$) leads to the formation of the dimetallic compound $[\text{Cp}^*\text{Zn}_2(\text{pyr-py})_2(\text{Ar}^{\text{Mes}}\text{O})]$, which is by far thermally more stable than the bridged dimeric compounds.



Scheme 6. Synthesis of $\text{Zn}^{\text{I}}\text{-Zn}^{\text{I}}$ bonded species exhibiting O-donor ligands.

1.4.2 Derivatives $[Zn_2L_n]$ ($L \neq Cp^*$) of $[Zn_2Cp^*_2]$

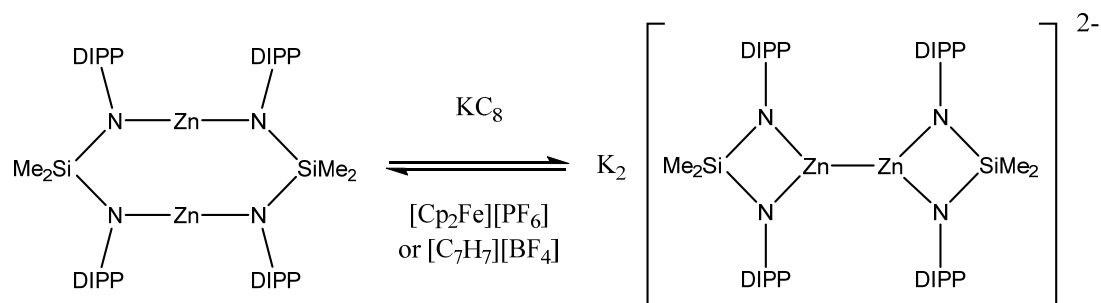
After the preparation of the first Zn^I - Zn^I bonded species $[Zn_2Cp^*_2]$, one of the focal points of research has been the preparation of novel derivatives of the type $[Zn_2L_n]$ ($L \neq Cp^*$), exhibiting an intact $[Zn_2]^{2+}$ moiety. Concerning this, two different strategies turned out to be quite effective, on the one hand the reductive coupling of Zn^{II} halide species which already bear stabilizing ligands L and on the other hand the simple substitution of the Cp^* groups starting from $[Zn_2Cp^*_2]$ (Scheme 7).



Scheme 7. Synthesis of $[Zn_2L_2]$ species *via* (1) reductive coupling and (2) protonation of $[Zn_2Cp^*_2]$.

Most often, the reductive coupling is based on the reduction of a $[LZnX]_n$ species ($X = Cl, I$) using an alkaline metal Me as a reducing agent. These reactions benefit from the precipitation of the by-product MeX as a driving force. According to this principle $[Zn_2(DDP)_2]$ ($DPP = HC(CMeNC_6H_3-2,6-Pr_2)_2$), which bears sterically demanding β -diketiminates as ligands, was prepared by Robinson *et al.* in the reaction of $[(DDP)Zn(\mu-I)_2Li(OEt)_2]$ with potassium.^[91] Similarly, the reductive coupling of $[(Ar^{Dipp})ZnI]$ with sodium yields $[Zn_2(Ar^{Dipp})_2]$, which was prepared by Power *et al.* in 2006, showing that it is also possible to encapsulate the $[Zn_2]^{2+}$ moiety with a sterically demanding monodentate terphenyl ligand.^[92] In contrast to $[Zn_2Cp^*_2]$ the Zn^I - Zn^I bond is not mainly formed by s-orbital interactions but rather by the interaction of the $4p_z(Zn)$ orbitals. Interestingly, when sodium hydride is used as a reducing agent instead the hydride-bridged compound $[(Ar^{Dipp})Zn(\mu-H)_2Zn(Ar^{Dipp})]$ without a $Zn-Zn$ bonding interaction is formed. Further treatment with another equivalent of sodium hydride gives the sodium

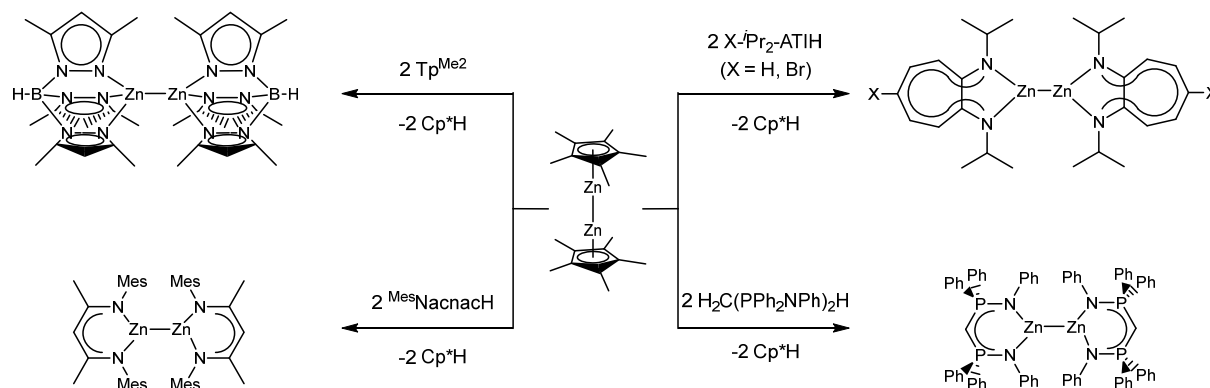
hydride-bridged species $[(Ar^{Dipp})Zn(\mu-H)(\mu-Na)Zn(Ar^{Dipp})]$, which exhibits a delocalized bonding orbital formed by the Zn atoms and the bridging H atom. In the following three years, a series of novel $[Zn_2L_2]$ derivatives like $[Zn_2(dpp-dian)_2]$ (dpp-dian = 1,2-bis[(dipp)imino]acenaphthene) or $[Na(THF)_2] \cdot [Zn_2L'_2]$ ($L' = [(2,6-iPr_2C_6H_3)N(Me)C]_2^{2-}$) were prepared in an analogous way.^[93, 94] In 2007 Tsai *et al.* reported the first intramolecular Zn-Zn coupling reaction. The reduction of the dinuclear Zn^{II} complex $[Zn_2(\mu-\eta^2-Me_2Si(NC_6H_3-2,6-iPr_2)_2)_2]$ with four equivalents of KC_8 yields the isomeric Zn-Zn bonded anion $[Zn_2(Me_2Si(NC_6H_3-2,6-iPr_2)_2)_2]^{2-}$.^[95] Note that the reaction is reversible using $[Cp_2Fe][PF_6]$ or $[C_7H_7][BF_4]$ as oxidants (Scheme 8).



Scheme 8. Reversible reaction of $[Zn_2(\mu-\eta^2-Me_2Si(NC_6H_3-2,6-iPr_2)_2)_2]$ to $[Zn_2(Me_2Si(NC_6H_3-2,6-iPr_2)_2)_2]^{2-}$.

Another effective approach to synthesize novel $[Zn_2L_2]$ compounds was first investigated by Schulz *et al.* in 2009. Similar to Ga-Cp* bonds,^[96] Zn-Cp* bonds are prone to hydrolytic cleavage. Regarding this $[Zn_2(dmap)_6][Al\{Al\{OC(CF_3)_4\}_4\}_2]$ was obtained by the reaction of $[Zn_2Cp^*_2]$ with $[H(Et_2O)_2][Al\{OC(CF_3)_3\}_4]$ in the presence of six equivalents of the strong donor dmap giving Cp*H as a by-product.^[97] Following up on this idea, they employed protonation agents, whose conjugated Brønsted bases can directly act as chelating ligands to stabilize the Zn^I-Zn^I moiety after Cp*H elimination. In this way, not only the mentioned heteroleptic complexes $[Zn_2Cp^*(pyr-py)(\mu-OCp^*)]_2$ and $[Zn_2Cp^*(DBU)(\mu-OCp^*)]_2$ could be synthesized, but also homoleptic Zn^I-Zn^I species. In particular the β -diketimate, the bis(iminophosphorano)methane and the pyrazolylhydridoborate assisted $[Zn_2L_2]$ compounds ($L = ^{Mes}Nacnac$, $HC(PPh_2NPh)_2$, Tp^{Me_2}) ($^{Mes}Nacnac = [(MesNCMe_2)_2CH]^-$, $Tp = tris(3,5-dimethylpyrazolyl)hydridoborate$) using the respective LH as acids have been prepared (Scheme 9).^[98-100] In addition Roesky *et al.* synthesized the N-isopropyl-2-

(isopropylamino)troponimine ($i\text{Pr}_2\text{ATI}$) derivatives $[\{i\text{Pr}_2\text{ATI}\}_2\text{Zn}_2]$ and $[\text{4-Br}\{i\text{Pr}_2\text{ATI}\}_2\text{Zn}_2]$.^[101]



Scheme 9. Synthesis of different $[\text{Zn}_2\text{L}_2]$ compounds *via* protonation of $[\text{Zn}_2\text{Cp}^*_2]$ with LH.

In comparison both methods are effective for the preparation of novel $[\text{Zn}_2\text{L}_2]$ compounds, but the reductive coupling has certain drawbacks such as the low yield and the difficulty to separate by-products, making the protonation route the more elegant approach.

Appart from that, most recently Fässler *et al.* prepared $\text{K}_2[\text{K}(\text{2.2.2-crypt})_4[\text{Ge}_9\text{Zn-ZnGe}_9](\text{NH}_3)_{26}]$ (2.2.2.-crypt = 4,7,13,16,21,24-Hexaoxa-1,10-diazabicyclo[8.8.8]hexacosan) by treating $[\text{Zn}_2\{\text{HC}(\text{PPh}_2\text{NPh})_2\}_2]$ with two equivalents of $\text{K}_4[\text{Ge}_9]$ in liquid ammonia.^[102] Formally, two bis(iminophosphaphorano)methan ligands are substituted by two nido- $[\text{Ge}_9]^{4-}$ cluster ligands. The anion $[\text{Ge}_9\text{Zn-ZnGe}_9]^{6-}$ is the second example of a sandwich complex having a Zn-Zn unit similar to $[\text{Zn}_2\text{Cp}^*_2]$. In particular, the anion can be formally described as two $[\text{Ge}_9\text{Zn}]^{3-}$ closo-clusters covalently bound through the Zn atoms.

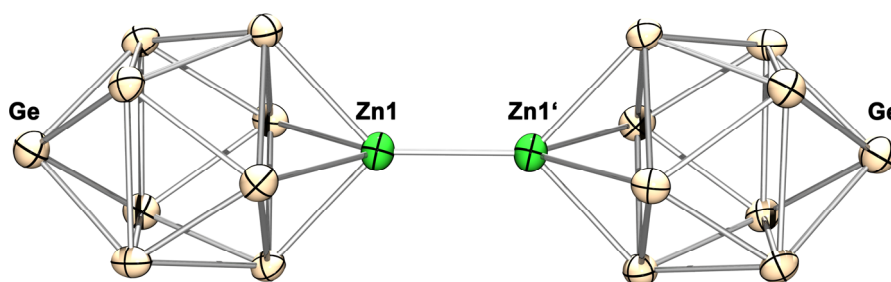


Figure 16. Molecular structure of $[\text{Ge}_9\text{Zn-ZnGe}_9]^{6-}$.

1.4.3 Stable Cationic Zn^I-Zn^I Bonded Species in the Environment of the Weakly Coordinating Anion [BAr₄^F]⁻

As mentioned, the protonation of [Zn₂Cp*₂] using [H(Et₂O)₂][Al{OC(CF₃)₃}₄] in the presence of dmap gives the respective base stabilized [Zn₂]²⁺ dication.^[97] Fischer *et al.* showed that the protonation of [Zn₂Cp*₂] with one equivalent of [H(Et₂O)₂][BAr₄^F] (BAr₄^F = B{C₆H₃(CF₃)₂}₄), in the absence of additional bases, leads to the formation of the complex [Cp*₃Zn₄(Et₂O)₂][BAr₄^F], exhibiting two intact Zn^I-Zn^I units.^[103] There are two Cp*ZnZn(Et₂O) moieties at which the Zn atoms bearing the coordinated Et₂O molecules gain additional stabilisation by sharing one Cp* group in a η³ fashion. This leads to a bent triple decker structure in the solid state (Figure 17). The cation is quite labile, as it rapidly decomposes at room temperature even in the solid state under an inert gas atmosphere.

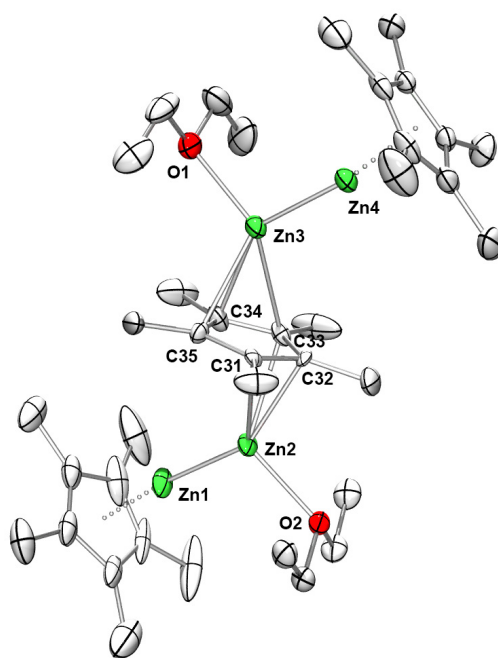


Figure 17. Molecular structure of [Cp*₃Zn₄(Et₂O)₂][BAr₄^F] without hydrogen atoms.^[103] Reproduced from K. Freitag, H. Banh, C. Ganesamoorthy, C. Gemel, R. W. Seidel and R. A. Fischer, *Dalton Trans.*, **2013**, 42, 10540-10544, with permission from the Royal Society of Chemistry.

Apart from the protonation route for the cleavage of Zn-Cp* bonds, Fischer *et al.* reported on the oxidative cleavage of Zn-Cp* bonds as a highly effective way to access cationic Zn^I-Zn^I

species using $[\text{Zn}_2\text{Cp}^*_2]$ as a starting compound. Again, like to Ga-Cp* bonds,^[104] Zn-Cp* bonds can be broken using $[\text{FeCp}_2][\text{BAR}_4^{\text{F}}]$ as an oxidizing agent. In this way the semi deprotected $[\text{Cp}^*\text{Zn}_2(\text{Et}_2\text{O})_3][\text{BAR}_4^{\text{F}}]$ is obtained by treating $[\text{Zn}_2\text{Cp}^*_2]$ with one equivalent $[\text{FeCp}_2][\text{BAR}_4^{\text{F}}]$ in Et_2O .^[103] The $[\text{Cp}^*]^-$ radical anion is oxidized under formation of decamethylfulvalene $(\text{Cp}^*)_2$, whereas the ferrocenium salt is reduced to give ferrocene $[\text{FeCp}_2]$. Note, that the $[\text{Cp}^*\text{Zn}_2(\text{Et}_2\text{O})_3]^+$ is quite labile towards disproportionation at room temperature in solution as well as an isolated crystalline material. In contrast the more symmetric naked $[\text{Zn}_2]^{2+}$ which can be obtained as the THF adduct $[\text{Zn}_2(\text{THF})_6][\text{BAR}_4^{\text{F}}]_2$ from the reaction of $[\text{Zn}_2\text{Cp}^*_2]$ with two equivalents of $[\text{FeCp}_2][\text{BAR}_4^{\text{F}}]$ in THF, respectively, is stable at room temperature in solution as well as in the solid state.^[105] This compound can be regarded as a zinc analogue of the calomel dication and the obtained molecular structure of the dication as an environmental snapshot of $[\text{Zn}_2]^{2+}$ solvated in THF (Figure 18). As a virtually naked $[\text{Zn}_2]^{2+}$ dication, its potential as a building block for novel $\text{Zn}^{\text{I}}-\text{Zn}^{\text{I}}$ species was investigated. Regarding this, the *in situ* ^1H NMR studies of $[\text{Zn}_2(\text{THF})_6][\text{BAR}_4^{\text{F}}]_2$ with two equivalents of KCp^* and KDDP at room temperature leads to the formation of $[\text{Zn}_2\text{Cp}^*_2]$ and $[\text{Zn}_2\text{DDP}_2]$, respectively. However, disproportionation occurred at the same time. Attempts to substitute the coordinated THF molecules with the stronger but softer σ -donor PMe_3 at room temperature lead to the complete disproportionation of the Zn^{I} species giving $[\text{Zn}(\text{PMe}_3)_4][\text{BAR}_4^{\text{F}}]$ and zinc metal as products. In contrast, the treatment of a solution of $[\text{Zn}_2(\text{THF})_6][\text{BAR}_4^{\text{F}}]_2$ in fluorobenzene with a constant stream (1 atm) of the strong σ -donor and π - acceptor CO does not proceed under any conversion of the starting compound.

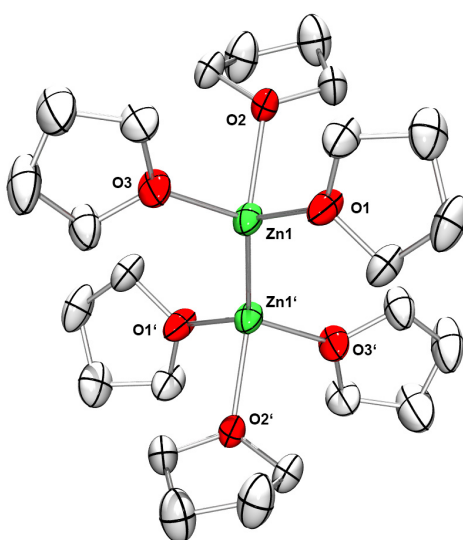


Figure 18. Molecular structure of the $[\text{Zn}_2(\text{THF})_6]^{2+}$ dication without hydrogen atoms.

Further investigations were focused on the feasibility of employing $[\text{Cp}^*\text{Zn}_2(\text{Et}_2\text{O})_3][\text{BAR}_4^{\text{F}}]$ and $[\text{Zn}_2(\text{THF})_6][\text{BAR}_4^{\text{F}}]_2$ as building blocks for intermetallic compounds. Previous studies have already reported on the preparation of $[\text{Zn}(\text{GaCp}^*)_4][\text{BAR}_4^{\text{F}}]_2$,^[106] in which Zn^{2+} is formed *in situ* from the treatment of ZnMe_2 with two equivalents of $[\text{H}(\text{Et}_2\text{O})_2][\text{BAR}_4^{\text{F}}]$ in the presence of GaCp^* . Similarly, $[\text{Cp}^*\text{Zn}_2(\text{Et}_2\text{O})_3][\text{BAR}_4^{\text{F}}]$ and $[\text{Zn}_2(\text{THF})_6][\text{BAR}_4^{\text{F}}]_2$ were reacted with the two electron donor GaCp^* in order to replace the coordinated solvent molecules.^[107] However, in both cases $[\text{Ga}_2(\text{ZnCp}^*)_2(\text{GaCp}^*)_4]^{2+}$ was formed which displays a Ga-Ga core in which each Ga bears two GaCp^* and one ZnCp^* ligand, respectively (Figure 19, left). Therefore, Cp^* transfer from gallium to zinc and homoleptic $\text{Zn}^{\text{I}}\text{-Zn}^{\text{I}}$ bond cleavage occurs. The elemental composition was confirmed by EA and AAS and the coordination environment by low temperature ^1H NMR spectroscopy that showed two chemically different sets of protons for ECp^* ($\text{E} = \text{Zn}$ or Ga) at $-40\text{ }^\circ\text{C}$ in a 4:2 ratio. Interestingly, the reaction of $[\text{Zn}_2\text{Cp}^*_2]$ with the Ga^+ transfer reagent $[\text{Ga}_2\text{Cp}^*][\text{BAR}_4^{\text{F}}]$ gives the isomeric $[\text{Zn}_2(\mu\text{-GaCp}^*)_2\text{GaCp}^*_4]^{2+}$ with a $\text{Zn}^{\text{I}}\text{-Zn}^{\text{I}}$ core and bridging and terminal GaCp^* ligands (Figure 19, right).^[108] Note, that there is an equilibrium in solution between the two coordination isomers $[\text{Zn}_2(\mu\text{-GaCp}^*)_2\text{GaCp}^*_4]^{2+}$ and $[\text{Zn}_2(\text{GaCp}^*)_6]^{2+}$. As a consequence, the low temperature ^1H NMR spectrum shows two GaCp^* proton peaks in a 1:5 ratio. In all cases, the presence of the weakly coordinating anion (WCA) $[\text{BAR}_4^{\text{F}}]^-$ is a crucial point for the stabilization and hence the successful isolation of such low valent zinc cations (very weakly coordinated *i.e.* “naked”).

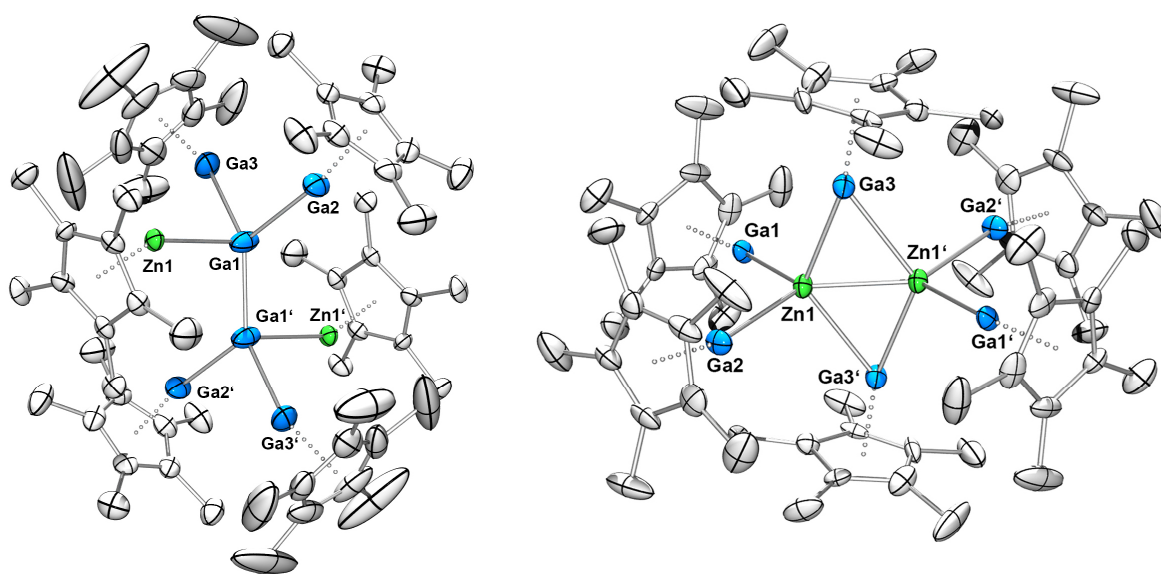


Figure 19. Molecular structures of $[\text{Ga}_2(\text{ZnCp}^*)_2(\text{GaCp}^*)_4]^{2+}$ (left) and $[\text{Zn}_2(\mu\text{-GaCp}^*)_2\text{GaCp}^*_4]^{2+}$ (right) without hydrogen atoms.

1.5 From Simple Coordination Chemistry to Hume-Rothery Type Clusters

Bearing in mind that monovalent $\bullet\text{ZnR}$ ($\text{R} = \text{Cp}^*, \text{CH}_3$) fragments can function as one electron donor ligands towards transition metals, it was reasonable to employ $[\text{Zn}_2\text{Cp}^*_2]$ as a natural source for the monovalent $\bullet\text{ZnCp}^*$ species. This is formed upon homolytic cleavage of the $\text{Zn}^{\text{I}}-\text{Zn}^{\text{I}}$ bond. The reactivity studies of homoleptic GaCp^* transition metal compounds towards ZnR_2 ($\text{R} = \text{Me}, \text{Et}$) gave the above mentioned zinc rich compounds $[\text{TM}(\text{ZnR})_n]$ ($\text{TM} = \text{Mo}, \text{Ru}, \text{Rh}, \text{Pd}$; $\text{R} = \text{Me}, \text{Et}, \text{Cp}^*$; $n = 8 - 12$), at which the transition metal exclusively bears $\bullet\text{ZnR}$ ($\text{R} = \text{Cp}^*, \text{Me}, \text{Et}$) ligands.^[58] Fischer *et al.* continued these studies in 2011 by treating $[\text{TM}(\text{GaCp}^*)_4]$ ($\text{TM} = \text{Pd}, \text{Pt}$) with four equivalents of $[\text{Zn}_2\text{Cp}^*_2]$ as a highly potential source for the $\bullet\text{ZnCp}^*$ ligand. As a result, a by their means inseparable product mixture between $[\text{TM}(\text{GaCp}^*)_2(\text{ZnCp}^*)_2(\text{ZnZnCp}^*)_2]$ and the distorted dodecahedral $[\text{TM}(\text{ZnCp}^*)_4(\text{ZnZnCp}^*)_4]$ in a 6:1 ratio was obtained (Figure 20).^[109] Interestingly both compounds not only feature the expected $\bullet\text{ZnCp}^*$ ligand but also the novel $\bullet\text{ZnZnCp}^*$ ligand which also serves as a one electron donor. These compounds are rare examples for molecular species exhibiting finite unsupported heterometallic chains ($\text{Cp}^*\text{ZnZnPdZnZnCp}^*$). In molecular compounds such alignments are usually stabilized by additional bridging ligands. Unsupported oligo metal chains are rather common in ligand free solid state chemistry, *e.g.* in $\text{Hg}_3(\text{AsF}_6)$ or $\text{Hg}_4(\text{AsF}_6)_2$.^[110, 111]

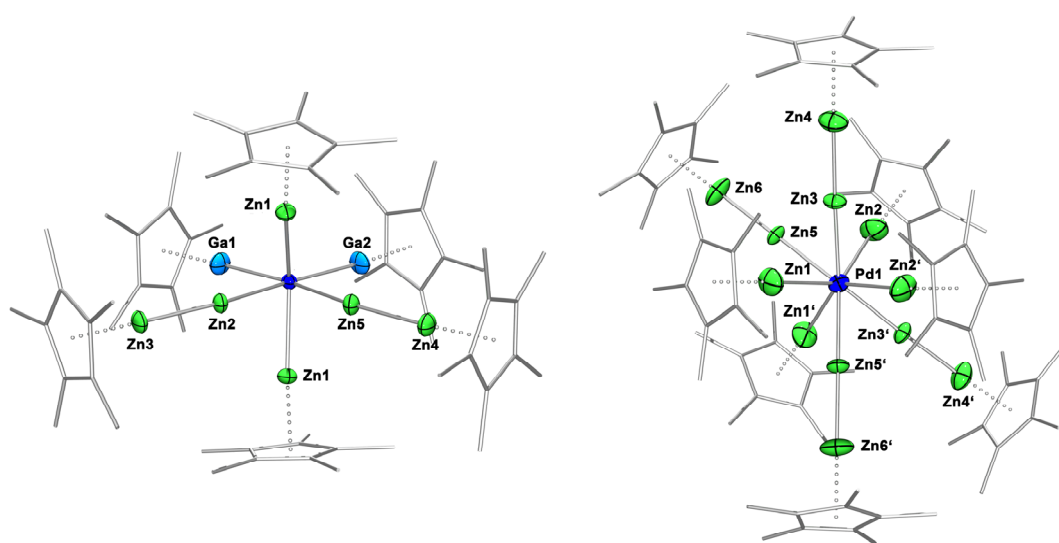


Figure 20. Molecular structures of $[\text{Pd}(\text{GaCp}^*)_2(\text{ZnCp}^*)_2(\text{ZnZnCp}^*)_2]$ (left) and $[\text{Pd}(\text{ZnCp}^*)_4(\text{ZnZnCp}^*)_4]$ (right) without hydrogen atoms.

The reaction proceeds *via* dissociation of GaCp* and subsequent addition of a Zn^I-Zn^I bond, *i.e.* association of •ZnCp* units at the electronically and coordinatively unsaturated palladium centers. Further GaCp* dissociation steps are equilibrium processes and consequently more difficult due to free GaCp* in solution. Hence, additional Pd-Zn bond formation is hindered resulting in the much lower yield of [TM(ZnCp*)₄(ZnZnCp*)₄]. Intermediates of the type [L_aTM(ZnCp*)_b] (L = GaCp* or ZnCp*) are able to react with [Zn₂Cp*₂] *via* Cp* transfer to give the novel Zn⁰Zn^ICp* ligand and [Zn^{II}Cp*₂] as a byproduct. Formally a disproportionation of Zn^I occurs (Zn⁰ ← 2 Zn^I → Zn^{II}).

Based on these reactions, [Zn₂Cp*₂] can be used as both, a valuable source for the ZnCp* moiety, but also for the novel ZnZnCp* fragment as ligands in coordination chemistry. Though similar to the reaction of [Pd(GaCp*)₄] with ZnMe₂, the reaction with [Zn₂Cp*₂] also leads to GaCp*/ZnCp* exchange, but the reaction pathways are totally different. In the following, the reactivity studies of [Zn₂Cp*₂] were extended to non GaCp* bearing transition metal complexes exhibiting substitution labile ligands. The exploration of this concept led to a series of TM/Zn complexes. In particular, the treatment of [PdMe₂(tmeda)] (tmeda = *N,N,N',N'*-tetramethylethan-1,2-diamine) with four equivalents of [Zn₂Cp*₂] yields [Pd(ZnCp*)₄(ZnMe)₂{Zn(tmeda)}] (tmeda = *N,N,N',N'*-tetramethylethan-1,2-diamine) as a main product (Figure 21, left).^[112] In addition, [ZnCp*₂], [Cp*Pd(ZnCp*)₃] and [Pd(ZnCp*)₄(ZnMe)₄] are obtained as byproducts demonstrating rather complex interconnected and also competitive formation pathways for these compounds. However, due to different solubility properties, [Pd(ZnCp*)₄(ZnMe)₂{Zn(tmeda)}] can be isolated as a pure crystalline material. Though the reaction mechanism is not fully elucidated, homolytic Zn-Cp* and Zn-Zn bond cleavage as well as Cp*/Me exchange between Zn and Pd centres are involved. Interestingly the tmeda ligand is transferred from the Pd center to a Zn center giving access to the unique Zn(tmeda) ligand. As a result, three different ZnR ligands coordinate to Pd, the one electron donors Zn^IMe and Zn^ICp* and the two electron donor Zn⁰(tmeda). Quantum chemical calculations confirmed that [Pd(ZnCp*)₄(ZnMe)₂{Zn(tmeda)}] can be regarded as a seven coordinated version of the eight coordinated 18 electron complex [Pd(ZnMe)₄(ZnCp*)₄], at which two ZnMe ligands are substituted by one Zn(tmeda) ligand. This is also true for the coordination geometry: based on a trigonal dodecahedral motif of [Pd(ZnMe)₄(ZnCp*)₄] two vertices are eliminated (ZnMe) and one new vertex (Zn(tmeda)) is placed in-between the missing vertices.

Additional studies have shown, that the other group homologues $[\text{Cp}^*\text{TM}(\text{ZnCp}^*)_3]$ (TM = Ni and Pt) of the piano stool complex $[\text{Cp}^*\text{Pd}(\text{ZnCp}^*)_3]$ can be prepared specifically by treating $[\text{TM}(\text{cod})_2]$ with two equivalents of $[\text{Zn}_2\text{Cp}^*_2]$ (Figure 21, right).^[113] Again a redox process takes place, at which Zn^{I} is reduced to Zn^0 (precipitation of metallic zinc) and the TM^0 center is oxidized to TM^{I} . This is accompanied by homolytic $\text{Zn}^{\text{I}}-\text{Zn}^{\text{I}}$ bond cleavage and Cp^* transfer from Zn to the TM centres.

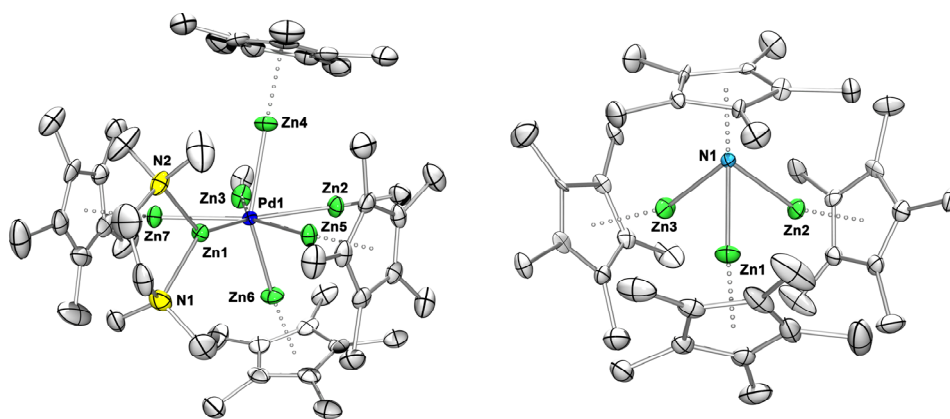


Figure 21. Molecular structures of $[\text{Pd}(\text{ZnCp}^*)_4(\text{ZnMe})_2\{\text{Zn}(\text{tmeda})\}]$ (left) and $[\text{Cp}^*\text{Ni}(\text{ZnCp}^*)_3]$ (right) without hydrogen atoms.

These reactivity studies have been the first indicators that Carmona's reagent behaves in a similar way like the isolobal H_2 towards transition metal centers. In fact, $[\text{Zn}_2\text{Cp}^*_2]$ coordinates to unsaturated moieties $[\text{L}_n\text{TM}]$ to form complexes of the type $[\text{L}_n\text{TM}(\text{ZnCp}^*)_2]$. This reaction principle is also true for H_2 , which oxidatively adds to electron rich unsaturated transition metal centers to give dihydride complexes $[\text{L}_n\text{TM}(\text{ZnCp}^*)_2]$. Regarding this $\bullet\text{ZnR}$ fragments are isolobal to the $\bullet\text{H}$ radical. Moreover, since the pioneering work from Kubas *et al.*, H_2 is also known for its ability to coordinate in a side on fashion to unsaturated electron poor transition metal fragments under preservation of the H-H bond. The first complexes of this kind were $[\text{TM}(\text{CO})_3(\text{PR}_3)_2(\eta^2-\text{H}_2)]$ (TM = Mo, W; R = Cy, *i*Pr) from 1984.^[114-116] Regarding this, there are two additional intermediate forms in between of a dihydride complex and a true H_2 complex to be distinguished. One is the elongated H_2 complex, which is based on a bonding situation closer to a true H_2 complex and the other one is the compressed dihydride, which exhibits closer resemblance to the classical dihydride, respectively. Using the isolobal principle, it was to be expected that $[\text{Zn}_2\text{Cp}^*_2]$ can also coordinate under preservation of the Zn-Zn bond to transition

metal centers. In the continuing investigations with group 10 transition metals, Fischer *et al.* treated $[\text{Zn}_2\text{Cp}^*_2]$ with $[\text{Pd}(\text{PCy}_3)_2]$ and $[\{\text{Pd}(\text{CN}^t\text{Bu})_2\}_3]$ giving $[\text{Pd}(\text{PdPCy}_3)_2(\text{Zn})(\mu\text{-Zn}_2\text{Cp}^*)(\mu\text{-ZnCp}^*)_3]$ and $[\text{Pd}(\text{CN}^t\text{Bu})_2(\text{ZnCp}^*)_4]$ (Figure 22, left), respectively.^[117] Both compounds feature some short Zn-Zn distances indicating Zn-Zn interactions in the ligand sphere, though quantum chemical calculations are missing to unambiguously elucidate the bonding situation. At this, $[\text{Ni}(\text{ZnCp}^*)_4(\text{ZnMe})_4]$ is suitable for comparison as quantum chemical calculations clearly reveal weak Zn-Zn interactions in the ligand sphere with distances in the range of 2.746(1) – 2.912(1) Å between adjacent Zn atoms. The compound $[\text{Pd}(\text{PdPCy}_3)_2(\text{Zn})(\mu\text{-Zn}_2\text{Cp}^*)(\mu\text{-ZnCp}^*)_3]$ exhibits a $[\text{Pd}_3\text{Zn}_6]$ core. The three Pd atoms are arranged in a bent fashion, in which the three Pd atoms are connected by a Zn atom leaving no ligand. The $\mu\text{-ZnCp}^*$ groups are unequally distributed along both Pd-Pd contacts. Note that there is one bridging Zn atom at each Pd-Pd contact respectively, which are sharing one Cp^* ligand. The short Zn-Zn distance of 2.729(1) allows the Cp^* moiety to be disordered over the respective zinc positions. In this context, a weak Zn-Zn interaction is to be expected similar to $[\text{Ni}(\text{ZnCp}^*)_4(\text{ZnMe})_4]$. As a consequence, $[\text{Pd}(\text{PdPCy}_3)_2(\text{Zn})(\mu\text{-Zn}_2\text{Cp}^*)(\mu\text{-ZnCp}^*)_3]$ might be a zinc analogue of an elongated dihydride complex. In comparison, $[\text{Pd}(\text{CN}^t\text{Bu})_2(\text{ZnCp}^*)_4]$ exhibits two quite shorter Zn-Zn contacts (Figure 22, left) with 2.595(2) and 2.609(2) Å. In this relation Fischer *et al.* also reported on $[\text{Ni}(\text{ZnCp}^*)(\text{ZnMe})(\text{PMe}_3)_3]$ (Figure 22, right), which was prepared by Ga/Zn exchange using ZnMe_2 and $[\text{Ni}(\text{PMe}_3)_3(\text{GaCp}^*)]$ as starting compounds. The Zn-Zn bond distance of 2.525(1) Å is comparable to those in $[\text{Pd}(\text{CN}^t\text{Bu})_2(\text{ZnCp}^*)_4]$ and only 9 % longer than in $[\text{Zn}_2\text{Cp}^*_2]$. Quantum chemical calculations have shown distinct Zn-Zn interactions in $[\text{Ni}(\text{ZnCp}^*)(\text{ZnMe})(\text{PMe}_3)_3]$. Of note, $[\text{Ni}(\text{ZnCp}^*)(\text{ZnMe})(\text{PMe}_3)_3]$ and $[\text{Pd}(\text{CN}^t\text{Bu})_2(\text{ZnCp}^*)_4]$ can be regarded as examples for zinc analogues of elongated H_2 complexes. However, the hydrogen analogy for $[\text{Pd}(\text{PdPCy}_3)_2(\text{Zn})(\mu\text{-Zn}_2\text{Cp}^*)(\mu\text{-ZnCp}^*)_3]$ and $[\text{Pd}(\text{CN}^t\text{Bu})_2(\text{ZnCp}^*)_4]$ is derived from structural properties only, with little information on the true nature metal-metal bonding. Nevertheless, the reactivity studies of $[\text{Zn}_2\text{Cp}^*_2]$ towards d^{10} transition metal complexes are in accordance to the suggested H_2 analogy. A side-on coordination is favored in the presence of the electron withdrawing $^t\text{BuNC}$, while Zn-Zn bond cleavage is favored upon coordination in the presence of the electron donating co-ligand PCy_3 . Recent computational studies on the reaction of $[\text{Zn}_2\text{R}_2]$ ($\text{R} = \text{Cp}$ or Ph) with $[\text{M}(\text{CO})_5]$ ($\text{M} = \text{Cr}, \text{Mo}, \text{W}$) and $[\text{Pd}(\text{PR}'_3)_2]$ ($\text{R}' = \text{F}, \text{H}, \text{Me}$) confirm the side on (η^2) coordination of $[\text{Zn}_2\text{R}_2]$ towards TM fragments with elongation but preservation of the Zn-Zn bond.^[118]

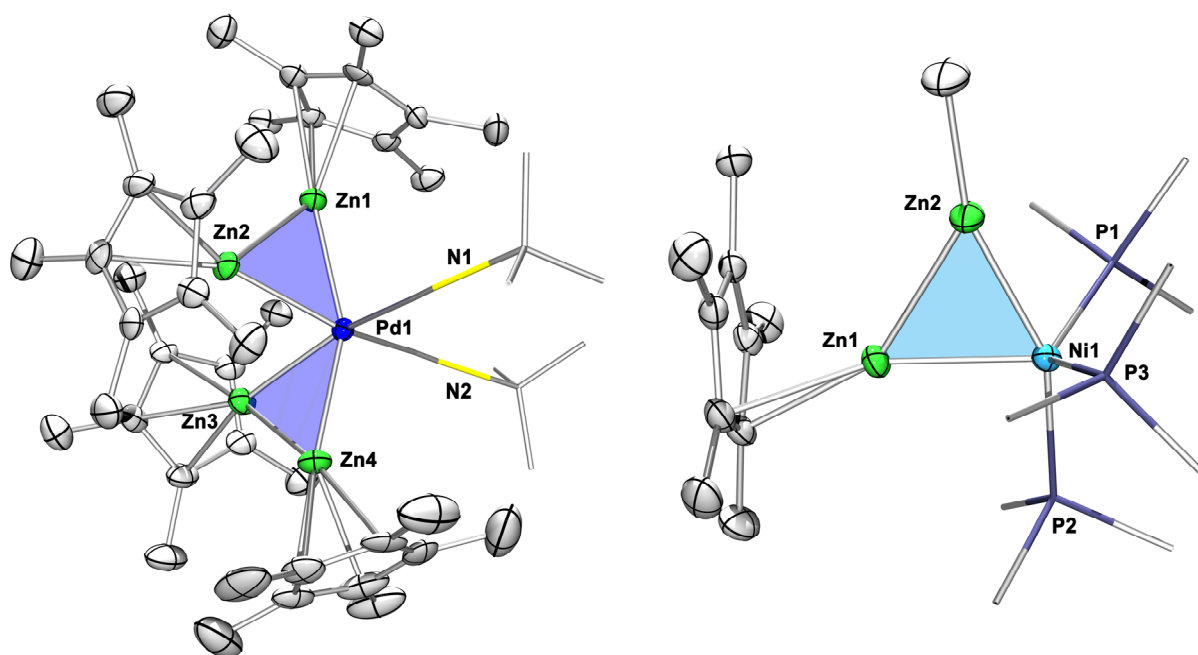


Figure 22. Molecular structures, without hydrogen atoms, of $[\text{Pd}(\text{CN}^t\text{Bu})_2(\text{ZnCp}^*)_4]$ (left) and $[\text{Ni}(\text{ZnCp}^*)(\text{ZnMe})(\text{PMe}_3)_3]$ (right) including Zn-Zn interactions.

To carry matters to extremes, $[\text{Zn}_2\text{Cp}^*_2]$ was reacted with *in situ* generated CuCp^* as simplest model for a $[\text{L}_n\text{TM}]$ fragment. Indeed, $[\text{Zn}_2\text{Cp}^*_2]$ coordinates in a side-on fashion to CuCp^* , yielding the triangular $[\text{Cp}^*\text{Cu}(\eta^2\text{-}[\text{Zn}_2\text{Cp}^*_2])]$ (Figure 23).^[119] In addition, $[\text{Zn}_2\text{Cp}^*_2]$ was treated with *in situ* formed $[\text{ZnCp}^*]^+$ to give $[\text{Zn}_3\text{Cp}^*_3]^+$. This compound can be regarded as a zinc analogue of $[\text{H}_3]^+$, one of the most abundant ions in the universe (Figure 23). It is the most fundamental example of a molecule exhibiting a three-centre-two-electron bonding situation^[120] and the prototype model for σ -aromaticity. In the cases of $[\text{Zn}_2\text{CuCp}^*_3]$ and $[\text{Zn}_3\text{Cp}^*_3]^+$ the strong negative calculated nucleus-independent chemical shift (NICS) values (-42.3 and -38 ppm) also indicate σ -aromaticity. Quantum chemical calculations show dominant σ donation $[\text{Zn}_2\text{Cp}^*_2] \rightarrow [\text{ZnCp}^*]^+$ (-59.1 kcal/mol) into the formally empty 4s orbital of the $[\text{ZnCp}^*]^+$ fragment. This is slightly different from $[\text{Zn}_2\text{CuCp}^*_3]$, the σ donation $[\text{Zn}_2\text{Cp}^*_2] \rightarrow [\text{CuCp}^*]$ (-21.8 kcal/mol) is only slightly stronger than the π back-donation $[\text{Zn}_2\text{Cp}^*_2] \leftarrow [\text{CuCp}^*]$ (-16.5 kcal/mol). As all larger clusters and bulk materials feature triangular $[\text{M}_3]$ units as structural motifs, $[\text{Zn}_2\text{CuCp}^*_3]$ and $[\text{Zn}_3\text{Cp}^*_3]$ can be regarded as models for embryonic brass and zinc, respectively. These molecules complete the set of different bonding modes adopted by $[\text{Zn}_2\text{Cp}^*_2]$ towards transition metal centers, which is fully analogous to the coordination chemistry of the isolobal H_2 .

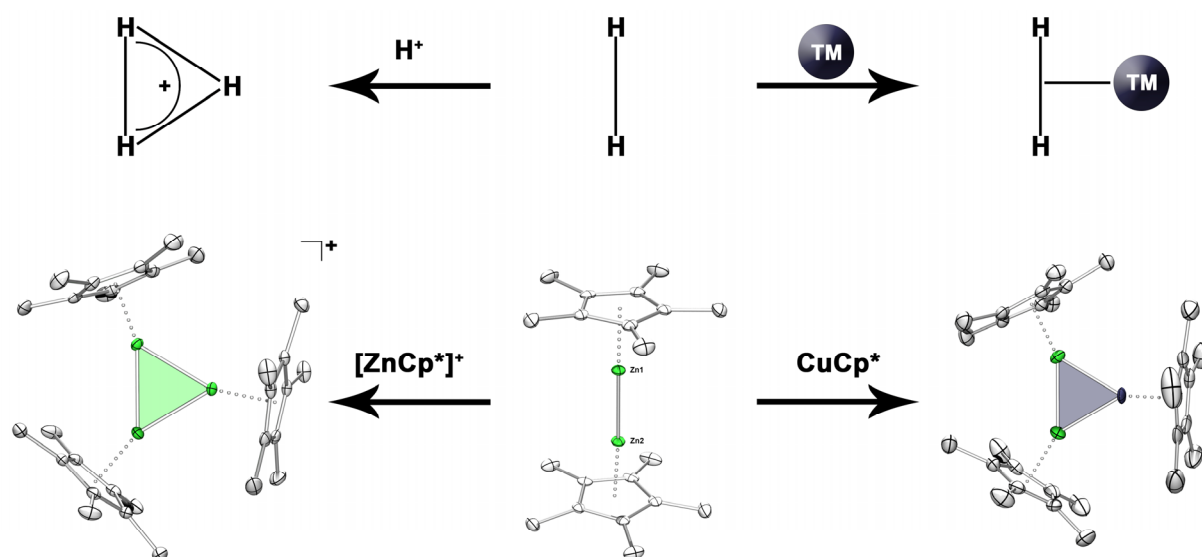


Figure 23. Analogy between H₂ and [Zn₂Cp*₂].

The preparation of [Zn₃Cp*₃]⁺ and [Zn₂CuCp*₃] as minimum units of larger deltahedral clusters emphasize the potential of [Zn₂Cp*₂] to be used for the systematic growth of zinc containing clusters. In fact, the treatment of [Zn₂Cp*₂] with an equimolar amount of [CpCuCN^tBu] leads to the formation of [(ZnCp*)₄(Cu(CN^tBu))₄] and [(ZnCp*)₃(ZnCp)(Cu(CN^tBu))₄] which co-crystallize from the reaction solution.^[121] The formation of [ZnCp*₂] indicates a redox chemical process at which Zn^I is oxidized to Zn^{II} and Cu^I reduced to Cu⁰. In addition, Cp*/Cp ligand exchange takes place. Both [Zn₄Cu₄] clusters are isostructural except for one Cp ligand. Due to similar solubility properties, attempts to separate both species by extraction, recrystallization, sublimation and column chromatography were unsuccessful. The structure of the [Zn₄Cu₄] core features the familiar motifs of [Zn₃] and [Zn₂Cu] triangles, which are interconnected with each other. In particular, the Cu atoms are arranged in the form of a tetrahedron capped by a [Zn₄] tetrahedral shell. As a consequence, the [Zn₄Cu₄] core adopts the shape of a tetrahedral star. This arrangement is also found in the γ -phase of the intermetallic Zn/Cu alloy brass (Figure 24). However, the tetrahedral motifs are inverted with [Zn₄] being inside the [Cu₄] tetrahedron. Nevertheless, the clusters [(ZnCp*)₄(Cu(CN^tBu))₄] and [(ZnCp*)₃(ZnCp)(Cu(CN^tBu))₄] can be regarded as unique examples of molecular cutouts of the common known alloy brass. Quantum chemical calculations present a closed shell structure with significant covalent bonding within the [Zn₄Cu₄] framework. The four available electron pairs occupy four bonding metallic σ -type

hybride orbitals with large 4s character. Apart from that, the stability of the clusters is in compliance with the jellium model as the sum of the cve gives the magic number 8.

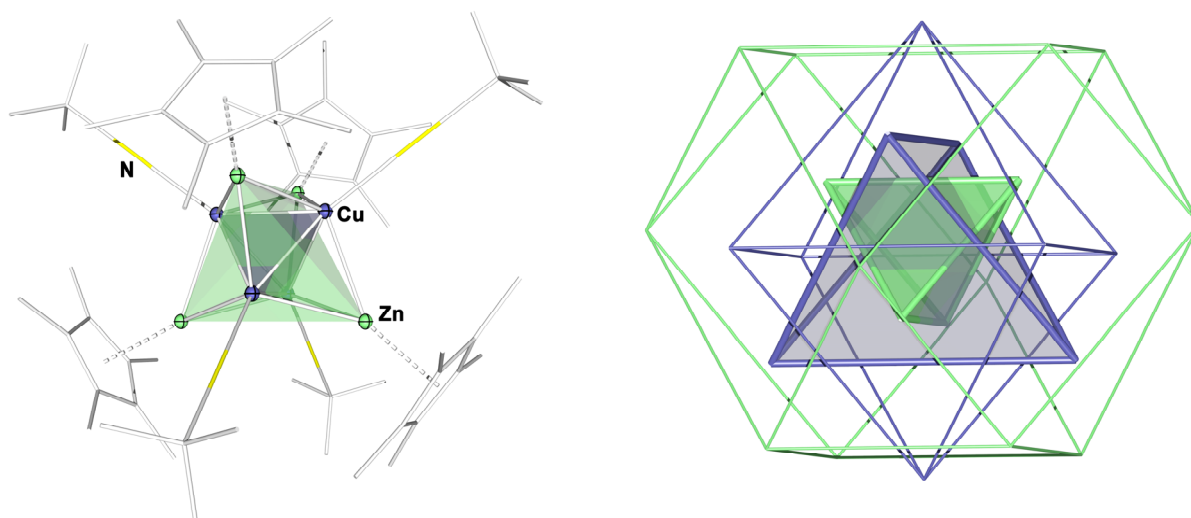


Figure 24. Molecular structure of $[(ZnCp^*)_4(Cu(CN^tBu))_4]$ without hydrogen atoms including tetrahedral polyhedra formed by Cu and Zn (left); cutout of a $[Zn_{16}Cu_{10}]$ cluster from the solid state structure of γ -brass showing the inversed tetrahedral motifs.

2 MOTIVATION

About 80 % of all natural elements are metals or semimetals. These elements are essential for our daily life, for the fabrication of tools, coins, cars, cables, decorations, *etc.* For this, the characteristic properties of metals like the high electrical and thermal conductivity, ductility, reflectivity or the ability to be fusible with other metals to form alloys, are of importance. On a macroscopic scale, the general malleableness as well as the ductility of such materials allow metals to be forged to tools for everyday life, which have been fundamental for the evolution of mankind. However, for the technological progress, it becomes more and more important to elucidate and manipulate M-M interactions on a nanometer scale. For this purpose, metal clusters as a bridge between molecular compounds and the bulk phase are perfect entities to study. The properties of such metal agglomerates are highly dependent on the number of atoms forming the clusters, even the removal or addition of a single atom can result in a drastic change of properties.^[31] Therefore, the preparation and isolation of atom precise clusters for its subsequent chemical and physical analysis is of utmost interest. Naked clusters of such kind can be readily prepared in the gas phase, but it is not possible to isolate and store such species for subsequent chemical reactions. The preparation of bulk quantities of atom precise clusters requires solution phase synthetic methods. As to that, *in situ* formed naked metal clusters have to be stabilized against agglomeration and bulk metal formation by protecting ligands. This so called bottom-up synthesis is rather straight forward for precious metals, for which a vast number of metalloid clusters is known. However, for base metals it is all the more difficult to obtain such species due to their intrinsic instability towards oxidation and the formation of bulk metal. The challenge here is to identify, or if necessary prepare, the suitable starting compounds as metal sources for cluster construction and growth. Schnöckel *et al.* demonstrated, that such endeavor is accomplishable in an impressive way by the preparation of a great spectrum of metalloid aluminum and gallium clusters.^[32] However, for other base metals such as zinc, a preparative way to access metalloid clusters is unknown. Regarding this, Fischer *et al.* succeeded in the systematic synthesis of zinc rich coordination compounds $[M@Zn_a](L)_a$ ($M = d$ block metal, $L = Cp^*, CH_3$; $a = 8-12$).^[58] Nevertheless, the $[Zn_a](L)_a$ cages are not stable without significant bonding interactions to the central metal atom. In 2004 Carmona *et al.* prepared the first compound with a Zn-Zn σ -bond $[Zn_2Cp^*_2]$, paving an extraordinary path to access low valent zinc chemistry.^[69] The systematic investigations of $[Zn_2Cp^*_2]$ towards transition metal compounds allowed the synthesis of Hume-Rothery-type intermetallic clusters,

at which similar reaction behaviour of $[\text{Zn}_2\text{Cp}^*_2]$ and the isolobal H_2 has been identified.^[117-119] Based on this, the focus of this work was the synthesis and evaluation of novel low valent zinc compounds, targeting their subsequent use as building blocks for the bottom-up preparation of novel intermetallic clusters. Meaning, the development of a zinc tool box for the systematic construction of atom precise organometallic clusters. Using $[\text{Zn}_2\text{Cp}^*_2]$ as a fundamental compound, the limits of the possibility to adjust its reactivity for individual purposes was to be explored.

3 SUMMARY

The removal of a Cp* protection group from $[\text{Zn}_2\text{Cp}^*_2]$ via oxidative Zn-Cp* cleavage leads to a highly labile and reactive cationic $[\text{Cp}^*\text{ZnZn}]^+$ species, at which the open coordination site requires stabilization by donor molecules L such as Et₂O or THF to prevent disproportionation. The nature of the donor molecule strongly affects the stability of the cation. As to that $[\text{Cp}^*\text{Zn}_2(\text{Et}_2\text{O})_3]^+$ is much more labile than $[\text{Cp}^*\text{Zn}_2(\text{THF})_3]^+$ (**1**) bearing the stronger THF donor. The coordinated Et₂O molecules in $[\text{Cp}^*\text{Zn}_2(\text{Et}_2\text{O})_3]^+$ can be readily substituted by THF. In addition, when **1** is precipitated from a THF solution with a non-polar solvent such as *n*-hexane, an intermolecular ligand exchange takes place, giving the more symmetric dication $[\text{Zn}_2(\text{THF})_6]^{2+}$ (**2**) as a crystalline material instead of **1**, indicating the increased stability of **2** compared to **1** in the solid state. However, previous attempts to prepare the analogous Et₂O adduct were not successful showing, that $[\text{Zn}_2]^{2+}$ is not sufficiently stabilized by the weaker Et₂O donor. Further studies of these cationic low valent zinc species indicate a great compatibility towards isonitrile ligands, which readily substitute the THF moieties in **2** to give $[\text{Zn}_2(\text{CNPh})_6]^{2+}$ (**3**). These results show, that the reactivity of the semi-protected and fully deprotected $[\text{Zn}_2\text{Cp}^*_2]$ is strongly dependent on the chosen stabilization of the open Zn^I coordination sites by weakly coordinating co-ligands L.

With first insights into the stability and accessibility of cationic low valent zinc species with virtually naked zinc sites to hand, it appeared plausible to make use of the general lability of $[\text{Zn}_2\text{Cp}^*]^+$ in a controlled way. As to that, $[\text{Zn}_2\text{Cp}^*]^+$ was formed *in situ* aiming the controlled disproportionation of the metastable Zn^I species. In the presence of the protecting Cp* ligands and ZnMe₂, the upon disproportionation formed naked Zn⁰ was trapped in the form of the first atom-precise organometallic zinc cluster $\{[\text{Zn}_{10}](\text{Cp}^*)_6\text{Me}\}^+$ (**4**). Due to the lability of **4**, which is only stable at temperatures below -10 °C in the solid state as well as in solution, **4** was treated with weakly coordinating ligands L in order to induce cluster expansion or degradation. At this Et₂O, THF and isonitrile were employed, which have proven to be compatible with low valent zinc species. As a result, the smaller clusters $\{[\text{Zn}_9](\text{Cp}^*)_6\}$ (**5**) and $\{[\text{Zn}_8](\text{Cp}^*)_5(\text{CN}^t\text{Bu})_3\}^+$ (**6**) have been obtained using the hard σ-donors Et₂O or THF and the softer ^tBuNC ligand, respectively. Although the isolated zinc clusters exhibit deltahedral structural motifs, they are electron deficient regarding to the Wade-Mingos rule as skeletal ZnCp* cluster fragments are missing frontier π-type orbitals for cluster bonding.

In possession of this toolbox of low valent zinc species, the potential of these compounds to function as building blocks for intermetallic clusters have been investigated. From previous studies by Fischer *et al.*, it has already been demonstrated that $[\text{Zn}_2\text{Cp}^*_2]$ can be employed in this matter. In a to the literature reported alternative approach to prepare $[\text{Zn}_2\text{CuCp}^*_3]$ (**7**) using $\text{Cu}(\text{OAc})$ instead of *in situ* formed CuCp^* to react with $[\text{Zn}_2\text{Cp}^*_2]$, a novel cluster of the composition $[\text{M}_7\text{Cp}^*_5]$ (**8**) ($\text{M} = \text{Zn}$ or Cu) is obtained as a by-product. However, the Zn/Cu ratio has not been determined to date. The isostructural cation $[\text{Zn}_5\text{Cu}_2\text{Cp}^*_5]^+$ (**9**) has been isolated using $[\text{Cp}^*\text{Zn}_2(\text{Et}_2\text{O})_3]^+$ as a molecular building block. Compound **8** and **9** give a pair of isostructural nanobrass clusters, which very well relate to $[\text{Zn}_3\text{Cp}^*_3]^+$ and **7** to yield a series of $[\text{Zn}_a\text{Cu}_b\text{Cp}^*_c]^{n+}$ species with different Zn:Cu:Cp* ratios.

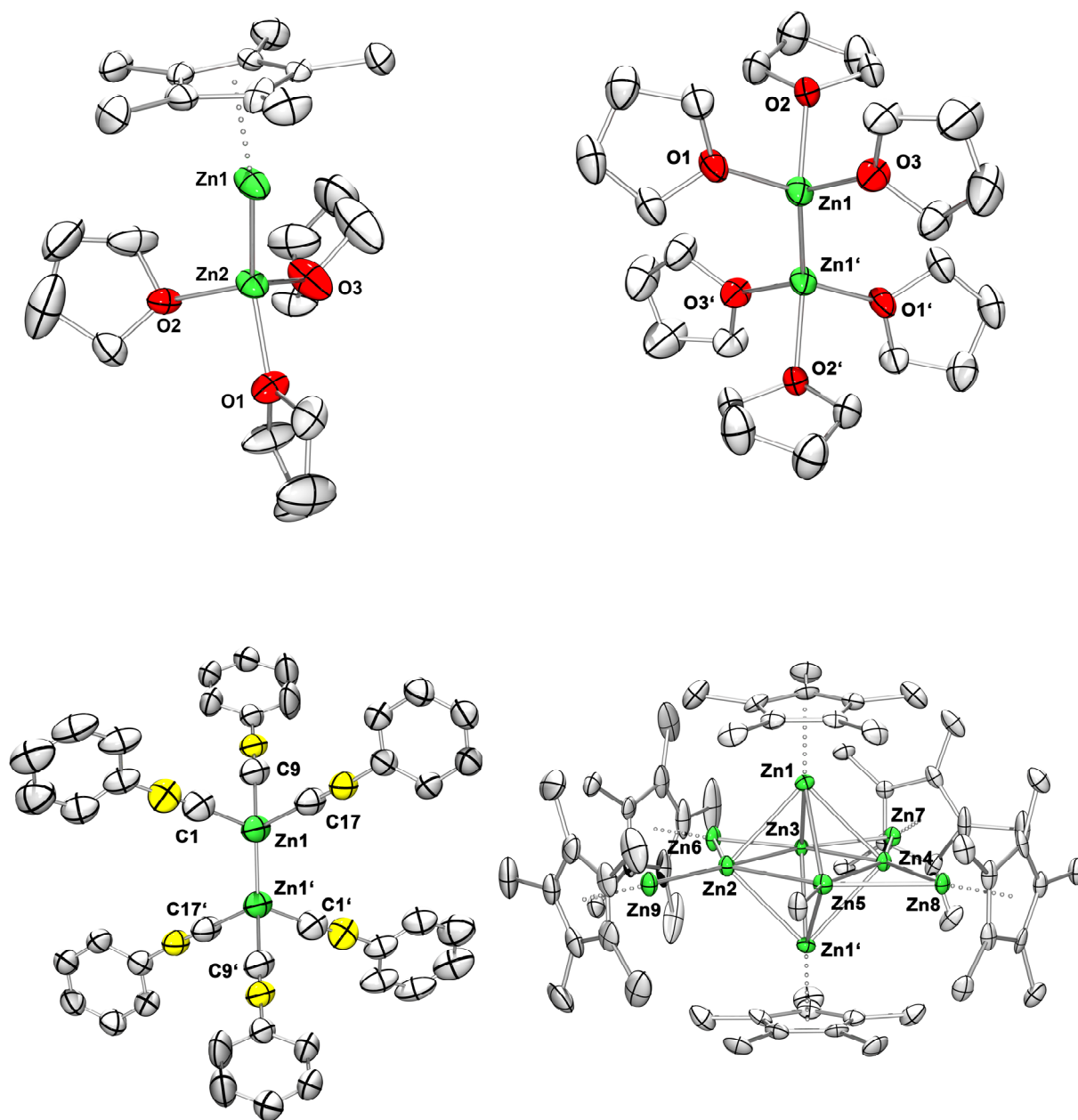


Figure 25. Overview of the synthesized compounds **1-4** or of their cations: **1** (top, left), **2** (top, right), **3** (bottom, left) and **4** (bottom right). Hydrogen atoms are not shown.

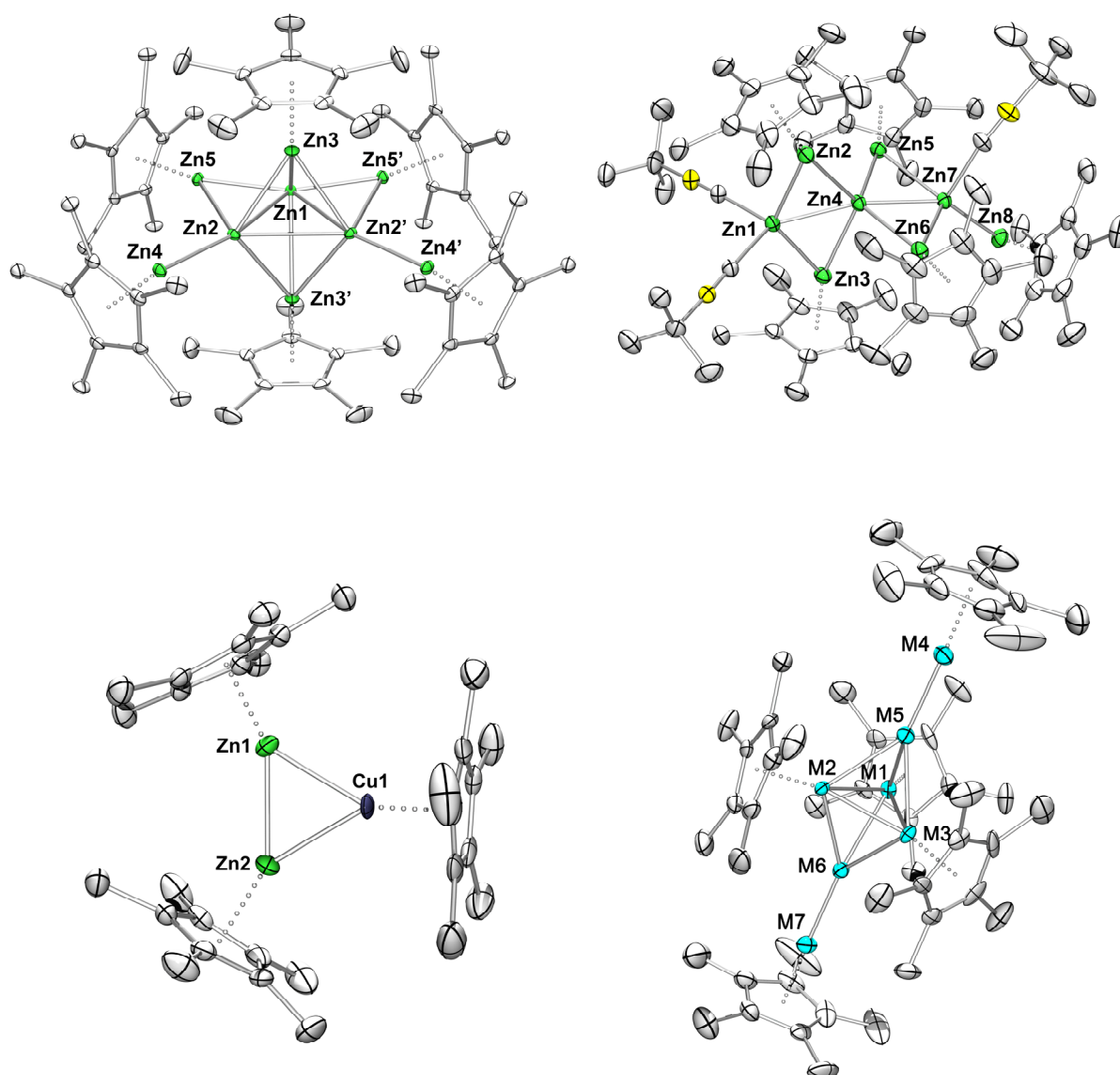


Figure 26. Overview of the synthesized compounds **5-8** or of their cations: **5** (top, left), **6** (top, right), **7** (bottom, left) and **8** (bottom right). Hydrogen atoms are not shown.

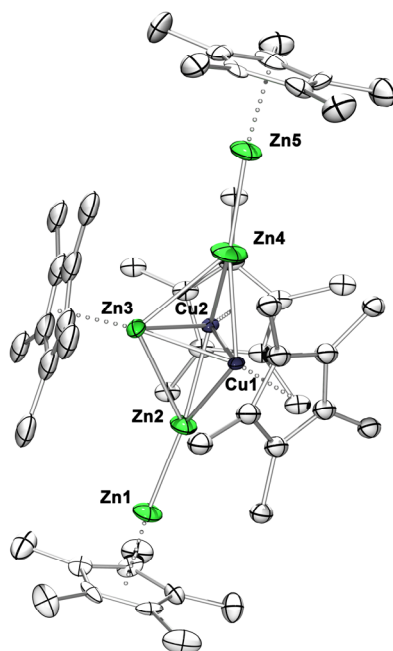


Figure 27. Overview of the synthesized cation **9**. Hydrogen atoms are not shown.

Table 1. List of the synthesized compounds.

Compound	Classification	Chapter
$[\text{Cp}^*\text{Zn}_2(\text{THF})_3][\text{BAR}_4^{\text{F}}]$ (1 $[\text{BAR}_4^{\text{F}}]$)	Semi deprotected $[\text{Zn}_2\text{Cp}^*_2]$	4.1
$[\text{Zn}_2(\text{THF})_6][\text{BAR}_4^{\text{F}}]_2$ (2 $[\text{BAR}_4^{\text{F}}]_2$)	Zn Analogue of the Calomel Dication	4.1
$[\text{Zn}_2(\text{CNPh})_6][\text{BAR}_4^{\text{F}}]_2$ (3 $[\text{BAR}_4^{\text{F}}]_2$)	$[\text{Zn}_2]^{2+}$ Isonitrile Adduct	4.1
$\{[\text{Zn}_{10}](\text{Cp}^*)_6\text{Me}\}[\text{BAR}_4^{\text{F}}]$ (4 $[\text{BAR}_4^{\text{F}}]$)	$[\text{Zn}_{10}]$ Atom-precise Zinc Cluster	4.2
$[\text{Zn}_9](\text{Cp}^*)_6$ (5)	$[\text{Zn}_9]$ Atom-precise Zinc Cluster	4.2
$\{[\text{Zn}_8](\text{Cp}^*)_5(\text{CN}^t\text{Bu})_3\}[\text{BAR}_4^{\text{F}}]$ (6 $[\text{BAR}_4^{\text{F}}]$)	$[\text{Zn}_8]$ Atom-precise Zinc Cluster	4.2
$[\text{Zn}_2\text{CuCp}^*_3]$ (7)	2:1, Zn/Cu Nanobrass	4.3
$[\text{M}_7\text{Cp}^*_5]$ (8)	4:3, Zn/Cu Nanobrass	4.3
$[\text{Zn}_5\text{Cu}_2\text{Cp}^*_5][\text{BAR}_4^{\text{F}}]$ (9 $[\text{BAR}_4^{\text{F}}]$)	5:2 Zn/Cu Nanobrass	4.3

4 RESULTS AND DISCUSSION

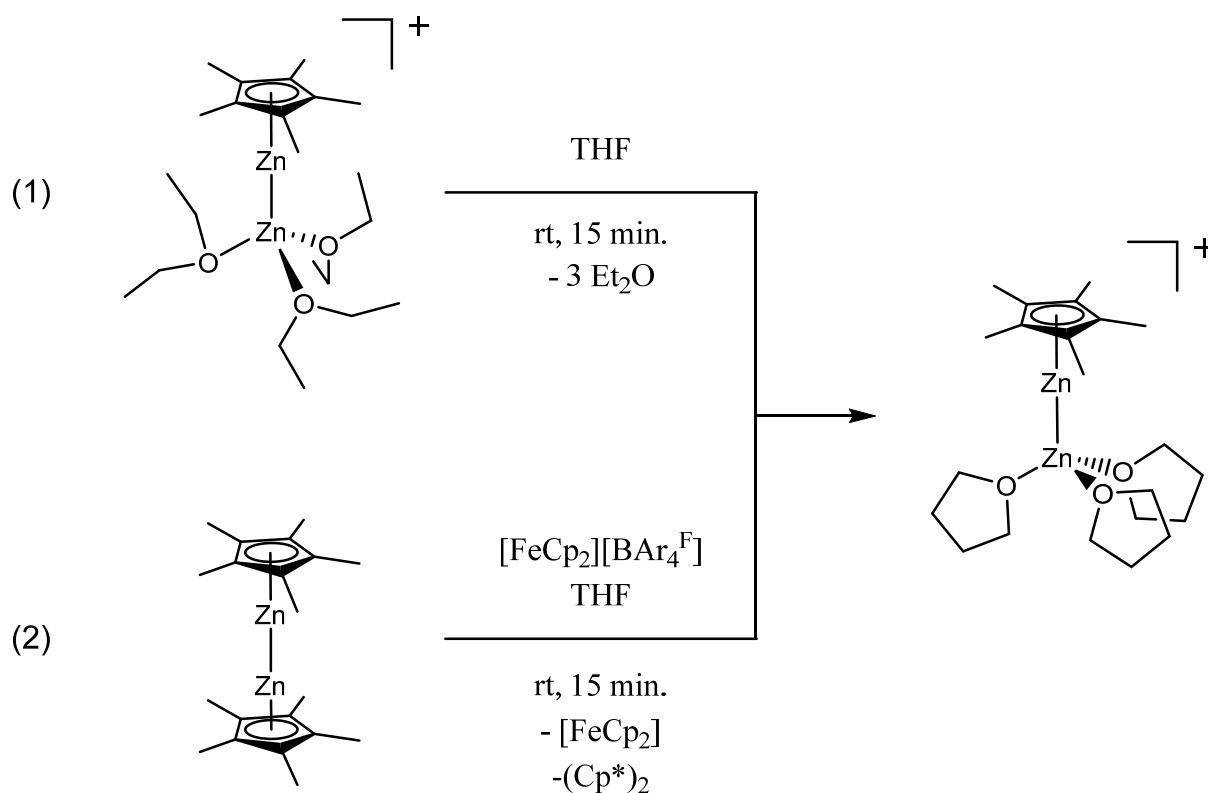
4.1 Effects of Different Ligands on $[\text{Cp}^*\text{Zn}_2(\text{THF})_3][\text{BAR}_4^{\text{F}}]$ and $[\text{Zn}_2(\text{THF})_6][\text{BAR}_4^{\text{F}}]_2$

As mentioned in the introduction several cationic $\text{Zn}^{\text{I}}\text{-Zn}^{\text{I}}$ bonded compounds have been prepared by Schulz *et al.* and Fischer *et al.*^[97, 103, 105] Herein, starting from $[\text{Zn}_2\text{Cp}^*_2]$ Zn-Cp* bonds are either protolytically or oxidatively cleaved. The resulting open coordination sites at Zn are subsequently occupied by present donor molecules like dmap, Et₂O or THF. The highly reactive cationic compounds can be stabilized by weakly coordinating anions. Regarding this it was shown that the doubly deprotected $[\text{Zn}^{\text{I}}\text{-Zn}^{\text{I}}]^{2+}$ can only be obtained as a THF or dmap adduct but not with the weaker donor Et₂O. In order to further investigate the influence of the donor molecules on the open coordination sites at Zn^{I} , $[\text{Cp}^*\text{Zn}_2(\text{Et}_2\text{O})_3][\text{BAR}_4^{\text{F}}]$ and $[\text{Zn}_2(\text{THF})_6][\text{BAR}_4^{\text{F}}]_2$ were treated with THF and PhNC, respectively. Indeed $[\text{Cp}^*\text{Zn}_2(\text{THF})_3]^+$ (**1**) was obtained as a substitution product, which can be further transformed to $[\text{Zn}_2(\text{THF})_6]^{2+}$ (**2**) and $[\text{Zn}_2\text{Cp}^*_2]$ by simple intermolecular ligand exchange reactions of **1**. In addition, the dication $[\text{Zn}_2(\text{CNPh})_6]^{2+}$ (**3**) was isolated by substitution of the THF molecules in **2** with PhNC.

4.1.1 Synthesis of $[\text{Cp}^*\text{Zn}_2(\text{THF})_3][\text{BAR}_4^{\text{F}}]$ (**1** $[\text{BAR}_4^{\text{F}}]$)

First investigations revealed the substitution lability of the Et₂O donors in $[\text{Cp}^*\text{Zn}_2(\text{Et}_2\text{O})_3][\text{BAR}_4^{\text{F}}]$ as the ¹H NMR spectrum of this compound in THF-d₈ at room temperature shows non-coordinated Et₂O in solution.^[103] Treatment of $[\text{Cp}^*\text{Zn}_2(\text{Et}_2\text{O})_3][\text{BAR}_4^{\text{F}}]$ with THF at room temperature leads to the substitution of the Et₂O ligands by the stronger donor THF and the formation of $[\text{Cp}^*\text{Zn}_2(\text{THF})_3][\text{BAR}_4^{\text{F}}]$ (**1** $[\text{BAR}_4^{\text{F}}]$) as a colourless crystalline powder in 80 % yield after removal of the excess THF and Et₂O in vacuum (Scheme 10, reaction (1)). Analogous to the reaction of $[\text{Zn}_2\text{Cp}^*_2]$ with one equivalent of $[\text{FeCp}_2][\text{BAR}_4^{\text{F}}]$ at room temperature in Et₂O giving $[\text{Cp}^*\text{Zn}_2(\text{Et}_2\text{O})_3][\text{BAR}_4^{\text{F}}]$,^[103] the same reaction can be conducted in THF instead, giving **1** $[\text{BAR}_4^{\text{F}}]$ as a crystalline powder in 45 % yield after the solvent is removed from the reaction mixture and the crude product is purified by washing with *n*-hexane (Scheme 10, reaction (2)). One Zn-Cp* ligand is oxidatively cleaved and ferrocene and decamethylfulvalene (Cp*₂) can be observed as stoichiometric by-products by *in situ* solution

^1H NMR spectroscopy. In contrast to $[\text{Cp}^*\text{Zn}_2(\text{Et}_2\text{O})_3][\text{BAR}_4^{\text{F}}]$ which readily decomposes as a crystalline powder at room temperature as well as in solution, $\mathbf{1}[\text{BAR}_4^{\text{F}}]$ is stable in the solid state at room temperature for several days under an inert gas atmosphere. The compound is soluble in polar solvents like CH_2Cl_2 , fluoro-benzene or THF.



Scheme 10. Two different pathways to synthesise $[\text{Cp}^*\text{Zn}_2(\text{THF})_3][\text{BAR}_4^{\text{F}}]$ ($\mathbf{1}[\text{BAR}_4^{\text{F}}]$).

4.1.2 Spectroscopic and Structural Features of $[\text{Cp}^*\text{Zn}_2(\text{THF})_3][\text{BAR}_4^{\text{F}}]$ ($\mathbf{1}[\text{BAR}_4^{\text{F}}]$)

Compound $\mathbf{1}[\text{BAR}_4^{\text{F}}]$ was characterized by ^1H , ^{13}C and ^{11}B NMR spectroscopy as well as IR spectroscopy. The molecular composition was confirmed by EA (C, H) and AAS (Zn, B, F) analysis. The ^1H NMR spectrum of $\mathbf{1}[\text{BAR}_4^{\text{F}}]$ in CD_2Cl_2 at room temperature exhibits the set of signals for the $[\text{BAR}_4^{\text{F}}]^-$ anion ($\delta = 7.72$ (s, 8H) and $\delta = 7.57$ (s, 4H) ppm) and the coordinated THF molecules ($\delta = 2.00$ (q, 12H) and $\delta = 3.85$ (t, 12H) ppm) as well as a singlet for the Cp^* protons at $\delta = 2.07$ ppm (15H). The ^{13}C NMR spectrum shows the expected set of signals for the $[\text{BAR}_4^{\text{F}}]^-$ anion with two singlets at $\delta = 117.86$ ((CCF_3) CH (CCF_3)) and 135.23 ppm

(BCCH(CCF₃)) and three quartets at $\delta = 125.08$ (CF₃), 129.27 (CCF₃) and 162.21 ppm (BC). In addition, there are two singlets according to the coordinated THF molecules ($\delta = 25.62$ and 70.95 ppm) and the Cp* group each ($\delta = 10.33$ (C₅Me₅) and 109.24 (C₅Me₅) ppm). The ¹¹B NMR spectrum exhibits the resonance expected for the [BAr₄^F]⁻ anion at $\delta = -6.56$ ppm (s). The FTIR spectrum of **1**[BAr₄^F] reveals typical bands for the Cp* ring at 2953, 2876 and 2835 cm⁻¹ as well as a signal due to the C–F vibration at 1266 cm⁻¹.

Colourless cuboid shaped crystals of **1**[BAr₄^F] appropriate for single crystal X-ray diffraction were obtained from a saturated THF solution of **1**[BAr₄^F] at -30 °C. Compound **1**[BAr₄^F] crystallizes in the orthorhombic space group *Pbca* containing eight ion pairs in the unit cell (Figure 28). The coordination geometry of the Cp*Zn₂O₃ unit resembles an “elongated” piano stool, at which the “seat” is slightly tilted towards the Zn-Zn axes. With regard to reaction (1) all Et₂O molecules are replaced by stronger THF donor molecules. With respect to reaction (2) one 6 π electron donor Cp* ligand is substituted by three THF solvent molecules. The equivalent reaction with the weaker donor Et₂O as a solvent was already reported by Fischer *et al.* in 2013.^[103] Compared to the parent compound [Zn₂Cp*₂] (2.305(3) Å) the Zn-Zn bond length of **1** (2.317(7)) Å is slightly elongated but almost identical to the distance in [(Ph₂PNPh)₂CH]₂Zn₂] (2.315(6) Å) (Figure 29, right).^[69, 99] The Zn-Cp*_{centr.} distance of 2.000 Å is well comparable with the respective distance in [Zn₂Cp*₂] (2.040 Å) or [Cp*Ru(ZnCp*)₃(ZnX)₂] (X = Me or Cl) (2.012, 2.000 Å) (Figure 29, left).^[69, 122] The Zn-O₁, Zn-O₂, Zn-O₃ distances are 2.036(3), 2.054(3) and 2.081(4) Å, respectively and in the range of those in the Zn-THF complex [Zn(THF)₆][BAr₄^F]₂ (2.060, 2.102, 2.058 Å).^[105]

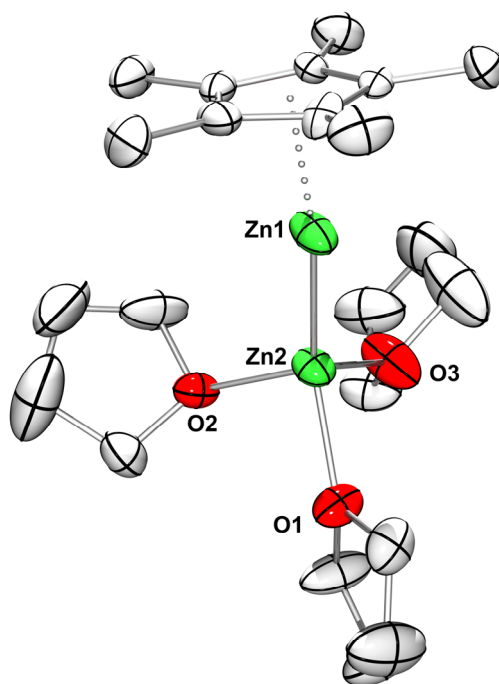


Figure 28. Molecular structure of the cation $[\text{Cp}^*\text{Zn}_2(\text{THF})_3]^+$ in the crystal of $1[\text{BAR}_4\text{F}]$. Displacement ellipsoids are shown at a 50 % probability level. The hydrogen atoms and the disorder of the Cp^* ring are omitted for clarity. Selected interatomic distances (\AA) and angles ($^\circ$): $\text{Zn1-Zn2} = 2.317(7)$, $\text{Zn1-Cp}^*_{\text{centr.}} = 2.000$, $\text{Zn2-O1} = 2.036(3)$, $\text{Zn2-O2} = 2.094(3)$, $\text{Zn2-O3} = 2.081(4)$; $\text{Cp}^*_{\text{centr.}}\text{-Zn1-Zn2} = 157.71$, $\text{Zn1-Zn2-O1} = 134.92(9)$, $\text{Zn1-Zn2-O2} = 116.58(9)$, $\text{Zn1-Zn2-O3} = 117.04(11)$.

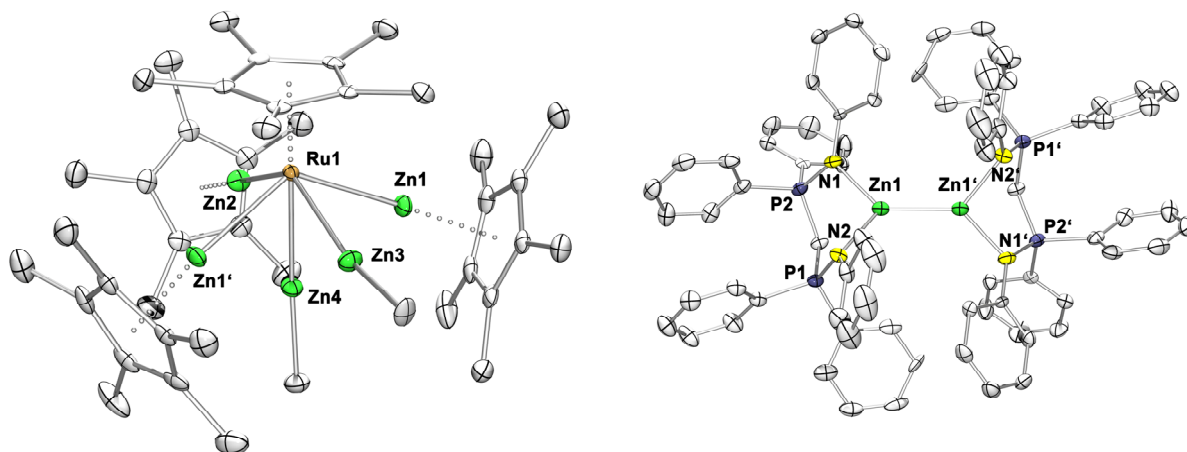


Figure 29. Molecular structures without hydrogen atoms of $[\text{Cp}^*\text{Ru}(\text{ZnCp}^*)_3(\text{ZnMe})_2]$ (left) and $[(\text{Ph}_2\text{P}(\text{NDipp})_2)_2\text{Zn}_2]$ (right).

The $\text{Zn2-Zn1-Cp}^*_{\text{centr.}}$ angle of 157.71° strongly deviates from linearity, similar to $[\text{Zn}_2\text{Cp}^*_2(\text{dmpa})_2] \cdot \text{PhMe}$ (159.6°), which was reported by *Schulz et al.* in 2009.^[88] Regarding

to the latter compound, the deviation is explained as an effect of the coordination of the dmpa molecules to $[\text{Zn}_2\text{Cp}^*_2]$. But considering the packing of the molecules in the crystals in both cases the deviation is rather caused by packing effects. In the crystals of $[\text{Zn}_2\text{Cp}^*_2(\text{dmpa})_2] \cdot \text{PhMe}$ the steric demand of a toluene molecule in the proximity of the respective Cp^* ligand leads to a strong deflection of the ring to the other side. In the crystals of $\mathbf{1}[\text{BAR}_4^{\text{F}}]^-$ the ion pairs are packed in such a way that the space on one side along the Zn-Zn axes of a $[\text{Cp}^*\text{Zn}_2(\text{THF})_3]^+$ cation is occupied by three CF_3 groups of two different $[\text{BAR}_4^{\text{F}}]^-$ anions (Figure 30.). The arising steric repulsion between the Cp^* ligand and the CF_3 groups causes the deviation from linearity. In the same way one of the coordinated THF molecules is influenced by the steric demand of the CF_3 groups ($\text{Zn1-Zn2-O1} = 134.92(9)^\circ$). The other Zn-Zn-O angles are significantly smaller ($116.58(9)$ and $117.04(1)^\circ$).

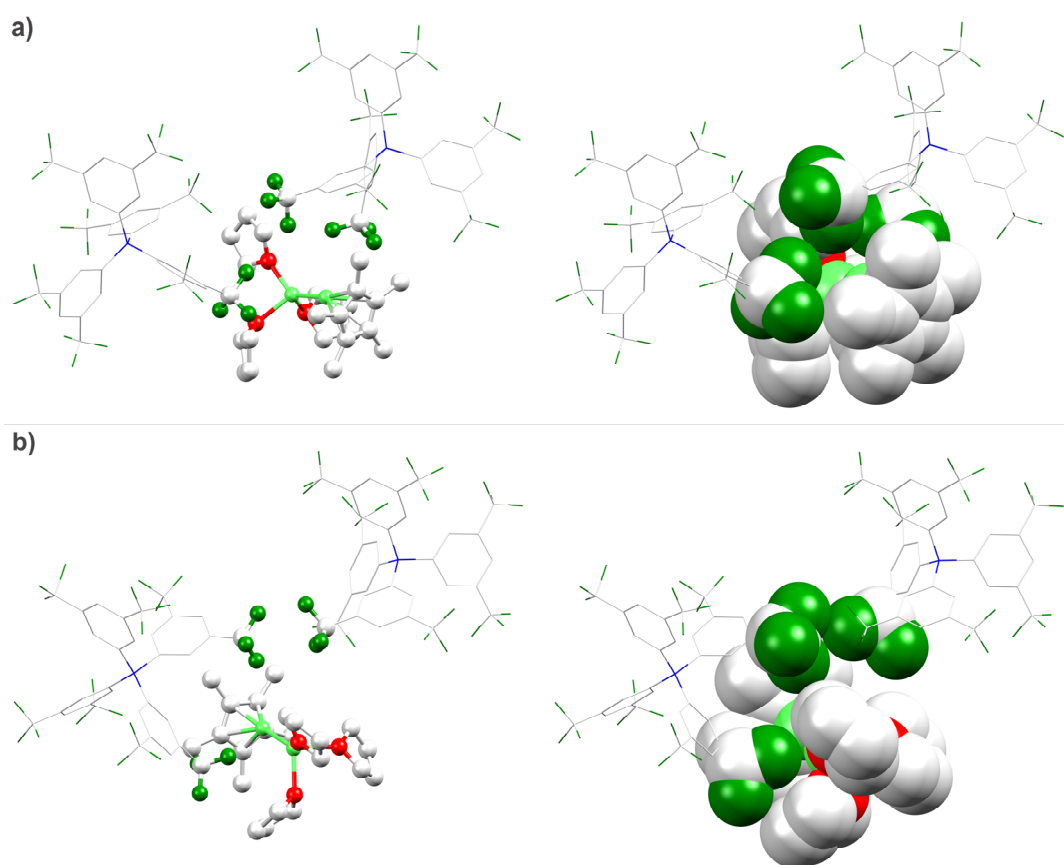
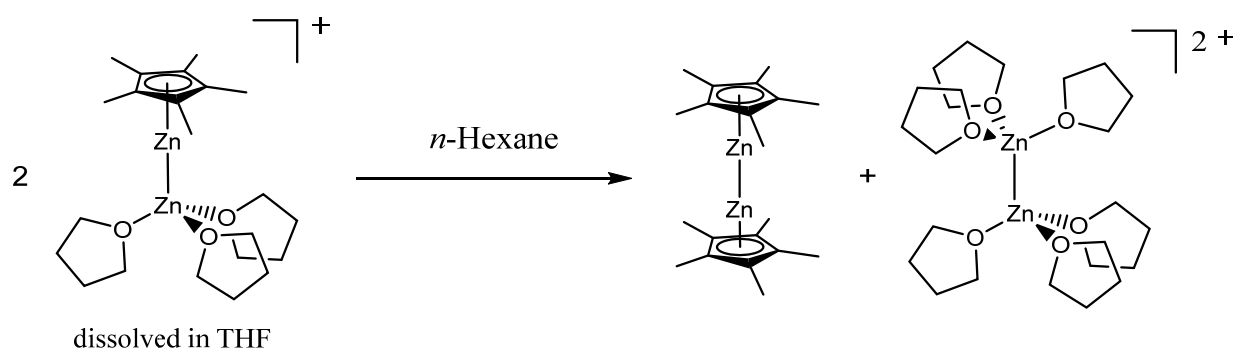


Figure 30. Steric influence of two adjacent $[\text{BAR}_4^{\text{F}}]^-$ anions on the $\text{Cp}^*\text{-Zn1-Zn2}$ and Zn1-Zn2-O1 angles of the molecular structure of $[\text{Cp}^*\text{Zn}_2(\text{THF})_3]^+$ due to the packing of the ion pairs in the crystals of **1**. Light green: zinc, red: oxygen, grey: carbon, dark blue: boron, dark green: fluorine. Sterically interacting components are shown in ball and stick and space fill depictions from two different views a) and b). The remaining parts of the $[\text{BAR}_4^{\text{F}}]^-$ anions are shown as wireframes. Hydrogen atoms are omitted for clarity.

4.1.3 Synthesis of $[\text{Zn}_2(\text{THF})_6][\text{BAr}_4^{\text{F}}]_2$ ($2[\text{BAr}_4^{\text{F}}]_2$)

The treatment of a solution of $1[\text{BAr}_4^{\text{F}}]$ in THF with *n*-hexane at room temperature does not lead to the precipitation of the unaltered semi deprotected **1** cation but to the formation of $[\text{Zn}_2(\text{THF})_6][\text{BAr}_4^{\text{F}}]_2$ ($2[\text{BAr}_4^{\text{F}}]_2$) as a crystalline powder in 87 % yield. Instead a by-product $[\text{Zn}_2\text{Cp}^*]_2$ is obtained, which was confirmed by ^1H NMR spectroscopy of the concentrated filtrate.



Scheme 11. Synthesis of $[\text{Zn}_2(\text{THF})_6][\text{BAr}_4^{\text{F}}]_2$ ($2[\text{BAr}_4^{\text{F}}]_2$) *via* precipitation from a THF solution of $[\text{Cp}^*\text{Zn}_2(\text{THF})_3][\text{BAr}_4^{\text{F}}]$ ($1[\text{BAr}_4^{\text{F}}]$).

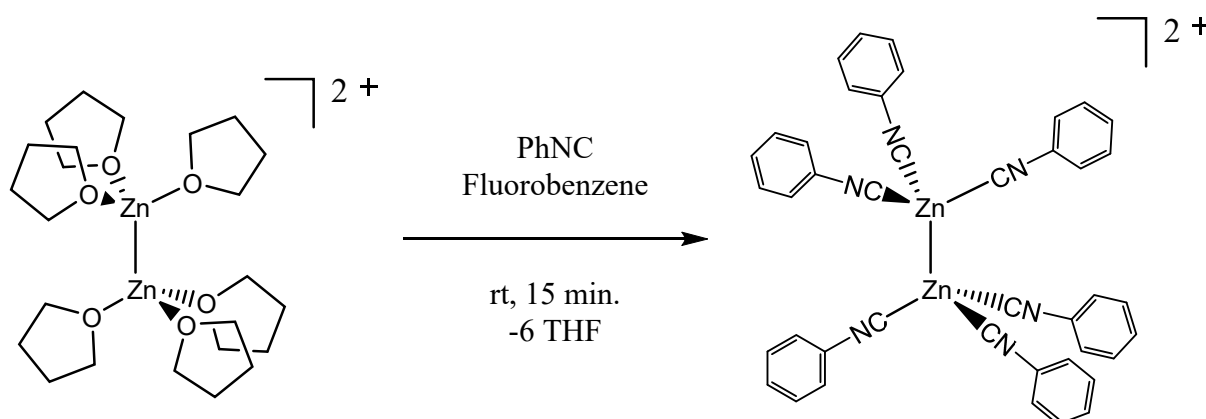
Starting from $1[\text{BAr}_4^{\text{F}}]$ the formation of two products $[\text{Zn}_2\text{Cp}^*]_2$ and $[\text{Zn}_2(\text{THF})_6][\text{BAr}_4^{\text{F}}]_2$ ($2[\text{BAr}_4^{\text{F}}]_2$) is entropically favoured. The gain in lattice energy due to the packing of the molecules in the solid state is greater for the symmetric $[\text{Zn}_2(\text{THF})_6]^{2+}$ than for the asymmetric compound **1**.

The NMR and mass spectroscopic data as well as the determined molecular structure are in accordance to the reported data by Fischer *et al.*^[105]

4.1.4 Synthesis of $[\text{Zn}_2(\text{CNPh})_6][\text{BAr}_4^{\text{F}}]_2$ ($3[\text{BAr}_4^{\text{F}}]_2$)¹

As a series of *in situ* ^1H NMR spectroscopic experiments have been conducted with $2[\text{BAr}_4^{\text{F}}]_2$ by Fischer *et al.* showing that $\text{Zn}^{\text{I}}\text{-Zn}^{\text{I}}$ bonded compounds of the type $[\text{Zn}_2\text{L}_2]$ like $[\text{Zn}_2\text{Cp}^*_2]$ or $[\text{Zn}_2(\text{DDP})_2]$ can be obtained, when reacted with the respective potassium salt. On the other hand the treatment of $2[\text{BAr}_4^{\text{F}}]_2$ with the stronger, but softer σ -donor PMe_3 leads to a clean disproportionation of the Zn^{I} -species forming metallic zinc and the Zn^{II} -complex $[\text{Zn}(\text{PMe}_3)_4][\text{BAr}_4^{\text{F}}]_2$. Attempts to substitute the THF molecules by the strong σ -donor and strong π -acceptor CO ligand failed leaving the starting material unaltered.

In the following $2[\text{BAr}_4^{\text{F}}]_2$ is reacted with the compared to CO stronger σ -donor but weaker π -acceptor PhNC. The reaction of $2[\text{BAr}_4^{\text{F}}]_2$ with an excess of PhNC in fluorobenzene at room temperature gives the substitution product $[\text{Zn}_2(\text{CNPh})_6][\text{BAr}_4^{\text{F}}]_2$ ($3[\text{BAr}_4^{\text{F}}]_2$) as a crystalline orange-red powder in 65 % yield (Scheme 12).



Scheme 12. Synthesis of $[\text{Zn}_2(\text{CNPh})_6][\text{BAr}_4^{\text{F}}]_2$ ($3[\text{BAr}_4^{\text{F}}]_2$).

The homoleptic compound $3[\text{BAr}_4^{\text{F}}]_2$ is stable as a crystalline powder at room temperature under an inert gas atmosphere and poorly soluble in polar solvents like CH_2Cl_2 or fluorobenzene.

¹ H. Banh, C. Gemel, R. W. Seidel and R. A. Fischer, *Chem. Commun.* **2015**, 51, 2170-2172.

4.1.5 Spectroscopic and structural features of $[\text{Cp}^*\text{Zn}_2(\text{CNPh})_6][\text{BAr}_4^{\text{F}}]_2$ ($\mathbf{3}[\text{BAr}_4^{\text{F}}]_2$)

Compound $\mathbf{3}[\text{BAr}_4^{\text{F}}]_2$ was characterised by NMR and IR spectroscopy, single crystal X-ray diffraction as well as elemental analysis and atom absorption spectroscopy. The molecular composition was confirmed by EA (C, H, N) and AAS (Zn). The ^1H NMR spectrum of $\mathbf{3}[\text{BAr}_4^{\text{F}}]_2$ in CD_2Cl_2 exhibits the resonances corresponding to the six coordinated PhNC molecules ($\delta = 7.38 - 7.65$ (m, 30H) ppm) as well as two singlets in a 2:1 integrated ratio for the $[\text{BAr}_4^{\text{F}}]^-$ anion ($\delta = 7.71$ (8H) and 7.52 (4H) ppm). The ^{13}C NMR spectrum shows singlets for the PhNC moieties at $\delta = 127.63$, 130.03 and 130.03 ppm. Due to the poor solubility of $\mathbf{3}[\text{BAr}_4^{\text{F}}]$ in CD_2Cl_2 the additional expected two signals were not detected. The ^{19}F and ^{11}B NMR spectra each exhibit the expected singlet for the $[\text{BAr}_4^{\text{F}}]^-$ anion. The IR spectrum shows an absorption band at 1263 cm^{-1} for the C–F vibration and a band at 2181 cm^{-1} characteristic for the $\tilde{\nu}(\text{CN})$ vibration.

Colourless needle shaped crystals of $\mathbf{3}[\text{BAr}_4^{\text{F}}]_2 \cdot 4\text{ CH}_2\text{Cl}_2$ suitable for single crystal X-ray diffraction were obtained from a concentrated solution of $\mathbf{3}[\text{BAr}_4^{\text{F}}]_2$ in CH_2Cl_2 at $-30\text{ }^\circ\text{C}$. $\mathbf{3}[\text{BAr}_4^{\text{F}}]_2 \cdot 4\text{ CH}_2\text{Cl}_2$ crystallizes in the monoclinic space group $P21/c$ with two formula units per unit cell (Figure 31). Note that the structural analysis of $\mathbf{3}$ is of rather limited precision due to the poor quality of the obtained crystals ($wR2 \sim 31\%$ of the refined data). The cation occupies a centre of symmetry. Each Zn atom bears three isonitrile ligands, resulting in a tetrahedral coordination environment like in $[\text{Zn}_2(\text{THF})_6]^{2+}$ (Figure 31).^[105] Similarly, the cation shows a staggered (D_{3d} -symmetric) conformation around the Zn–Zn axis. The Zn–Zn distance of $2.366(14)\text{ \AA}$ is comparable to that in $[\text{Zn}_2(\text{THF})_6]^{2+}$ ($2.363(8)\text{ \AA}$).^[105]

Note, that similar results have been obtained using $t\text{BuNC}$ instead of PhNC. The compound $[\text{Zn}_2(\text{CN}^t\text{Bu})_6][\text{BAr}_4^{\text{F}}]_2$ has been isolated as a crystalline powder. NMR and atom absorption spectroscopic as well as elemental analysis confirmed the molecular composition. But the quality of the obtained single crystals was very poor. As a consequence, no structural analysis was possible.

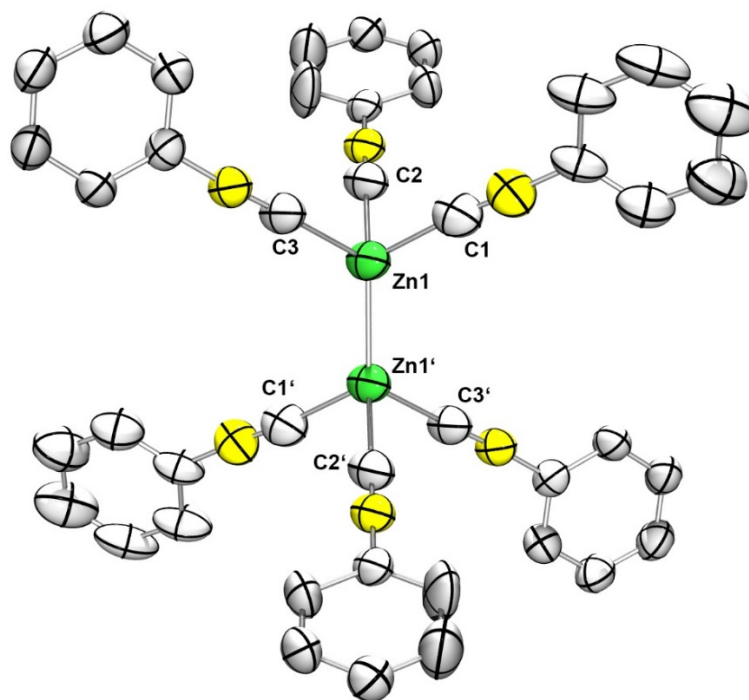
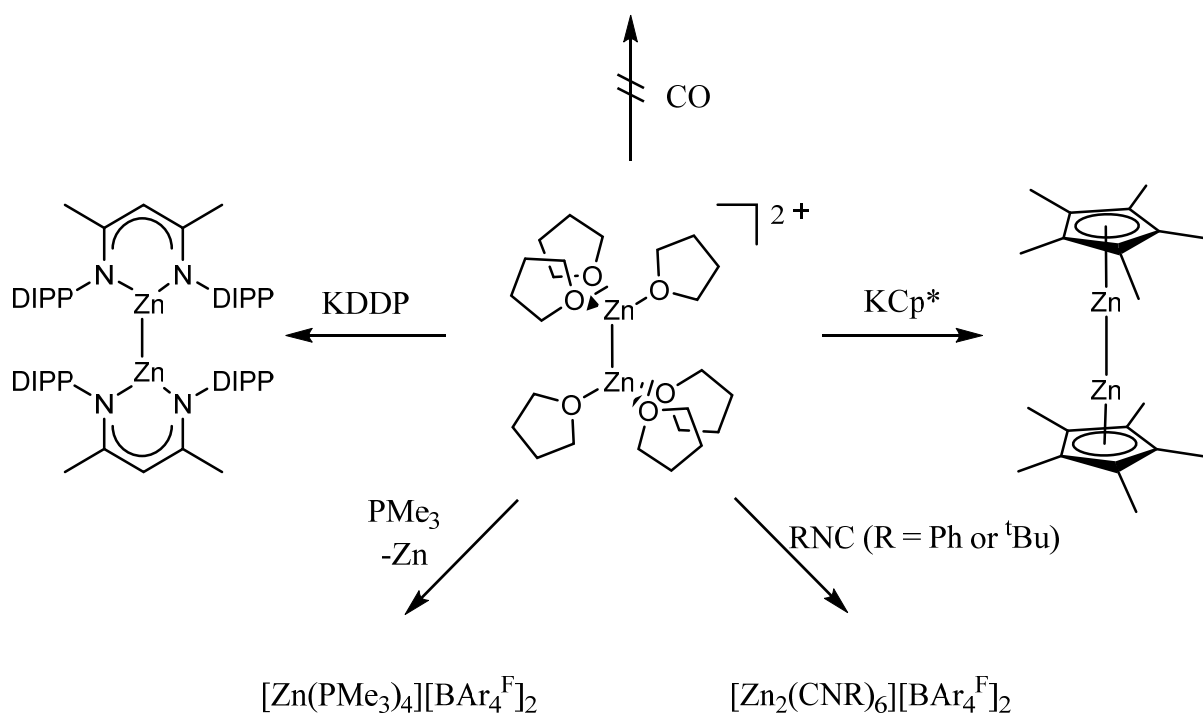


Figure 31. Molecular structure of the dication $[\text{Zn}_2(\text{CNPh})_6]^{2+}$ in the crystals of $2[\text{BAR}_4^{\text{F}}]_2 \cdot 4 \text{CH}_2\text{Cl}_2$ as determined by single crystal X-ray diffraction. Displacement ellipsoids are shown at the 50 % probability level. Hydrogen atoms and the disorder of the molecule are not shown for clarity. The disorder is confined to the anion, solvent molecules and one phenyl group of the cation. Symmetry-related atoms are primed.

4.1.6 Summary

These studies give insight into the general feasibility to stabilize quasi naked Zn(I) centres by employing different donor–acceptor species. At this, starting from $[\text{Zn}_2\text{Cp}^*]_2$ the solvent controlled oxidative cleavage of a Zn–Cp* bond is a very efficient pathway to access cationic di-zinc species of the oxidation state Zn(I). From substitution studies a general affinity series of different ligands L towards Zn(I) centres without cleavage of the intact $\text{Zn}^{\text{I}}\text{–Zn}^{\text{I}}$ bond can be concluded, which is isonitrile > THF > Et₂O. Additionally the choice of L exhibit a great influence on the stability of the $\text{Zn}^{\text{I}}\text{–Zn}^{\text{I}}$ species, at which the semi-protected $[\text{Cp}^*\text{Zn}_2]^+$ is disproportionation labile at room temperature as a Et₂O adduct but stable as a THF adduct (**1**). The compounds $[\text{Zn}_2(\text{dmap})_6][\text{Al}\{\text{Al}\{\text{OC}(\text{CF}_3)\}_4\}_2]$ and $(\mathbf{2}[\text{BAR}_4^{\text{F}}]_2)$ show that even the fully deprotected $[\text{Zn}_2]^{2+}$ dication is stable in the form of the respective homoleptic solvent adduct species. These studies complement the investigations of Cp* being a reactive protection group which can be efficiently cleaved in a protolytic or oxidative way. From this perspective it can

be expected that novel Zn^I - Zn^I and intermetallic zinc species can be prepared by using $1[BAr_4^F]$ and $2[BAr_4^F]_2$ as sources for $[Cp^*Zn_2]^+$ and $[Zn_2]^{2+}$. The presented studies in chapter 5.1 are partially included in the publication “A solvated zinc analogue of the calomel dication” (H. Banh, C. Gemel, R. W. Seidel and R. A. Fischer, *Chem. Commun.* **2015**, 51, 2170-2172). Herein the direct synthesis of $[Zn_2(THF)_6]^{2+}$ by oxidative cleavage of both Zn-Cp* bonds in $[Zn_2Cp^*_2]$ is reported. Furthermore the reactivity of $[Zn_2(THF)_6]^{2+}$ towards different donor-acceptor ligands were explored as summarized in Scheme 13.



Scheme 13. Reactivity of $[Zn_2(THF)_6][BAr_4^F]_2$ ($2[BAr_4^F]_2$).^[105]

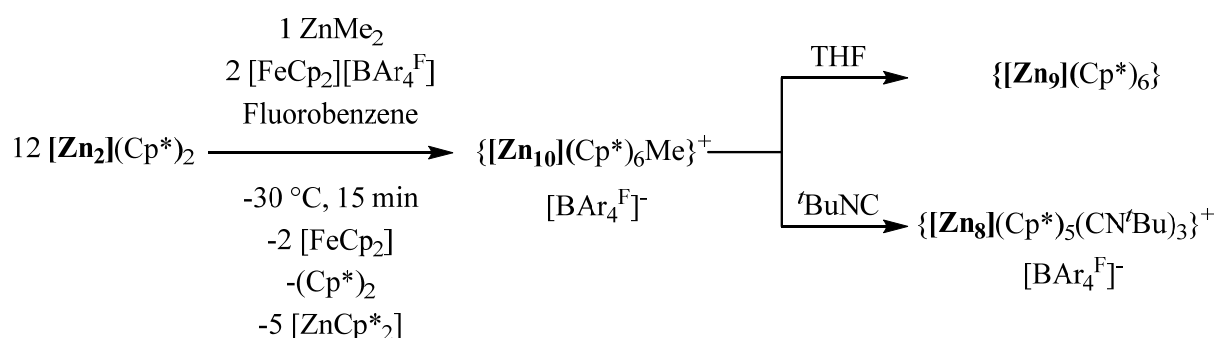
4.2 Atom Precise Zinc Clusters²

Quantum-chemical calculations have shown that naked metalloids zinc clusters Zn_a ($a > 8$) can have a large spectrum of electronic properties, ranging from a metallic to an insulating character, and may also show special features that uniquely combine both phenomena.^[123] Ligand-protected metal clusters $[M_a](L)_b$ ($a > b$), linking molecular and bulk materials, have

² H. Banh, K. Dilchert, C. Schulz, C. Gemel, R. W. Seidel, R. Gautier, S. Kahlal, J.-Y. Saillard and R. A. Fischer, *Angew. Chem. Int. Ed.* **2016**, 55, 3285-3289.

been the focus of research for a long time. Zinc, however, has remained an exception. Naked Zn clusters have only been studied in the gas phase,^[123] as a guest in Zeolite X,^[66] or as discrete structural units in intermetallic frameworks^[124, 125] and porous materials.^[126] The closed-shell electron configuration of Zn only allows for weak van der Waals interactions in small homoleptic clusters (35 meV between two zinc atoms).^[127] Stabilization by the effective mixing of s/p states requires larger nuclearities. Notably, the series of compounds, $[M@Zn_a](L)_a$ ($M =$ d block metal, $L = Cp^*, CH_3$; $a = 8-12$), represents examples of Zn-rich cluster-like molecules.^[58] However, the “empty” $[Zn_a](L)_a$ cages are not stable without the strong binding to the interstitial metal M, for example, in $[Mo@Zn_{12}](Cp^*)_3(Me)_9$. Ligand-protected molecular Zn clusters $[Zn_a](L)_b$ have not been reported to date. Recently, Jones and co-workers employed the bulky amido ligand LN ($LN=N(Ar)SiMe_3$, $Ar = 2,6\text{-}\{C(H)Ph_2\}2\text{-}4\text{-}iPr\text{-}C_6H_2$) to stabilize the mixed-valence three-membered zinc chain $[LNZnZnZnLN]$.^[128] On the one hand, the bulkiness of LN supports the unique linear structure of the $[Zn_3]$ unit, but on the other hand, it reduces the flexibility of coordination modes and the reactivity at the Zn atoms. This is different for the trigonal cluster cation $\{[Zn_3](Cp^*)_3\}^+$, which becomes important in this context.^[69, 119] It was obtained by the addition of the in situ formed solvated cation $[ZnCp^*]^+$ to Carmona’s compound, $[Zn_2Cp^*_2] = [Zn_2](Cp^*)_2$. Regarded as a minimal building unit of larger deltahedral Zn-containing clusters, it points towards the accessibility of $[Zn_a]L_b$ below the critical size limit for naked jellium super-atom-like Zn clusters. Interestingly, gallium, as the right neighbor of Zn in the periodic table, features a rich metalloid cluster chemistry, and the same is true for Al, the lighter homologue. A library of anionic $\{[M_a]L_b\}^{n-}$ ($M = Al, Ga$; $a > b$; $L = N(SiMe_3)_2$) complexes were previously obtained and thoroughly studied.^[31] The key to this bottom-up wet chemical synthesis of metalloid clusters is the controlled disproportionation of the metastable monohalides MX in solution at low temperatures and the trapping of intermediates by the addition of a judiciously chosen ligand L. Inspired by Schnöckel’s pioneering work the transfer of this reaction concept to ligand protected Zn clusters have been explored using $[Zn_2](Cp^*)_2$ as a primary Zn-source exhibiting the Cp* group as removable protecting group. Regarding this the semi deprotected $[Cp^*Zn_2(Et_2O)_3]^+$ can be isolated at room temperature by oxidative cleavage of one Zn-Cp* bond and it is prone to disproportionation.^[103] This species can be used as a Zn-source and as shown in the previous chapter the reactivity and lability towards disproportionation of $\{[Cp^*Zn_2](L'_n)\}^+$ can be modulated by the choice of the solvent or weakly coordinating co-ligands L'. However, as the lability of $[Cp^*Zn_2]^+$ is important to form Zn^0 , unwanted stabilization of the open Zn^I coordination site is to be minimized. As to that, the *in*

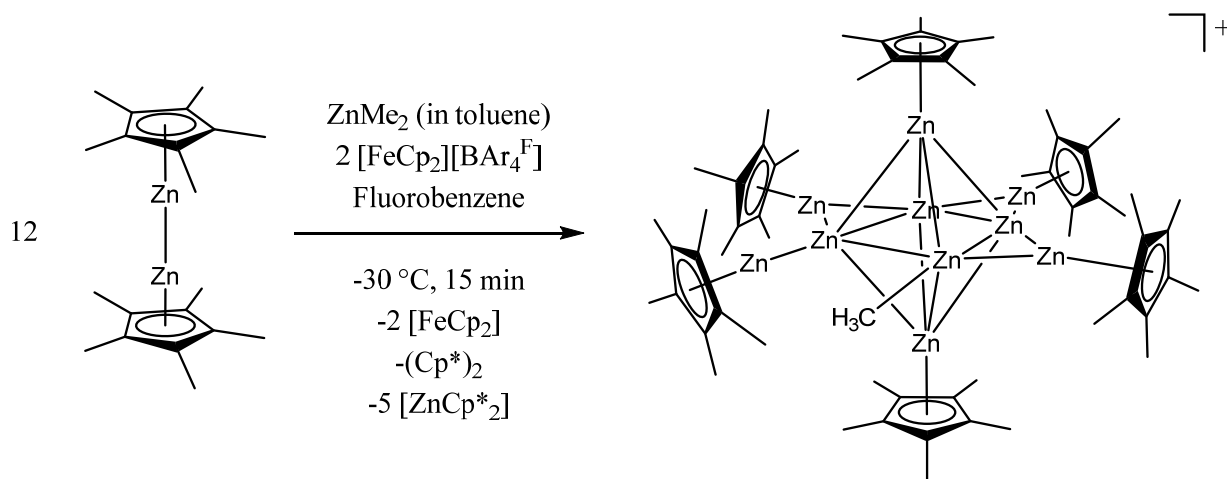
situ activation of $[\text{Zn}_2](\text{Cp}^*)_2$ by single electron oxidation of one Zn-Cp* bond was investigated. The addition of small quantities of ZnMe_2 proved crucial as a methyl-transfer and/or trapping reagent. Accordingly (Scheme 14), the first all-hydrocarbon-ligand protected medium nuclearity clusters $[\text{Zn}_n]\text{L}_b$ **4-6** were obtained.



Scheme 14. Synthesis of the first examples of medium sized ligand protected zinc clusters: $\{[\text{Zn}_{10}](\text{Cp}^*)_6\text{Me}\}^+$ (**4**), $\{[\text{Zn}_9](\text{Cp}^*)_6\}$ (**5**), and $\{[\text{Zn}_8](\text{Cp}^*)_5(\text{CN}^t\text{Bu})_3\}^+$ (**6**).

4.2.1 Synthesis of $\{[\text{Zn}_{10}](\text{Cp}^*)_6\text{Me}\}[\text{BAr}_4^{\text{F}}]$ (**4**)

Reaction of $[\text{Zn}_2](\text{Cp}^*)_2$ with $[\text{FeCp}_2][\text{BAr}_4^{\text{F}}]$ and ZnMe_2 (12:2:1 molar ratio) in fluorobenzene at $-30\text{ }^\circ\text{C}$ leads to the salt $\{[\text{Zn}_{10}](\text{Cp}^*)_6\text{Me}\}[\text{BAr}_4^{\text{F}}]$ (**4**) as red microcrystals in 41 % isolated yield (based on Zn) (Scheme 15). The over-all reaction involves an oxidative Zn-Cp* bond cleavage by $[\text{FeCp}_2][\text{BAr}_4^{\text{F}}]$. The by-products $[\text{FeCp}_2]$, Cp^*_2 and Cp^*_2Zn were identified by in situ NMR spectroscopy. Note, if $[\text{Zn}_2](\text{Cp}^*)_2$ is treated with $[\text{FeCp}_2][\text{BAr}_4^{\text{F}}]$ in the absence of ZnMe_2 under otherwise identical conditions no reaction takes place. From these observations the (conceptual) conclusion is drawn that in situ formation of the dimeric intermediate Zn^{I} species $[\text{RZn}-\text{ZnMe}]$ ($\text{R} = \text{Me}$ or Cp^*) involving rapid Me/Cp*-group exchange may lead to $\text{Zn}(0)$ upon disproportionation, which species are subsequently stabilized by the abundant $\cdot\text{ZnCp}^*$ radicals. Cp*/Me exchange at Zn is known for the reaction of $[\text{ZnCp}^*_2]$ with ZnMe_2 giving $[\text{Cp}^*\text{ZnMe}]$ as a product.^[129] Note, that the direct treatment of $[\text{Zn}_2](\text{Cp}^*)_2$ with ZnMe_2 leads to a rapid disproportionation of $[\text{Zn}_2](\text{Cp}^*)_2$ indicated by the precipitation of metal black.



Scheme 15. Synthesis of $\{[\text{Zn}_{10}](\text{Cp}^*)_6\text{Me}\}[\text{BAR}_4^{\text{F}}]$ ($4[\text{BAR}_4^{\text{F}}]$).

Compound $4[\text{BAR}_4^{\text{F}}]$ is soluble in non-coordinating, polar, aprotic solvents, such as fluorobenzene or CH_2Cl_2 , under strict exclusion of moisture. However, without continuous cooling to $-10\text{ }^\circ\text{C}$, it rapidly decomposes in solution as well as in the solid state.

4.2.2 Spectroscopic and Structural Features of $\{[\text{Zn}_{10}](\text{Cp}^*)_6\text{Me}\}[\text{BAR}_4^{\text{F}}]$ ($4[\text{BAR}_4^{\text{F}}]$)

The elemental analysis (C, H) and AAS (Zn, B, F) data are in reasonable agreement with the assigned composition, in particular considering its very high (air, moisture and thermal) sensitivity, which impedes storage and sample transfer. Accordingly, the ^1H NMR data (CD_2Cl_2 , $25\text{ }^\circ\text{C}$) reveal yet unidentified decomposition products, including CH_4 ($\delta = 0.21\text{ ppm}$). The ^1H NMR spectrum recorded at $-90\text{ }^\circ\text{C}$ (isolated, pure sample) is clean and shows one singlet at 0.02 ppm (s, 3H, ZnCH_3) and one singlet at 1.75 ppm (s, 30H, $\mu_4\text{-ZnCp}^*$ groups). Another two, not fully decoalesced singlets are assigned to terminal and edge-bridging $\mu_2\text{-ZnCp}^*$ groups ($\delta = 2.04, 2.06\text{ ppm}$ (60H)), indicating rapid fluxional behavior in the equatorial plane of **4** (Figure 32). As expected, the set of signals for the $[\text{BAR}_4^{\text{F}}]^-$ anion ($\delta = 7.53$ (4H) and 7.72 ppm (8H)) are also observed. The FTIR spectrum of $4[\text{BAR}_4^{\text{F}}]$ reveals typical bands for the Cp^* ring at $2935, 2888$ and 2839 cm^{-1} as well as a signal due to the C–F vibration at 1263 cm^{-1} .

Red needle shaped crystals of $4[\text{BAR}_4^{\text{F}}] \cdot 5\text{ C}_6\text{H}_5\text{F}$ suitable for single crystal X-ray diffraction were obtained from a saturated fluorobenzene solution of $4[\text{BAR}_4^{\text{F}}]$ at $-30\text{ }^\circ\text{C}$. Compound

$4[\text{BAR}_4^{\text{F}}] \cdot 5 \text{C}_6\text{H}_5\text{F}$ crystallizes in the monoclinic space group Pm with one formula unit per unit cell (Figure 32). The structure of **4** resembles a quite symmetric Zn_6 octahedron, bearing three edge bridging ZnCp^* , one terminal ZnCp^* and one terminal CH_3 -group. The equatorial Zn-atoms of the core (Zn2 - Zn5) are coplanar with the bridging and terminal Zn-atoms. Interestingly, there is an elongated unsupported edge in the equatorial plane (Zn2-Zn5 2.833(3) Å) compared to the other three edges capped by ZnCp^* (Zn3-Zn4 2.425(2)-Zn2-Zn3 2.456(2) Å). As there are few molecular Zn-containing clusters, the anionic intermetallic cluster $[\text{Zn}_{\text{cen}}@(\text{Zn}_8\text{Bi}_4)_{\text{ico}}@(\text{Bi}_7)]^{5-}$ (Figure 33, left) may be useful for comparison here.^[130] It shows that the long Zn2-Zn5 distance of **4** is well in the range of the bonding $\text{Zn}_{\text{cen}}\text{-Zn}_{\text{ico}}$ contacts of 2.832(2) – 2.594(3) Å. However, in comparison to the parent compound $[\text{Zn}_2](\text{Cp}^*)_2$ ^[69] (2.305(3) Å) all Zn-Zn bond lengths are elongated but in the range of Zn-Zn distances of literature known compounds with the smallest distance 2.295(3) Å in $[\text{Zn}_2(\text{C}_5\text{Me}_4\text{Et})_2]$ ^[71] and the largest 3.594(3) Å in the mentioned heterobimetallic cluster $[\text{Zn}_{\text{cen}}@(\text{Zn}_8\text{Bi}_4)_{\text{ico}}@(\text{Bi}_7)]^{5-}$.^[130] The shortest Zn-Zn bond length in **4** between Zn2 and the terminal Zn9Cp^* group (2.342(2) Å) is similar to the distances found in $[\text{Zn}_2\text{Cp}^*_2(\text{t}^{\text{Bu}})]$ ($\text{t}^{\text{Bu}} = 1,3\text{-bis}(2,6\text{-diisopropylphenyl})\text{imidazole-2-ylidene}$) (2.339(4) Å),^[72] $[\text{Pd}(\text{GaCp}^*)_2(\text{ZnCp}^*)_2(\text{ZnZnCp}^*)_2]$ (2.345(1) and 2.346(1) Å) and $[\text{Pd}(\text{ZnCp}^*)_4(\text{ZnZnCp}^*)_4]$ (2.347(3) Å) (Figure 20).^[109] The Zn9-Cp*_{centr.} distance (1.909 Å) is in the range of the distances found in $[\text{Cp}^*_3\text{Zn}_4(\text{Et}_2\text{O})_3]^+$ (1.889 Å, 1.935 Å) and $[\text{Cp}^*\text{Zn}_2(\text{Et}_2\text{O})_3]^+$ (1.92 Å),^[103] but distinctly shorter than that in $[\text{Zn}_2](\text{Cp}^*)_2$ (2.04 Å).^[69] The length of the Zn5-CH₃ bond (1.968(9) Å) is comparable with the respective bond lengths in $[\text{Pd}(\text{ZnCp}^*)_4(\text{ZnMe})_2\{\text{Zn}(\text{tmeda})\}]$ ^[112] (1.972(5) Å, 1.981(6) Å) or in $[\text{Ni}(\text{ZnCp}^*)_4(\text{ZnMe})_4]$ ^[58] (1.958(5) – 1.970(5) Å) (Figure 33, right). Due to the close proximity of the terminal ZnCp^* and the methyl group, their sterical repulsion not only causes an elongated edge but also the distorted motif of the octahedron as indicated by the bond angles between the $\text{Zn}_{\text{equatorial}}$ atoms (80.13(5) (Zn3-Zn2-Zn5) – 100.71(6) ° (Zn4-Zn3-Zn2). Despite the vicinity of the terminal ZnCp^* and Me unit, Zn2, Zn3 and Zn9 are arranged almost linearly (178.02(7) °). Zn3, Zn4 and Zn7 form an almost equilateral triangle (bond angles 61.39(4), 59.62(4) and 58.99(4) °) with an average Zn-Zn bond length of 2.455(2) Å similar to $\{[\text{Zn}_3]\text{Cp}^*_3\}^{+}$ ^[119] (61.06(2), 59.22(1) and 59.71(1) °) with an average bond length of 2.430(1) Å, whereas the triangles formed by the bridging ZnCp^* units next to the terminal ZnCp^* and methyl group are rather distorted (bond angles 55.32(4) - 67.09(5) ° for Zn2, Zn3, Zn6 and 53.94(4) – 69.66(5) ° for Zn4, Zn5, Zn8).

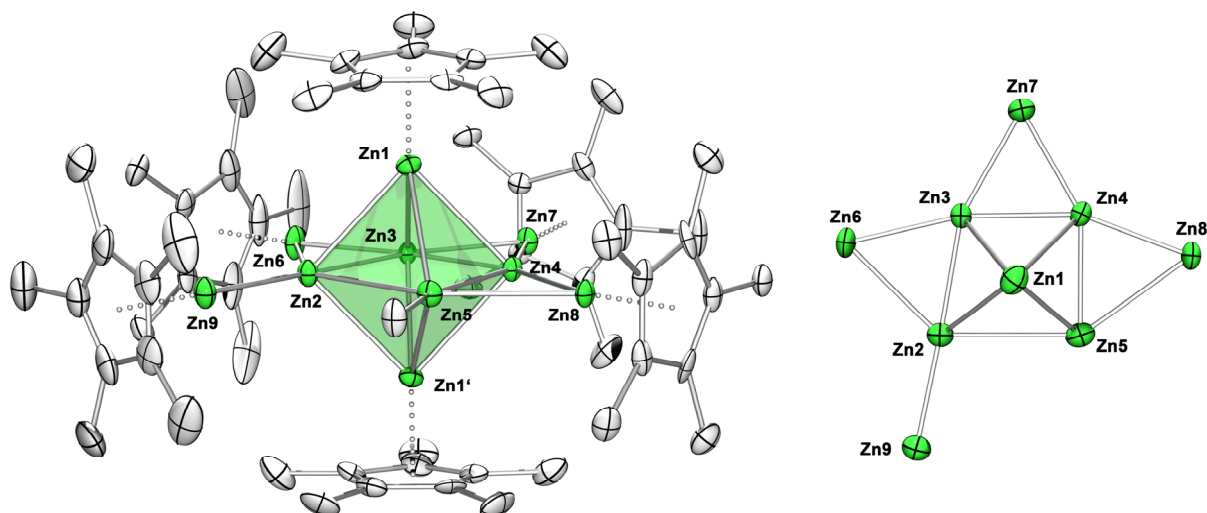


Figure 32. Molecular structure of $\{[Zn_{10}](Cp^*)_6Me\}^+$ (**4**) in the crystal of $4[BAr_4^F] \cdot 5 C_6H_5F$ (left). The distorted octahedron is highlighted. View from the top on the Zn2, Zn3, Zn4 plane of the Zn framework showing the elongated Zn2-Zn5 edge (right). Displacement ellipsoids are shown at the 50 % probability level and the hydrogen atoms are omitted for clarity. The symmetry-related zinc atom is primed. Selected interatomic distances [Å] and angles [°]: Zn2-Zn9 = 2.342(2), Zn2-Zn3 = 2.454(2), Zn1-Zn4 = 2.759(9), Zn5-Zn4 = 2.453(2), Zn4-Zn3 = 2.425(2), Zn1-Cp*_{centr.} = 1.878, Zn9-Cp*_{centr.} = 1.909; Zn3-Zn4-Zn7 = 61.39(4), Zn4-Zn3-Zn7 = 59.62(4), Zn4-Zn7-Zn3 = 58.99(4), Zn9-Zn2-Zn3 = 178.02(7).

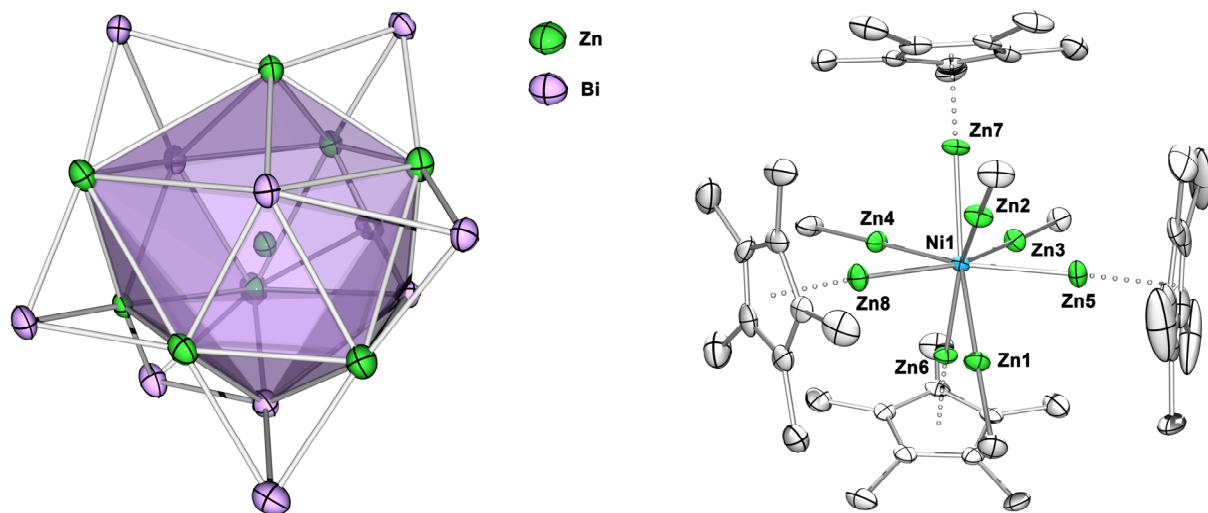
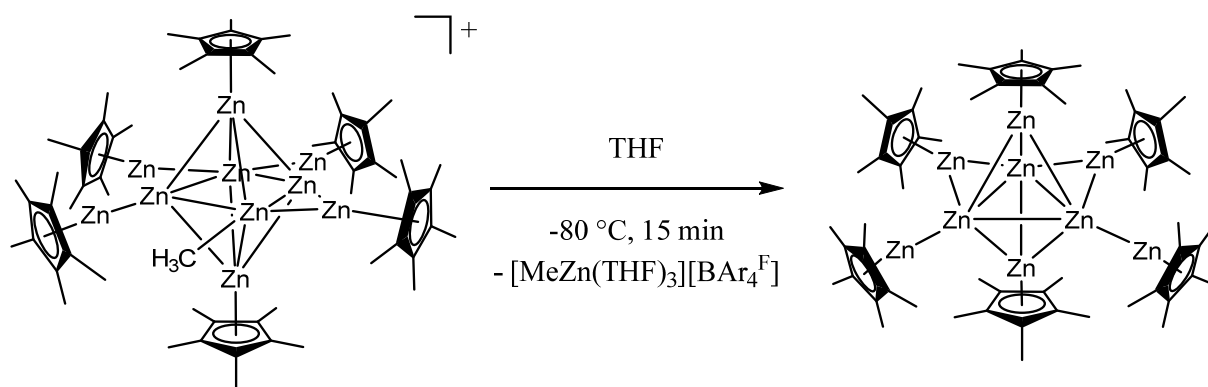


Figure 33. Molecular structure of $[Zncen@(Zn_8Bi_4)_{ico}@Bi_7]^{5-}$ (left) and $[Ni(ZnCp^*)_4(ZnMe)_4]$ without hydrogen atoms (right).

4.2.3 Synthesis of $\{[Zn_9](Cp^*)_6\}$ (**5**)

The lability of $4[BAr_4^F]$ suggests further transformations are possible, namely cluster expansion or degradation. Due to the stability of $4[BAr_4^F]$ in inert, polar, non coordinating solvents at temperatures below $-10\text{ }^\circ\text{C}$ an investigation of the reactivity of $4[BAr_4^F]$ towards various donor ligands was feasible. Hence, the reactivity of $4[BAr_4^F]$ towards solvents with hard σ -donor properties, such as THF or Et₂O (L), which have proven to be compatible with low valent zinc, has been investigated at $-80\text{ }^\circ\text{C}$. In fact, selective abstraction of $[MeZn(L)_3][BAr_4^F]$ occurred, and the neutral cluster $[Zn_9](Cp^*)_6$ (**5**) was obtained. One single framework Zn atom is selectively excised as the cationic $[MeZn(L)_3]^+$ adduct, that is, as a Zn^{II} species. The triangular cation $\{[Zn_3](Cp^*_3)\}^+$ shows a similar behaviour. It is selectively fragmented into $[Zn_2](Cp^*_2)$ and $[Cp^*Zn(THF)_3]^+$ upon addition of THF.



Scheme 16. Synthesis of $\{[Zn_9](Cp^*)_6\}$ (**5**).

The neutral $[Zn_9]$ cluster **5** is soluble and stable in both coordinating and non-coordinating solvents. However, like $4[BAr_4^F]$, it needs to be handled with great care under rigorous air and moisture exclusion, and continuous cooling is needed to avoid or minimize decomposition. Slow diffusion of *n*-pentane into a concentrated toluene solution of **5** at $-90\text{ }^\circ\text{C}$ afforded single crystals of $\mathbf{5} \cdot 2\text{ PhMe}$.

4.2.4 Spectroscopic and Structural Features of $\{[\text{Zn}_9](\text{Cp}^*)_6\}$ (**5**)

Considering the high reactivity of **5**, which makes sample transfer and storage difficult, the elemental analysis (C, H) and AAS (Zn) data are in reasonable agreement to the assigned composition. The ^1H NMR spectrum of **5** · 2 PhMe in CD_2Cl_2 at $-90\text{ }^\circ\text{C}$ shows two resonances at 1.87 (s, 30H) and 1.97 ppm (s, 60H) in a 1:2 ratio although decoalescence is still not complete, indicating a high fluxionality of all Cp^* groups in contrast to the solid state molecular structure determined by single crystal X-ray analysis which shows three chemical different pairs of Cp^* groups in a 1:1:1 ratio. The signals at 2.27 (s, 6H) and 7.05–7.27 ppm (m, 10H) are due to toluene solvate molecules incorporated into the single crystals. By increasing the temperature of the NMR sample, the Cp^* groups slowly start to coalesce at which the Cp^* groups are almost indistinguishable at $-30\text{ }^\circ\text{C}$ (Figure 34).

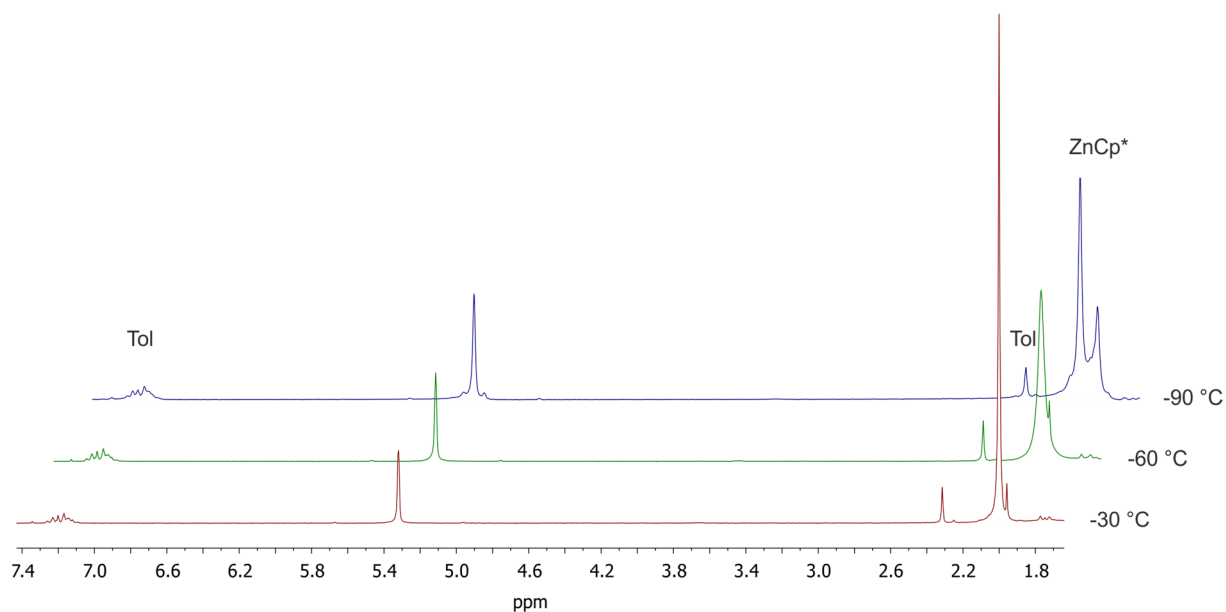


Figure 34. ^1H NMR spectra of **5** · 2 PhMe in CD_2Cl_2 at temperatures between $(-30) - (-90)\text{ }^\circ\text{C}$.

The FTIR spectrum of **5** · 2 PhMe reveals typical bands for the Cp^* ring at 2939, 2879 and 2833 cm^{-1} .

Yellow crystals of **5** · THF (orthorhombic, *Cmcm*, four molecules in the unit cell) were obtained by slow diffusion of *n*-hexane into the reaction solution at -30 °C. The molecular structure of **5** features a distorted trigonal bipyramidal Zn₅ core whose equatorial plane (Zn1, Zn2, Zn2') contains two edge-bridging and two terminal ZnCp* units. This structure can be derived by removing the ZnMe group (Zn5) from **4** and forming a bond between Zn2 and Zn4. The resulting structure of **5** exhibits an elongated edge (Zn2–Zn2' 2.829(8) Å) without a bridging ZnCp* group.

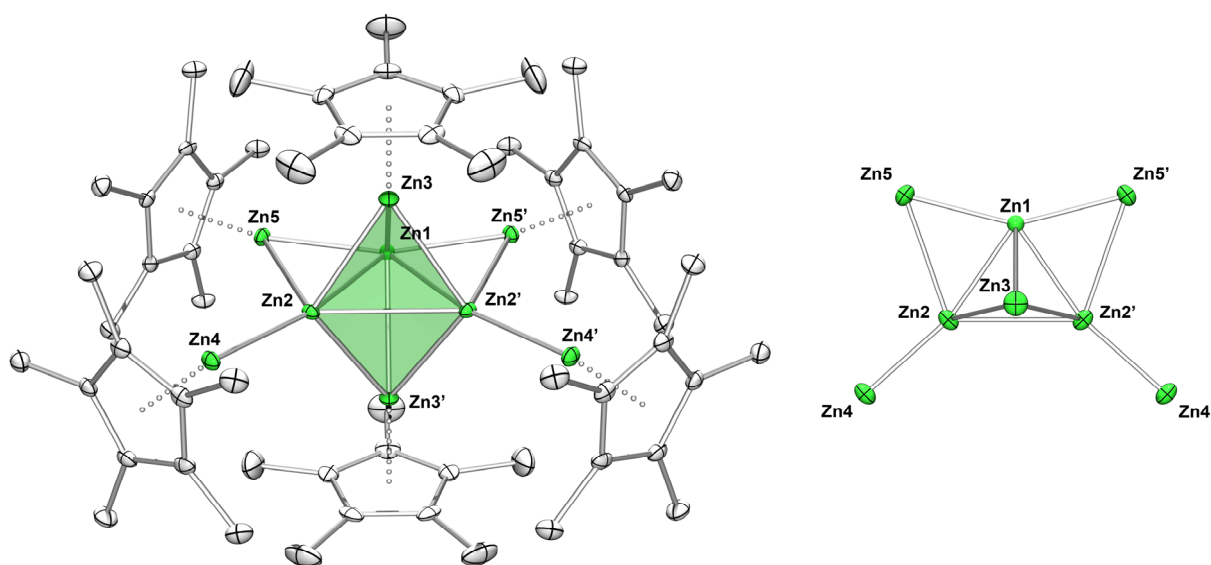


Figure 35. Molecular structure of $\{[Zn_9](Cp^*)_6\}$ in the crystals of **5** · THF (left). The distorted trigonal bipyramid is highlighted. View from the top on the Zn2, Zn2', Zn1 plane of the Zn framework showing the elongated Zn2–Zn2' edge (right). Displacement ellipsoids are shown at the 50 % probability level and the hydrogen atoms are omitted for clarity. Symmetry-related atoms are primed. Selected interatomic distances [Å] and angles [°]: Zn1–Zn5 = 2.405(4), Zn1–Zn3 = 2.710(5), Zn2–Zn4 = 2.338(6), Zn2–Zn5 = 2.776(6), Zn2–Zn2' = 2.829(8), Zn3–Cp*_{centr.} = 1.922, Zn4–Cp*_{centr.} = 1.938, Zn5–Cp*_{centr.} = 1.933; Zn5–Zn1–Zn2 = 69.37(2), Zn4–Zn2–Zn1 = 166.22(2).

Another similarity to **4** is the plane spanned by the edge bridging ZnCp* ligands and the equatorial Zn atoms. However, **4** appears to be more contracted within the equatorial plane (cf. Zn2–Zn4 distance (3.757 Å) in **4** and Zn2–Zn2' distance (2.829(8) Å) in **5**) as a result of the removal of the ZnMe group, and accordingly, it is slightly expanded in the orthogonal direction (Zn1–equatorial plane 2.009 Å in **4** and Zn3–equatorial plane 2.137 Å in **5**). However, the overall bond lengths from the Zn_{equatorial} atoms to the Zn_{apical} atoms are shortened ((2.609(1) -

2.759(9) Å for **4** and Zn2-Zn3 2.588(4), Zn1-Zn3 2.710(5) Å for **5**). The interatomic Zn distances between Zn1-Zn2 of 2.472(6) Å is slightly elongated compared to the Zn2-Zn3 distance (2.454(2) Å in **4**, but significantly longer than the respective Zn3-Zn4 distance of 2.425(1) Å. The Zn2-Zn4 bond length (2.338(6) Å) is similar to the Zn2-Zn9 distance (2.342(2) Å) in **4**, though the Zn4-Cp*centroid distance (1.938 Å) is slightly elongated in comparison to the respective distance in **4** (1.909 Å) and similar to the Zn5-Cp*centroid distance (1.933 Å).

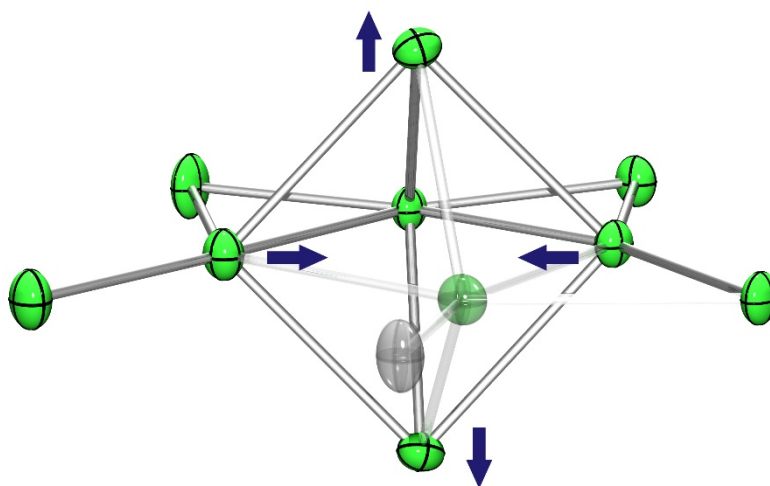
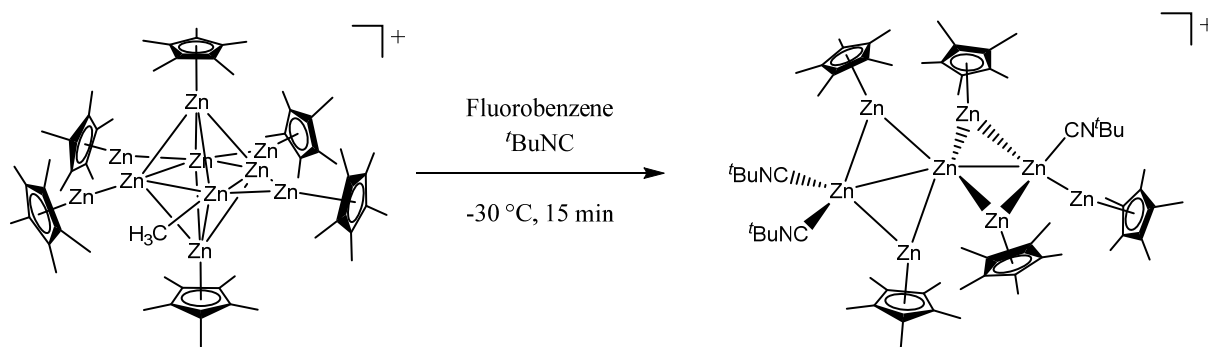


Figure 36. Relation of the Zn cores of **4** and **5**. Contraction and expansion from [Zn₁₀] to [Zn₉] is indicated by arrows. Cleaved bonds and removed atoms are transparent.

4.2.5 Synthesis of {[Zn₈](Cp*)₅(CN^tBu)₃}[BAR₄^F] · 4 C₆H₅F (**6**[BAR₄^F] · 4 C₆H₅F)

The controlled deconstruction of the cationic [Zn₁₀] cluster **4** dissolved in fluorobenzene using ^tBuNC as a somewhat softer ligand at -30 °C gives the [Zn₈] cluster **6** as the salt {[Zn₈](Cp*)₅(CN^tBu)₃}[BAR₄^F]. The by-products have not yet been identified.



Scheme 17. Synthesis of $\{[\text{Zn}_8](\text{Cp}^*)_5(\text{CN}^t\text{Bu})_3\}[\text{BAR}_4^{\text{F}}] \cdot 4 \text{C}_6\text{H}_5\text{F}$ (**6** $[\text{BAR}_4^{\text{F}}] \cdot 4 \text{C}_6\text{H}_5\text{F}$).

4.2.6 Structural Features of $\{[\text{Zn}_8](\text{Cp}^*)_5(\text{CN}^t\text{Bu})_3\}[\text{BAR}_4^{\text{F}}] \cdot 4 \text{C}_6\text{H}_5\text{F}$ (**6** $[\text{BAR}_4^{\text{F}}] \cdot 4 \text{C}_6\text{H}_5\text{F}$)

Compound **6** $[\text{BAR}_4^{\text{F}}] \cdot 4 \text{C}_6\text{H}_5\text{F}$ was isolated and separated from by-products by selecting individual single crystals in perfluoropolyether using an optical microscope. The crystals are highly labile and rapidly decompose even at room temperature, which prevents the isolation of substantial amounts of **6** for spectroscopic or elemental analyses.

However, yellow rhombus shaped single crystals of **6** $[\text{BAR}_4^{\text{F}}] \cdot 4 \text{C}_6\text{H}_5\text{F}$ (monoclinic, $C2/c$, eight formula units in the unit cell) suitable for single crystal X-ray analysis were obtained by slow diffusion of *n*-hexane into the reaction solution at $-30\text{ }^\circ\text{C}$. The molecular structure consists of two corner-connected Zn_4 rhombi (flipped by ca. 90°) with one additional terminal ZnCp^* ligand at Zn7 (Figure 37). The bridging Zn atoms feature Cp^* ligands, and the open sites (Zn1 , Zn7) at the corners of the Zn_4 rhombi are saturated by $t\text{BuNC}$. The two rhombi are slightly twisted with respect to each other along the Zn1-Zn4-Zn7 axis ($163.98(2)^\circ$). Each rhombus is divided into two almost equilateral triangles (bond angles for $\text{Zn1, Zn4, Zn2} = 61.76(2), 60.49(2), 57.75(2)^\circ$, $\text{Zn1, Zn3, Zn4} = 58.05(2), 59.26(2), 62.69(2)^\circ$, $\text{Zn4, Zn5, Zn6} = 63.05(2), 58.98(2), 57.98(2)^\circ$, $\text{Zn4, Zn6, Zn7} = 61.93(2), 59.50(2), 58.57(2)^\circ$) by the Zn1-Zn4 and Zn4-Zn7 axes, respectively. As a result of the close proximity of the Zn3Cp^* group to the terminal Zn8Cp^* group the $\text{Zn7-Zn8-Cp}^*_{\text{centr.}}$ bond angle is not linear (164.06°). The Zn4-Zn7 bond length ($2.484(7)\text{ \AA}$) is comparable with the Zn3-Zn7 bond distance in $[\text{Zn}_{10}]$ and slightly longer than the Zn1-Zn4 distance ($2.433(7)\text{ \AA}$). The $\text{Zn8-Cp}^*_{\text{centr.}}$ bond distance (1.969 \AA) is similar to the respective bond lengths of the terminal ZnCp^* groups in $[\text{Zn}_9]$ (1.938 \AA) and $[\text{Zn}_2](\text{Cp}^*)_2$ (1.936 \AA). All the $\text{Zn-C}_{\text{isonitrile}}$ bond lengths ($2.069(4), 2.084(4), 2.137(4)\text{ \AA}$), are well comparable to the respective distances found in **3** ($\sim 2.1\text{ \AA}$).

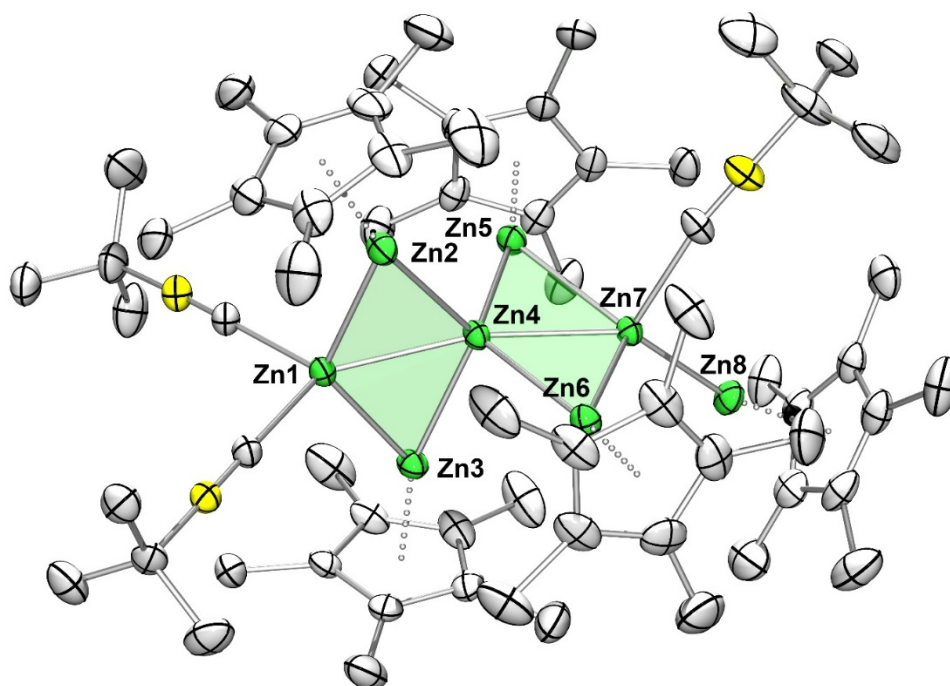


Figure 37. Molecular structure of $\{[Zn_8](Cp^*)_5(CN^tBu)_3\}^+$ in the crystals of $6[BAr_4^F] \cdot 4 C_6H_5F$. Trigonal faces are highlighted. Displacement ellipsoids are shown at the 50 % probability level and the hydrogen atoms are omitted for clarity. Selected interatomic distances [Å] and angles [°] for $6[BAr_4^F] \cdot 4 C_6H_5F$: Zn1-Zn4 = 2.433(7), Zn4-Zn7 = 2.484(7), Zn7-Zn8 = 2.361(7), Zn1-C56 = 2.069(4), Zn1-C51 = 2.084(4), Zn7-C61 = 2.137(4), Zn8-Cp*_{centr.} = 1.969; Zn7-Zn8-Cp*_{centr.} = 164.08, Zn4-Zn1-Zn2 = 61.76(2), Zn1-Zn3-Zn4 = 58.05(19), Zn5-Zn4-Zn7 = 63.05(2), Zn6-Zn4-Zn7 = 61.93(2), Zn1-Zn4-Zn7 = 163.98(3).

4.2.7 Theoretical Investigations on $\{[Zn_{10}](Cp^*)_6Me\}^+$ (**4**) and $\{[Zn_9](Cp^*)_6\}$ (**5**)³

In order to elucidate the electronic structures of the clusters $\{[Zn_{10}](Cp^*)_6Me\}^+$ (**4**) and $\{[Zn_9](Cp^*)_6\}$ (**5**) DFT calculations were conducted at the PBE0/Def2TZVP level of theory. In addition the optimized structures for the Cp derivatives $\{[Zn_{10}](Cp)_6Me\}^+$ (**4'**) and $[Zn_9](Cp)_6$ (**5'**) have been calculated for comparison. All optimized structures **4**, **4'** and **5**, **5'** are in fairly good agreement with the molecular structures obtained by single crystal X-ray diffraction (Table 5 and Table 6). The unsupported Zn-Zn bonds in the equatorial planes of **4**_{exp} (2.832(2) Å) and **5**_{exp} (2.829(8) Å) are well represented in the computed structures of **4** and **4'** with 2.833

³ The following paragraph regarding the quantum chemical analysis of the compounds $\{[Zn_{10}](Cp^*)_6Me\}^+$ (**4**) and $\{[Zn_9](Cp^*)_6\}$ (**5**) cites/paraphrases respective parts of H. Banh, K. Dilchert, C. Schulz, C. Gemel, R. W. Seidel, R. Gautier, S. Kahlal, J.-Y. Saillard and R. A. Fischer, *Angew. Chem. Int. Ed.* **2016**, *55*, 3285-3289. They are based on the work of the group of Prof. Dr. J.-Y. Saillard especially involving Dr. S. Kahlal and Dr. R. Gautier, Institut des Sciences Chimiques de Rennes, France.

and 2.573 Å as well as of **5** and **5'** with 3.066 and 2.804 Å, respectively. The calculated HOMO-LUMO gaps (**4**: 3.20 eV, **5**: 3.86 eV) indicate closed-shell structures for both clusters and are in accordance to the (relative) kinetic stability of the compounds.

The total number of valence electrons available for Zn-Zn bonding in **4** can be easily obtained upon fragmentation of the cluster. The Zn₆ core consist of two axial μ_4 -ZnCp* units, two ZnR (R = Me and ZnCp*) units and two Zn atoms. Additionally, three edges of the octahedron are bridged by μ_2 -ZnCp* moieties. Each ZnCp* and ZnR unit provides one electron, whereas each Zn atom contributes two electrons. Considering the positive charge of the cluster the total number of skeletal electron pairs (SEPs) is five. In contrast, according to the Wade-Mingos electron counting rules^[49, 50, 131, 132] a total number of seven SEPs is required for a regular octahedral cluster such as [B₆H₆]²⁻. The four electron discrepancy arises, because these particular rules are in fact only applicable to clusters made of fragments which possess three frontier orbitals (one σ - and two π -type orbitals).^[131, 132] This *e.g.* applies to BH, a ZnR unit or a bare Zn atom, but not to a ZnCp* fragment. Instead, ZnCp* only exhibits one singly occupied σ -type orbital and is isolobal to H. As a consequence, the formal “deprotonation” of **1** by removing the μ_2 -ZnCp*⁺ groups gives the hypothetical octahedral system {[Zn₆](Cp*)₂RR'}²⁻ (R = Me and R' = ZnCp*).

The seven SEPs of [B₆H₆]²⁻ correspond to a (a_{1g})²(t_{2g})⁶(t_{1u})⁶ configuration. The skeletal-bonding a_{1g} MO is a pure σ -type combination, the t_{1u} MOs consist of mixed σ - and π -type combinations and the t_{2g} orbitals are of pure π -type in origin. An octahedron can be described as three interpenetrating squares, at which each t_{2g} component can be associated with one of these squares (Figure 38, top). In the case of **4** there are no π -type frontier orbitals from the ZnCp* fragments available at the apical positions. This results in two “t_{2g}-derived” components lacking apical contribution (Figure 38, bottom). In contrast to [B₆H₆]²⁻ these components are high in energy and not strongly bonding but rather non-bonding due to their 4p(Zn) character. Thus, they are not available to electrons and the closed shell configuration of **4** corresponds to five SEPs instead of seven SEPs as it is expected for Wade-Mingos-type clusters.

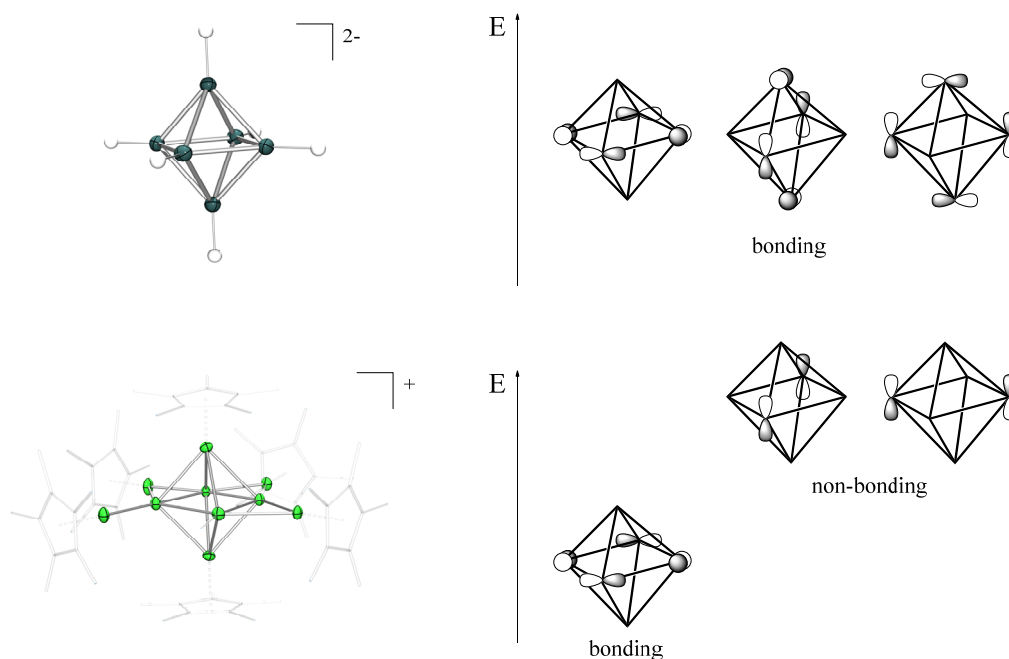


Figure 38. Top: Occupied t_{2g} skeletal orbitals $[\text{B}_6\text{H}_6]^{2-}$. Bottom: The related t_{2g} -derived orbitals of **4** lacking π -type contributions from the apical positions.

Another equivalent approach to understand this particular electron count is to examine the fully “deprotonated” planar system $\{[\text{Zn}_4]\text{RR}'\}^{4+}$. Four electron pairs can be associated with four localized Zn-Zn σ bonds and the fifth pair to an in phase π -type bonding orbital. Regarding this the Zn-Zn bonding is equivalent to the C-C bonding in the planar cyclobutadiene $\text{C}_4\text{H}_4^{2+}$. In the case of the octahedral system $\{[\text{Zn}_6](\text{Cp}^*)_2\text{RR}'\}^{2-}$ the π -type bonding is additionally stabilized by the out of phase σ -type contribution of the apical ZnCp^* groups. However, the five SEPs are not only associated with the Zn-Zn bonding within the octahedral core but also with the bonding to the bridging $\mu_2\text{-ZnCp}^*$ groups. Apart from the templating effect of the edge bridges, this is the reason for the shorter bridged edges of the octahedron compared to the weaker unsupported edge.

Due to the low symmetry of **4** and **4'** substantial mixing is allowed preventing the possibility to clearly identify five major occupied Kohn-Sham MOs assigned to the five available SEPs. Hence, the optimized structure of isoelectronic and isostructural model $\{[\text{Zn}_9](\text{Cp})_5\text{Me}_2\}^+$ (**4''**) with higher C_{2v} symmetry was calculated in order to obtain the respective Kohn-Sham MOs (Figure 39). The model **4''** is derived from **4'** by substituting the terminal ZnCp^* group by a methyl group (unsupported Zn-Zn distance: 2.783 Å).

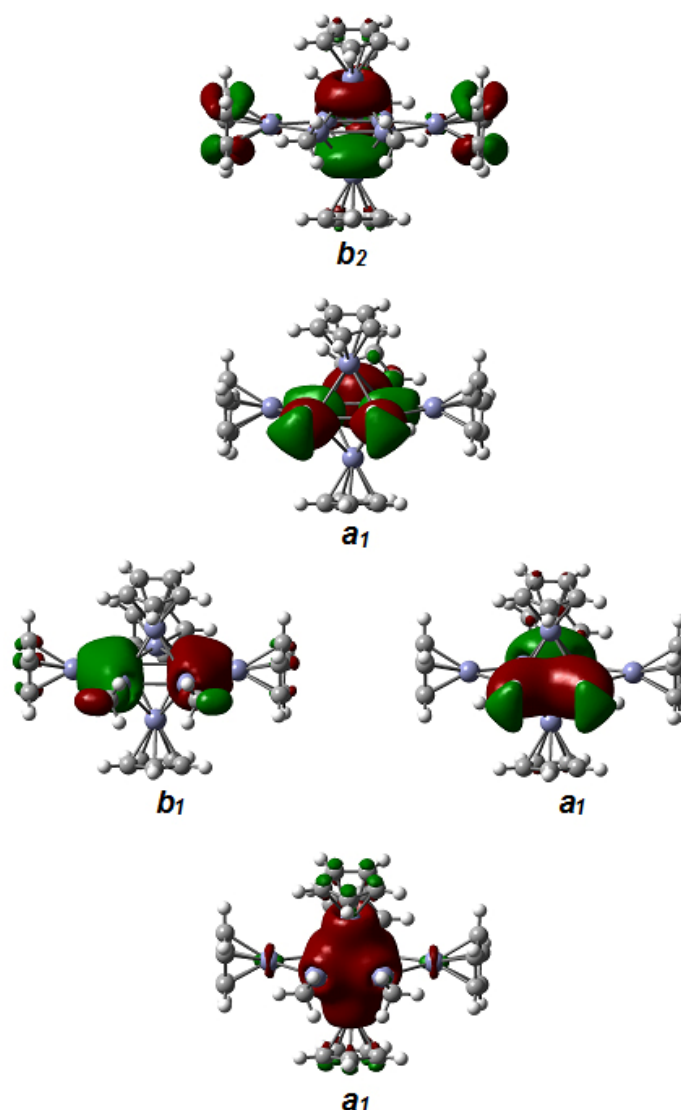


Figure 39. The major Kohn-Sham orbitals of the model cluster $\{[Zn_9](Cp)_5Me_2\}^+$ (**4''**, C_{2v}) associated with the five SEPs.

The same procedure employed to determine the number of SEPs for **4** can be used for **5**. Compound **5** can also be described as $\{[Zn_7](Cp^*)_4R_2\}$ ($R = ZnCp^*$). The formal “deprotonation” gives the hypothetical trigonal bipyramidal dianion $\{[Zn_5](Cp^*)_2R_2\}^{2-}$ exhibiting four SEPs. In contrast the Wade-Mingos rules predict a total number of six SEPs for a regular trigonal bipyramid.^[50, 131] Similar to compound **4** this SEP discrepancy can be related to the lack of π -type frontier orbitals at the apical $ZnCp^*$ positions of **5** causing the absence of two low lying bonding skeletal MOs of e'' symmetry.

Alternatively, the molecular orbital picture of the fully “deprotonated” species $\{[Zn_3]R_2\}^{4+}$ can be elucidated. At this, three SEPs are associated with Zn-Zn σ -bonds along the triangle and the

remaining one with the an in-phase fully bonding π -type combination in this triangle. This combination is further stabilized by the out of phase combination of the σ -type combination from the apical ZnCp^* fragments similar like in **4**. The weaker unbridged Zn-Zn edge is also caused by the electron deficiency and large delocalization in **5**. The four occupied MOs that most accurately represents the four delocalized SEPs in **5'** are shown in Figure 40.

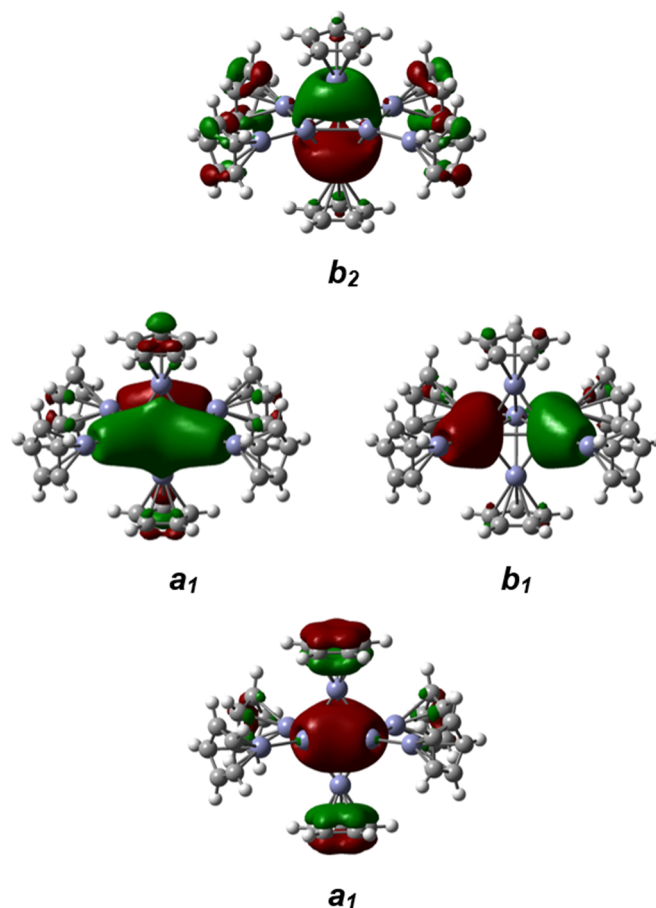


Figure 40. The major Kohn-Sham orbitals of the model cluster $\{[\text{Zn}_9](\text{Cp})_6\}$ (**5'**, C_{2v}) associated with the four SEPs.

In order to relatively quantify the strengths of the long, unbridged Zn-Zn bonds in **4** and **5**, the Wiberg indices associated with these bonds were computed with the NBO 5.0 program.^[133] The respective values for **4'** and **5'** are 0.06 and 0.05 (similar values were determined for **4** and **5** using a slightly contracted basis set) and as expected lower compared to the average values corresponding to the equatorial bridged bonds (0.11 for **4'** and 0.07 for **5'**). The natural atomic orbital overlap-weighted bond indices are 0.21 for the unsupported Zn-Zn bonds in both **4'** and

5'. The corresponding average values for the bridged bonds in **4'** and **5'** are 0.36 and 0.30, respectively. Additional insight into the nature of the bonding is provided by the electron localization function (ELF) density in the Zn2-Zn9-Zn5 plane for cluster **4'** which is shown in Figure 41. With regard to the Zn-Zn bonds, larger ELF densities (signifying localization) are primarily found in the centers of the Zn₃ triangles resulting from the bridging of the respective octahedron edges and at the center of the Zn2-Zn5-Zn9 triangle. In this context the ELF topology does not discriminate the elongated Zn-Zn-5 bond from the bridged Zn-Zn bonds. However, all data support the hypothesis that significant bonding exists even along the unsupported equatorial Zn-Zn contacts of the clusters **4** and **5**. This is consistent with the overall electron deficiency of these compounds in which zinc behaves flexibly in building skeletal metal-metal bonds, sometimes using one major frontier orbital (like Group 11 metals) and sometimes using three frontier orbitals (like Group 13 elements).

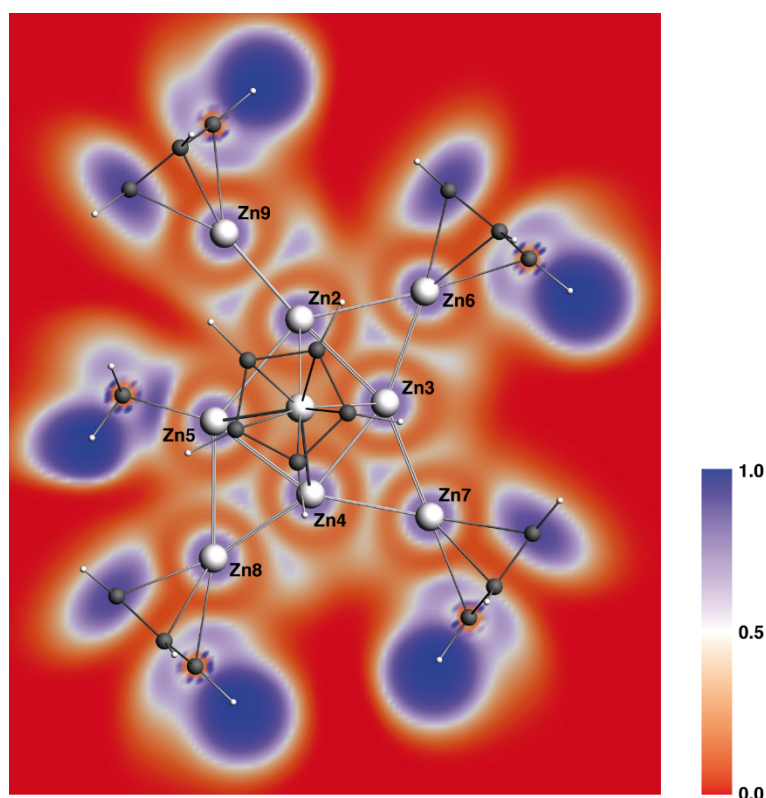


Figure 41. ELF color density plot of a cross section through the Zn2-Zn9-Zn5 plane in the cation $\{[Zn_{10}](Cp)_6Me\}^+$ (**4'**).

4.2.8 Summary

In summary, clusters **4**, **5**, **6**, (Figure 42) and $\{[\text{Zn}_3](\text{Cp}^*)_3\}^+$ are the first examples of ligand-protected deltahedral Zn clusters. The controlled disproportionation of metastable organometallic Zn^{I} species with removable protecting ligands is key to access these structures. The new clusters are electron deficient with regard to the Wade–Mingos rules, which is due to the lack of π -type frontier orbitals on the ZnCp^* moieties. They are isolobal to H rather than to BH. The comparatively weak skeletal bonding suggests a rich chemistry and the existence of other and larger atom-precise $[\text{Zn}_a]$ clusters, which could be obtained by varying the reaction partners, conditions, and stabilizing ligands. It is feasible to employ **4** and **5** as precursors for Hume–Rothery-type intermetallic clusters. For this purpose, it is highly desirable to follow up on the isolation of **5** in higher yields, which has not been possible due to the limited time of this thesis. However, *e.g.* flash chromatography of the reaction solution using alumina as a stationary phase at low temperatures in order to separate to ionic by-product might be feasible. One example for the employment of **4** as a zinc source for an intermetallic Zn/Cu cluster $\{[\text{Cu}_3\text{Zn}_5](\text{Cp}^*)_4(\text{CN}^t\text{Bu})_4\}^+$ (**10**) is discussed in the outlook. A further extension to mimic complex alloy structures remains a fascinating target. Can more complex molecular cut-outs be obtained, for example, from zinc-rich quasicrystalline phases such as Zn_6Sc ?^[134, 135]

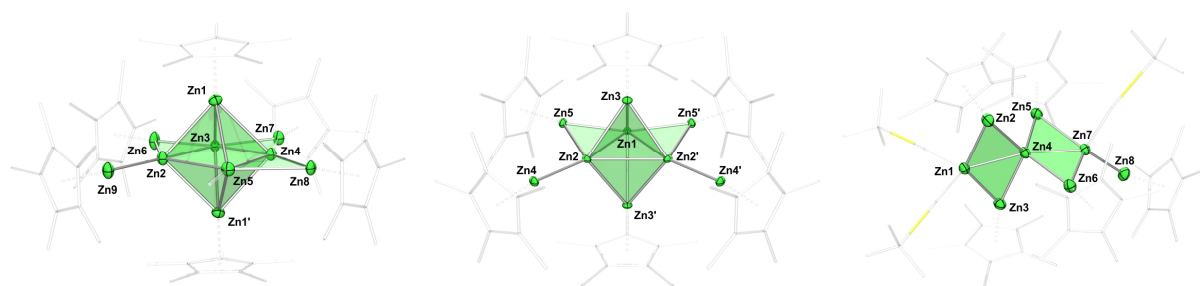


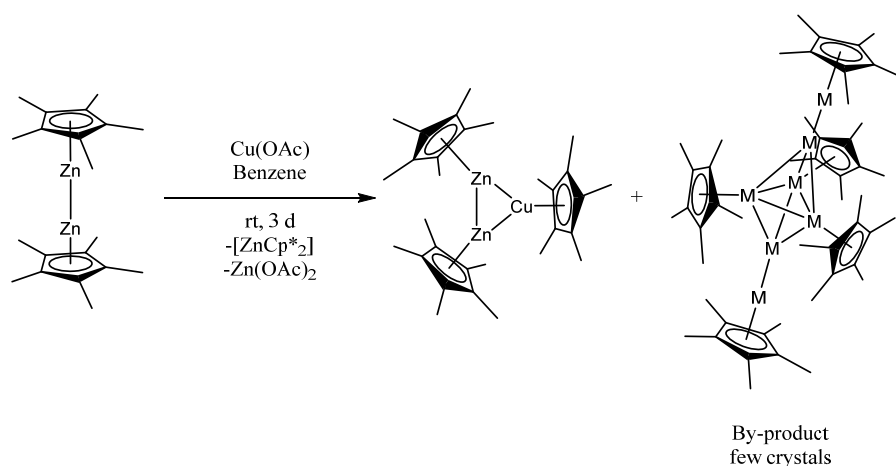
Figure 42. Zinc cores of the ligand-protected clusters $\{[\text{Zn}_{10}](\text{Cp}^*)_6\text{Me}\}^+$ (left), $\{[\text{Zn}_9](\text{Cp}^*)_6\}$ (middle), and $\{[\text{Zn}_8](\text{Cp}^*)_5(\text{CN}^t\text{Bu})_3\}^+$ (right). Thermal ellipsoids set at 50% probability. Symmetry-related atoms are indicated by '. All clusters feature Zn_3 triangles as a structural motif.

4.3 Nanobrass

Despite brass being one of the most common alloys found in everyday life and has been used by mankind for millennia now as a bulk material, molecular bimetallic Zn/Cu compounds remain scarce. This is all the more surprising, because copper can be readily mixed with zinc to form a broad range of uniform solid solutions with different Zn/Cu ratios, making brass a highly homogeneous material. Consequently, an almost infinite number of different Zn/Cu alloys are theoretically within the reach of preparation by altering the proportional composition. This is quite useful with regard to fine tuning the material's properties according to individual physical and chemical requirements, especially where the electrical conductance of the material in combination with the ductility, brittleness and the resistance to corrosion are of technical interest.^[136] However, on the molecular level only two species have been reported so far, exhibiting a $[Zn_nCu_b]$ core. On the one hand Fischer *et al.* reported in 2014 on $[(ZnCp^*)_4(Cu(CN^tBu))_4]$ and $[(ZnCp^*)_3(ZnCp)(Cu(CN^tBu))_4]$, at which the $[Zn_4Cu_4]$ unit features a tetrahedral star geometry.^[121] This motif is also found in γ -brass, although the arrangement of an inner zinc tetrahedron being surrounded by an outer copper tetrahedron is inverted with respect to the molecular species. On the other hand, the σ -aromatic trigonal $[Zn_2CuCp^*_3]$ has been prepared most recently.^[119] The compounds are referred to as molecular and embryonic brass, respectively. Especially $[Zn_2CuCp^*_3]$ can be expected to be useful as a building block for the bottom-up synthesis of larger deltahedral clusters as a trigonal M_3 unit is the fundamental feature of such species. In accordance, the liquid injection field desorption ionisation mass spectrometry (LIFDI-MS) spectra of $[Zn_2CuCp^*_3]$ shows larger nuclear species $[Zn_4Cu_3Cp^*_5]^{+}$, $[Zn_4Cu_2Cp^*_6]^{+}$ and $[Zn_3CuCp^*_3]^{+}$, suggesting rich Zn/Cu chemistry for this compound, when the right precursors and reaction conditions are identified.^[119] With regard to the bonding in $[Zn_2CuCp^*_3]$ as side-on coordinated $[Zn_2Cp^*_2] \rightarrow CuCp^*$ species, the straightforward reaction of both species indeed gives the respective product. However, *in situ* formed $CuCp^*$ has to be handled with great care as permanent cooling to $-78\text{ }^\circ\text{C}$ is necessary to prevent decomposition. Herein an alternative route of synthesis for $[Zn_2CuCp^*_3]$ (**7**) is presented employing commercially available $Cu(OAc)$ as a copper source. In addition, the isostructural compounds $[M_7Cp^*_5]$ ($M = Zn$ or Cu) (**8**) and $[(ZnCu_2Cp^*_3)(\mu_3-ZnZnCp^*)_2][BAR_4^F]$ (**9** $[BAR_4^F]$) have been prepared giving a series of atom precise $[Zn_nCu_bCp^*_c]^{n+}$ clusters with different Zn/Cu ratios.

4.3.1 Synthesis of $[\text{Zn}_2\text{CuCp}^*_3]$ (**7**) and $[\text{M}_7\text{Cp}^*_5]$ (**8**)

The treatment of $\text{Cu}(\text{OAc})$ with equimolar amounts of $[\text{Zn}_2\text{Cp}^*_2]$ in benzene at room temperature for three days leads to the formation of a dark red suspension containing a mixture of insoluble $\text{Zn}(\text{OAc})_2$, $[\text{Zn}_2\text{CuCp}^*_3]$ (**7**) and $[\text{M}_7\text{Cp}^*_5]$ (**8**) ($\text{M} = \text{Zn}$ or Cu) (Scheme 18). From the concentrated filtrate, the literature known **7** crystallizes as the main product in the form of yellow fragments at $8\text{ }^\circ\text{C}$ in 57 % isolated yield (based on Cp^*). Further workup of the filtrate gives a mixture of **7** and **8**, co-crystallizing from a concentrated THF solution at $-30\text{ }^\circ\text{C}$ as yellow and dark red fragments, respectively. Crystals of **8** have been manually separated from **7** with the aid of an optical microscope in a glovebox under argon atmosphere. *In situ* ^1H NMR spectroscopy of the reaction mixture indicates a clean formation of **7** under complete consumption of $[\text{Zn}_2\text{Cp}^*_2]$ (Figure 50). As minor by-products $[\text{ZnCp}^*_2]$ and **8** can be identified. Small amounts of additional by-products have not yet been identified. However, an unknown Cp^* containing species is formed *in situ* and is almost completely consumed during the reaction. The reaction involves Cp^* transfer from Zn to Cu giving rise to yet unidentified intermediate Cp^* species. Nonetheless, the naked Zn^{I} sites are not stable without further stabilization and especially not towards strong basic oxygen donors such as OAc^- ,^[69, 87, 90] most likely leading to the disproportionation of Zn^{I} giving Zn^0 and Zn^{II} in the form of $[\text{ZnCp}^*_2]$ and $\text{Zn}(\text{OAc})_2$. When CuCp^* is formed *in situ*, $[\text{Zn}_2\text{Cp}^*_2]$ side on coordinates to the electronically unsaturated fragment to yield **7**.



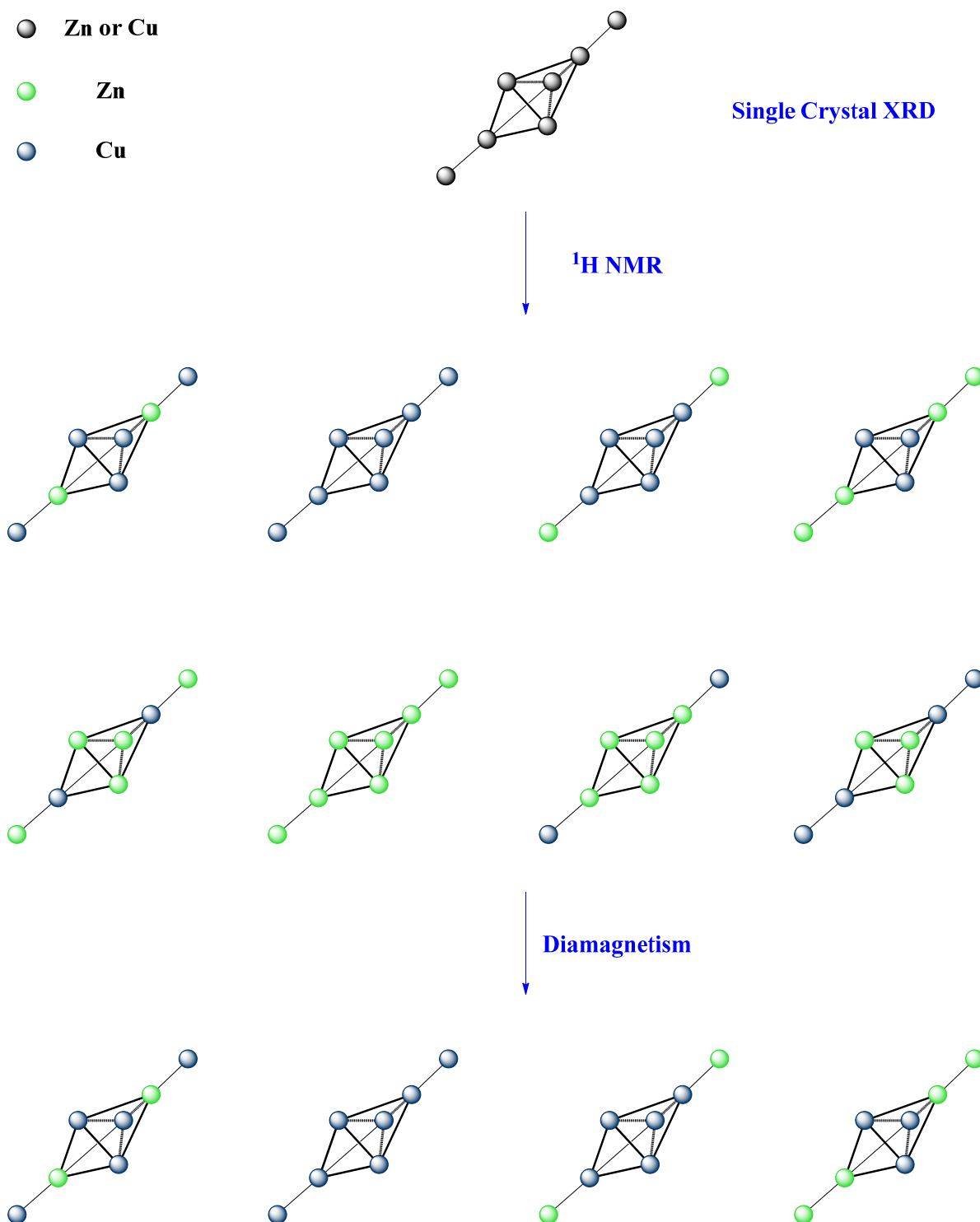
Scheme 18. Synthesis of $[\text{Zn}_2\text{CuCp}^*_3]$ (**7**) and $[\text{M}_7\text{Cp}^*_5]$ ($\text{M} = \text{Zn}$ or Cu) (**8**).

Single crystals of the new compound **8** are stable under an inert gas atmosphere for several months at -30 °C. It is fairly soluble in non-polar solvents like *n*-hexane and benzene, but very soluble in more polar solvents such as toluene, THF or fluorobenzene. However, it readily decomposes at room temperature in solution within few hours under precipitation of metallic particles.

The identity of compound **7** has been confirmed by single crystal XRD measurement as well as NMR spectroscopic analysis. The data is in total agreement with the reported data by Fischer *et al.*

4.3.2 Spectroscopic and Structural Features of $[M_7Cp^*_5]$ (**8**)

The general molecular structure of compound **8** was elucidated by single crystal XRD. However, common single crystal XRD devices using CuK_α or MoK_α irradiation do not allow to distinguish between zinc and copper, since these elements electronically differ by only one electron and therefore exhibit similar scattering properties. The exact assignment of zinc and copper requires more analytical data. Regarding this, the 1H and ^{13}C NMR spectra of compound **8** show two chemically different Cp^* units in a 2:3 ratio indicating D_{3h} symmetry in solution. This limits the number of possible compounds to eight, as the basal MCp^* groups as well as the two apical $MMCp^*$ groups have to be chemically equal. In addition, the sharp resonances in the NMR spectra suggest a diamagnetic species. As a consequence, the number of copper atoms has to be uneven to end up with an even VE count ($Cu \cong 1$, $Zn \cong 2$ and $Cp^* \cong 5 e^-$). Combining these data, leaves four possible structures (Scheme 19). In order to unambiguously determine the structural composition of compound **8**, either AAS (Zn and Cu) or LIFDI-MS measurements are required in order to evaluate the Zn/Cu ratio or the molecular mass, respectively. Unfortunately, the amount of **8**, which can be obtained by crystal picking is very low, making AAS analyses extremely difficult. LIFDI-MS measurement have not been conducted yet. However, in the cases of the two $[Zn_2Cu_5Cp^*_5]$ isomers LIFDI-MS would not distinguish between the two species. In this case additional anomalous scattering, neutron diffraction experiments or quantum chemical calculations would be necessary to clearly assign Zn and Cu to the correct positions in the $MMCp^*$ units.



Scheme 19. Systematic determination of the composition and the assignment of Zn/Cu to the correct position in the molecular structure of **8**. The Cp* rings in the isomer models are omitted for clarity.

The ^1H NMR spectrum of **8** in C_6D_6 at room temperature shows two Cp^* resonances at 2.08 and 2.19 ppm in a 45:30 integral ratio, corresponding to three chemical equivalent Cp^* groups of the trigonal M_3 ring and two equivalent apical Cp^* groups. In accordance the ^{13}C NMR spectrum shows the expected set of signals for two different Cp^* moieties ($\delta = 10.90$ (s, MC_5Me_5), 12.17 (s, MMC_5Me_5), 104.62 (s, MC_5Me_5), 110.18 (s, MMC_5Me_5) ppm).

Compound **8** crystallizes in the monoclinic space group Pn with four distinct molecules in the asymmetric unit. Figure 43 only shows one plot of a crystallographic distinct unit of **8** for clarity. The metal atoms are arranged in a trigonal bipyramidal fashion, at which the apical positions are occupied by MMCp^* units. The $\text{M-Cp}^*_{\text{centr.}}$ bond lengths in the trigonal base range from 1.825-1.831 Å and are shorter than the respective bonds from the terminal $\text{M4-Cp}^*_{\text{centr.}}$ (1.901 Å) and $\text{M7Cp}^*_{\text{centr.}}$ (1.918 Å) units. However, all values are in good agreement to literature known $\text{Zn-Cp}^*_{\text{centr.}}$ (1.83-2.19 Å) and $\text{Cu-Cp}^*_{\text{centr.}}$ (1.82-1.96 Å) bond lengths. The M4-M5 and M6-M7 distances are almost identical with 2.318(2) and 2.319(2) Å, respectively and well comparable with the Zn-Zn distance in **1** (2.317(7) Å). The other M-M distances are distinctively longer with a narrow range of 2.430(2) (M1-M3)-2.462(2) Å (M1-M6), which is similar to the Cu-Cu distance in $[(\text{ZnCp}^*)_4(\text{Cu}(\text{CN}^t\text{Bu}))_4]$ (2.471(4) Å)^[121] (Figure 24) and the average Zn-Zn distance in $[\text{Zn}_3\text{Cp}^*_3]^+$ (2.430 Å).^[119] As a result, the trigonal bipyramid consists of two almost perfect tetrahedrons sharing one trigonal face (Figure 43). In accordance the M-M-M angles of the trigonal faces are all close to 60° (59.38° (M6-M1-M2)- 60.83° (M1-M3-M6)). The $\text{M5-M4-Cp}^*_{\text{centr.}}$ and $\text{M6-M7-Cp}^*_{\text{centr.}}$ units deviate slightly from linearity with angles of 175.41° and 175.85° , respectively.

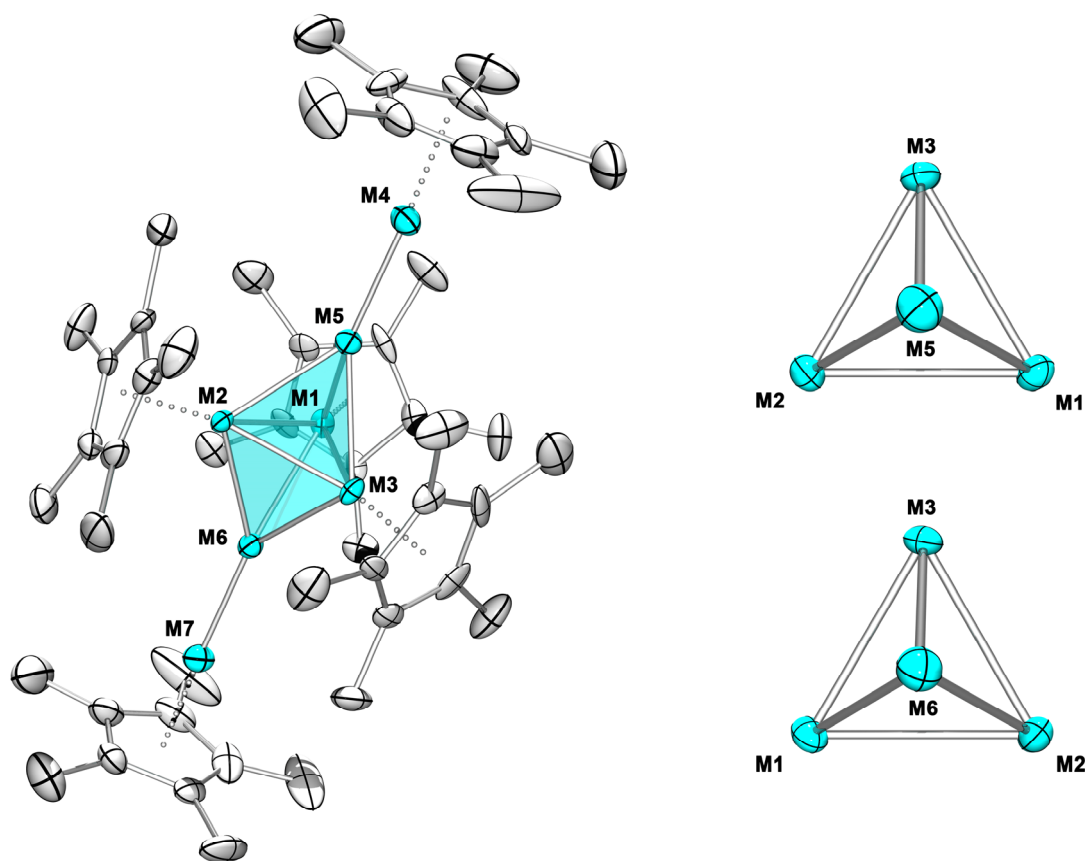
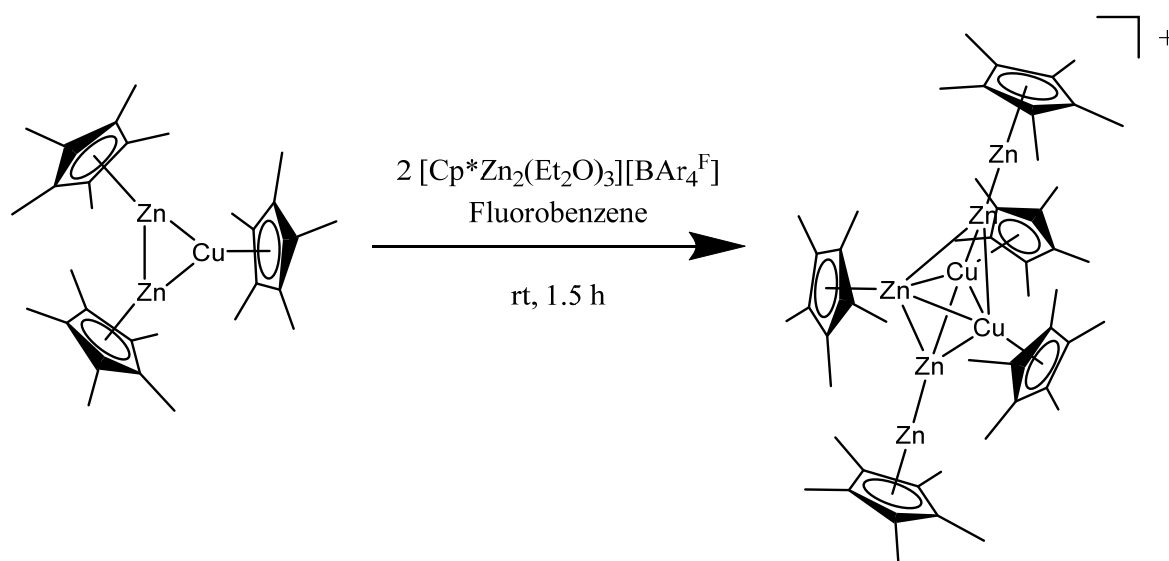


Figure 43. Molecular structure of $[M_7Cp^*_5]$ ($M = Zn$ or Cu) (**8**) (left). The trigonal bipyramid is highlighted. Orthogonal view on the $M1, M2, M3$ plane showing the $M1, M2, M3, M5$ tetrahedron (right, top). Orthogonal view on the $M1, M2, M3$ plane showing the $M1, M2, M3, M6$ tetrahedron (right, bottom). Displacement ellipsoids are shown at the 50% probability level and the hydrogen atoms are omitted for clarity. Selected interatomic distances [\AA] and angles [$^\circ$]: $M4-M5 = 2.318(2)$, $M7-M6 = 2.319(2)$, $M3-M2 = 2.440(2)$, $M1-M2 = 2.447(2)$, $M1-M3 = 2.430(2)$, $M1-Cp^*_{\text{centr.}} = 1.831$, $M2-Cp^*_{\text{centr.}} = 1.825$; $M3-Cp^*_{\text{centr.}} = 1.831$; $M4-Cp^*_{\text{centr.}} = 1.901$; $M7-Cp^*_{\text{centr.}} = 1.918$; $M1-M2-M3 = 59.65(5)$, $M1-M3-M2 = 60.32(5)$, $M5-M4-Cp^*_{\text{centr.}} = 175.41$, $M6-M7-Cp^*_{\text{centr.}} = 175.85$.

4.3.3 Synthesis of $[Zn_5Cu_2Cp^*_5][BAR_4^F]$ (**9** $[BAR_4^F]$)

According to LIFDI-MS studies of **7** a rich Zn/Cu bottom-up chemistry can be expected using this compound as a starting material. Therefore **7** was reacted with $[Cp^*Zn_2(Et_2O)_3][BAR_4^F]$ as a building block for zinc rich clusters. The treatment of **7** with two equivalents of $[Cp^*Zn_2(Et_2O)_3][BAR_4^F]$ in fluorobenzene at room temperature for 1.5 h gives a dark red solution with minimal amount of metallic precipitate (Scheme 20). Dark red needle shape crystals of $[Zn_5Cu_2Cp^*_5][BAR_4^F] \cdot 5 C_6H_5F$ (**9** $[BAR_4^F] \cdot 5 C_6H_5F$) suitable for single crystal XRD have been obtained from the concentrated filtered reaction solution at -30 $^\circ\text{C}$. Minor

impurities in the form of an unidentified $[\text{Cp}^*\text{M}][\text{BAr}_4^{\text{F}}]$ species have been removed by repeated recrystallization of the crude product in fluorobenzene at $-30\text{ }^\circ\text{C}$ giving $\mathbf{9}[\text{BAr}_4^{\text{F}}]$ in 23 % isolated yield (based in Cu). The reaction proceeds *via* Cp* exchange between zinc and copper. This is in accordance to the reactivity studies of $[\text{Cp}^*\text{Zn}_2(\text{THF})_3]^+$ (**1**) towards *n*-hexane, which have shown that the cation can act as a Cp* donor as well as Cp* acceptor by forming $[\text{Zn}_2\text{Cp}^*_2]$ and $[\text{Zn}_2(\text{THF})_6]^{2+}$ (**2**). In addition, it is assumed that rapid Me/Cp* exchange is feasible between $[\text{Cp}^*\text{Zn}_2]^+$ and ZnMe_2 .^[137] Likewise, the addition of $[\text{Cp}^*\text{Zn}_2(\text{Et}_2\text{O})_3]^+$ to **7** induces rapid Cp* exchange between the metal atoms, which is indicated by a broad Cp* coalescence peak in *in situ* ^1H NMR studies of the reaction mixture at room temperature (Figure 51). This peak slowly decoalesces with lower temperatures into two peaks, at which the separation of the resonances is not completed even at $-50\text{ }^\circ\text{C}$. During the reaction Zn-Cu and Zn-Zn bonds are cleaved and new Zn-Zn, Cu-Zn and Cu-Cu bonds are formed. However, the detailed reaction mechanism as well as reaction by-products have not yet been elucidated.



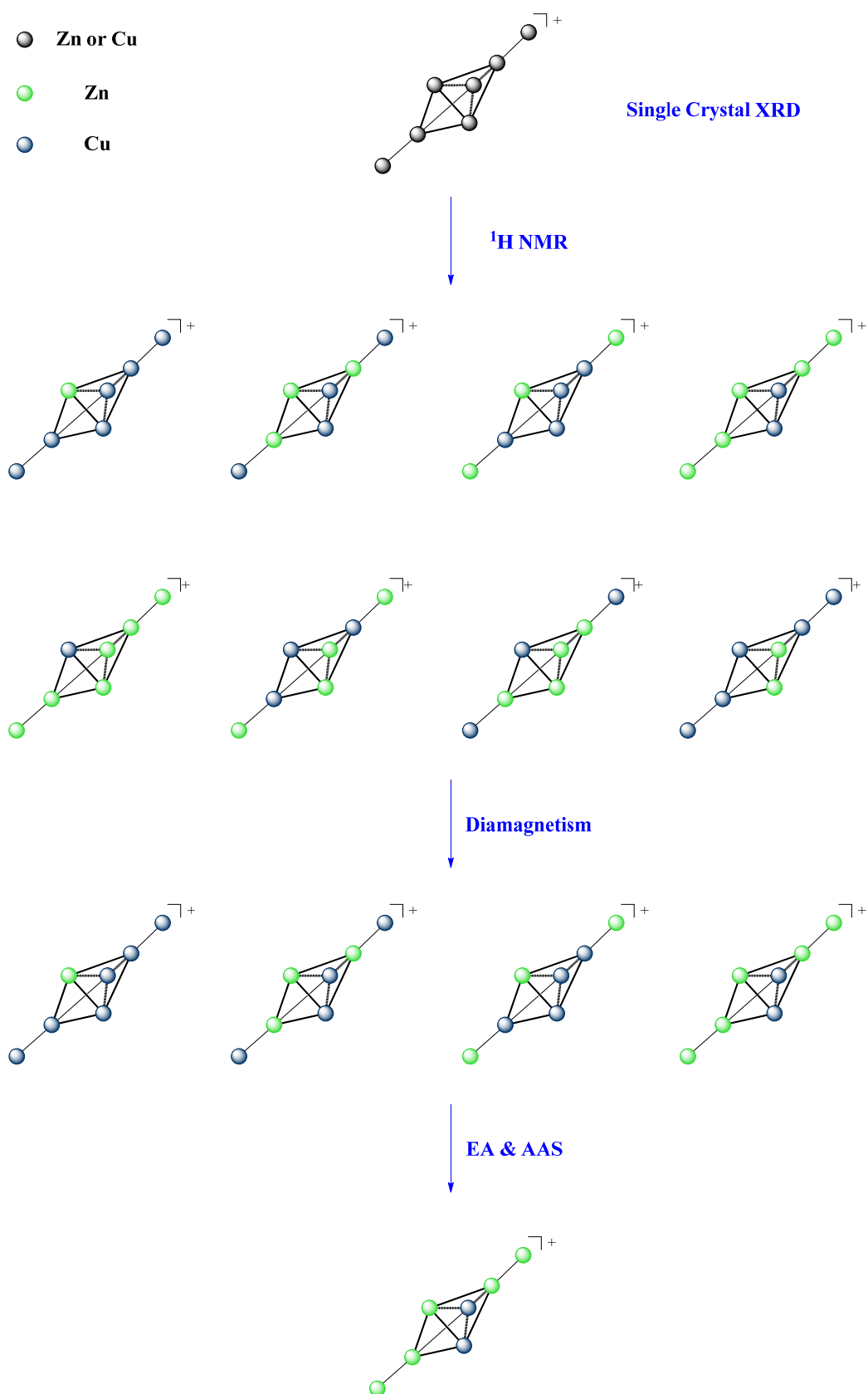
Scheme 20. Synthesis of $[\text{Zn}_5\text{Cu}_2\text{Cp}^*_5][\text{BAr}_4^{\text{F}}]$ ($\mathbf{9}[\text{BAr}_4^{\text{F}}]$).

Compound $\mathbf{9}[\text{BAr}_4^{\text{F}}]$ is stable at $-30\text{ }^\circ\text{C}$ in an argon atmosphere as a microcrystalline powder. It is soluble in fluorobenzene and CH_2Cl_2 , but rapidly decomposes in CH_2Cl_2 at room temperature within few minutes under precipitation of metal. Furthermore, it is highly labile towards THF and even *n*-hexane, giving yet unidentified decomposition products.

4.3.4 Spectroscopic and structural features of $[\text{Zn}_5\text{Cu}_2\text{Cp}^*_5][\text{BAr}_4^{\text{F}}]$ ($\mathbf{9}[\text{BAr}_4^{\text{F}}]$)

In an analogous way to compound **8** the general molecular structure of compound $\mathbf{9}[\text{BAr}_4^{\text{F}}]$ was elucidated by single crystal XRD. The exact assignments of zinc and copper to the metal positions was elucidated by ^1H NMR and AAS analysis (Scheme 21). Regarding this, the ^1H NMR spectra of $\mathbf{9}[\text{BAr}_4^{\text{F}}]$ suggests a diamagnetic species, which exhibits three chemically different Cp^* moieties in a 2:1:2 ratio indicating C_{2v} symmetry in solution. For this symmetry one of the basal MCp^* group have to differ from the other two equal basal MCp^* groups and the apical MMCp^* groups have to be equal as well. Moreover, the number of copper atoms has to be even in order to give a diamagnetic compound. According to the AAS analysis (Zn an Cu) the compound exhibits a Zn:Cu ratio of 5:2. In conclusion the NMR and AAS data unambiguously point to the fact, that $\mathbf{9}[\text{BAr}_4^{\text{F}}]$ corresponds to $[(\text{ZnCu}_2\text{Cp}^*_3)(\mu_3\text{-ZnZnCp}^*)_2][\text{BAr}_4^{\text{F}}]$.

The molecular composition of $\mathbf{9}[\text{BAr}_4^{\text{F}}]$ as determined by EA (C, H) and AAS (Zn, Cu, B, F) is in good agreement with the given sum formula (calculated for $\text{H}_{87}\text{BC}_{82}\text{F}_{24}\text{Cu}_2\text{Zn}_5$ [%]: H 4.40, B 0.54, C 49.41, F 22.87, Cu 6.38, Zn 16.40; found: H 4.62, B 0.47, C 51.48, F 20.20, Cu 6.48, Zn 15.98. Slight deviations in the carbon and fluorine values can be ascribed to the thermal instability of the compound. The ^1H NMR spectrum of $\mathbf{9}[\text{BAr}_4^{\text{F}}]$ in CD_2Cl_2 at room temperature shows three resonances at 1.96 (s, 30, $\text{ZnZnC}_5\text{Me}_5$), 2.04 (s, 15H, ZnC_5Me_5) and 2.12 (s, 30 H, CuC_5Me_5) ppm for the three chemically non-equivalent Cp^* groups in a 2:1:2 ratio as well as the expected set of signals for the $[\text{BAr}_4^{\text{F}}]^-$ anion (7.56 (s, 4H) and 7.72 ppm (s, 8H). Due to the high lability of $\mathbf{9}[\text{BAr}_4^{\text{F}}]$ in solution and the moderate solubility of $\mathbf{9}[\text{BAr}_4^{\text{F}}]$ at low temperatures no ^{13}C NMR spectrum has been recorded. The IR spectrum of $\mathbf{9}[\text{BAr}_4^{\text{F}}]$ reveals typical absorption bands for the Cp^* moieties at 2905 and 2860 cm^{-1} and the C-F vibration of the $[\text{BAr}_4^{\text{F}}]^-$ anion at 1272 cm^{-1} .



Scheme 21. Systematic determination of the composition and the assignment of Zn/Cu to the correct position in the molecular structure of **9**. The Cp* rings in the isomer models are omitted for clarity.

Single crystals of $9[\text{BAR}_4^{\text{F}}] \cdot 5 \text{C}_6\text{H}_5\text{F}$ manifest in the monoclinic space group Cc with two distinct ion pairs in the asymmetric unit. Only one plot of the molecular structure of **9** is shown in Figure 44 for clarity. The cation **9** is isostructural to **8** featuring a trigonal bipyramidal metal core, at which the triangle consists of a $[\text{Cu}_2\text{Zn}]$ unit capped by a ZnZnCp^* unit on each side. The Zn1-Zn2 (2.299(6) Å) and Zn4-Zn5 (2.323(6) Å) bond lengths are comparable to the respective M4-M5 (2.318(2) Å) and M6-M7 (2.319(2) Å) distances in **8**. The Cu1-Cu2 bond length of 2.415(3) Å is shorter than the Cu-Cu value in $[(\text{ZnCp}^*)_4(\text{Cu}(\text{CN}^t\text{Bu}))_4]$ (2.471(4) Å).^[121] The trigonal base consists of an almost equilateral triangle (Cu1-Cu2 = 2.415(3), Cu1-Zn3 = 2.400(4), Cu2-Zn3 = 2.396(3) Å). The centers of the bipyramidal apices are distorted towards the Cu1-Cu2 edge with regard to the Zn3, Cu1, Cu2 plane as the Zn3-Zn2 (2.745(6) Å) and Zn3-Zn4 (2.688(7) Å) edges are elongated compared to the $\text{Cu}_{\text{triangle}}\text{-Zn2}$ (avg. 2.463 Å) and $\text{Cu}_{\text{triangle}}\text{-Zn4}$ (avg. 2.487 Å) edges (Figure 44). This distortion might be a result of the hetero metallic basal triangle of the bipyramid as it is not observed for the isostructural compound **8**, which exhibits a homo metallic basal triangle. In contrast to compound **8** the bipyramid in **9** does not feature more or less equally long edges. Instead the bipyramid is elongated in apical direction (average $\text{M}_{\text{triangle}}\text{-Zn2}$ = 2.557, average $\text{M}_{\text{triangle}}\text{-Zn4}$ = 2.554 Å) with clinched M-M-M angles at the apices (avg. 56.1 ° at Zn4 and 55.9 ° at Zn2).

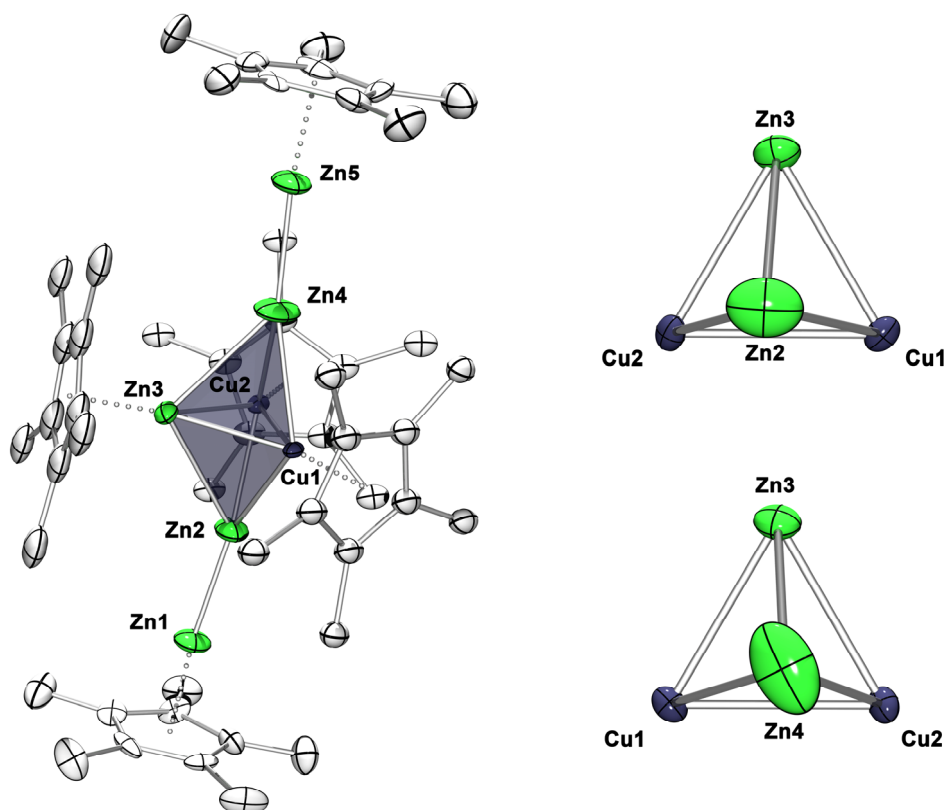


Figure 44. Molecular structure of $[\text{Zn}_5\text{Cu}_2\text{Cp}^*_5]^+$ (**9**) in the crystals of $9[\text{BAR}_4^{\text{F}}] \cdot 5 \text{C}_6\text{H}_5\text{F}$ (left). The distorted trigonal bipyramid is highlighted. Orthogonal view on the Cu1, Cu2, Zn3 plane showing the distorted Cu1, Cu2, Zn2, Zn3 tetrahedron (right, top). Orthogonal view on the Cu1, Cu2, Zn3 plane showing the distorted Cu1, Cu2, Zn2, Zn4 tetrahedron (right, bottom). Displacement ellipsoids are shown at the 50 % probability level and disorder and the hydrogen atoms are omitted for clarity. Selected interatomic distances [\AA] and angles [$^\circ$]: Zn1-Zn2 = 2.299(6), Zn4-Zn5 = 2.323(6), Cu1-Cu2 = 2.415(3), Cu1-Zn3 = 2.400(4), Zn3-Zn4 = 2.688(7), Cu1-Zn4 = 2.527(6), Cu2-Zn4 = 2.446(6); Cu1-Zn3-Cu2 = 60.47(9), Cu2-Cu1-Zn3 = 59.68(9), Zn3-Cu2-Cu1 = 59.85(10).

4.3.5 Theoretical investigations on $[\text{Zn}_5\text{Cu}_2\text{Cp}^*_5]^+$ (**9**)⁴

The following quantum chemical calculations have been conducted by J. Hornung. In order to get more insight into the bonding situation of **9**, DFT calculations have been conducted at the BP86/TZVPP level of theory. The optimized structure of **9** is in good agreement with the experimental molecular structure obtained by single crystal XRD, when the bond distances and angles are compared (Table 7). Also the distortion of the bipyramid's apices towards the Cu1-Cu2 edges is well represented in the calculated structure with average $\text{Cu}_{\text{triangle}}\text{-Zn}_2$ and

⁴ Quantum chemical analysis of the compound $[\text{Zn}_5\text{Cu}_2\text{Cp}^*_5]^+$ (**9**) has been conducted by J. Hornung and is part of his PhD studies.

Cu_{triangle}-Zn₄ interaction lengths of 2.440 (exp. 2.463) and 2.447 (exp. 2.487) Å, respectively and Zn₃-Zn₂ and Zn₃-Zn₄ distances of 2.695 (exp. 2.745(6)) and 2.660 (exp. 2.688(7)) Å.

The Laplacian distribution of **9** in the Cu1-Cu2-Zn3 plane shows bond paths between all the three metal atoms in the equatorial plane as well as a ring critical point in the centre of the triangle (Figure 45).

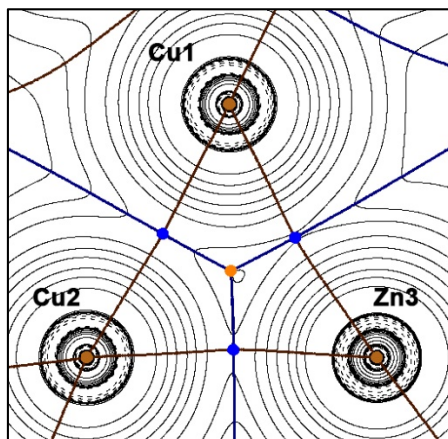


Figure 45. Molecular graph and contour map of the Laplacian $\nabla^2\rho(r)$ of **9** in the molecular plane which contains Cu1, Cu2 and Zn3. The solid lines between the atomic nuclei are bond paths. The solid blue lines show areas of charge concentration ($\nabla^2\rho(r) < 0$) and the thin black lines show areas of charge depletion ($\nabla^2\rho(r) > 0$). The thick solid lines separating the atomic basins indicate zero-flux surfaces intercepting the molecular plane. Critical points are indicated as coloured dots (blue = bond, orange = ring).

This result is in accordance to the ELF density plotted for the Cu1-Cu2-Zn3 plane, at which larger electron localization densities are found between the metal atoms and the centre of the triangle. As expected larger electron localization densities are also found between the apical Zn-Zn atoms indicating an intact Zn-Zn bond as shown by the ELF density in the Zn₃-Zn₄-Zn₅ plane. This electron density distribution is very well comparable to the distribution found for the [Zn₃] triangles and the terminal Zn-ZnCp* moiety in the Zn₂-Zn₉-Zn₅ plane of **4'** (Figure 41).

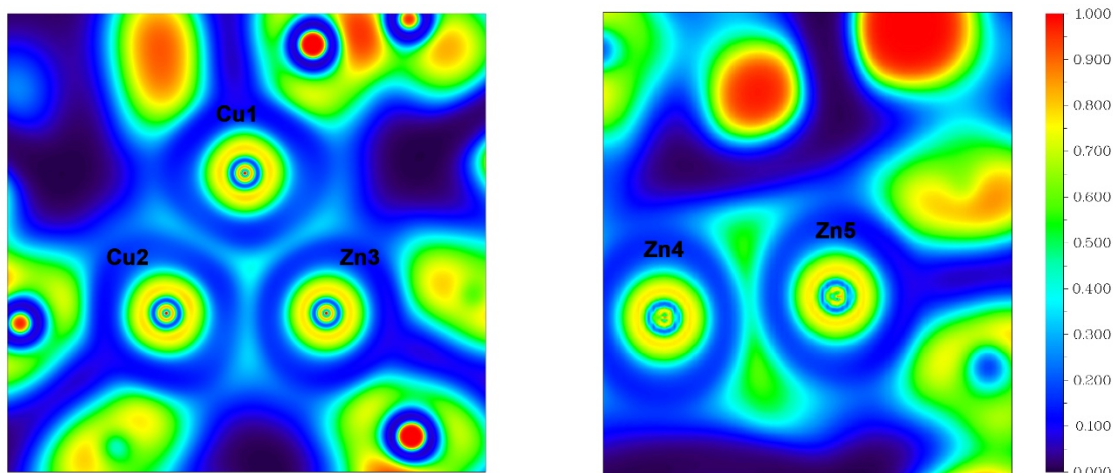
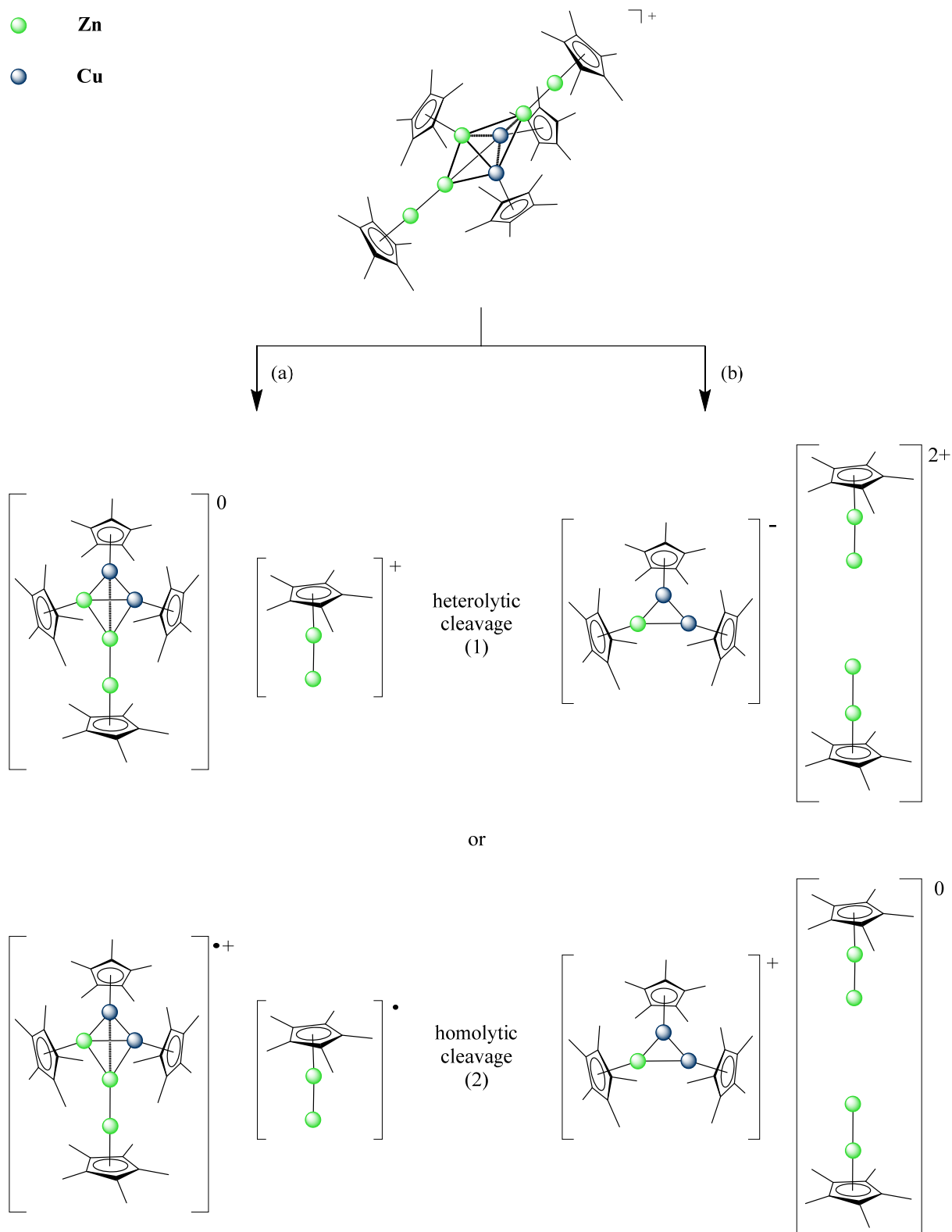


Figure 46. ELF color density plot of a slice through the Cu1–Cu2–Zn3 plane (left) and the Zn3–Zn4–Zn5 plane (right) in the cation **9**.

Note, the isolobal analogy of $[\text{ZnCu}_2\text{Cp}^*_3]^-$ to the known σ -aromatic $2 e^-$ $[\text{Zn}_2\text{CuCp}^*_3]$ and $[\text{Zn}_3\text{Cp}^*_3]^+$ species. Therefore cation **9** can be conceptionally constructed from a σ -aromatic $2 e^-$ $[\text{ZnCu}_2\text{Cp}^*_3]^-$ trigonal ring, which is capped by two $[\text{ZnZnCp}^*]^+$ units. As to that, energy decomposition analysis (EDA) on **9** has been performed. The following fragmentations are feasible (Scheme 22):

- a1) the heterolytic splitting giving one $[\text{ZnZnCp}^*]^+$ and one $[(\mu_3\text{-ZnZnCp}^*)(\text{ZnCu}_2\text{Cp}^*_3)]$ moiety,
- a2) the homolytic splitting giving one $[\mu_3\text{-ZnZnCp}^*]^*$ and one $[(\mu_3\text{-ZnZnCp}^*)(\text{ZnCu}_2\text{Cp}^*_3)]^{*+}$ moiety,
- b1) the heterolytic splitting giving two $[\text{ZnZnCp}^*]^+$ units interacting as a combined $[(\text{ZnZnCp}^*)_2]^{2+}$ fragment with $[\text{ZnCu}_2\text{Cp}^*_3]^-$,
- b2) the homolytic splitting giving two $[\text{ZnZnCp}^*]^*$ units interacting as a combined $[(\text{ZnZnCp}^*)_2]^0$ fragment with $[\text{ZnCu}_2\text{Cp}^*_3]^+$.



Scheme 22. Possible fragmentation patterns for the EDA of **9**.

The numerical results for the heterolytic fragmentation a1) are shown in Table 2. The intrinsic bonding interactions ΔE_{int} are quite strong with -96.93 kcal/mol. The major contribution to the total orbital bonding interactions $\Delta E_{\text{orb}} = -104.99$ kcal/mol is attributed to the σ -donation of $[(\mu_3\text{-ZnZnCp}^*)(\text{ZnCu}_2\text{Cp}^*_3)] \rightarrow [\text{ZnZnCp}^*]^+$ (Figure 47). At this the electron density mainly originates from the Zn in the $[\text{Cu}_2\text{Zn}]$ triangle.

When **9** is fragmented homolytically instead (a2) to give $[(\mu_3\text{-ZnZnCp}^*(\text{ZnCu}_2\text{Cp}^*_3))]^{2+}$ and $[\mu_3\text{-ZnZnCp}^*]^-$ the total orbital bonding interactions $\Delta E_{\text{int}} = 192.46$ kcal/mol increases significantly (Table 3) compared to the heterolytic fragmentation a1) (-104.99 kcal/mol) indicating, that the fragmentation a1) is energetically favoured. This means, that a1) with two diamagnetic fragments interacting with each other is the better model to describe the bonding situation in **9** as the combination of the fragments efforts less energy for the relaxation than in a2).

In contrast, the heterolytic fragmentation of **9** in the form of b1) giving two $[\text{ZnZnCp}^*]^+$ units interacting as a combined $[(\text{ZnZnCp}^*)_2]^{2+}$ fragment with $[\text{ZnCu}_2\text{Cp}^*_3]^-$ does not lead to reasonable energy values (Table 3). The numerical values are extremely high with $\Delta E_{\text{int}} = -538.96$ kcal/mol or $\Delta E_{\text{orb}} = -558.53$ kcal/mol. These values describe the interaction of two $[\text{ZnZnCp}^*]^+$ fragments as an entity with $[\text{ZnCu}_2\text{Cp}^*_3]^-$ and should consequently be divided in half for comparison with a1) and a2). Nevertheless, this gives values of $\Delta E_{\text{int}} = -269.48$ kcal/mol and $\Delta E_{\text{orb}} = -279.27$ kcal/mol for the interaction of one $[\text{ZnZnCp}^*]^+$ with $[\text{ZnCu}_2\text{Cp}^*_3]^-$, which is still significantly higher than the calculated values for a1) and a2). The analog EDA for the homolytic fragmentation b2) has not been conducted yet.

Table 2. EDA-NOCV results for $[\text{Zn}_5\text{Cu}_2\text{Cp}^*_5]^+$ (**9**) at BP86/TZVPP upon homolytic fragmentation giving the interacting fragments $[(\mu_3\text{-ZnZnCp}^*)(\text{ZnCu}_2\text{Cp}^*_3)]$ and $[\mu_3\text{-ZnZnCp}^*]^+$.

$[(\mu_3\text{-ZnZnCp}^*)(\text{ZnCu}_2\text{Cp}^*_3)] \leftrightarrow [\mu_3\text{-ZnZnCp}^*]^+$	
	[kcal/mol]
ΔE_{int}	-96.93
ΔE_{Pauli}	149.29
ΔE_{elstat}	-109.66 (51.09 %)
ΔE_{orb}	-104.99 (48.91 %)
$\Delta E_{\text{orb}, \sigma}$	-54 (51.4 %)
$\Delta E_{\text{orb}, \pi}$	-12 (11.4 %)
$\Delta E_{\text{orb}, \sigma \text{ back}}$	-10 (9.5 %)
$\Delta E_{\text{orb}, \text{rest}}$	-28.99 (27.6 %)

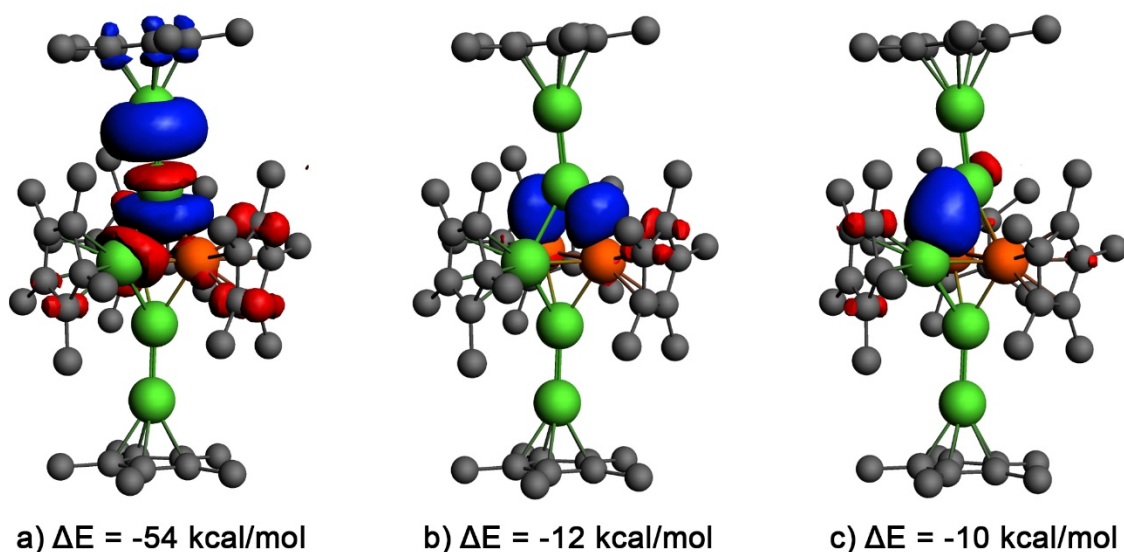
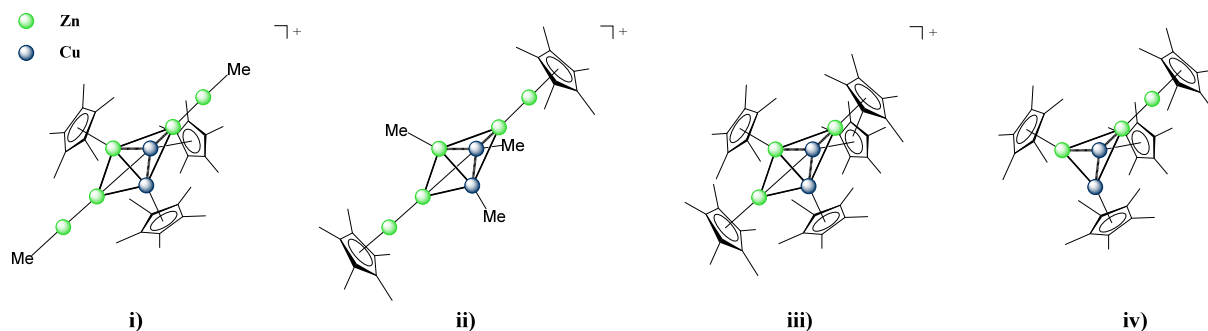


Figure 47. Deformation densities $\delta\rho$ which are associated with pair-wise orbital interactions in $[\text{Zn}_5\text{Cu}_2\text{Cp}^*_5]^+$ (**9**). a) $[(\text{Cu}_2\text{ZnCp}^*_3)(\mu_3\text{-ZnZnCp}^*)] \rightarrow [\text{Cp}^*\text{Zn}_2]^+$ σ -donation, b) $[(\text{Cu}_2\text{ZnCp}^*_3)(\mu_3\text{-ZnZnCp}^*)] \rightarrow [\text{Cp}^*\text{Zn}_2]^+$ π -donation, c) $[\text{Cp}^*\text{Zn}_2]^+ \rightarrow [(\text{Cu}_2\text{ZnCp}^*_3)(\mu_3\text{-ZnZnCp}^*)]$ σ back-donation. The direction of the charge flow is from red to blue.

Table 3. EDA-NOCV results for $[\text{Zn}_5\text{Cu}_2\text{Cp}^*_5]^+$ (**9**) at BP86/TZVPP upon homolytic fragmentation giving the interacting fragments $[(\mu_3\text{-ZnZnCp}^*)(\text{ZnCu}_2\text{Cp}^*_3)]^{+\cdot}$ and $[\mu_3\text{-ZnZnCp}^*]^\cdot$ as well as upon heterolytic fragmentation giving the interacting fragments $[(\mu_3\text{-ZnZnCp}^*)(\mu_3\text{-ZnZnCp}^*)]^{2+\cdot}$ and $[\text{ZnCu}_2\text{Cp}^*_3]^\cdot$.

	$[(\mu_3\text{-ZnZnCp}^*)(\text{ZnCu}_2\text{Cp}^*_3)]^{+\cdot} \leftrightarrow$	$[(\mu_3\text{-ZnZnCp}^*)(\mu_3\text{-ZnZnCp}^*)]^{2+\cdot} \leftrightarrow$
	$[\mu_3\text{-ZnZnCp}^*]^\cdot$	$[\text{ZnCu}_2\text{Cp}^*_3]^\cdot$
	[kcal/mol]	[kcal/mol]
ΔE_{int}	-90.55	-538.96
ΔE_{Pauli}	328.72	560.73
ΔE_{elstat}	-195.24 (50.36 %)	-483.42 (46.4 %)
ΔE_{orb}	-192.46 (48.91 %)	-558.53 (53.6 %)

With regard to the synthetic accessibility of kinetically labile organometallic compounds, bulky ligands are often essential for their stabilisation and therefore isolation in the laboratory. However, these boundaries are less pronounced with respect to quantum chemical calculations, which allow to elucidate the general thermodynamic stability of a compound in the gas phase. More insight into the influence of the Cp* ligands on the stability of **9** can be obtained by means of quantum chemical methods. On the one hand dispersion forces between Cp* ligands can contribute to a great extent to the stability of a compound. On the other hand, the stability can also be influenced by the donor properties of a ligand such as the π -donor or σ -donor character. In order to investigate the impact of such effects, the apical or the basal Cp* groups of **9** can be formally substituted by methyl groups (Scheme 23, i) and ii)). Furthermore, it is feasible to replace the one electron ZnZnCp* ligand by a one electron ZnCp* unit (iii)). Eventually, it is highly interesting whether the formal removal of one apical ZnZnCp* unit would give a stable tetrahedral species (iv)).



Scheme 23. Related compounds to **9**, which can be evaluated by quantum mechanical methods.

Compound **9** can also be evaluated in the background of classical cluster concepts. However, cluster **9** exhibits six effective valence electrons ($5 \times \text{Zn} + 2 \times \text{Cu} + 5 \times \text{Cp}^* + 1 \times \text{positive charge} = 5 \times 2 + 2 \times 1 + 5 \times (-1) + 1 \times (-1) = 6$), which is not a magic number according to the jellium model.^[132, 138] When the Wade-Mingos electron rule is considered a total number of 6 SEPs is necessary for a closed shell regular trigonal bipyramid. For this purpose, **9** can be fragmented in order to easily derive the number SEP. The $[\text{Zn}_5\text{Cu}_2]$ trigonal bipyramid consists of two axial $\mu_3\text{-ZnZnCp}^*$ units, one basal ZnCp^* and two basal CuCp^* moieties. Each ZnZnCp^* and ZnCp^* unit provides one electron, whereas no electrons are provided from a CuCp^* unit. Considering the positive charge of the cluster one is left with only one SEP for all M-M interactions in the bipyramidal metal framework. Thus, compound **9** is extremely hypoelectronic with regard to the Wade-Mingos rule. However, similar to the clusters $[\text{Zn}_{10}\text{Cp}^*_6\text{Me}]^+$ (**4**) and $[\text{Zn}_9\text{Cp}^*_6]$ (**5**), it has to be noted, that the Wade-Mingos rule is only applicable to fragments exhibiting one σ -type and two π -type frontier orbitals.^[131, 132] This is not the case for the basal ZnCp^* and CuCp^* units in **9** as the π -type orbitals are already in use for the M-Cp* interaction. But, when assuming the one SEP of **9** to be mainly associated to the M-M bonding in the $[\text{ZnCu}_2]$ trigonal base, the situation is well in accordance to the formal concept with a $2 e^- [\text{ZnCu}_2\text{Cp}^*_3]^-$ sigma aromatic ring, at which electron accepting $[\text{ZnZnCp}^*]^+$ fragments coordinate from both sites. A similar coordination situation is known from the inverted sandwich complex $[\text{Ga}_2\text{Cp}^*]^+$ with a pentagonal bipyramidal double cone structure. Instead of a $2 e^-$ σ -aromatic metallo ring, there is a $6 e^-$ π -aromatic organic ring to which the electron accepting Ga^+ ion coordinates. The aromatic ring system acts as a bridging ligand in an electron deficient compound with multicentre bonds.

As cluster geometries are often strongly related to their electronic structure, it can be assumed that compound **8** exhibits the same electronic architecture as the isostructural cation **9**. A different electronic configuration often goes along with a strong distortion of the compounds geometry.^[46] This is nicely described by Khanna *et al.* for $[Al_{11}Mg_2]^-$: “A vivid example of the relationship between electronic and geometric structure is that geometrical distortions can lead to the splitting of electronic shells into subshells with a large HOMO-LUMO gap [...]. Unlike atoms, a cluster with a partially filled subshell can stabilize itself either by having a high spin multiplicity (Hund’s rule) or by undergoing a Jahn-Teller distortion to form a singlet state with a gap within a subshell. [...] $Al_{11}Mg_2^-$ would require 40 valence electrons for a filled electronic shell. The cluster has 38 valence electrons so it may form an icosahedral structure with a triplet multiplicity or undergo an oblate distortion. The oblate structure is 0.003 eV more stable than the pseudoicosahedral triplet structure.”^[139] As to that, the easiest way to retain the electronic situation from **9** when going from a cationic to a isostructural neutral compound like **8**, is to exchange one $[ZnCp^*]^+$ fragment by an isoelectronic $[CuCp^*]$ fragment giving $[Zn_4Cu_3Cp^*_5]$. From the four possibilities left after elucidation of the analytical data of **8** (Scheme 19), the only compound, which fits to this composition is $[(\mu_3-ZnZnCp^*)_2(Cu_3Cp^*_3)]$. This means, that formally one basal $[ZnCp^*]^+$ fragment in cation **9** is substituted by one $[CuCp^*]$ fragment to give **8**. An example for such formal substitution are the isoelectronic and isostructural compounds $[Zn_3Cp^*_3]^+$ and $[Zn_2CuCp^*_3]$. However, the unambiguously correct metal composition of **8**, still has to be determined by AAS or mass spectroscopic methods.

4.3.6 Summary

In summary, a novel synthetic pathway to access $[Zn_2CuCp^*_3]$ (**7**) using a commercially available copper source has been reported. In addition, the novel isostructural clusters $[M_7Cp^*_5]$ ($M = Zn$ or Cu) (**8**) and $[Zn_5Cu_2Cp^*_5]^+$ (**9**) have been synthesized, giving a series of unique $[Zn_aCu_bCp^*_c]^{n+}$ compounds with different Zn/Cu ratio and Cp* content. However, the concrete structural composition of **8** is still to be determined by LIFDI-MS. In accordance to the studies of $[Zn_3Cp^*_3]^+$ and $[Zn_2CuCp^*]$, these results demonstrate the feasibility to exchange Zn and Cu on a molecular level, while keeping the structural constitution. Compound **9** is electron deficient with regard to the Wade-Mingos rule as the basal MCp^* units lack π -type frontier orbitals, but EDA analysis shows, that the cationic cluster can also be regarded as a coordination compound,

with $[(\mu_3\text{-Zn}_2\text{Cp}^*)(\text{Cu}_2\text{ZnCp}^*_3)] \rightarrow [\text{Zn}_2\text{Cp}^*]^+$. In all reactions Cp* transfer between Cu and Zn was observed as a fundamental step in cluster growth, at which open coordination sites like in $[\text{Cp}^*\text{Zn}_2]^+$ facilitate this process. From this perspective it can be expected that **9** can be employed as a precursor for larger intermetallic Hume-Rothery-type clusters. Furthermore, as $[\text{Zn}_2\text{CuCp}^*_3]$ is in principle a σ -aromatic compound, reactions of $[\text{Zn}_2\text{CuCp}^*_3]$ with $[\text{ML}_x]$ (M = metal, L = ligand) fragments exhibiting not fully occupied sigma type frontier orbitals potentially give novel intermetallic cluster building blocks. Compounds such as Cu(OTf) or Ag(OTf) are ideal examples for this purpose.

5 OUTLOOK

The main focus of this work was the synthesis and evaluation of novel low oxidation state zinc compounds, targeting their subsequent use as building blocks for the bottom up preparation of novel Hume-Rothery-type atom precise intermetallic clusters. All the reported compounds of this work eventually originate from Carmona's reagent $[\text{Zn}_2\text{Cp}^*_2]$ as a zinc source. The challenge was to explore the limits of manipulating and fine tuning this versatile species in order to obtain a library of tailor designed low valent zinc sources. The partially deprotection of $[\text{Zn}_2\text{Cp}^*_2]$ by oxidative Zn-Cp* bond cleavage leads to highly reactive and labile cationic low valent zinc species, whose reactivity can be tuned by stabilizing the open coordination sites with appropriate solvent ligands L. Regarding this, isonitriles exhibit a great affinity to Zn^{I} centres as in the cation $[\text{Zn}_2(\text{CNPh})_6]^+$ (**3**). Recent theoretical studies by Alvarez *et al.* have demonstrated the general stability of molecular Zn=Zn double bond species in the form of $[\text{L}_2\text{Zn}=\text{ZnL}_2]$ (L = CO, NHC, CNMe).^[140] Thus, compound **3** seems to be predestined to be an appropriate starting material to achieve Zn^0 species upon reduction with a suitable reducing agent. Apart from that, the highly reactive cationic zinc species $[\text{Cp}^*\text{Zn}_2(\text{Et}_2\text{O})_3]^+$ ^[103] or $[\text{Zn}_2(\text{THF})_6]^{2+}$ (**2**) have already demonstrated their great potential as building blocks for intermetallic clusters. The cations $[\text{Cp}^*\text{Zn}_2(\text{Et}_2\text{O})_3]^+$ and **2** have been successfully employed to prepare the intermetallic $[\text{Ga}_2\text{Zn}_4\text{Cp}^*_6]^{2+}$ species.^[107, 108] Moreover $[\text{Cp}^*\text{Zn}_2(\text{Et}_2\text{O})_3]^+$ was used to prepare $[\text{Zn}_5\text{Cu}_2\text{Cp}^*_5]^+$ (**9**). In all cases Zn/M Cp* exchange is essential in the process of the formation of the novel compounds. The virtually naked Zn^{I} coordination sites in the compounds $[\text{Cp}^*\text{Zn}_2(\text{THF})_3]^+$ (**1**), (**2**) and (**3**) are prone to facilitate this process. Thus it can be expected that these cationic compounds can be readily used to synthesize a great variety of Hume-Rothery-type clusters, when the right reaction partner is chosen. Especially Cp* bearing reaction partners are promising due to the facile Cp* exchange between the metal centres. Apart from that, by manipulating the lability of such cationic Zn^{I} species controlled disproportionation for the preparation of the zinc cluster $\{[\text{Zn}_{10}](\text{Cp}^*)_6\text{Me}\}[\text{BAr}_4^{\text{F}}]$ **4** $[\text{BAr}_4^{\text{F}}]$ have been achieved. Such disproportionation reactions in the presence of further TM species, especially with labile ligands, might give novel intermetallic cluster compounds. The weak skeletal bonding in the zinc clusters **4**, $\{[\text{Zn}_9](\text{Cp}^*)_6\}$ **5** and $\{[\text{Zn}_8](\text{Cp}^*)_5(\text{CN}^t\text{Bu})_3\}^+$ **6** suggest the possibility of other $[\text{Zn}_a]$ clusters and their use as zinc rich starting materials for intermetallic clusters. An example for the potential of such zinc clusters as building blocks for novel intermetallic clusters, is the synthesis of $\{[\text{Cu}_3\text{Zn}_5](\text{R})_4(\text{CN}^t\text{Bu})_4\}^+$ (R = Cp* or Cp) (**10**) (Figure 44). The cationic cluster

is prepared by treating $4[\text{BAR}_4^{\text{F}}]$ with three equivalents of $[\text{CpCu}(\text{CN}^t\text{Bu})]$. The compound is isostructural and isoelectronic to the literature known $[(\text{ZnCp}^*)(\text{Cu}(\text{CN}^t\text{Bu}))_4]$.^[121] However, the disorder of the Cu/Zn sites as well as the presence of Cp, which is not distinguishable from Cp* in the crystal structure makes the characterization extremely difficult as only mixtures of non-separable isomers are obtained. A specific reaction pathway, giving only one isomer has not been discovered yet, so that the characterisation of this compound has not been completed within the scope of this work and is only mentioned as an outlook of zinc clusters being promising building blocks for Hume-Rothery-type clusters.

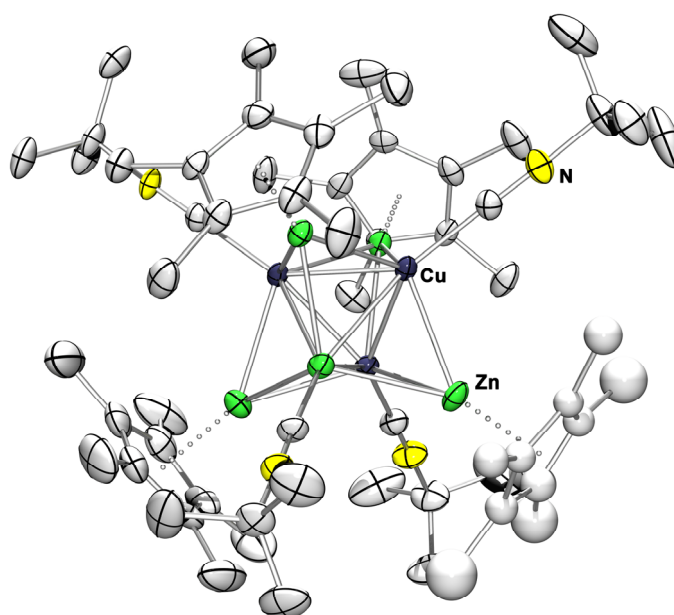


Figure 48. Preliminary molecular structure of $\{[\text{Cu}_3\text{Zn}_5](\text{Cp}^*)_4(\text{CN}^t\text{Bu})_4\}^+$ (**10**). Displacement ellipsoids are shown at the 30 % probability level and the hydrogen atoms are omitted for clarity. The Cu and Zn sites were tentatively assigned due to expected disorder at each metal site.

However, with this, three pairs of isostructural cationic and neutral Zn/Cu compounds exist, **10** and $[(\text{ZnCp}^*)_4(\text{Cu}(\text{CN}^t\text{Bu}))_4]$, **7** and $[\text{Zn}_3\text{Cp}^*_3]^+$ ^[119] as well as **9** and **8**. In each pair the Zn/Cu ratio is different in the cationic and neutral species. Regarding this, it is feasible that the formal exchange of Zn^+ with isoelectronic Cu and *vice versa* under preservation of the respective compounds structure is in principle also possible for other clusters. For the future more of such isostructural pairs with different Zn/Cu ratio can be expected to be reported.

6 EXPERIMENTAL SECTION

6.1 General Methods

All experiments were conducted in vacuum or under an atmosphere of purified argon inert gas, which was provided by using standard Schlenk technique and gloveboxes. For this purpose, the argon was dried by passing it through columns containing heated copper catalyst (42 wt%, CuO, 47 wt% ZnO, 10 wt% Al₂O₂) and activated molecular sieves (4 Å).

Commonly used solvents were dried and purified by using an MBraun SPS-Solvent Purification System, in which the solvents pass a series of two filter columns containing moisture absorbing materials by applying an argon pressure. Herein, alumina is used as an adsorbent for THF, Et₂O and toluene and activated molecular sieve and a copper catalyst for *n*-pentane and *n*-hexane. Benzene, fluorobenzene and CH₂Cl₂ were dried and purified by passing the respective solvent through a column containing neutral alumina under an argon atmosphere. The solvents treated by this means exhibit a purity of > 99 % and a residual water content of < 5 ppm, which was frequently verified by Karl-Fischer titration. At this, in a mixture of iodine and sulphur dioxide, iodine is reduced to iodide as long as water is present. In the case of the complete conversion of the available water free iodine is available. This equivalent point can be determined by means of amperometric measurements, because a current flux is only observable in the presence of iodide and iodine.

All glassware were dried at elevated temperatures in vacuum and silylated with boiling 1,1,1,3,3,3-Hexamethyldisilazan prior usage. Excess 1,1,1,3,3,3-Hexamethyldisilazan was removed in vacuum.

All temperature sensitive compounds were stored at -30 °C in a glovebox.

6.2 Nuclear Magnetic Resonance Spectroscopy (NMR)

NMR spectra were recorded on a Bruker Avance DPX-250, a Bruker Avance III AV400US and a Bruker Avance III AV500 with a cryo probe. For the measurements gas-tight J. Young NMR tubes were used, which offer an optimal protection towards air. The samples **4**[BAr^F₄] and **5** ·

2 PhMe were introduced into the NMR tubes inside a glovebox but the solvents were added using standard Schlenk technique outside the glovebox. At this, the solvent was precooled to $-30\text{ }^{\circ}\text{C}$ and the NMR tube including sample cooled to $-80\text{ }^{\circ}\text{C}$ (Figure 49). After the removal of the cooling bath the NMR tube was directed into the nitrogen stream of the spectrometer, wiped with an acetone wetted tissue and directly introduced to the precooled probehead.

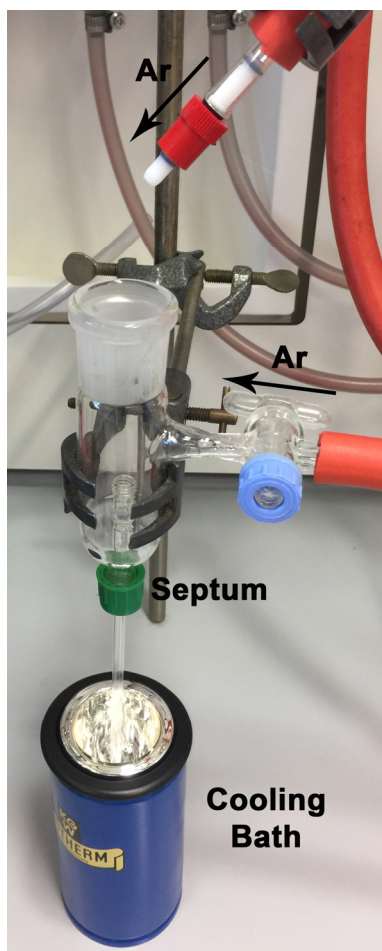


Figure 49. Introducing solvent to a J. Young NMR tube at low temperatures.

All used deuterated solvents were degassed by freeze-pump-thaw method and stored over molecular sieves. The chemical shifts δ are given in ppm. As an internal standard the residual protons in the deuterated solvents (^1H : C_6D_6 7.15 ppm, CD_2Cl_2 5.32 ppm; ^{13}C : C_6D_6 128 ppm, CDCl_2 53.8 ppm) were used. All ^{13}C NMR spectra are fully proton decoupled. Multiplicities are indicated using following abbreviations: s = singlet, d = doublet, t = triplet, q = quartet, m = multiplet. The spectra obtained were manipulated with MestReNova V. 9.0.1.

6.3 Infrared Spectroscopy (IR)

The IR spectra were recorded using the ATR unit of a FT-IR (Fourier-Transform-Infrared-Spectroscopy) ALPHA spectrometer of the Bruker company, whereby the system was located in a glovebox. The band intensities are indicated using following abbreviations: w = weak, m = medium, s = strong. The spectra were edited with OriginPro 9.0G.

6.4 Elemental Analysis (EA) and Atom Absorption Spectroscopy (AAS)

Elemental Analysis and AAS measurements were conducted in the Microanalytical Laboratory Kolbe in Mülheim an der Ruhr on an elemental CHNOS-Analyzer (Vario EL) and an AAnalyst 200 of the Perkin-Elmer company (AAS).

6.5 Mass Spectrometry (MS)

6.5.1 Liquid Injection Field Desorption Ionization (LIFDI) MS

Mass spectrometry of $2[\text{BAR}_4^{\text{F}}]_2$ was performed on a Waters LCT Classic orthogonal acceleration reflectron-TOF (time of flight) mass spectrometer using a liquid injection field desorption ionization (LIFDI) source from the Linden CMS GmbH. This mild ionization method limits the fragmentation to a minimum and is compared to other methods not restricted by the polarity of the sample. This ionisation method is especially suitable for the analysis of labile air sensitive complexes. The sample was prepared for measurement by dissolving the sample in the CH_2Cl_2 inside a glass vial which was closed with a septum carrying cap. An air free atmosphere during sample introduction was ensured by withdrawing the prepared solution from the closed vessel through the septum with a glass capillary under reduced pressure. The sample solution is transmitted to a tungsten wire which is coated with thousands of micro graphite dendrites. The sample is distributed over the emitter and the employed solvent is evaporated in the prevacuum of the mass spectrometer. By applying a potential between the emitter and the counter electrode of 10 kv the sample molecules are ionised and subsequently

accelerated to the counter electrode and eventually to the detector. In order to increase the mobility of the molecules on the emitter an electrical current of up to 120 mA is applied through the tungsten wire. The recorded spectra were manipulated with MestReNova V. 9.0.1.

6.5.2 Electrospray Ionization (ESI) MS

Mass spectrometry of $10[\text{BAr}_4^{\text{F}}] \cdot 1.5 \text{ C}_6\text{H}_5\text{F}$ was performed on a Waters Micromass Q-TOF micro mass spectrometer using an electrospray ionization source. This mild ionization method limits the fragmentation to a minimum but is restricted to ionic compounds or compounds which can either be protonated by the employed solvent or form ionic adducts with added solvent modifiers. The sample was dissolved in THF inside a glovebox and further introduced into a syringe. The sample solution was injected *via* a nebulizer into the mass spectrometer. A strong electrical charge is imparted to the sample solution at the nebuliser resulting in an aerosol of charged droplets. The droplets become smaller in size due to the evaporation of the employed solvent. The continuous evaporation leads to a concentration of the charge density inside the droplets. As a consequence, the charged molecules are repelled from each other (Coulomb explosion) eventually giving individual naked ions, which are accelerated towards the detector. The recorded spectra were manipulated with MestReNova V. 9.0.1.

6.6 Single Crystal X-ray Diffraction (XRD)

The crystals were coated with a perfluoropolyether, picked up with a glass fiber, and immediately mounted in the nitrogen cold gas stream (100 K) of the diffractometer. The X-ray diffraction reflections for $1[\text{BAr}_4^{\text{F}}]$, $3[\text{BAr}_4^{\text{F}}] \cdot 4 \text{ CH}_2\text{Cl}_2$, $4[\text{BAr}_4^{\text{F}}] \cdot 5 \text{ C}_6\text{H}_5\text{F}$, $5 \cdot \text{THF}$, $6[\text{BAr}_4^{\text{F}}] \cdot 4 \text{ C}_6\text{H}_5\text{F}$ and $10[\text{BAr}_4^{\text{F}}] \cdot 1.5 \text{ C}_6\text{H}_5\text{F}$ were collected on an Oxford SuperNova diffractometer with an Atlas CCD detector using Cu-K α irradiation ($\lambda = 1.54178 \text{ \AA}$) from multilayer X-ray optics. Data collection and reduction were conducted with the software CrysAlisPro (steadily updated) of the Agilent company.^[141] Absorption corrections based on multiple-scanned reflections were carried out with ABSPACK in CrysAlisPro. The X-ray diffraction reflections for **8** and $9[\text{BAr}_4^{\text{F}}] \cdot 5 \text{ C}_6\text{H}_5\text{F}$ were collected on a Bruker diffractometer equipped with a IMS microsource and a CMOS detector (APEX III, κ -CMOS) using Mo-K α irradiation ($\lambda = 0.71073$

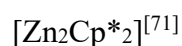
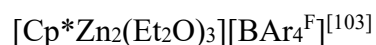
Å) from a Helios optic. Data collection and reduction were conducted with the software APEX III of the Bruker company.^[142] Absorption corrections were performed using SADABS in APEX III. All crystal structures were solved by direct methods using SHELXS-97^[143] and also refined with SHELXL-2014.^[144] Herein, the method of the least squares was applied, whereby the refinement was proceeded against F02 data (F02 = observed intensities). Standard similar distance restraints and constraints on atomic displacement parameters (ADPs) were used to model disordered regions. Anisotropic ADPs were introduced for all non-hydrogen atoms. Hydrogen atoms were placed at geometrically calculated positions and refined with the appropriate riding model. $4[\text{BAr}_4^{\text{F}}] \cdot 5 \text{C}_6\text{H}_5\text{F}$ was refined as a four-component inversion twin, applying the twin law:

$$\begin{pmatrix} 0 & 0 & 1 \\ 0 & -1 & 0 \\ 1 & 0 & 0 \end{pmatrix}$$

Disordered fluorobenzene solvent molecules in $4[\text{BAr}_4^{\text{F}}] \cdot 5 \text{C}_6\text{H}_5\text{F}$, $6[\text{BAr}_4^{\text{F}}] \cdot 4 \text{C}_6\text{H}_5\text{F}$ and $9[\text{BAr}_4^{\text{F}}] \cdot 5 \text{C}_6\text{H}_5\text{F}$ were visible in the difference Fourier maps but could not be modelled reasonably and were therefore removed with the PLATON/SQUEEZE.^[145] The tetrahydrofuran solvent molecule in $5 \cdot \text{THF}$ contains a crystallographic mirror plane and appears to be affected by slight disorder. Introducing a split model did not improve the refinement results. The model with large ADPs for the tetrahydrofuran oxygen atom was thus preferred.

6.7 Starting Compounds

All starting compounds were purchased from commercial sources and used without further purification unless otherwise stated. The following compounds were synthesised according to literature procedures:



6.8 Synthesis and Characterisation of Compounds

[Cp*Zn₂(THF)₃][BAr₄^F] (1[BAr₄^F]) i) A mixture of 100 mg (0.249 mmol) [Zn₂Cp*₂] and 262 mg (0.249 mmol) [FeCp₂][BAr₄^F] were dissolved in THF (5 mL) at room temperature and stirred for 15 min, whereupon the initial blue solution immediately turned orange. The solvent was removed in vacuum and the residue was washed with *n*-hexane (3 x 4 mL). Recrystallization from a saturated THF solution of [Cp*Zn₂(THF)₃][BAr₄^F] at -30 °C gave suitable colourless crystals for single crystal X-ray diffraction. *Yield*: 152 mg (113 mmol) of colourless crystals (45 %); ii) A solution of 100 mg (0.074 mmol) [Cp*Zn₂(Et₂O)₃] in 3 mL THF was stirred for 15 min at room temperature. The solvent was removed in vacuum and the residue was washed with *n*-hexane (3 x 4 mL). Recrystallization of the crude product from a saturated THF solution at -30 °C gave suitable colourless crystals for single crystal X-ray diffraction. *Yield*: 80 mg (59 mmol) of colourless crystals (80 %).

Elemental and AAS analysis [%] calculated for C₅₄H₅₁BF₂₄O₃Zn₂: C, 48.20; B, 0.80; H, 3.82; F, 33.89; Zn, 9.72; Found: C, 48.16; B, 0.78; H, 3.93; F, 33.81; Zn, 9.69.

¹H NMR (298 K, 250.1 MHz, CD₂Cl₂): δ [ppm] = 2.00 (q, 12H, THF), 2.07 (s, 15H, Cp*), 3.85 (t, 12H, THF), 7.57 (s, 4H, [BAr₄^F]), 7.72 (s, 8H, [BAr₄^F]).

¹³C NMR (298 K, 62.9 MHz, CD₂Cl₂): δH [ppm] = 10.33 (s, C₅Me₅), 25.62 (s, THF), 70.95 (s, THF), 109.24 (s, C₅Me₅), 117.86 (s, [BAr₄^F]), 125.08 (q, J_{C-F} = 272.4 Hz, CF₃), 129.27 (q, J_{C-F} = 31.5 Hz, [BAr₄^F]), 135.23 (s, [BAr₄^F]), 162.21 (q, J_{C-B} = 51.5 Hz, [BAr₄^F]).

¹¹B NMR (298 K, 80.3 MHz, CD₂Cl₂): δ [ppm] = -6.56 (s, [BAr₄^F]).

IR (ATR, 298 K): $\tilde{\nu}$ [cm⁻¹] = 2876.19 (w), 1597.15 (w), 1450.46 (s), 1342.48 (s), 1266.29 (s), 1102.55 (s), 1011.83 (m), 943.72 (m), 917.42 (m), 878.93 (m), 830.71 (m), 737.66 (w), 708.65 (m), 676.40 (m), 663.75 (m), 575.31 (w), 506.26 (w), 443.37 (w).

[Zn₂(THF)₆][BAr₄^F]₂ (2[BAr₄^F]₂) A quantity of 100 mg (0.074 mmol) [Cp*Zn₂(Et₂O)₃][BAr₄^F] was dissolved in THF (3 ml). The solution was stirred at room temperature for 15 min. A volume of *n*-hexane (20 ml) was added resulting in the precipitation of a colourless solid. The precipitate was isolated by filtration and washed with *n*-hexane (5 x 4 ml). *Yield*: 147 mg (0.064 mmol) of a colourless crystalline powder (87 %).

¹H NMR (298 K, 250.1 MHz, CD₂Cl₂): δ [ppm] = 2.07 (bs, 24H, THF), 3.97 (q, 24H, THF), 7.56 (s, 8H, [BAr₄^F]), 7.72 (s, 16H, [BAr₄^F]).

^{13}C NMR (298 K, 62.9 MHz, CD_2Cl_2): δH [ppm] = 27.66 (bs, THF), 74.06 (bs, THF), 117.86 (s, $[\text{BAr}_4^{\text{F}}]^-$), 125.01 (q, $J_{\text{C-F}} = 272.4$ Hz, CF_3), 129.26 (q, $J_{\text{C-F}} = 31.5$ Hz, $[\text{BAr}_4^{\text{F}}]^-$), 135.18 (s, $[\text{BAr}_4^{\text{F}}]^-$), 162.09 (q, $J_{\text{C-B}} = 51.5$, $[\text{BAr}_4^{\text{F}}]^-$).

^{11}B NMR (298 K, 80.3 MHz, CD_2Cl_2): δ [ppm] = -62.84 (s, $[\text{BAr}_4^{\text{F}}]^-$).

^{19}F NMR (298 K, 235.3 MHz, CD_2Cl_2): δ [ppm] = -6.63 (s, CF_3).

IR (ATR, 298 K): $\tilde{\nu}$ [cm^{-1}] = 2962 (w), 2876 (w), 1597 (w), 1451 (s), 1263 (s), 1100 (s), 1012 (s), 878 (s), 849 (m), 831 (m), 738 (m), 704 (m), 676 (m).

MS (LIFDI, CH_2Cl_2): m/z 496 $[\text{Zn}(\text{THF})_6]^+$, 424 $[\text{Zn}(\text{THF})_5]^+$.

$[\text{Zn}_2(\text{CNPh})_6][\text{BAr}_4^{\text{F}}]_2$ (3** $[\text{BAr}_4^{\text{F}}]_2$)** To a solution of 100 mg (0.044 mmol) $[\text{Zn}_2(\text{THF})_6][\text{BAr}_4^{\text{F}}]_2$ in CH_2Cl_2 (3 mL), 0.03 mL (0.297 mmol) PhNC were added at room temperature. The resulting red solution was stirred for 1 h. 15 mL of *n*-hexane were added, giving a red precipitate, which was isolated by filtration and washed with *n*-hexane (4 x 2 ml). Recrystallization from a saturated CH_2Cl_2 solution of $[\text{Zn}_2(\text{CNPh})_6][\text{BAr}_4^{\text{F}}]_2$ at -30 °C gave suitable crystals for single crystal X-ray diffraction as **2** $[\text{BAr}_4^{\text{F}}]_2 \cdot 4 \text{CH}_2\text{Cl}_2$. Yield: 70 mg (25 mmol) of crystalline red powder (65 %).

Elemental and AAS analysis [%] calculated for $\text{C}_{106}\text{H}_{54}\text{B}_2\text{F}_{48}\text{N}_6\text{Zn}_2$: C, 51.45; H, 2.20; N, 3.40; Zn, 5.17; Found: C, 51.42; H, 2.29; N, 3.37; Zn, 5.27.

^1H NMR (298 K, 250.1 MHz, CD_2Cl_2): δ [ppm] = 7.38-7.64 (m, 30H, $\text{C}_6\text{H}_5\text{NC}$), 7.52 (s, 8H, $[\text{BAr}_4^{\text{F}}]^-$), 7.71 (s, 16H, $[\text{BAr}_4^{\text{F}}]^-$).

^{13}C NMR (298 K, 62.9 MHz, CD_2Cl_2): δH [ppm] = 117.80 (s, $[\text{BAr}_4^{\text{F}}]^-$), 124.97 (q, $J_{\text{C-F}} = 272.4$ Hz, CF_3), 127.63 (s, PhNC), 129.26 (q, $J_{\text{C-F}} = 31.5$ Hz, $[\text{BAr}_4^{\text{F}}]^-$), 130.03 (s, PhNC), 130.94 (s, PhNC) 135.15 (s, $[\text{BAr}_4^{\text{F}}]^-$), 162.17 (q, $J_{\text{C-B}} = 50$ Hz, $[\text{BAr}_4^{\text{F}}]^-$).

^{11}B NMR (298 K, 80.3 MHz, CD_2Cl_2): δ [ppm] = -6.59 (s, $[\text{BAr}_4^{\text{F}}]^-$).

^{19}F NMR (298 K, 235.3 MHz, CD_2Cl_2): δ [ppm] = -62.81 (s, CF_3).

IR (ATR, 298 K): $\tilde{\nu}$ [cm^{-1}] = 2180.77 (m), 1596.93 (w), 1578.89 (w), 1473.92 (w), 1447.06 (w), 1341.51 (s), 1262.95 (s), 1148.69 (s), 1107.21 (s), 1016.21 (w), 993.94 (w), 939.01 (w), 916.62 (w), 889.89 (s), 878.75 (s), 831.48 (s), 771.28 (w), 747.44 (s), 707.83 (s), 675.09 (s), 661.95 (s), 573.60 (w), 511.60 (w), 499.74 (w), 444.15 (w).

$\{[\text{Zn}_{10}(\text{Cp}^*)_6\text{Me}][\text{BAr}_4^{\text{F}}]_4$ (4** $[\text{BAr}_4^{\text{F}}]_4$)** To a solution of 65 mg (0.062 mmol) $[\text{FeCp}_2][\text{BAr}_4^{\text{F}}]$ in fluorobenzene (4 mL) at -30 °C, 0.23 mL (0.276 mmol) of a 1.2 M solution of ZnMe_2 in toluene were added *via* syringe. A solution of 150 mg (0.373 mmol) $[\text{Zn}_2\text{Cp}^*_2]$ in fluorobenzene (1 mL)

at -30 °C was added to this mixture through a PTFE canula. The red reaction mixture was stirred for 15 min. at -30 °C upon which a microcrystalline red powder forms. The mixture was stored at -30 °C over night and the red powder was isolated by filtration and washed with cold hexane (3 x 2 mL). Red crystals suitable for single crystal X-ray diffraction were obtained from a saturated fluorobenzene solution at -30 °C as $4[\text{BAr}_4^{\text{F}}] \cdot 5 \text{C}_6\text{H}_5\text{F}$. At this microcrystalline $\{[\text{Zn}_{10}](\text{Cp}^*)_6\text{Me}\}[\text{BAr}_4^{\text{F}}]$ powder is dissolved in a minimum amount of to -10 °C cooled fluorobenzene. The solution is then stored at -30 °C for crystallization. *Yield*: 116 mg (0.041 mmol) of a crystalline red powder (41 % based on zinc).

Elemental and AAS analysis [%] calculated for $\text{H}_{110}\text{BC}_{99}\text{F}_{25}\text{Zn}_{10}$ ($\{[\text{Zn}_{10}](\text{Cp}^*)_6\text{Me}\}[\text{BAr}_4^{\text{F}}] \cdot \text{C}_6\text{H}_5\text{F}$): H 4.54, B 0.44, C 48.74, F 19.47, Zn 26.80; found: H 4.60, B 0.43, C 46.89, F 18.40, Zn 25.72.

$^1\text{H NMR}$ (183 K, 250.1 MHz, CD_2Cl_2): δ [ppm] = 0.02 (s, 3H, Me), 1.75 (s, 30H, $\mu_4\text{-ZnC}_5\text{Me}_5$), 1.99-2.12 (m, 60H, ZnC_5Me_5 and $\mu_2\text{-ZnC}_5\text{Me}_5$), 7.53 (s, 4H, $[\text{BAr}_4^{\text{F}}]$), 7.72 ppm (s, 8H, $[\text{BAr}_4^{\text{F}}]$).

IR (ATR, 298 K): $\tilde{\nu}$ [cm^{-1}] = 3631 (w), 2935(m), 2888 (m), 2839 (m), 1597 (w), 1440 (w), 1404 (w), 1374 (w), 1341 (m), 1263 (s), 1150 (s), 1111 (s), 878 (m), 831 (m), 789 (m), 707 (m), 676 (m), 663 (m), 582 (m).

$\{[\text{Zn}_9](\text{Cp}^*)_6\}$ (**5**) A quantity of 65 mg (0.028 mmol) $\{[\text{Zn}_{10}](\text{Cp}^*)_6\text{Me}\}[\text{BAr}_4^{\text{F}}]$ was dissolved in 3 mL cold THF (-80 °C) to give a yellow solution and stirred for 15 min. The solvent was removed in vacuum at -20 °C. The residue was washed with cold *n*-pentane (3 x 2 mL) and extracted with 3 mL cold toluene (-30 °C). Slow diffusion of *n*-pentane into the concentrated toluene solution of **5** at -30 °C gave $\mathbf{5} \cdot 2 \text{PhMe}$ in the form of yellow crystals. *Yield*: 17 mg (0.011 mmol) of a crystalline yellow powder (39 %). Recrystallization by slow diffusion of *n*-hexane into a THF solution of **5** at -30 °C gave suitable yellow crystals for single crystal X-ray diffraction as $\mathbf{5}[\text{BAr}_4^{\text{F}}] \cdot \text{THF}$.

Elemental and AAS analysis [%] calculated for $\text{H}_{90}\text{C}_{60}\text{Zn}_9$: H 6.48, C 51.48, Zn 42.04; found: H 6.36, C 50.77, Zn 40.97.

$^1\text{H NMR}$ (183 K, 250.1 MHz, CD_2Cl_2): δ [ppm] = 1.87 (s, 30H, $\mu_3\text{-ZnC}_5\text{Me}_5$), 1.97 (s, 60H, $\mu_2\text{-ZnC}_5\text{Me}_5$ and ZnC_5Me_5).

IR (ATR, 298 K): $\tilde{\nu}$ [cm^{-1}] = 2939 (m), 2879 (s), 2833 (s), 2700 (m), 1468 (m), 1437 (m), 1407 (s), 1369 (s), 1268 (m), 1168 (m), 1118 (m), 1013 (m), 790 (m), 721 (s), 687 (m), 582 (s), 460 (m).

$\{[\text{Zn}_8](\text{Cp}^*)_5(\text{CN}^t\text{Bu})_3\}[\text{BAR}_4^{\text{F}}] \cdot 4 \text{C}_6\text{H}_5\text{F}$ (**6** $[\text{BAR}_4^{\text{F}}] \cdot 4 \text{C}_6\text{H}_5\text{F}$) To a solution of 45 mg $\{[\text{Zn}_{10}](\text{Cp}^*)_6\text{Me}\}[\text{BAR}_4^{\text{F}}]$ (0.019 mmol) dissolved in $-30\text{ }^\circ\text{C}$ cold fluorobenzene (2.5 mL), 0.01 mL (0.088 mmol) $t\text{BuNC}$ was added, at which the initially red solution immediately turned yellow. The reaction solution was stirred for 15 min at $-30\text{ }^\circ\text{C}$. Slow diffusion of *n*-hexane into the reaction solution at $-30\text{ }^\circ\text{C}$ gave pale yellow crystals of $5[\text{BAR}_4^{\text{F}}] \cdot 4 \text{C}_6\text{H}_5\text{F}$, which could be individually isolated from a colorless participate by crystal picking.

$[\text{Zn}_2\text{CuCp}^*_3]$ (**7**) A suspension of 600 mg (1.50 mmol) $[\text{Zn}_2\text{Cp}^*_2]$ and 183 mg (1.50 mmol) $\text{Cu}(\text{OAc})$ in benzene (5 mL) was stirred at room temperature for 2 days. The dark red suspension was filtered. The residue was extracted with warm benzene (2 x 3 mL). The volume of the combined filtrates was reduced under vacuum for crystallization of the product at $8\text{ }^\circ\text{C}$ overnight. Pale-yellow crystals were isolated by filtration and washed with *n*-hexane (3 x 2 mL). The volume of the filtrate was further reduced in vacuum to give another crop of yellow crystals at $8\text{ }^\circ\text{C}$ overnight. *Yield*: 340 mg of pale-yellow crystals (57 % based on Cp^*).

$^1\text{H NMR}$ (298 K, 400 MHz, C_6D_6): δ [ppm] = 2.07 (s, 30H, ZnC_5Me_5), 2.23 (s, 15H, CuC_5Me_5).

$^{13}\text{C NMR}$ (298 K, 100 MHz, C_6D_6): δ [ppm] = 10.90 (ZnC_5Me_5), 12.17 (CuC_5Me_5), 104.62 (CuC_5Me_5), 110.18 (ZnC_5Me_5).

IR (ATR 298 K): $\tilde{\nu}$ [cm^{-1}] = 2970 (m), 2901 (s), 2856 (s), 2722 (w), 1476 (m), 1419 (s), 1375 (s), 1159 (m), 1020 (w), 976 (m), 794 (m), 616 (w), 588 (m).

$[\text{M}_7\text{Cp}^*_5]$ (**8**) (**M = Zn or Cu**) The solvent of the filtrate from the second crop of the synthesis of **7** is removed in vacuum. The residue is dissolved in a minimum amount of THF. Crystallization at $-30\text{ }^\circ\text{C}$ afforded red single crystals of **8**, which were individually isolated and separated from single crystals of **7** by crystal picking.

$^1\text{H NMR}$ (298 K, 400 MHz, C_6D_6): δ [ppm] = 2.08 (s, 45H, MC_5Me_5), 2.19 (s, 30H, MMC_5Me_5).

$^{13}\text{C NMR}$ (298 K, 125 MHz, C_6D_6): δ [ppm] = 10.48 (MC_5Me_5), 11.38 (MMC_5Me_5), 105.32 (MC_5Me_5), 108.18 (MMC_5Me_5).

$[(\text{ZnCu}_2\text{Cp}^*_3)(\mu_3\text{-ZnZnCp}^*)_2][\text{BAR}_4^{\text{F}}]$ (**9** $[\text{BAR}_4^{\text{F}}]$) A mixture of 80 mg (0.133 mmol) $[\text{Zn}_2\text{CuCp}^*_3]$ and 360 mg (0.266 mmol) $[\text{Cp}^*\text{Zn}_2(\text{Et}_2\text{O})_3][\text{BAR}_4^{\text{F}}]$ was dissolved in fluorobenzene (3 mL). The red solution was stirred for 1.5 h at room temperature and subsequently filtered. The filtrate was concentrated and stored at $-30\text{ }^\circ\text{C}$ for a week giving dark red crystals as $9[\text{BAR}_4^{\text{F}}] \cdot 5\text{C}_6\text{H}_5\text{F}$ covered by a sticky red residue. The crystals were isolated

by filtration and recrystallized from fluorobenzene at $-30\text{ }^{\circ}\text{C}$. After two recrystallization steps, **9**[BAr^F₄]⁻ was isolated as an analytically pure sample. *Yield*: 30 mg (0.015 mmol) of dark red crystals (23 % based on Cu).

Elemental and AAS analysis [%] calculated for H₈₇BC₈₂F₂₄Cu₂Zn₅: H 4.40, B 0.54, C 49.41, F 22.87, Cu 6.38, Zn 16.40; found: H 4.62, B 0.47, C 51.48, F 20.20, Cu 6.48, Zn 15.98.

¹H NMR (298 K, 400 MHz, CD₂Cl₂): δ [ppm] = 1.96 (s, 30H, ZnZnC₅Me₃), 2.04 (s, 15H, ZnC₅Me₃), 2.12 (s, 30 H, CuC₅Me₃), 7.56 (s, 4H, [BAr^F₄]⁻), 7.72 ppm (s, 8H, [BAr^F₄]⁻).

IR (ATR 298 K): $\tilde{\nu}$ [cm⁻¹] = 2905(w), 2860 (w), 1610 (w), 1454 (w), 1416 (w), 1380 (w), 1272 (w), 1272 (m), 1154 (s), 1116 (m), 1022 (s), 934 (w), 886 (w), 838 (m), 794 (m), 714 (m), 681 (m), 669 (m).

Table 4. Selected thesis related reactions and preliminary outcome.

Reaction	Outcome
$2[\text{BAr}_4^{\text{F}}]_2 + 6 \text{P}(\text{OMe})_3$ in $\text{C}_6\text{H}_5\text{F}$ at rt	Disproportionation of Zn^{I}
$2[\text{BAr}_4^{\text{F}}]_2 + 2 \text{BorylLi}$ in THF at rt (Boryl = $\text{B}(\text{NDippCH}_2)_2$)	Disproportionation of Zn^{I}
$2[\text{BAr}_4^{\text{F}}]_2 + \text{Zn}(\text{Boryl})_2$ in $\text{C}_6\text{H}_5\text{F}$ at rt	Immediate precipitation of metal
$2[\text{BAr}_4^{\text{F}}]_2 + \text{NPhCN}$ in $\text{C}_6\text{H}_5\text{F}$ at rt	Sticky residue after solvent removal
$2[\text{BAr}_4^{\text{F}}]_2 + [\text{Fe}(\text{CO})_5]$ in $\text{C}_6\text{H}_5\text{F}$ at rt	No reaction
$[\text{Zn}_2\text{Cp}^*_2] + \text{NOPF}_6$ in CH_2Cl_2 at rt	Violett solution with purple residue
$[\text{ZnCp}^*_2] + \text{ZnMe}_2 + [\text{FeCp}_2][\text{BAr}_4^{\text{F}}]$ in $\text{C}_6\text{H}_5\text{F}$ at $-30\text{ }^\circ\text{C}$	Single crystals of $[\text{Zn}_2\text{Cp}^*_3]^+$
$[\text{Zn}_2\text{Cp}^*_2] + \text{IPrCuMe} + [\text{FeCp}_2][\text{BAr}_4^{\text{F}}]$ in $\text{C}_6\text{H}_5\text{F}$ at $-30\text{ }^\circ\text{C}$	Immediate precipitation of metal
$4[\text{BAr}_4^{\text{F}}] + \text{PdMe}_2(\text{tmeda})$ in $\text{C}_6\text{H}_5\text{F}$ at $-30\text{ }^\circ\text{C}$	Single crystals of 5
$4[\text{BAr}_4^{\text{F}}] + [\text{Pd}(\text{PCy}_3)_2]$ $[\text{Zn}_2\text{Cp}^*_2] + \text{ZnMe}_2$ in toluene at $-60\text{ }^\circ\text{C}$	Single crystals of 5 Red solution after 1 h, precipitation of metal over night
$4[\text{BAr}_4^{\text{F}}] + \text{dmpa}$ in $\text{C}_6\text{H}_5\text{F}$ at $-30\text{ }^\circ\text{C}$	Precipitation of an amorphous green powder
$[\text{Zn}_2\text{Cp}^*_2] + \text{Ag}(\text{OAc})$ in benzene at rt	Red solution, no reaction according to NMR
$[\text{Zn}_2\text{Cp}^*_2] + \text{Sn}(\text{OAc})$ in benzene at rt	Precipitation of metal
$[\text{Zn}_2\text{Cp}^*_2] + 6\text{DippCuH}$ in THF at rt (6Dipp = 1,3-bis(2,6-diisopropylphenyl)- 3,4,5,6-tetrahydropyrimidin-2-ylidene)	No reaction
$[\text{Zn}_2\text{CuCp}^*_3] + [\text{H}(\text{Et}_2\text{O})][\text{BAr}_4^{\text{F}}]$ in $\text{C}_6\text{H}_5\text{F}$ at rt	Precipitation of metal and small amounts of 9 $[\text{BAr}_4^{\text{F}}]$
$[\text{Zn}_2\text{CuCp}^*_3] + [\text{FeCp}_2][\text{BAr}_4^{\text{F}}]$ in Et_2O at rt	No conversion of $[\text{Zn}_2\text{CuCp}^*_3]$

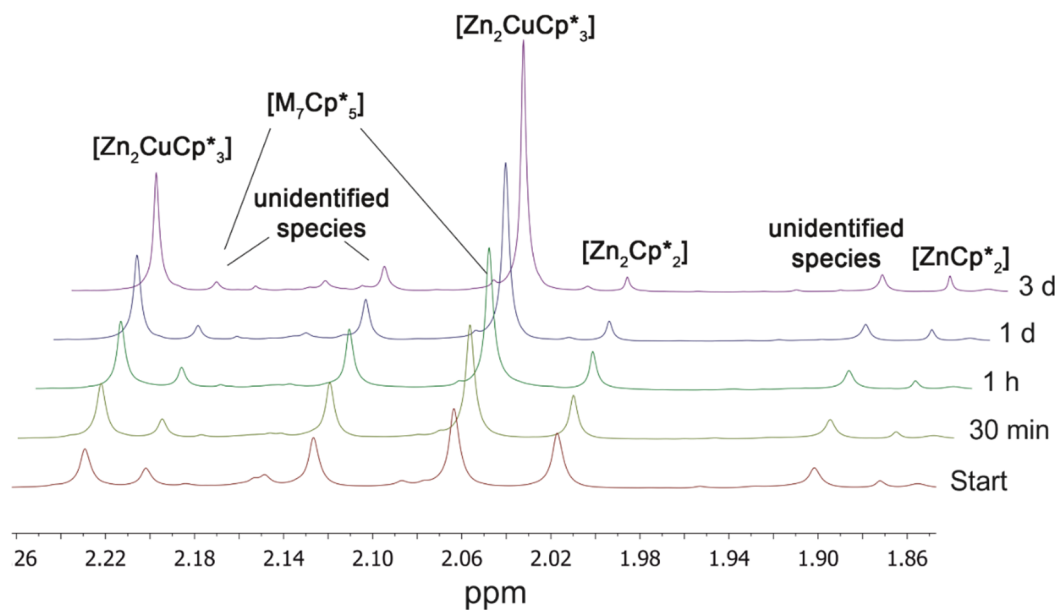
6.9 Supplementary NMR spectra of *in situ* experiments from chapter 4.3

Figure 50. ^1H NMR spectra of a 1:1 mixture of $\text{Cu}(\text{OAc})$ and $[\text{Zn}_2\text{Cp}^*_2]$ in C_6D_6 at room temperature over a period of 3 days.

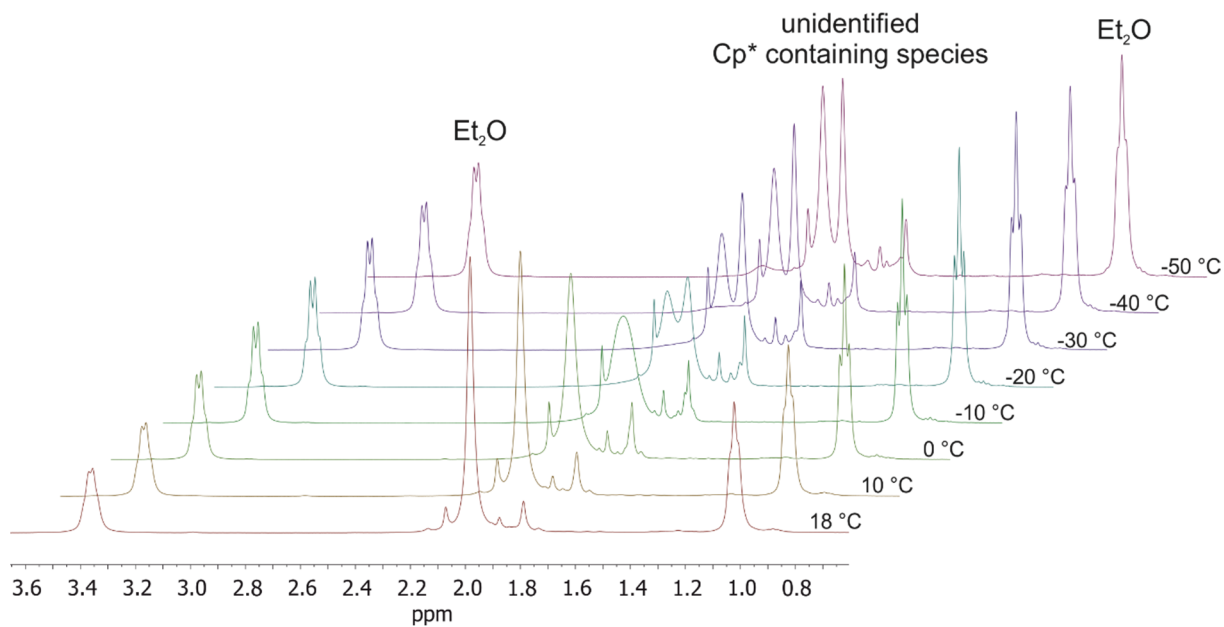


Figure 51. ^1H NMR of a 1:2 mixture of $[\text{Zn}_2\text{CuCp}^*_3]$ and $[\text{Cp}^*\text{Zn}_2(\text{Et}_2\text{O})_3][\text{BAR}_4^{\text{F}}]$ at temperatures between $(-50) - 18$ °C in fluorenebenzene/ C_6D_6 (90:10 Vol%).

6.10 Packing of the salts $1[\text{BAr}_4^{\text{F}}]_2$, $3[\text{BAr}_4^{\text{F}}]_2 \cdot 4 \text{CH}_2\text{Cl}_2$, $4[\text{BAr}_4^{\text{F}}] \cdot 5 \text{C}_6\text{H}_5\text{F}$, $6[\text{BAr}_4^{\text{F}}] \cdot 4 \text{C}_6\text{H}_5\text{F}$ and $9[\text{BAr}_4^{\text{F}}] \cdot 5 \text{C}_6\text{H}_5\text{F}$ in the respective unit cell

The following figures show the packing of $1[\text{BAr}_4^{\text{F}}]_2$, $3[\text{BAr}_4^{\text{F}}]_2$, $4[\text{BAr}_4^{\text{F}}]$, $6[\text{BAr}_4^{\text{F}}]$ and $9[\text{BAr}_4^{\text{F}}] \cdot 5 \text{C}_6\text{H}_5\text{F}$ in the respective unit cells in a stick representation. Co-crystallized solvent molecules and atoms from molecules whose centroids are inside the unit cell are included. Hydrogen atoms are omitted for clarity. Disordered parts are presented as dots. Boron atoms are represented in dark blue, carbon in grey, chlorine in turquoise, copper in midnight blue, fluorine in dark green, nitrogen in yellow, oxygen in red and zinc in bright green.

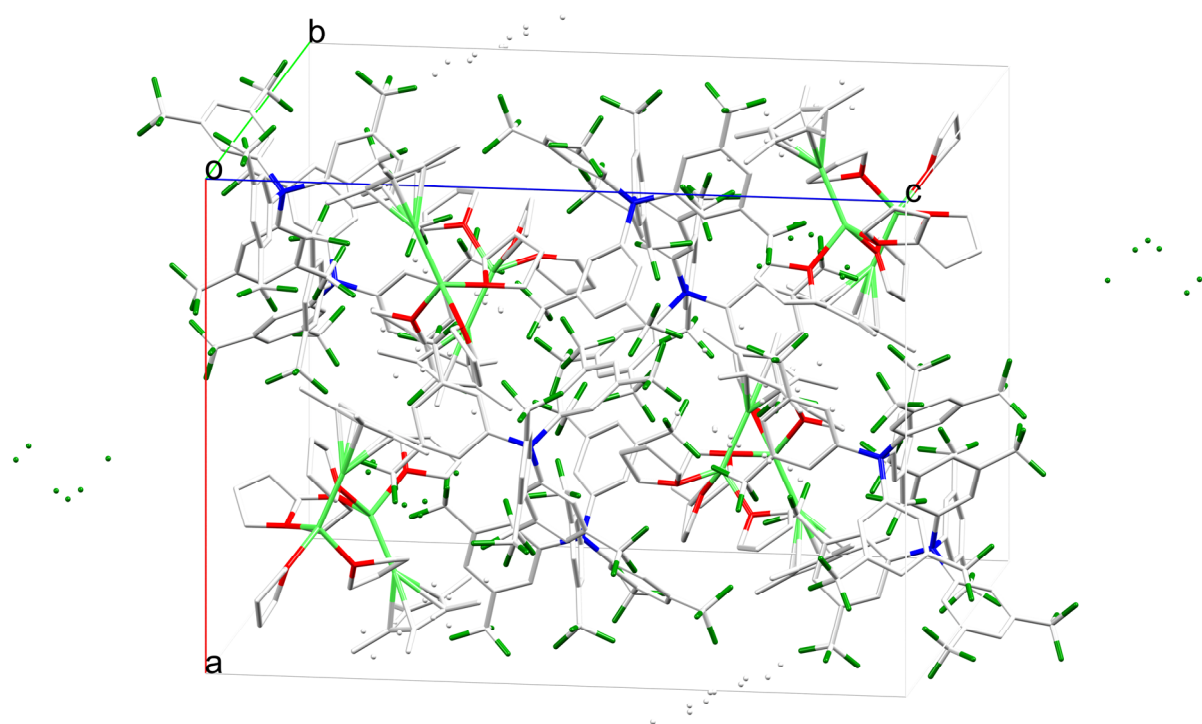


Figure 52. Packing of $1[\text{BAr}_4^{\text{F}}]_2$ in the unit cell.

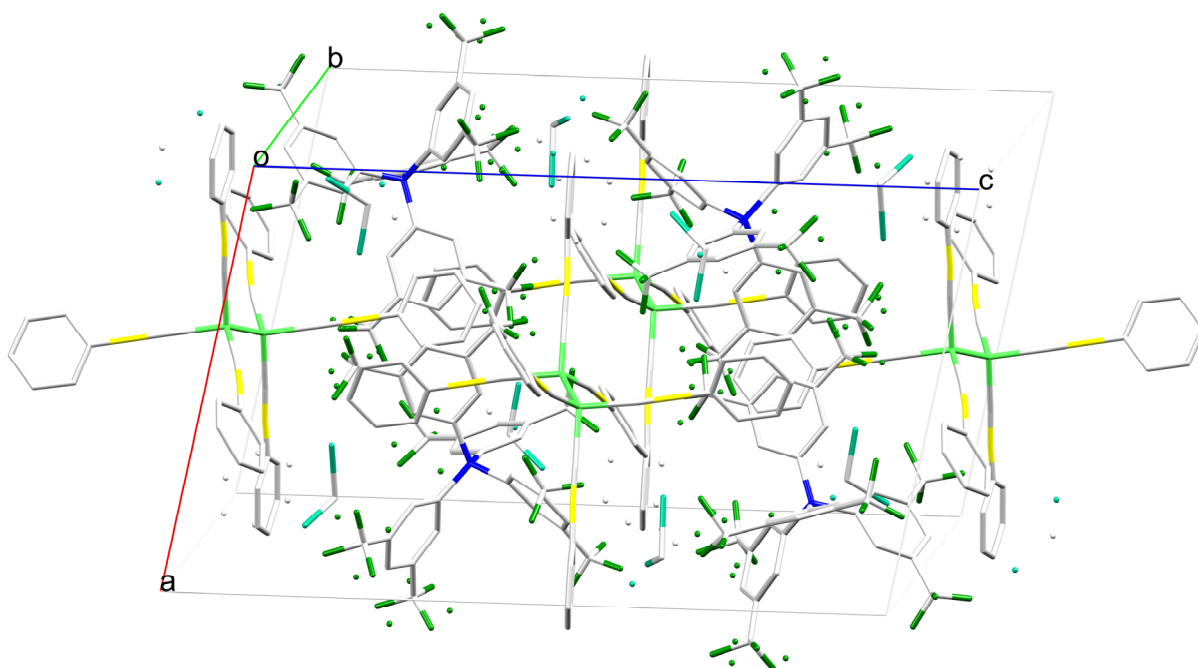


Figure 53. Packing of $3[\text{BAr}_4^{\text{F}}]_2 \cdot 4 \text{CH}_2\text{Cl}_2$ in the unit cell.

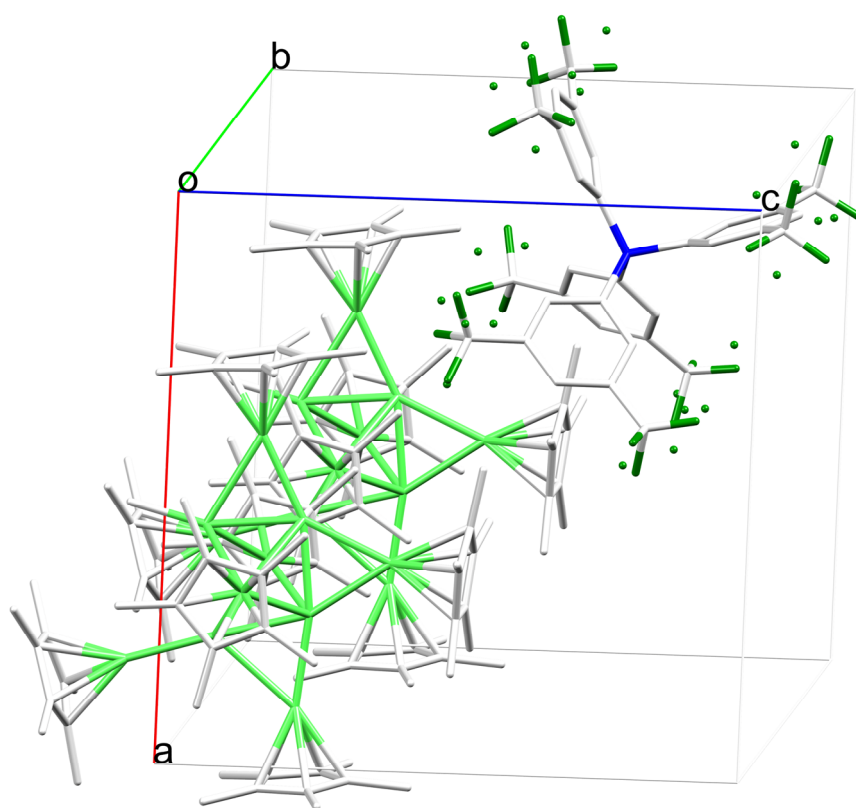


Figure 54. Packing of $4[\text{BAr}_4^{\text{F}}] \cdot 5 \text{C}_6\text{H}_5\text{F}$ in the unit cell.

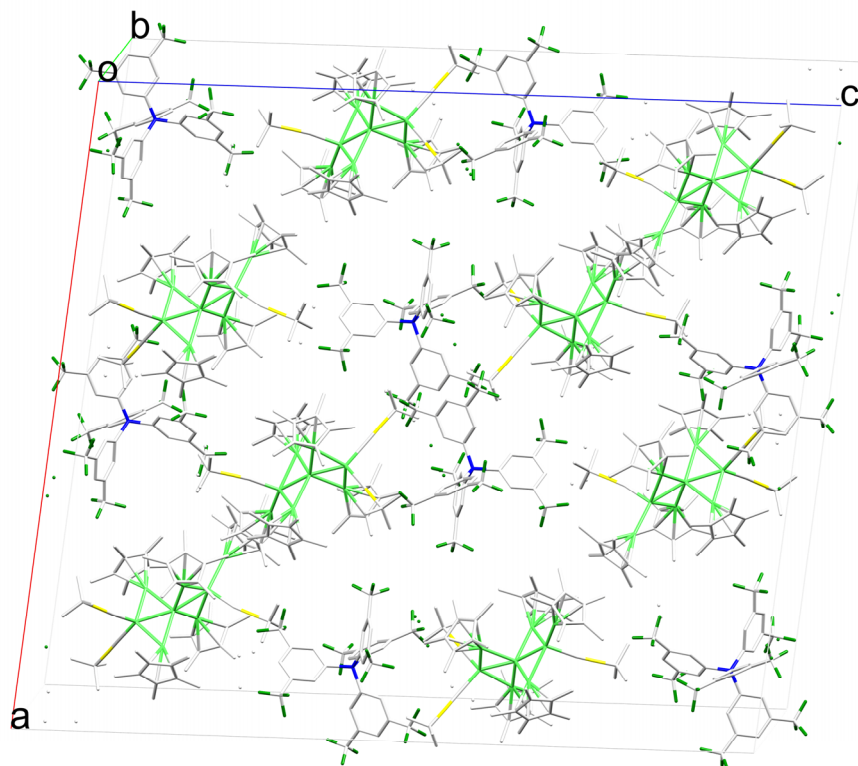


Figure 55. Packing of 6[BAr^F] · 4 C₆H₅F in the unit cell.

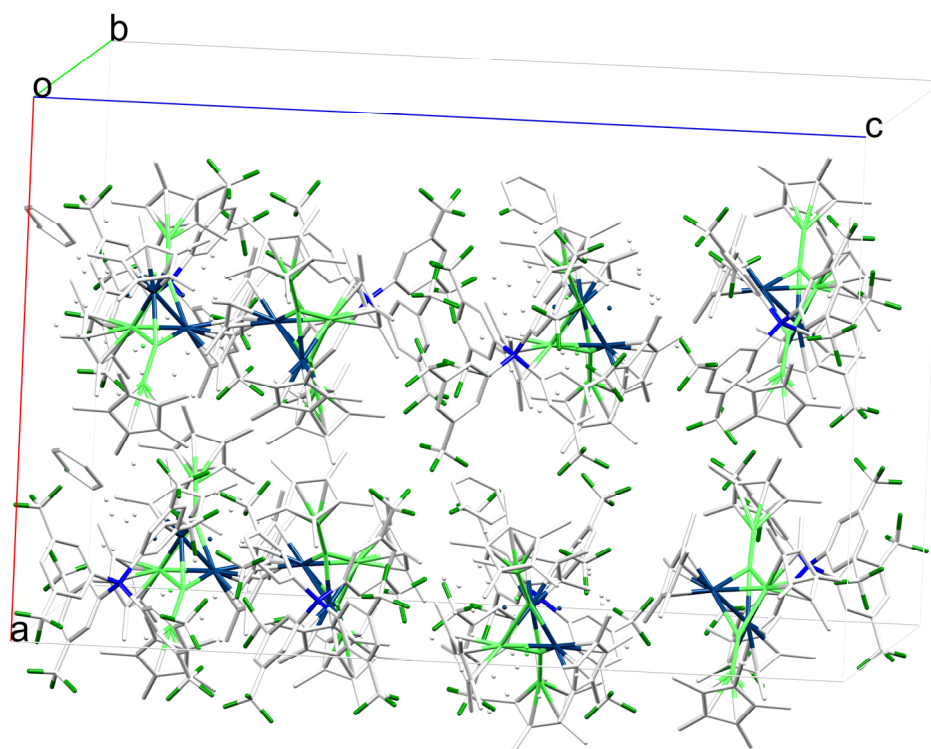


Figure 56. Packing of 9[BAr^F] · 5 C₆H₅F in the unit cell.

6.11 Computational details

Quantum chemical analysis for the compounds **4** and **5** were conducted by the group of Prof. Dr. Jean-Yves Saillard (Dr. Samia Kahlal) and Dr. Régis Gautier at the Institut des Sciences Chimiques de Rennes, France. In the case of compound **9**, quantum chemical calculations have been conducted by J. Hornung. The following chapter gives a short overview of the computational details of the employed methods.

6.11.1 Computational Details for $\{[Zn_{10}](Cp^*)_6Me\}^+$ (**4**), $\{[Zn_{10}](Cp)_6Me\}^+$ (**4'**), $\{[Zn_9](Cp)_5Me_2\}^+$ (**4''**), $\{[Zn_9](Cp^*)_6\}$ (**5**) and $\{[Zn_9](Cp)_6\}$ (**5'**)

DFT calculations were conducted for the geometry optimizations of **4**, **4'**, **4''**, **5** and **5'** with the software package Gaussian 09,^[148] using the PBE0 functional^[149-151] and the all-electron Def2-TZVPP basis set from the EMSL (Environmental Molecular Science Laboratory) Basis Set Exchange Library.^[152] Vibrational analysis manifest the geometry optimized structures to be true minima. The models of **4'** and **5'** were found to be very close to C_s and C_{2v} symmetry, respectively. The NBO 5.0 program^[133] was used to obtain the Wiberg and overlap weighted bond indices. ELF calculations for **4'** were performed using the DGrid program.^[153]

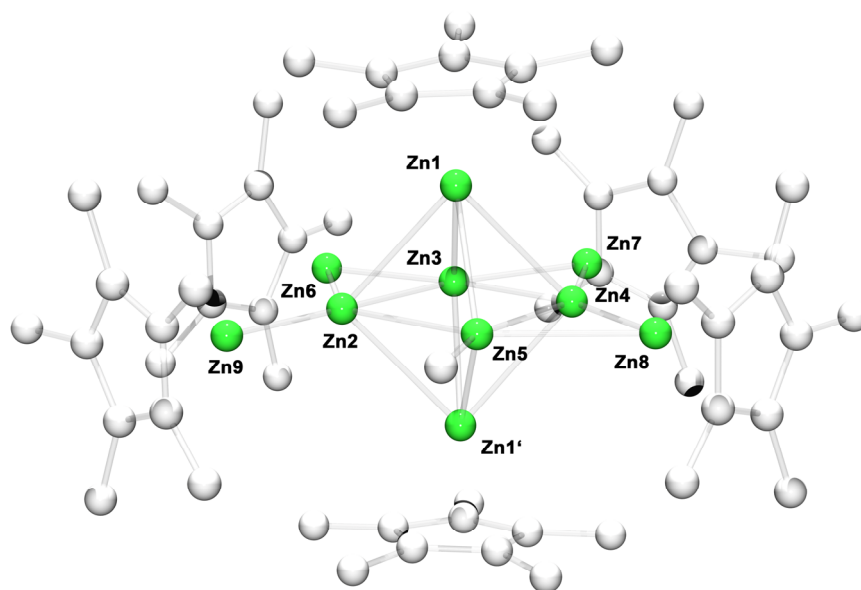


Figure 57. Optimized structure of $\{[Zn_{10}](Cp^*)_6Me\}^+$ (**4**) (PBE0/Def2-TZVPP). The hydrogen atoms are omitted for clarity.

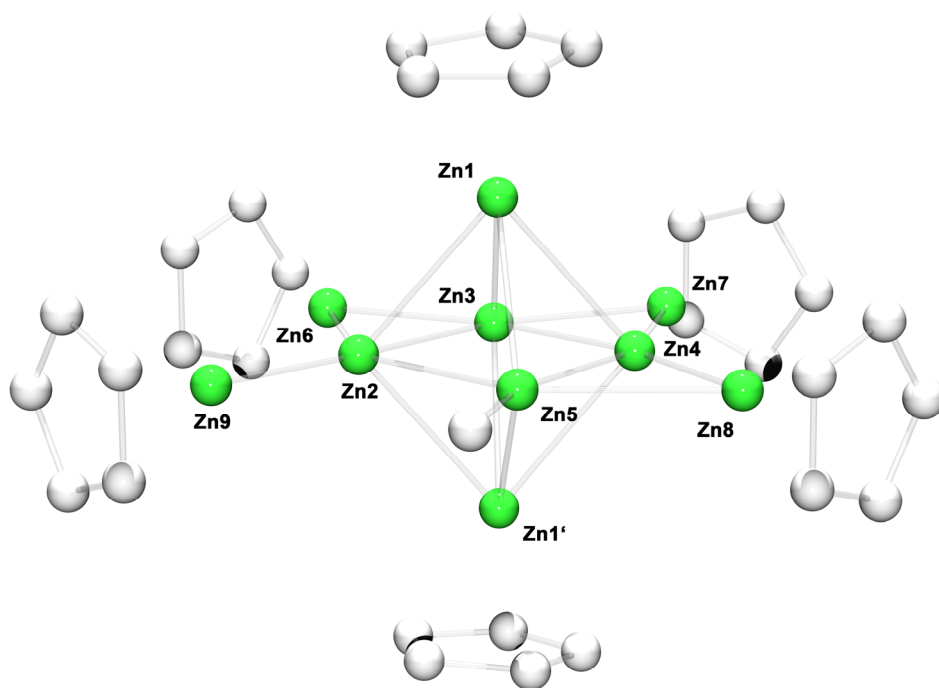


Figure 58. Optimized structure of $\{[Zn_{10}](Cp)_6Me\}^+$ (4') (PBE0/Def2-TZVPP). The hydrogen atoms are omitted for clarity.

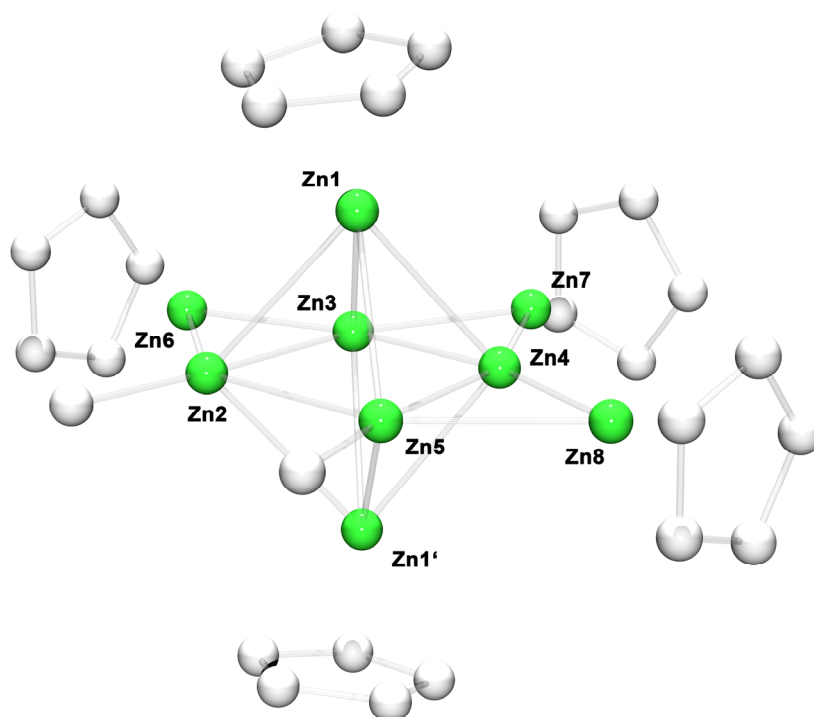


Figure 59. Optimized structure of $\{[Zn_{10}](Cp)_5Me_2\}^+$ (4'') (PBE0/Def2-TZVPP). The hydrogen atoms are omitted for clarity. Symmetry related Zn positions are primed.

Table 5. Comparison of the Zn-Zn distances as determined from the molecular structure of **4** in the solid state and the calculated values obtained from the geometry optimized models **4**, **4'** and **4''**.

	4 (exp.) [Å]	4 (cal.) [Å]	4' [Å]	4'' [Å]
Zn1-Zn2	2.746	2.862	2.787	2.838
Zn1-Zn3	2.609	2.681	2.735	2.705
Zn1-Zn4	2.759	2.847	2.768	2.738
Zn1-Zn5	2.674	2.709	2.776	2.801
Zn2-Zn9	2.342	2.401	2.370	-
Zn2-Zn6	2.677	2.712	2.656	2.712
Zn2-Zn3	2.454	2.502	2.474	2.456
Zn2-Zn5	2.832	2.833	2.753	2.873
Zn3-Zn4	2.425	2.459	2.438	2.421
Zn3-Zn6	2.390	2.462	2.455	2.438
Zn3-Zn7	2.484	2.551	2.532	2.516
Zn4-Zn5	2.453	2.500	2.835	2.467
Zn4-Zn7	2.441	2.509	2.512	2.521
Zn4-Zn8	2.381	2.429	2.412	2.431
Zn5-Zn8	2.762	2.907	2.835	2.741
Zn-Zn (\emptyset)	2.590	2.745	2.738	2.740

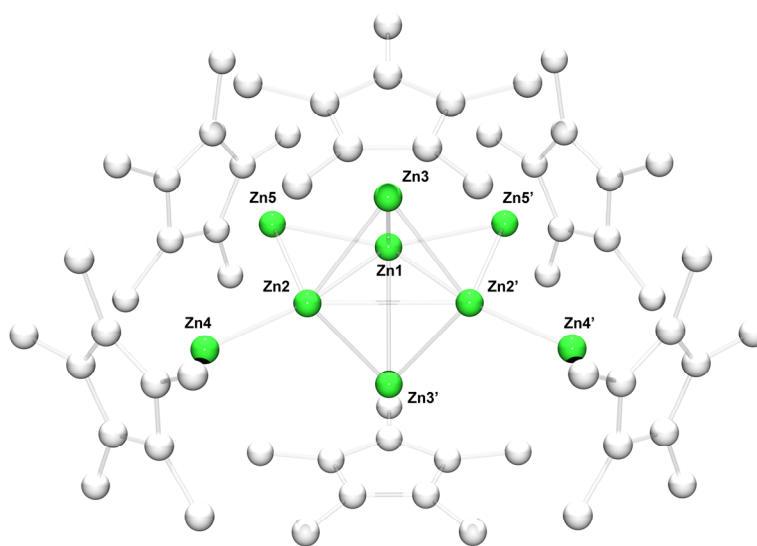


Figure 60. Optimized structure of $\{[Zn_9](Cp^*)_6\}^+$ (**4**) (PPBE0/Def2-TZVPP). The hydrogen atoms are omitted for clarity. Symmetry related Zn positions are primed.

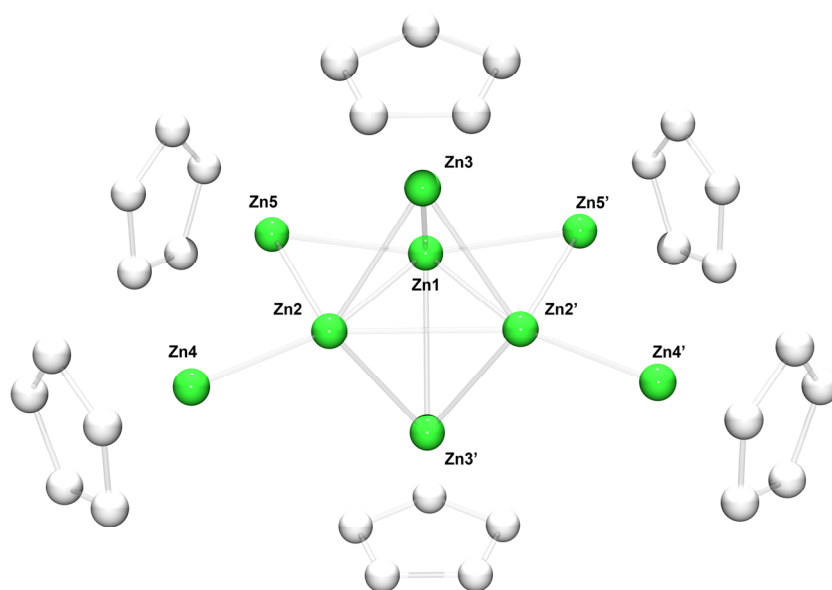


Figure 61. Optimized structure of $\{[Zn_9](Cp)_6\}^+$ (**5'**) (PPBE0/Def2-TZVPP). The hydrogen atoms are omitted for clarity. Symmetry related Zn positions are primed.

Table 6. Comparison of the Zn-Zn distances as determined from the molecular structure of **5** in the solid state and the calculated values obtained from the geometry optimized models **5** and **5'**.

	5 (exp.) [Å]	5 (cal.) [Å]	5' [Å]
Zn1-Zn2	2.472	2.487	2.518
Zn1-Zn5	2.405	2.436	2.434
Zn1-Zn3	2.710	2.683	2.728
Zn2-Zn5	2.776	2.898	2.840
Zn2-Zn4	2.338	2.409	2.379
Zn2-Zn3	2.588	2.664	2.629
Zn2-Zn2'	2.829	3.066	2.804
Zn-Zn (\emptyset)	2.641	2.753	2.660

6.11.2 Computational Details for $[\text{Zn}_5\text{Cu}_2\text{Cp}^*_5]^+$ (**9**).

Geometry optimization of **9** have been processed using TURBOMOLE V6.3.1 based on Ahlrichs' def2-TZVPP basis set.^[152] Stationary points were characterized by the analytical calculation of the Hessian matrix using TURBOMOLE's AOFORCE module. Dispersion effects have been accounted using Grimme's D3 correction. ELF calculations for **9** were conducted using the Multiwfn program.^[154]

For the EDA-NOCV calculations at the BP86/TZ2P+ level of theory the ADF(2012.01) program package has been employed. EDA divides the total interaction energy ΔE_{int} between two fragments into three parts, the quasiclassical electrostatic attraction ΔE_{elstat} , the Pauli repulsion ΔE_{Pauli} and the stabilizing orbital interaction ΔE_{orb} . The ΔE_{orb} term consists of contributions for the σ -type interaction ΔE_{σ} and π -type interaction ΔE_{π} .

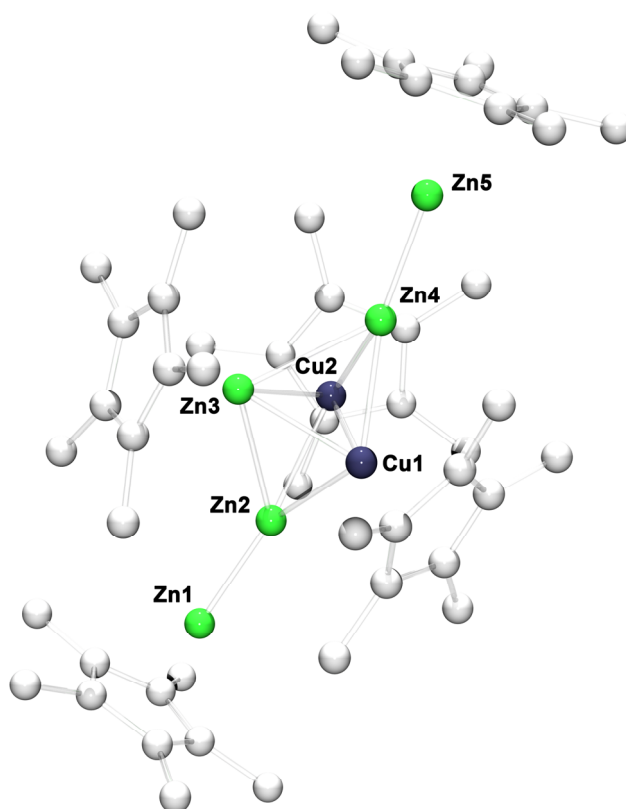


Figure 62. Optimized structure of $[\text{Zn}_5\text{Cu}_2\text{Cp}^*_5]^+$ (**9**) (BP86/TZVPP). The hydrogen atoms are omitted for clarity.

Table 7. Comparison of selected interatomic distances and angles as determined from the molecular structure of **9** in the solid state and the calculated values obtained from the geometry optimized model **9**.

	9 (exp.) [Å]/[°]	9 (cal.) [Å]/[°]
Cu1-Cu2	2.415	2.402
Cu1-Zn3	2.400	2.392
Cu2-Zn3	2.396	2.423
Zn1-Zn2	2.299	2.302
Zn4-Zn5	2.323	2.304
Cu2-Zn2	2.403	2.446
Zn3-Zn2	2.745	2.695
Cu1-Zn2	2.523	2.433
Cu2-Zn4	2.446	2.426
Zn3-Zn4	2.688	2.660
Cu1-Zn4	2.527	2.468
Cu1-Zn3-Cu2	60.5	59.9
Cu2-Cu1-Zn3	59.7	60.7
Zn3-Cu2-Cu1	59.9	59.5

6.12 Crystallographic Data

	1 [BAr ₄ F ⁻]	3 [BAr ₄ F ⁻] ₂ · 4 CH ₂ Cl ₂	4 [BAr ₄ F ⁻] · 5 C ₆ H ₅ F
Empirical formula	C ₅₄ H ₅₁ BF ₂₄ O ₃ Zn ₂	C ₁₁₁ H ₆₄ B ₂ C ₁₈ F ₄₈ N ₆ Zn ₂ Cl ₂	C ₁₂₃ H ₁₃₀ BF ₂₉ Zn ₁₀
<i>M</i> _r	1345.50	2815.61	2823.77
<i>T</i> [K]	110(2)	116(2)	105(2)
λ [Å]	1.54184	1.54184	1.54184
Crystal size [mm ³]	0.143 x 0.142 x 0.095	0.146 x 0.054 x 0.052	0.163 x 0.156 x 0.116
Crystal system	Orthorhombic	Monoclinic	Monoclinic
Space group	<i>Pbca</i>	<i>P21/c</i>	<i>Pm</i>
<i>a</i> [Å]	18.4540(2)	15.1012(5)	14.6062(2)
<i>b</i> [Å]	24.1318(3)	16.1231(5)	14.9083(2)
<i>c</i> [Å]	25.8120(2)	24.7275(7)	14.6711(2)
α [°]	90	90	90
β [°]	90	102.147(3)	92.414(1)
γ [°]	90	90	90
<i>V</i> [Å ³]	11494.8(2)	5885.8(3)	3191.85(8)
<i>Z</i>	8	2	1
ρ _{calc.} [g cm ⁻³]	1.555	1.589	1.469
μ [mm ⁻¹]	2.114	3.311	2.774
<i>F</i> (000)	5440	2804	1434
θ range [°]	3.467 - 69.999	3.295 - 74.929	2.964 - 74.129
Reflections collected / unique	30207 / 10879	25281 / 11758	23608 / 10053
<i>R</i> _{int}	0.0212	0.0343	0.0328
Reflections observed [<i>I</i> > 2σ(<i>I</i>)]	9553	8576	9913
Completeness to θ = 67.684° [%]	99.8	100.0	100.0
Data / restraints / Parameters	10879 / 0 / 875	11758 / 373 / 889	10053 / 254 / 669
Goodness-of-fit on <i>F</i> ²	1.059	1.077	1.068
<i>R</i> ₁ [<i>I</i> > 2σ(<i>I</i>)]	0.0745	0.0951	0.0361
<i>wR</i> ₂ (all data)	0.2170	0.3105	0.0957
Δ <i>F</i> _{max} ; Δ <i>F</i> _{min} [e Å ⁻³]	4.117; -1.191	0.875 / -0.994	0.406; -0.440

	5 · THF	6 [BAr ₄ ^F] · 4 C ₆ H ₅ F	8
Empirical formula	C ₆₄ H ₉₈ OZn ₉	C ₁₂₁ H ₁₃₄ BF ₂₈ N ₃ Zn ₈	C ₅₀ H ₇₅ Cu ₃ Zn ₄
<i>M</i> _r	1471.75	2696.07	1116.46
<i>T</i> [K]	111(2)	110(2)	100
<i>λ</i> [Å]	1.54184	1.54184	0.71073
Crystal size [mm ³]	0.076 x 0.071 x 0.067	0.405 x 0.145 x 0.054	0.320 x 0.143 x 0.136
Crystal system	Orthorhombic	Monoclinic	Monoclinic
Space group	<i>Cmcm</i>	<i>C2/c</i>	<i>Pn</i>
<i>a</i> [Å]	15.9901(4)	41.2620(5)	16.1793(14)
<i>b</i> [Å]	18.8473(5)	13.0922(2)	37.930(3)
<i>c</i> [Å]	21.9285(6)	46.1414(6)	17.4798(15)
<i>α</i> [°]	90	90	90
<i>β</i> [°]	90	97.5633(12)	105.636(3)
<i>γ</i> [°]	90	90	90
<i>V</i> [Å ³]	6608.6(3)	24709.2(6)	10330.0(15)
<i>Z</i>	4	8	2
<i>ρ</i> _{calc.} [g cm ⁻³]	1.479	1.449	1.451
<i>μ</i> [mm ⁻¹]	3.797	2.454	3.067
<i>F</i> (000)	3040	10576	4656
<i>θ</i> range [°]	3.625 - 74.006	3.545 - 76.538	2.217 - 25.350
Reflections collected / unique	8232 / 3483	52549 / 25212	347753 / 37767
<i>R</i> _{int}	0.0226	0.0264	0.0510
Reflections observed [<i>I</i> > 2σ(<i>I</i>)]	3103	20452	34345
Completeness to <i>θ</i> = 67.684° [%]	99.9	99.8	99.9
Data / restraints / Parameters	3483 / 0 / 195	25212 / 135 / 1253	37767 / 2 / 2154
Goodness-of-fit on <i>F</i> ²	1.073	1.039	1.065
<i>R</i> ₁ [<i>I</i> > 2σ(<i>I</i>)]	0.0297	0.0610	0.0363
<i>wR</i> ₂ (all data)	0.0740	0.1578	0.0878
<i>ΔF</i> _{max} ; <i>ΔF</i> _{min} [e Å ⁻³]	0.793; -0.639	0.871; -0.579	0.756; -0.792

	9 [BAr ₄ ^F] · 5 C ₆ H ₅ F	10 [BAr ₄ ^F] · 1.5 C ₆ H ₅ F
Empirical formula	C ₁₂₄ H ₁₂₂ BCu ₂ F ₃₁ Zn ₅	C ₁₀₁ H _{115.50} BCu ₃ F _{25.50} N ₄ Zn ₅
<i>M_r</i>	2666.10	2398.25
<i>T</i> [K]	100	112(2)
λ [Å]	0.71073	1.54184
Crystal size [mm ³]	0.053 x 0.051 x 0.021	0.094 x 0.092 x 0.037
Crystal system	Monoclin	Monoclinic
Space group	<i>Cc</i>	<i>C2/c</i>
<i>a</i> [Å]	23.729(3)	39.7722(9)
<i>b</i> [Å]	22.495(3)	14.7299(3)
<i>c</i> [Å]	36.442(5)	36.5894(10)
α [°]	90	90
β [°]	90.573(4)	36.5894(10)
γ [°]	90	90
<i>V</i> [Å ³]	19451(4)	21435.4(9)
<i>Z</i>	4	8
ρ_{calc} [g cm ⁻³]	1.394	1.486
μ [mm ⁻¹]	1.726	2.629
<i>F</i> (000)	8264	9768
θ range [°]	2.236 – 25.026	3.422 - 76.290
Reflections collected / unique	104015 / 32525	27852 / 18532
<i>R</i> _{int}	0.0665	0.0314
Reflections observed [<i>I</i> > 2 σ (<i>I</i>)]	21607	13571
Completeness to $\theta = 67.684^\circ$ [%]	99.9	86.2
Data / restraints / Parameters	32525 / 1064 / 2454	18532 / 30 / 1086
Goodness-of-fit on <i>F</i> ²	1.021	1.022
<i>R</i> 1 [<i>I</i> > 2 σ (<i>I</i>)]	0.0649	0.0644
<i>wR</i> 2 (all data)	0.1635	0.1919
ΔF_{max} ; ΔF_{min} [e Å ⁻³]	1.724; -0.581	0.992; -0.601

7 LITERATURE

1. F. A. Cotton, *Quarterly Reviews, Chemical Society*, **1966**, *20*, 389-401.
2. H. Pauly, *Atom, Molecule, and Cluster Beams II*, Springer Verlag, Berlin, **2000**.
3. L. Holmgren, H. Grönbeck, M. Andersson and A. Rosén, *Physical Review B*, **1996**, *53*, 16644-16651.
4. R. A. Larsen, S. K. Neoh and D. R. Herschbach, *Review of Scientific Instruments*, **1974**, *45*, 1511-1516.
5. O. F. Hagen, *Zeitschrift für Physik D Atoms, Molecules and Clusters*, **1991**, *20*, 425-428.
6. O. F. Hagen and W. Obert, *The Journal of Chemical Physics*, **1972**, *56*, 1793-1802.
7. J. B. Anderson and J. B. Fenn, *The Physics of Fluids*, **1965**, *8*, 780-787.
8. C. Binns, *Surface Science Reports*, **2001**, *44*, 1-49.
9. K. Sattler, J. Mühlbach and E. Recknagel, *Physical Review Letters*, **1980**, *45*, 821-824.
10. F. Frank, W. Schulze, B. Tesche, J. Urban and B. Winter, *Surface Science*, *156*, 90-99.
11. S. J. Riley, E. K. Parks, C. R. Mao, L. G. Pobo and S. Wexler, *The Journal of Physical Chemistry*, **1982**, *86*, 3911-3913.
12. U. Zimmermann, N. Malinowski, U. Näher, S. Frank and T. P. Martin, *Zeitschrift für Physik D Atoms, Molecules and Clusters*, **1994**, *31*, 85-93.
13. I. M. Goldby, B. von Issendorff, L. Kuipers and R. E. Palmer, *Review of Scientific Instruments*, **1997**, *68*, 3327-3334.
14. P. Fayet and L. Wöste, *Surface Science*, **1985**, *156*, 134-139.
15. W. Begemann, S. Dreihöfer, K. H. Meiwes-Broer and H. O. Lutz, *Zeitschrift für Physik D Atoms, Molecules and Clusters*, **1986**, *3*, 183-188.
16. I. Katakuse, T. Ichihara, Y. Fujita, T. Matsuo, T. Sakurai and H. Matsuda, *International Journal of Mass Spectrometry and Ion Processes*, **1985**, *67*, 229-236.
17. V. E. Bondybey and J. H. English, *The Journal of Chemical Physics*, **1982**, *76*, 2165-2170.
18. R. E. Smalley, *Laser Chemistry*, **1983**, *2*, 167-184.
19. W. A. de Heer and P. Milani, *Zeitschrift für Physik D Atoms, Molecules and Clusters*, **1991**, *20*, 437-439.
20. S. Maruyama, L. R. Anderson and R. E. Smalley, *Review of Scientific Instruments*, **1990**, *61*, 3686-3693.

21. H. R. Siekmann, C. Lüder, J. Faehrmann, H. O. Lutz and K. H. Meiwes-Broer, *Zeitschrift für Physik D Atoms, Molecules and Clusters*, **1991**, *20*, 417-420.
22. J. Politiek, P. K. Rol, J. Los and P. G. Ikelaar, *Review of Scientific Instruments*, **1968**, *39*, 1147-1150.
23. M. Zhao, L. Sun and R. M. Crooks, *J. Am. Chem. Soc.*, **1998**, *120*, 4877-4878.
24. L. Balogh and D. A. Tomalia, *J. Am. Chem. Soc.*, **1998**, *120*, 7355-7356.
25. J. Zheng, J. T. Petty and R. M. Dickson, *J. Am. Chem. Soc.*, **2003**, *125*, 7780-7781.
26. K. Yamamoto, T. Imaoka, W. J. Chun, O. Enoki, H. Katoh, M. Takenaga and A. Sonoi, *Nat. Chem.*, **2009**, *1*, 397-402.
27. T. Imaoka, H. Kitazawa, W. J. Chun, S. Omura, K. Albrecht and K. Yamamoto, *J. Am. Chem. Soc.*, **2013**, *135*, 13089-13095.
28. T. Imaoka, H. Kitazawa, W. J. Chun and K. Yamamoto, *Angew. Chem. Int. Ed.*, **2015**, *54*, 9810-9815.
29. N. T. Tran, D. R. Powell and L. F. Dahl, *Angew. Chem. Int. Ed.*, **2000**, *39*, 4121-4125.
30. G. Schmid, R. Pfeil, R. Boese, F. Bandermann, S. Meyer, G. H. M. Calis and J. W. A. van der Velden, *Chemische Berichte*, **1981**, *114*, 3634-3642.
31. H. Schnöckel, *Dalton Trans.*, **2008**, 4344-4362.
32. H. Schnöckel, *Chemical Reviews*, **2010**, *110*, 4125-4163.
33. A. Purath, R. Koppe and H. Schnöckel, *Chem. Commun.*, **1999**, 1933-1934.
34. A. Purath, R. Köppe and H. Schnöckel, *Angew. Chem. Int. Ed.*, **1999**, *38*, 2926-2928.
35. H. Köhnlein, A. Purath, C. Klemp, E. Baum, I. Krossing, G. Stösser and H. Schnöckel, *Inorg. Chem.*, **2001**, *40*, 4830-4838.
36. A. Ecker, E. Weckert and H. Schnöckel, *Nature*, **1997**, *387*, 379-381.
37. J. Vollet, J. R. Hartig and H. Schnöckel, *Angew. Chem. Int. Ed.*, **2004**, *43*, 3186-3189.
38. A. Schnepf, G. Stösser and H. Schnöckel, *J. Am. Chem. Soc.*, **2000**, *122*, 9178-9181.
39. K. Weiß and H. Schnöckel, *Z. anorg. allg. Chem.*, **2003**, *629*, 1175-1183.
40. K. Weiß, R. Köppe and H. Schnöckel, *International Journal of Mass Spectrometry*, **2002**, *214*, 383-395.
41. A. Schnepf and H. Schnöckel, *Angew. Chem. Int. Ed.*, **2001**, *40*, 711-715.
42. T. A. Nguyen, Z. R. Jones, B. R. Goldsmith, W. R. Buratto, G. Wu, S. L. Scott and T. W. Hayton, *J. Am. Chem. Soc.*, **2015**, *137*, 13319-13324.
43. K. K. Chakrahari, J. H. Liao, S. Kahlal, Y. C. Liu, M. H. Chiang, J. Y. Saillard and C. W. Liu, *Angew. Chem. Int. Ed.*, **2016**, *55*, 14704-14708.

44. W. D. Knight, K. Clemenger, W. A. de Heer, W. A. Saunders, M. Y. Chou and M. L. Cohen, *Physical Review Letters*, **1984**, *52*, 2141-2143.
45. D. M. P. Mingos, T. Slee and L. Zhenyang, *Chemical Reviews*, **1990**, *90*, 383-402.
46. H. A. Jahn and E. Teller, *Proceedings of the Royal Society of London. Series A - Mathematical and Physical Sciences*, **1937**, *161*, 220.
47. K. Clemenger, *Physical Review B*, **1985**, *32*, 1359-1362.
48. W. A. de Heer, *Reviews of Modern Physics*, **1993**, *65*, 611-676.
49. K. Wade, *Chem. Commun.*, **1971**, 792-793.
50. D. M. P. Mingos, *Nature*, **1972**, *236*, 99-102.
51. H. C. Longuet-Higgins and M. D. Robberts, *Proc. R. Soc.*, **1955**, *A230*, 110.
52. T. P. Fehlner, J.-F. Halet and J.-Y. Saillard, *Molecular Clusters*, Cambridge University Press, New York, **2007**.
53. T. Cadenbach, T. Bollermann, C. Gemel, I. Fernandez, M. von Hopffgarten, G. Frenking and R. A. Fischer, *Angew. Chem. Int. Ed.*, **2008**, *47*, 9150-9154.
54. A. Werner, *Zeitschrift für anorganische Chemie*, **1893**, *3*, 267-330.
55. E. N. Esenturk, J. Fettingner, Y.-F. Lam and B. Eichhorn, *Angew. Chem. Int. Ed.*, **2004**, *116*, 2184-2186.
56. J. R. Gispert, *Coordination Chemistry*, Wiley-VHC, Weinheim, 1st edn., **2008**.
57. T. Nasch and W. Jeitschko, *J. Solid State Chem.*, **1999**, *143*, 95-103.
58. T. Cadenbach, T. Bollermann, C. Gemel, M. Tombul, I. Fernandez, H. M. van, G. Frenking and R. A. Fischer, *J. Am. Chem. Soc.*, **2009**, *131*, 16063-16077.
59. D. Bravo-Zhivotovskii, M. Yuzefovich, M. Bendikov, K. Klinkhammer and Y. Apeloig, *Angew. Chem., Int. Ed.*, **1999**, *38*, 1100-1102.
60. R. Faggiani, R. J. Gillespie and J. E. Vekris, *J. Chem. Soc., Chem. Commun.*, **1986**, 517-518.
61. D. L. Reger, S. S. Mason and A. L. Rheingold, *J. Am. Chem. Soc.*, **1993**, *115*, 10406-10407.
62. Z. Zhu, R. C. Fischer, J. C. Fettingner, E. Rivard, M. Brynda and P. P. Power, *J. Am. Chem. Soc.*, **2006**, *128*, 15068-15069.
63. D. H. Kerridge and S. A. Tariq, *J. Chem. Soc. A*, **1967**, 1122-1125.
64. F. Rittner, A. Seidel and B. Boddenberg, *Microporous Mesoporous Mater.*, **1998**, *24*, 127-131.
65. Y. Tian, G.-D. Li and J.-S. Chen, *J. Am. Chem. Soc.*, **2003**, *125*, 6622-6623.

66. S. Zhen, D. Bae and K. Seff, *J. Phys. Chem. B*, **2000**, *104*, 515-525.
67. T. M. Greene, W. Brown, L. Andrews, A. J. Downs, G. V. Chertihin, N. Runeberg and P. Pyykko, *J. Phys. Chem.*, **1995**, *99*, 7925-7934.
68. X. Wang and L. Andrews, *J. Phys. Chem. A*, **2004**, *108*, 11006-11013.
69. I. Resa, E. Carmona, E. Gutierrez-Puebla and A. Monge, *Science*, **2004**, *305*, 1136-1138.
70. D. del Río, A. Galindo, I. Resa and E. Carmona, *Angew. Chem. Int. Ed.*, **2005**, *44*, 1244-1247.
71. A. Gorrane, I. Resa, A. Rodriguez, E. Carmona, E. Alvarez, E. Gutierrez-Puebla, A. Monge, A. Galindo, D. del Río and R. A. Andersen, *J. Am. Chem. Soc.*, **2007**, *129*, 693-703.
72. P. Jochmann and D. W. Stephan, *Angew. Chem. Int. Ed.*, **2013**, *52*, 9831-9835.
73. D. del Río, I. Resa, A. Rodriguez, L. Sanchez, R. Koppe, A. J. Downs, C. Y. Tang and E. Carmona, *J. Phys. Chem. A*, **2008**, *112*, 10516-10525.
74. S. S. Hepperle and Y. A. Wang, *J. Phys. Chem. A*, **2008**, *112*, 9619-9622.
75. J. W. Kress, *J. Phys. Chem. A*, **2005**, *109*, 7757-7763.
76. Y. Kan, *J. Mol. Struct.: THEOCHEM*, **2007**, *805*, 127-132.
77. M. R. Philpott and Y. Kawazoe, *J. Mol. Struct.: THEOCHEM*, **2006**, *773*, 43-52.
78. K. K. Pandey, *J. Organomet. Chem.*, **2007**, *692*, 1058-1063.
79. Z.-Z. Xie and W.-H. Fang, *Chem. Phys. Lett.*, **2005**, *404*, 212-216.
80. M. R. Philpott and Y. Kawazoe, *Chem. Phys.*, **2006**, *327*, 283-290.
81. M. R. Philpott and Y. Kawazoe, *J. Mol. Struct.: THEOCHEM*, **2006**, *776*, 113-123.
82. Z.-Z. Liu, W. Q. Tian, J.-K. Feng, G. Zhang and W.-Q. Li, *J. Mol. Struct.: THEOCHEM*, **2006**, *758*, 127-138.
83. Y. Xie, H. F. Schaefer, III and R. B. King, *J. Am. Chem. Soc.*, **2005**, *127*, 2818-2819.
84. M. R. Philpott and Y. Kawazoe, *Chem. Phys.*, **2007**, *333*, 201-207.
85. S. L. Richardson, T. Baruah and M. R. Pederson, *Chem. Phys. Lett.*, **2005**, *415*, 141-145.
86. X. Li, S. Huo, Y. Zeng, Z. Sun, S. Zheng and L. Meng, *Organometallics*, **2013**, *32*, 1060-1066.
87. M. Carrasco, R. Peloso, I. Resa, A. Rodriguez, L. Sanchez, E. Alvarez, C. Maya, R. Andreu, J. J. Calvente, A. Galindo and E. Carmona, *Inorg. Chem.*, **2011**, *50*, 6361-6371.

88. D. Schuchmann, U. Westphal, S. Schulz, U. Florke, D. Blaser and R. Boese, *Angew. Chem. Int. Ed.*, **2009**, *48*, 807-810.
89. P. Jochmann and D. W. Stephan, *Chem. Eur. J.*, **2014**, *20*, 8370-8378.
90. M. Carrasco, R. Peloso, A. Rodriguez, E. Alvarez, C. Maya and E. Carmona, *Chem. Eur. J.*, **2010**, *16*, 9754-9757.
91. Y. Wang, B. Quillian, P. Wei, H. Wang, X.-J. Yang, Y. Xie, R. B. King, P. V. R. Schleyer, H. F. Schaefer, III and G. H. Robinson, *J. Am. Chem. Soc.*, **2005**, *127*, 11944-11945.
92. Z. Zhu, R. J. Wright, M. M. Olmstead, E. Rivard, M. Brynda and P. P. Power, *Angew. Chem. Int. Ed.*, **2006**, *45*, 5807-5810.
93. I. L. Fedushkin, A. A. Skatova, S. Y. Ketkov, O. V. Eremenko, A. V. Piskunov and G. K. Fukin, *Angew. Chem. Int. Ed.*, **2007**, *46*, 4302-4305.
94. X.-J. Yang, J. Yu, Y. Liu, Y. Xie, H. F. Schaefer, Y. Liang and B. Wu, *Chem. Commun.*, **2007**, 2363.
95. Y. C. Tsai, D. Y. Lu, Y. M. Lin, J. K. Hwang and J. S. Yu, *Chem. Commun.*, **2007**, 4125-4127.
96. B. Buchin, C. Gemel, T. Cadenbach, R. Schmid and R. A. Fischer, *Angew. Chem., Int. Ed.*, **2006**, *45*, 1074-1076.
97. S. Schulz, D. Schuchmann, I. Krossing, D. Himmel, D. Blaser and R. Boese, *Angew. Chem. Int. Ed.*, **2009**, *48*, 5748-5751.
98. S. Schulz, D. Schuchmann, U. Westphal and M. Bolte, *Organometallics*, **2009**, *28*, 1590-1592.
99. S. Schulz, S. Gondzik, D. Schuchmann, U. Westphal, L. Dobrzycki, R. Boese and S. Harder, *Chem. Commun.*, **2010**, *46*, 7757.
100. S. Gondzik, D. Blaser, C. Wolper and S. Schulz, *Chem. Eur. J.*, **2010**, *16*, 13599-13602.
101. H. P. Nayek, A. Luehl, S. Schulz, R. Koeppel and P. W. Roesky, *Chem. Eur. J.*, **2011**, *17*, 1773-1777.
102. K. Mayer, L.-A. Jantke, S. Schulz and T. F. Fässler, *Angew. Chem. Int. Ed.*, **2017**, *56*, 2350-2355.
103. K. Freitag, H. Banh, C. Ganesamoorthy, C. Gemel, R. W. Seidel and R. A. Fischer, *Dalton Trans.*, **2013**, *42*, 10540-10544.
104. M. Halbherr, T. Bollermann, C. Gemel and R. A. Fischer, *Angew. Chem. Int. Ed.*, **2010**, *49*, 1878-1881.

105. H. Banh, C. Gemel, R. W. Seidel and R. A. Fischer, *Chem. Commun.*, **2015**, *51*, 2170-2172.
106. A. Kempter, C. Gemel, T. Cadenbach and R. A. Fischer, *Inorg. Chem.*, **2007**, *46*, 9481-9487.
107. H. Banh, *Master Thesis, Ruhr-Universität Bochum*, **2013**.
108. K. Freitag, H. Banh, C. Gemel, P. Jerabek, R. W. Seidel, G. Frenking and R. A. Fischer, *Inorg. Chem.*, **2015**, *54*, 352-358.
109. T. Bollermann, K. Freitag, C. Gemel, R. W. Seidel, M. von Hopffgarten, G. Frenking and R. A. Fischer, *Angew. Chem. Int. Ed.*, **2011**, *50*, 772-776.
110. B. D. Cutforth, C. G. Davies, P. A. W. Dean, R. J. Gillespie, P. R. Ireland and P. K. Ummat, *Inorg. Chem.*, **1973**, *12*, 1343-1347.
111. B. D. Cutforth, R. J. Gillespie, P. Ireland, J. F. Sawyer and P. K. Ummat, *Inorg. Chem.*, **1983**, *22*, 1344-1347.
112. T. Bollermann, K. Freitag, C. Gemel, M. Molon, R. W. Seidel, M. von Hopffgarten, P. Jerabek, G. Frenking and R. A. Fischer, *Inorg. Chem.*, **2011**, *50*, 10486-10492.
113. T. Bollermann, K. Freitag, C. Gemel, R. W. Seidel and R. A. Fischer, *Organometallics*, **2011**, *30*, 4123-4127.
114. G. J. Kubas, R. R. Ryan, B. I. Swanson, P. J. Vergamini and H. J. Wasserman, *J. Am. Chem. Soc.*, **1984**, *106*, 451-452.
115. G. J. Kubas, *Proceedings of the National Academy of Sciences*, **2007**, *104*, 6901-6907.
116. B. Eguillor, M. A. Esteruelas, V. Lezáun, M. Oliván and E. Oñate, *Chem. Eur. J.*, **2017**, *23*, 1526-1530.
117. K. Freitag, M. Molon, P. Jerabek, K. Dilchert, C. Rosler, R. W. Seidel, C. Gemel, G. Frenking and R. A. Fischer, *Chem. Sci.*, **2016**, *7*, 6413-6421.
118. R. Ayala, E. Carmona and A. Galindo, *Inorganica Chimica Acta*, **2017**, DOI: 10.1016/j.ica.2017.06.008.
119. K. Freitag, C. Gemel, P. Jerabek, I. M. Oppel, R. W. Seidel, G. Frenking, H. Banh, K. Dilchert and R. A. Fischer, *Angew. Chem. Int. Ed.*, **2015**, *54*, 4370-4374.
120. J. O. Hirschfelder, *The Journal of Chemical Physics*, **1938**, *6*, 795-806.
121. K. Freitag, H. Banh, C. Gemel, R. W. Seidel, S. Kahlal, J.-Y. Saillard and R. A. Fischer, *Chem. Commun.*, **2014**, *50*, 8681.
122. M. Molon, C. Gemel, R. W. Seidel, P. Jerabek, G. Frenking and R. A. Fischer, *Inorg. Chem.*, **2013**, *52*, 7152-7160.

123. A. Aguado, A. Vega, A. Lebon and B. von Issendorff, *Angew. Chem. Int. Ed.*, **2015**, *54*, 2111-2115.
124. U. Häußermann, P. Viklund, C. Svensson, S. Eriksson, P. Berastegui and S. Lidin, *Angew. Chem. Int. Ed.*, **1999**, *38*, 488-492.
125. P. Viklund, C. Svensson, S. Hull, S. I. Simak, P. Berastegui and U. Häußermann, *Chem. Eur. J.*, **2001**, *7*, 5143-5152.
126. P. Cui, H.-S. Hu, B. Zhao, J. T. Miller, P. Cheng and J. Li, *Nat. Commun.*, **2015**, *6*, 1-5.
127. H. J. Flad, F. Schautz, Y. Wang, M. Dolg and A. Savin, *Eur. Phys. J. D*, **1999**, *6*, 243-254.
128. J. Hicks, E. J. Underhill, C. E. Kefalidis, L. Maron and C. Jones, *Angew. Chem. Int. Ed.*, **2015**, *54*, 10000-10004.
129. I. Resa, E. Álvarez and E. Carmona, *Z. anorg. allg. Chem.*, **2007**, *633*, 1827-1831.
130. J. M. Goicoechea and S. C. Sevov, *Angew. Chem. Int. Ed.*, **2006**, *45*, 5147-5150.
131. K. Wade, in *Transistion Metal Clusters*, ed. B. F. G. Johnhson, John Wiley & Sons, Chichester, 1980, pp. 193-264.
132. D. J. W. D. M. Mingos, in *Introduction to cluster chemistry*, Prentice-Hall, Englewood Cliffs, 1990.
133. J. K. B. E. D. Glendening, A. E. Reed, J. E. Carpenter, J. A. Bohmann, C. M. Morales, F. Weinhold, F. Theoretical Chemistry Institute, University of Wisconsin, Madison, WI, 2001, <http://www.chem.wisc.edu/~nbo5>.
134. Y. Kaneko, Y. Arichika and T. Ishimasa, *Philos. Mag. Lett.*, **2001**, *81*, 777-787.
135. H. Euchner, T. Yamada, S. Rols, T. Ishimasa, J. Ollivier, H. Schober, M. Mihalkovic and M. de Boissieu, *J. Phys. Condens. Matter.*, **2014**, *26*, 055402.
136. Deutsches Kupferinstitut, *Kupfer-Zink-Legierungen (Messing und Sondermessing)*, **2007**, *Informationsdruck i.5*, 2-9.
137. H. Banh, K. Dilchert, C. Schulz, C. Gemel, R. W. Seidel, R. Gautier, S. Kahlal, J. Y. Saillard and R. A. Fischer, *Angew. Chem. Int. Ed.*, **2016**, *55*, 3285-3289.
138. H. Häkkinen, *Chemical Society reviews*, **2008**, *37*, 1847-1859.
139. A. C. Reber and S. N. Khanna, *Acc. Chem. Res.*, **2017**, *50*, 255-263.
140. J. Echeverria, A. Falceto and S. Alvarez, *Angew. Chem. Int. Ed.*, **2017**, *56*, 10151-10155.
141. CrysAlisPro Software system, Agilent Technologies UK Ltd, Oxford, UK.

142. APEX suite of crystallographic software, APEX 3, version 2015.5-2, Bruker AXS Inc., Madison, Wisconsin, USA (2015).
143. G. M. Sheldrick, *Acta Cryst.*, **2008**, *A64*, 112-122.
144. G. M. Sheldrick, *Acta Cryst.*, **2015**, *C71*, 3-8.
145. A. L. Spek, *Acta Cryst.*, **2015**, *C71*, 9-18.
146. B. J. Le, H. Jiao, W. E. Meyer, F. Hampel and J. A. Gladysz, *J. Organomet. Chem.*, **2000**, *616*, 54-66.
147. B. Janza and A. Studer, *Organic Letters*, **2006**, *8*, 1875-1878.
148. R. A. Gaussian 09, M. J. Frisch, G. W. Trucks, H. B. Schlegel, G. E. Scuseria, M. A. Robb, J. R. Cheeseman, G. Scalmani, V. Barone, B. Mennucci, G. A. Petersson, H. Nakatsuji, M. Caricato, X. Li, H. P. Hratchian, A. F. Izmaylov, J. Bloino, G. Zheng, J. L. Sonnenberg, M. Hada, M. Ehara, K. Toyota, R. Fukuda, J. Hasegawa, M. Ishida, T. Nakajima, Y. Honda, O. Kitao, H. Nakai, T. Vreven, J. A. Montgomery, Jr., J. E. Peralta, F. Ogliaro, M. Bearpark, J. J. Heyd, E. Brothers, K. N. Kudin, V. N. Staroverov, R. Kobayashi, J. Normand, K. Raghavachari, A. Rendell, J. C. Burant, S. S. Iyengar, J. Tomasi, M. Cossi, N. Rega, J. M.; Millam, M. Klene, J. E. Knox, J. B. Cross, V. Bakken, C. Adamo, J. Jaramillo, R. Gomperts, R. E. Stratmann, O. Yazyev, A. J. Austin, R. Cammi, C. Pomelli, J. W. Ochterski, R. L. Martin, K. Morokuma, V. G. Zakrzewski, G. A. Voth, P. Salvador, J. J. Dannenberg, S. Dapprich, A. D. Daniels, O. Farkas, J. B. Foresman, J. V. Ortiz, J. Cioslowski, D. J. Fox, Gaussian, Inc., Wallingford CT, 2009M.
149. J. P. Perdew, M. Ernzerhof and K. Burke, *The Journal of Chemical Physics*, **1996**, *105*, 9982-9985.
150. J. P. Perdew, K. Burke and M. Ernzerhof, *Physical Review Letters*, **1996**, *77*, 3865-3868.
151. J. P. Perdew, K. Burke and M. Ernzerhof, *Physical Review Letters*, **1997**, *78*, 1396-1396.
152. F. Weigend and R. Ahlrichs, *Phys. Chem. Chem. Phys.*, **2005**, *7*, 3297-3305.
153. D. M. Kohout, version 4.6, Radebeul, 2011.
154. T. Lu and F. Chen, *J. Comput. Chem.*, **2012**, *33*, 580-592.

8 SUPPLEMENT

8.1 Conferences: Poster Presentations

- H. Banh, K. Dilchert, C. Schulz, C. Gemel, R. W. Seidel, R. Gautier, S. Kahlal, J.-Y. Saillard, R. A. Fischer, “*Atom-Precise Organometallic Zinc Clusters*“, 27th International Conference on Organometallic Chemistry, Melbourne, Australia, July **2016**.
- H. Banh, K. Dilchert, C. Schulz, C. Gemel, R. W. Seidel, R. Gautier, S. Kahlal, J.-Y. Saillard, R. A. Fischer, “*Ligand Protected Zinc Clusters*“, The 14th International Symposium on Inorganic Ring Systems, Regensburg, Deutschland, July **2015**.
- H. Banh, C. Gemel, R. A. Fischer, “*Cationic Low Valent Zinc Compounds*“, Ruhr-Universität Bochum Research School Plus: Research Day 2014, Bochum, Deutschland, November **2014**.
- H. Banh, C. Gemel, R. A. Fischer, “*Oxidative cleavage of Zn-Cp* bonds: [Zn₂]²⁺ as a building block for novel low valent zinc compounds*“, 246th ACS National Meeting & Exposition, Indianapolis, United States, September **2013**.

8.2 Publications

8.2.1 Thesis Related Publications

- H. Banh, K. Dilchert, C. Schulz, C. Gemel, R. W. Seidel, R. Gautier, S. Kahlal, J.-Y. Saillard, R. A. Fischer, “*Atom-Precise Organometallic Zinc Clusters*“, *Angew. Chem. Int. Ed.* **2016**, *55*, 3285-3289.
- H. Banh, C. Gemel, R. W. Seidel, R. A. Fischer, “*A solvated zinc analogue of the calomel-dication*“, *Chem. Commun.* **2015**, *51*, 2170-2172.
- H. Banh, J. Hornung, T. Kratz, C. Gemel, A. Pöthig, R. A. Fischer, “*Nanobrass*“, manuscript in preparation, c.f. chapter 4.3.

8.2.2 Other Publications

- A. Schneemann, R. Rudolf, S. Henke, Y. Takahashi, H. Banh, I. Hante, C. Schneider, S. Noro, R. A. Fischer, “Linker Functionalization Triggers an Alternative 3D-Topology for Zn-Isophthalate-4,4'-Bipyridine Frameworks“, *Dalton Trans.* **2017**, DOI: 10.1039/C7DT01195D
- C. Roch-Marchal, T. Hidalgo, H. Banh, R. A. Fischer, P. Horcajada, “A Promising Catalytic and Theranostic Agent Obtained through the In-Situ Synthesis of Au Nanoparticles with a Reduced Polyoxometalate Incorporated within Mesoporous MIL-101”, *Eur. J. Inorg. Chem.* **2016**, 27, 4387–4394.
- K. Freitag, C. Gemel, P. Jerabek, R. W. Seidel, G. Frenking, H. Banh, K. Dilchert, R. A. Fischer, “Embryonic Brass: The σ -aromatic Clusters $[\text{Zn}_3]^+$ und $[\text{Zn}_2\text{Cu}]^+$ “, *Angew. Chem. Int. Ed.* **2015**, 54, 4370-4374.
- K. Freitag, H. Banh, C. Gemel, P. Jerabek, R. W. Seidel, G. Frenking, R. A. Fischer, “Dizinc Cation $[\text{Zn}_2]^{2+}$ Trapped in a Homoleptic Metalloid Coordination Environment Stabilized by Dispersion Forces: $[\text{Zn}_2(\text{GaCp}^*)_6][\text{BAr}_4^{\text{F}}]_2$ “, *Inorg. Chem.* **2015**, 54, 352-358.
- K. Freitag, H. Banh, C. Gemel, R. W. Seidel, S. Kahlal, J.-Y. Saillard, R. A. Fischer, “Molecular Brass: Cu_4Zn_4 , a Ligand Protected Superatom Cluster“, *Chem. Commun.* **2014**, 50, 8681-8684.
- K. Freitag, H. Banh, C. Ganesamoorthy, C. Gemel, R. W. Seidel, R. A. Fischer, “Cp* as a Removable Protecting Group: Low Valent Zn(I) Compounds by Reductive Elimination, Protolytic and Oxidative Cleavage of Zn–Cp*“, *Dalton Trans.* **2013**, 42, 10540-10544.

8.3 Curriculum Vitae

Personal Details

- Nationality German
- Date of birth 15th May 1988
- Place of birth Moers, Germany

Academic Background

- 11/2013 – 10/2017 PhD student in the group of Prof. Dr. Roland A. Fischer at the Ruhr-University Bochum and at the Technical University Munich, Germany
- 10/2011 – 09/2013 Master studies in Chemistry at the Ruhr-University Bochum, Germany
 - Master of Science: Average Grade 1.0
- 10/2008 – 09/2011 Bachelor studies in Chemistry at the Ruhr-University Bochum, Germany
 - Bachelor of Science: Average Grade 1.2
- 02/1999 – 06/2007 Gymnasium Adolfinum in Moers, Germany
- 08/1998 – 02/1999 Heisenberg-Gymnasium in Gladbeck, Germany

International Experience

- 06/2016 – 09/2016 Research stay in the group of Prof. Dr. Simon Aldridge at the University of Oxford, United Kingdom

Special Achievements

- 06/2016 – 09/2016 Project International (PR.INT) scholarship of the Ruhr-University Bochum Research School Plus for a research stay at the University of Oxford
- 07/2016 Price of the University of Western Australia for the best Poster at the “27th International Conference on Organometallic Chemistry“ in Melbourne, Australia
- 07/2016 Scholarship of the Gesellschaft Deutscher Chemiker (GDCh) for a scientific conference participation
- 03/2014 – 02/2016 PhD scholarship of the Fonds der Chemischen Industrie (FCI)
- 12/2013 GDCh price for the best Master graduation in chemistry at the Ruhr-University Bochum
- 10/2010 – 09/2012 Deutschlandstipendium sponsored by the
 - Evonik Industries AG (2011/2012)
 - Sensolytics GmbH (2010/2011)
- 06/2007 GDCh price for the best graduate in chemistry at the Gymnasium Adolfinum in Moers, Germany